

2022

Partial Wave Analysis Of Strange Mesons Decaying To $K + \pi - \pi$ + In The Reaction $\Gamma p \rightarrow K + \pi + \pi - \Lambda(1520)$ And The Commissioning Of The Gluex Dirc Detector

Andrew Hurley

College of William and Mary - Arts & Sciences, Andhurley14@gmail.com

Follow this and additional works at: <https://scholarworks.wm.edu/etd>

Part of the [Physics Commons](#)

Recommended Citation

Hurley, Andrew, "Partial Wave Analysis Of Strange Mesons Decaying To $K + \pi - \pi$ + In The Reaction $\Gamma p \rightarrow K + \pi + \pi - \Lambda(1520)$ And The Commissioning Of The Gluex Dirc Detector" (2022). *Dissertations, Theses, and Masters Projects*. William & Mary. Paper 1686662893.

<https://dx.doi.org/10.21220/s2-b26x-tb15>

This Dissertation is brought to you for free and open access by the Theses, Dissertations, & Master Projects at W&M ScholarWorks. It has been accepted for inclusion in Dissertations, Theses, and Masters Projects by an authorized administrator of W&M ScholarWorks. For more information, please contact scholarworks@wm.edu.

Partial Wave Analysis of Strange Mesons Decaying to $K^+\pi^+\pi^-$ in the Reaction
 $\gamma p \rightarrow K^+\pi^+\pi^-\Lambda(1520)$ and the Commissioning of the GlueX DIRC Detector

Andrew Hurley

Saint Augustine, Florida

Master of Science, William & Mary, 2018
Bachelor of Science, Florida State University, 2016

A Dissertation presented to the Graduate Faculty
of The College of William & Mary in Candidacy for the Degree of
Doctor of Philosophy

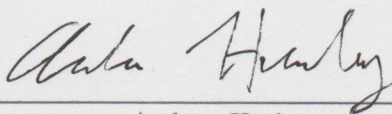
Department of Physics

College of William & Mary
January 2023

APPROVAL PAGE

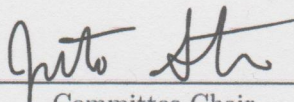
This Dissertation is submitted in partial fulfillment of
the requirements for the degree of

Doctor of Philosophy



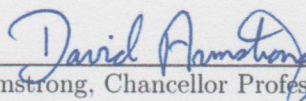
Andrew Hurley

Approved by the Committee, October 2022

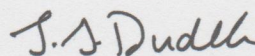


Committee Chair

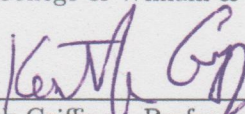
Justin Stevens, Associate Professor, Physics
College of William & Mary



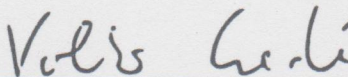
David Armstrong, Chancellor Professor, Physics
College of William & Mary



Jozef Dudek, Sallie Gertrude Smoot Spears Associate Professor, Physics
College of William & Mary



Keith Griffioen, Professor, Physics
College of William & Mary



Volker Crede, Professor, Physics
Florida State University

ABSTRACT

Hadron spectroscopy is a cornerstone of our understanding of the strong nuclear interactions. Studying the hadron spectrum led to the postulation of quarks and gluons, and the development of Quantum Chromodynamics (QCD), the theory of the strong nuclear force. Today hadron spectroscopy provides an important test of QCD, particularly in the non-perturbative energy regime. One such test is the existence of hybrid hadrons that have gluonic degrees of freedom, *e.g.* $q\bar{q}g$ states, that are allowed by QCD but have remained elusive in experimental searches. The GlueX experiment located at Thomas Jefferson National Accelerator Facility, is designed to map the light meson spectrum, including hybrid mesons, produced by a linearly polarized photon beam that is scattered off of a liquid hydrogen target. This dissertation concerns the installation and commissioning of the GlueX DIRC upgrade and the analysis of three reactions measured by the GlueX experiment.

The GlueX DIRC is a particle identification detector installed as an upgrade to the GlueX experiment in 2019 to improve the experiment's ability to distinguish pions and kaons. The DIRC uses Cherenkov photons radiated by charged particles that travel faster than the speed of light in the detector medium to determine the velocity of said particles. The velocity measurement is used in conjunction with momentum measurements from other detectors to determine the mass of the particle. The DIRC will be essential to the future of strange meson spectroscopy in GlueX.

The reactions $\gamma p \rightarrow K^+K^-\pi^+\pi^-p$, $\gamma p \rightarrow K^+K^-\pi^0\pi^0p$, $\gamma p \rightarrow K^+K^-\pi^0\eta p$ were initially chosen for this analysis to search for the hybrid meson candidate $\phi(2170)$ and related resonances. The $\phi(2170)$ has been observed in e^+e^- collider experiments decaying to $K^+K^-\pi^+\pi^-$ and $K^+K^-\pi^0\pi^0$, among other final states. The $\phi(2170)$ was not observed in this analysis. The reaction $\gamma p \rightarrow K^+\pi^+\pi^-\Lambda(1520)$, a subset of the $\gamma p \rightarrow K^+K^-\pi^+\pi^-p$ reaction, was analyzed with a Partial Wave Analysis (PWA) in order to study strange mesons that decay to $K^+\pi^+\pi^-$. In the PWA, a useful model for the angular distributions was found but no significant structures could be observed due to statistical limitations.

TABLE OF CONTENTS

Acknowledgments	vi
List of Tables	vii
List of Figures	viii
CHAPTER	1
1 Introduction	2
1.1 Standard Model and The Strong Nuclear Force	2
1.1.1 Strong Nuclear Force	4
1.2 The Quark Model	7
1.2.1 Hadron Spectroscopy	9
1.2.2 Resonances Beyond The Quark Model	12
1.3 Observations and Interpretations of $\phi(2170)$	16
1.4 Partial Wave Analysis	19
1.4.1 S-Matrix Scattering	21
1.4.2 PWA with a Polarized Photon Beam in the Reflectivity Basis	23
1.4.3 Angular Distributions due to Isobar Decays	29
2 GlueX Experiment	32
2.1 Jefferson Lab Electron Accelerator	35
2.2 Polarized Photon Beam and the GlueX Beamline	35
2.2.1 Photon beam production and radiators	38
2.2.2 Photon Tagging	39
2.2.3 Absorber, Profiler, and Collimator	40

2.2.4	Beam Flux and Polarimetry	41
2.3	GlueX Detector	43
2.3.1	Target	43
2.3.2	Timing Detectors	44
2.3.3	Solenoid Magnet	45
2.3.4	Tracking Detectors	46
2.3.5	Calorimetry Detectors	47
2.4	Trigger and Data Acquisition	49
2.4.1	GlueX Trigger	50
3	GlueX DIRC Upgrade	52
3.1	Cherenkov Radiation	52
3.2	GlueX DIRC Design	55
3.2.1	Radiator Bars	56
3.2.2	Optical Box	57
3.2.3	PMT Plane and Enclosure	58
3.3	MAPMT Electronics Stack	60
3.4	Hamamatsu H12700 Multi-Anode Photo Multiplier Tubes	61
3.5	Laser Bench Test	62
3.5.1	Setup	62
3.5.2	Magnetic Field Test	63
3.5.3	MAPMT ADC Spectrum	64
3.5.4	General Characteristics of the ADC Spectrum	68
3.5.5	Effect of DAC Threshold Cuts	69
3.5.6	Model for Fitting the ADC Spectrum	69
3.5.7	Fitting the ADC spectra and results	75

3.5.8	MAPMT gain matching with ADC	77
3.5.9	MAPMT gain matching with TDC	80
3.6	DIRC Simulation	83
3.7	Cherenkov Angle Reconstruction	85
3.7.1	Geometrical Reconstruction	87
3.7.2	Other Methods	88
3.8	Early DIRC Performance	90
4	Reconstruction and Selection of the $K^+K^-\pi^+\pi^-p$, $K^+K^-\pi^0\pi^0p$, and $K^+K^-\pi^0\eta p$ Final States	93
4.1	Data Set	94
4.2	Event Selection	94
4.3	$K^+K^-\pi^0\eta p$ Event Selection	98
4.4	Features of the $K^+K^-\pi^0\eta p$ Final State	99
4.4.1	Mass Distributions	103
4.4.2	Yields	103
4.5	$K^+K^-\pi^0\pi^0p$ Event Selection	105
4.6	Features of the $K^+K^-\pi^0\pi^0p$ Final State	109
4.6.1	Mass Distributions	109
4.6.2	Yields	109
4.7	$K^+K^-\pi^+\pi^-p$ Selection	111
4.8	Features of the $K^+K^-\pi^+\pi^-p$ Final State	113
4.8.1	Mass Distributions	113
4.8.2	Baryon Excitations in $\gamma p \rightarrow K^+K^-\pi^+\pi^-p$	119
4.8.3	van Hove Analysis	120
4.8.4	Yields	125
4.9	Discussion of Final State Surveys	127

5	Partial Wave Analysis Tools	130
5.1	Fitting with IU AmpTools	131
5.1.1	Extended Unbinned Maximum Likelihood	132
5.1.2	Error Estimation	134
5.2	Model Selection Techniques	134
5.2.1	Likelihood Ratio Tests	135
5.2.2	Akaike's Information Criterion	136
5.2.3	Bayesian Information Criterion	137
6	PWA Fit Results	138
6.1	Event Selection	138
6.2	Input/output tests with Monte-Carlo	139
6.2.1	Signal Monte Carlo Example	141
6.2.2	Test of Model Selection Criteria	146
6.3	Model Selection in Fits to Data	150
6.4	Fit Results	152
6.4.1	1^+ amplitudes	153
6.4.2	1^- amplitudes	154
6.4.3	Unaccounted-for Systematic Errors	154
6.4.4	PWA conclusions	155
7	Summary and Discussion	160
7.1	Summary	160
7.2	Discussion	162
7.2.1	On the Search for the $\phi(2170)$	162
7.2.2	On the Excited Kaon Spectrum	163
7.2.3	Outlook	164

APPENDIX A	
Rest Frames	165
A.1 Center of Mass frame	165
A.1.1 t' Definition	165
A.2 Gottfried-Jackson frame	166
A.3 Helicity frame	167
APPENDIX B	
Fits to the K^+K^- Mass for ϕ Yields	168
Bibliography	178

ACKNOWLEDGMENTS

Firstly, I want to thank my PhD advisor Justin Stevens. Your seemingly encyclopedic knowledge of all things GlueX related is just as impressive to me now as when I first joined your group. Few things are easy when pursuing a PhD, but having an advisor with such a depth of knowledge from hardware to software to analysis techniques made working as a graduate student as easy as could be. Beyond the technical aspects of advising, your kindness, patience, and encouragement is something I will always appreciate and never forget.

I could not have made it this far without my entire family. My parents, Mary and Jeff, have never wavered in their support and were always there to help with anything in any way they could. It would be difficult to overstate how valuable it is to have that kind of support. My brothers, Nick, Chris, and Josh always gave me examples to look up to growing up. My family has my eternal gratitude for all they have done for me and helping shape me into the person I am today.

I'd like to thank Volker Crede who was my undergraduate honors thesis advisor at Florida State University. Working in your group gave me my first real look into what being an experimental physicist was like, and also where I found my love for nuclear physics that carried me through to this PhD.

I would also like to thank all of the members of the GlueX collaboration, The GlueX collaboration is filled with great people, and it has been an absolute pleasure to be a part of it. A special thanks to Bill Li with whom I worked closely with on the DIRC and learned so much from.

I also want to thank the faculty and fellow graduate students at William & Mary that made for a memorable and fantastic experience throughout my time here.

Saving the most important tribute for last, I thank my wife Haley. All of the credit for my sanity remaining intact belongs to you. My appreciation for everything you've done for me over the last nine years is immeasurable. With you, I have the confidence we can surmount any mountain. I am lucky to have you in my life. So with all of my being, thank you. Ever shall I be grateful.

LIST OF TABLES

1.1	Quantum Numbers of Resonances	7
2.1	Hall-D Electron Beam Properties	37
3.1	MAPMT ADC Spectra Fit Parameters	76
4.1	$\gamma p \rightarrow K^+ K^- \pi^0 \eta p$ Particle Timing Cuts	99
4.2	$\gamma p \rightarrow K^+ K^- \pi^0 \eta p$ Analysis Cuts	99
4.3	$\gamma p \rightarrow K^+ K^- \pi^0 \pi^0 p$ Charged Particle Cuts	107
4.4	$\gamma p \rightarrow K^+ K^- \pi^0 \pi^0 p$ Analysis cuts	107
4.5	$\gamma p \rightarrow K^+ K^- \pi^+ \pi^- p$ Charged Particle Timing Cuts	112
4.6	$\gamma p \rightarrow K^+ K^- \pi^+ \pi^- p$ Analysis Cuts	112
4.7	van Hove Cut Study on Monte Carlo	127
5.1	Excited Kaon PDG Properties	131
6.1	$\Lambda(1520)$ Side Band Subtraction Regions	139
6.2	I/O Test Signal Monte Carlo Amplitudes	143
6.3	I/O Fit Fraction Table	145
6.4	I/O Test Fit Model Amplitudes	146
6.5	I/O Fit Fraction Table 2	147
6.6	I/O Model Selection Criteria	150
6.7	Fit Models for Data	151
6.8	AIC and BIC Values for Fits to Data	152

LIST OF FIGURES

1.1	Standard Model of Particle Physics	3
1.2	Running of the QCD Coupling Strength	6
1.3	Light Baryon Nonet	8
1.4	Light Meson Nonet	9
1.5	$\pi_1(1600)$ Observation	14
1.6	LQCD Spectrum	15
1.7	XYZ in Charmonium Spectrum	17
1.8	$\phi(2170)$ BaBar, Belle, and BES-III Observation	19
1.9	$\phi(2170)$ in GlueX by A. Hamdi	20
1.10	CoM Frame Sketch of Resonance Production	24
1.11	Feynman Sketch of $\gamma p \rightarrow K^+ \pi^+ \pi^- \Lambda(1520)$	30
2.1	GlueX-I Schematic Cartoon	33
2.2	Jefferson Lab Accelerator	34
2.3	RF Accelerator Cavities	36
2.4	GlueX Beamline Schematic	36
2.5	GlueX Photon Beam Energy and Polarization Fraction	37
2.6	GlueX Tagger System Schematic	39
2.7	GlueX Tagger Microscope Schematic	40
2.8	GlueX Target Diagram	42
2.9	GlueX Start Counter Diagram	43
2.10	GlueX Time of Flight Detector	45
2.11	GlueX Drift Chamber Straws	47
2.12	GlueX Forward Drift Chamber Rendering	48
2.13	GlueX Central Drift Chamber Rendering	48
2.14	GlueX Forward Calorimeter	50
3.1	GlueX-I Schematic Cartoon	53
3.2	Cherenkov Angle Diagram	53

3.3	Cherenkov Angle vs P Calculation	54
3.4	GlueX DIRC Picture and Optical Box Diagram	55
3.5	GlueX Radiation Bars	56
3.6	Cherenkov in Radiator Bar Cartoon	57
3.7	GlueX Optical Box Diagram (Detailed)	58
3.8	GlueX DIRC Dark Box	59
3.9	GlueX MAPMT Electronics Stack	60
3.10	MAPMT Dynode Structure	61
3.11	MAPMT Laser Bench Test	62
3.12	GlueX MAPMT Laser Bench Test with Magnetic Field	65
3.13	GlueX MAPMT Magnetic Field Test Results 1	66
3.14	GlueX MAPMT Magnetic Field Test Results 2	66
3.15	GlueX MAPMT ADC Spectra Fit Examples	67
3.16	GlueX MAPMT Threshold Cut Plot	70
3.17	Poisson Fit to MAPMT ADC Spectrum	74
3.18	MAPMT ADC Fit Fixing ξ Parameter	78
3.19	MAPMT ADC Fit Fixing ν Parameter	79
3.20	MAPMT ADC Spectra Fit χ^2/NDF Distribution	80
3.21	MAPMT ΔT vs Equalized Gain	83
3.22	MAPMT ΔT for Different Gain Values	84
3.23	MAPMT Relative Efficiency Using Two Sets of Equalized Gains	85
3.24	GlueX Photon Multiplicity and Propagation Time	86
3.25	GlueX DIRC π Hit Pattern	87
3.26	GlueX DIRC Ambiguous Path Schematic	89
3.27	GlueX DIRC Cherenkov Angle Determination	89
3.28	GlueX DIRC Cherenkov Angle Results	92
4.1	$\Delta_T RF$	95
4.2	$\gamma p \rightarrow K^+ K^- \pi^0 \eta p$ MM^2	100
4.3	$\gamma p \rightarrow K^+ K^- \pi^0 \eta p$ Kinematic Fit Quality	101
4.4	$\gamma p \rightarrow K^+ K^- \pi^0 \eta p$ Photon Beam Energy	102
4.5	Meson Masses Spectra in $\gamma p \rightarrow K^+ K^- \pi^0 \eta p$	104
4.6	ϕ Yield Fit Example	106
4.7	ϕ Yields in $\gamma p \rightarrow K^+ K^- \pi^0 \eta p$	106
4.8	$\gamma p \rightarrow K^+ K^- \pi^0 \pi^0 p$ MM^2	108
4.9	$\gamma p \rightarrow K^+ K^- \pi^0 \pi^0 p$ Kinematic Fit Quality	108
4.10	$\gamma p \rightarrow K^+ K^- \pi^0 \pi^0 p$ Photon Beam Energy	108

4.11	Meson Masses Spectra in $\gamma p \rightarrow K^+ K^- \pi^0 \pi^0 p$	110
4.12	ϕ Yields in $\gamma p \rightarrow K^+ K^- \pi^0 \pi^0 p$	111
4.13	$\gamma p \rightarrow K^+ K^- \pi^+ \pi^- p$ MM^2	113
4.14	$\gamma p \rightarrow K^+ K^- \pi^+ \pi^- p$ Kinematic Fit Quality	114
4.15	$\gamma p \rightarrow K^+ K^- \pi^+ \pi^- p$ Kinematic Fit Quality	115
4.16	$\gamma p \rightarrow K^+ K^- \pi^+ \pi^- p$ Photon Beam Energy	116
4.17	Two Meson Mass Spectra in $\gamma p \rightarrow K^+ K^- \pi^+ \pi^- p$	117
4.18	Three Mass Spectra in $\gamma p \rightarrow K^+ K^- \pi^+ \pi^- p$	118
4.19	$K^+ K^- \pi^+ \pi^-$ Mass Spectrum	119
4.20	Baryon Mass Spectra in $\gamma p \rightarrow K^+ K^- \pi^+ \pi^- p$	121
4.21	van Hove Cubeoctahedron	122
4.22	van Hove Projection	124
4.23	van Hove Cut Selection Example	125
4.24	van Hove Cut Selection Example	126
4.25	ϕ Yields in $\gamma p \rightarrow K^+ K^- \pi^+ \pi^- p$	128
6.1	Side Band Subtraction to Select Λ Events for PWA	139
6.2	Mass and t Distributions After Side Band Subtraction	140
6.3	Input/Output Fit (Example 1)	142
6.4	Input/Output Fits Fractions (Example 1)	144
6.5	Input/Output Fit (Example 2)	148
6.6	Input/Output Fits Fractions (Example 2)	149
6.7	Fit to Data Diagnostic Plots	157
6.8	PWA Fit Total, 1^+ , 1^- , and 2^+ Intensities	158
6.9	1^+ amplitudes	158
6.10	1^- amplitudes	159
B.1	ϕ yields in $\pi^0 \eta$ Mass	169
B.2	ϕ yields in $\pi^0 \eta$ Mass	170
B.3	ϕ yields in $K^+ K^- \pi^0 \eta$ Mass	171
B.4	ϕ yields in $\pi^0 \pi^0$ Mass	172
B.5	ϕ yields in $K^+ K^- \pi^0 \pi^0$ Mass	173
B.6	ϕ yields in $K^+ K^- \pi^+ \pi^-$ Mass	174
B.7	ϕ yields in $K^+ K^- \pi^+ \pi^-$ Mass	175
B.8	ϕ yields in $K^+ K^- \pi^+ \pi^-$ Mass	176
B.9	ϕ yields in $K^+ K^- \pi^+ \pi^-$ Mass	177

PARTIAL WAVE ANALYSIS OF STRANGE MESONS DECAYING TO $K^+\pi^+\pi^-$ IN
THE REACTION $\gamma p \rightarrow K^+\pi^+\pi^-\Lambda(1520)$ AND THE COMMISSIONING OF THE
GLUEX DIRC DETECTOR

CHAPTER 1

Introduction

1.1 Standard Model and The Strong Nuclear Force

The standard model of particle physics, represented in Figure 1.1, aims to describe the properties and behavior of the universe at a fundamental level. The model is written in the language of quantum field theory and consists of fermion fields describing matter, gauge fields describing fundamental forces, the scalar Higgs field, and couplings between the various fields [1]. The standard model is a living model in the sense that the fields, their properties, and their interactions contained therein are only those with compelling experimental evidence, and it may be modified to reflect the current understanding of particle physics. The most recent component to be confirmed in the standard model was the Higgs boson with its observation in 2012 [2], although it was proposed independently in three different publications in 1964 [3][4][5]. There are many observations that are not described by the standard model (neutrino mass and flavor oscillations, gravity, dark matter, and dark energy to name some examples), and so the standard model should not be mistaken for a complete theory. It is the goal of experimental particle physics to both

Standard Model of Elementary Particles

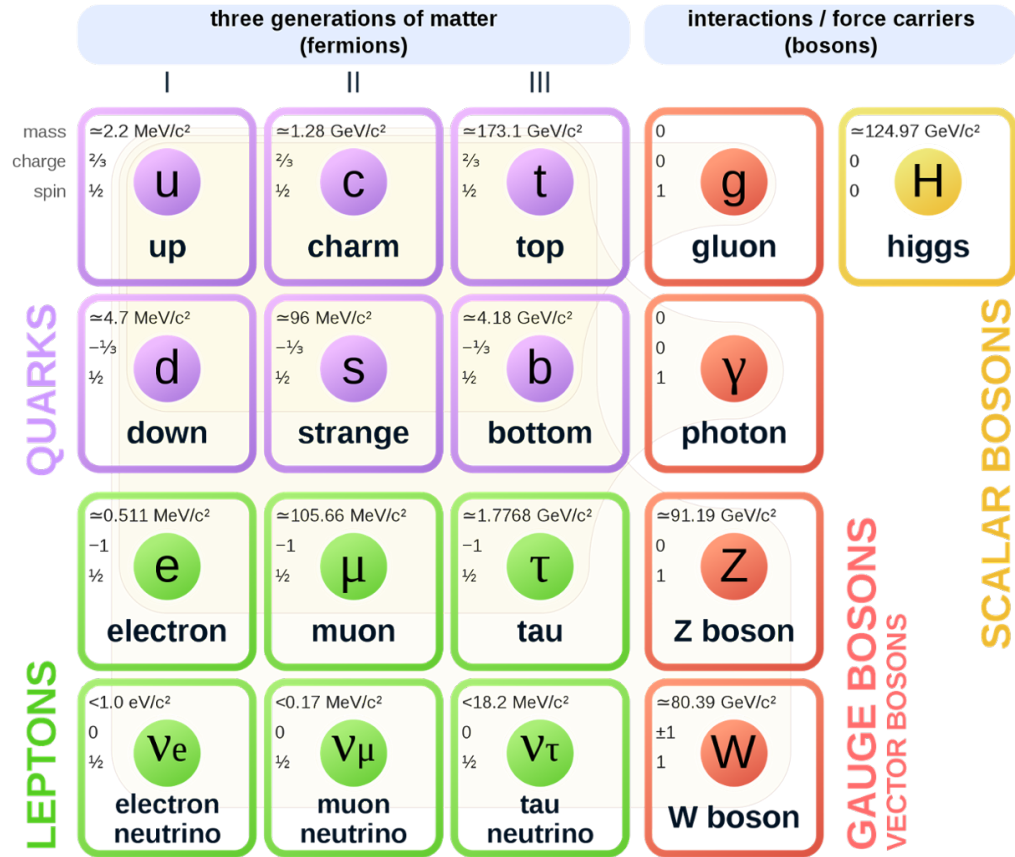


FIG. 1.1: The standard model of particle physics. Matter fields are the quarks(purple): up, down, charm, stange, top, and bottom, and the leptons(green): electron, muon, tau, and the corresponding neutrinos. The gauge bosons (red) give rise to the fundamental forces, the gluons giving rise to the strong nuclear force, and the photon, Z, and W bosons giving rise to the electroweak force. The Higgs boson in yellow is the only known scalar boson field, and it is responsible for the masses of the other fundamental fields.

study phenomena that can be described from the standard model and seek phenomena that gives evidence of physics beyond the standard model.

1.1.1 Strong Nuclear Force

If one considers the common, familiar depiction of an atom with a nucleus consisting of protons and neutrons being orbited by electrons, one can immediately infer the existence of a force capable of overcoming the electromagnetic repulsion of the protons from each other. We call this force, unimaginatively, the strong nuclear force. In the standard model, the strong nuclear force is described by Quantum Chromodynamics (QCD) which follows an SU(3) gauge symmetry. Some of the observations that motivate this form of quantum field theory are discussed in section 1.2. The QCD Lagrangian density is given by

$$\mathcal{L}_{QCD} = -\frac{1}{4}G_{\mu\nu}^i G^{i\mu\nu} + \sum_r \left(\bar{q}_r^\alpha i \not{D}_\alpha^\beta q_{r\beta} - m_r \bar{q}_r^\alpha q_{r\alpha} \right) + \frac{\theta_{QCD}}{32\pi^2} g_s^2 G_{\mu\nu}^i \tilde{G}^{i\mu\nu}, \quad (1.1)$$

where $G_{\mu\nu}^i$ is the field strength tensor comprised of the $i = 1\dots 8$ SU(3) gluon fields, $\not{D}_\alpha^\beta q_{r\beta}$ is the product of the covariant derivative with the Dirac matrices, q_r^α are the quark fields with flavor r ($= u, d, c, s, t, b$), bare mass m_r , and color charge α ($= R, G, B$), g_s is the QCD coupling strength, θ_{QCD} is a dimensionless constant, and $\tilde{G}^{i\mu\nu}$ is the dual field strength tensor. The term containing dual field strength tensor allows for parity violating interactions which are not observed in strong nuclear interactions in experiments (*e.g.* no neutron electric dipole moment observed), and so θ_{QCD} is often set to zero [1].

QCD has a number of related features worth discussing. The first feature is the self interaction of the gluon fields. The expanded form of the field strength tensor in Eq. 1.1 is

$$G_{\mu\nu}^i = \partial_\mu G_\nu^i - \partial_\nu G_\mu^i - g_s f_{ijk} G_\mu^j G_\nu^k. \quad (1.2)$$

Here G_ν^i are the gluon fields, and the structure constants f_{ijk} of the SU(3) gauge symmetry define its Lie algebra. The Lie algebra for a group is defined by the commutator of the generators, or in this case (neglecting the lorentz indices)

$$[X_i, X_j] = if_{ijk}X_k, \quad (1.3)$$

where X_i are the generators of the group. Because the generators of SU(3) do not commute, the structure constants are non-zero and QCD is referred to as a non-Abelian gauge theory. Given the form of Eq. 1.2, the first term of Eq. 1.1 contains gluon-gluon interactions. Put another way, gluons have color charge in QCD (in contrast with photons, which are the gauge field of quantum electrodynamics, but do not have an electric charge).

The next features worth pointing out, are asymptotic freedom and color confinement. The former is the observed behavior that the effective strength of strong interactions become vanishingly small in the small distance/ high energy limit. The latter is a statement that no free color charge has ever been observed, or in other words, strongly interacting particles are always arranged in color singlets. Color confinement arises from the fact that the strong force increases with distance (in the low energy limit). Both of these features are (likely) direct consequences of the self interaction of the gluon fields already discussed [1], and is reflected in the running of the QCD coupling seen in Fig. 1.2 courtesy of [6]. In Fig. 1.2, experimental values for the QCD fine structure constant, $\alpha_s = g_s^2/4\pi$, is shown, and the decrease of the interaction strength can be seen as function Q . Q is the momentum transfer of a given process and is used to set the scale of the renormalization of QCD in this instance [6].

Because the coupling strength at low energy is large and color is confined, studying strongly interacting systems becomes challenging. Perturbation theory, one of the most powerful and ubiquitous tools in field theory calculations, relies on having a small inter-

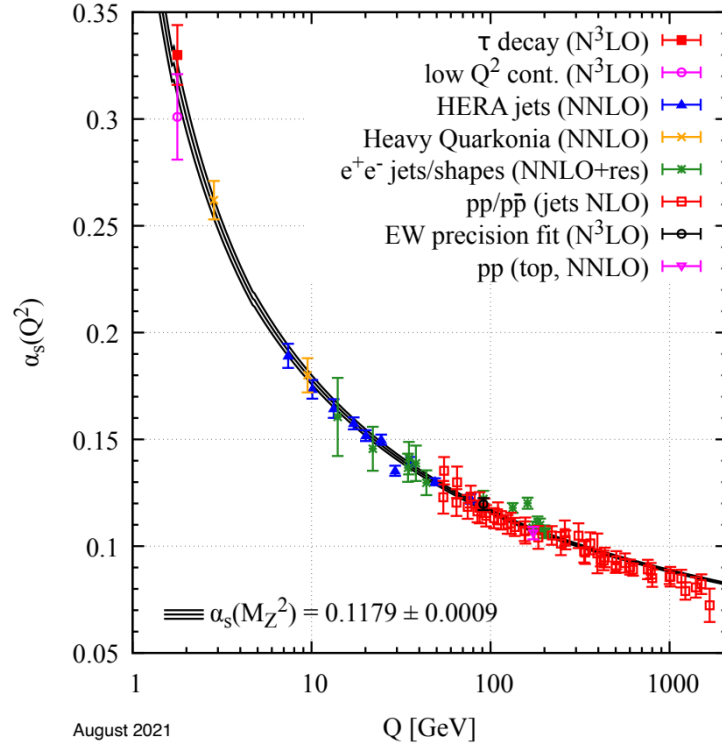


FIG. 1.2: Measurements of the QCD coupling α_s as a function of energy Q . $\alpha_s = g_s^2/4\pi$ gets larger as Q gets smaller, or the strength of the strong force gets stronger as distance increases.

action strength in order to perform a series expansion in orders of the coupling constant. And so, low to medium energy strong interactions are often modelled instead of being directly calculated from QCD. However, modern computing resources have made numerical calculations, such as lattice QCD (LQCD), viable. Furthermore, because of color confinement, studying strong interactions at low energies experimentally must be done with composite particles. In these complex systems, it can be difficult (or impossible) to isolate and study the factors that lead to emergent properties of the system. Experimental efforts in this regime can be broken down into two broad categories: 1) the behavior of quarks and gluons within bound systems, and 2) what bound states and scattering resonances are possible. The latter is called hadron spectroscopy and is the focus of this work.

1.2 The Quark Model

Conserved Quantity	Symbol
Electric Charge	Q
Isospin	I
Isospin 3rd Component	I₃
Spin	J
Parity	P
Charge Conjugation	C
G-parity	G
Baryon Number	B
Flavor	N_q
Hypercharge	Y

TABLE 1.1: Quantum numbers used to identify strongly interacting resonances

Beginning in the middle of the 20th century, advancements in particle accelerators and particle detectors led to the discovery of numerous unexpected, short lived particles. The name ‘hadron’ was originally used for any particle that interacted through the strong force, and historically, the hadrons with masses close to (or greater than) the proton

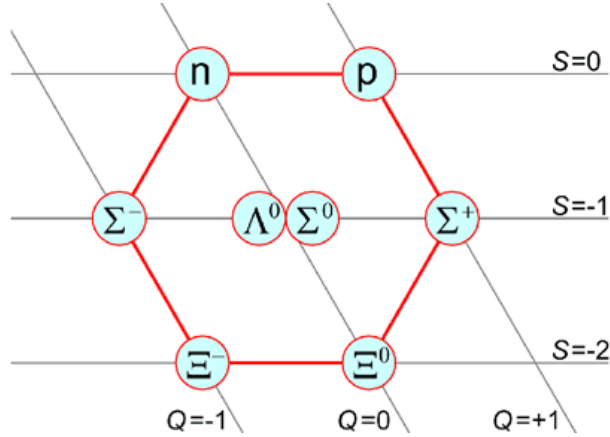


FIG. 1.3: SU(3) spin $\frac{1}{2}$ baryon nonet. The vertical axis is the strangeness (S) of the baryon, the horizontal axis is organized by the third component of the isospin (I_3), and the diagonal lines are lines of constant electric charge (Q). Public domain image from [7].

were originally named baryons, while the lighter hadrons were called mesons (these terms were later redefined). To make sense of all of these new particles, the hadrons were classified by their mass, lifetime, decay processes, and a number of other quantum numbers. The quantum numbers that are used to identify these hadrons are determined through properties conserved in strong interactions and are listed in Table 1.1, some of which are self descriptive, and the others will be described in more detail in the following Sec. (1.2.1).

What quickly followed from classifying these states was a pattern that hinted at an underlying structure. In 1961, M. Gell-Mann and Y. Ne'eman independently showed that the known hadrons at the time could be organized into multiplets derived from an SU(3) symmetry [8][9]. An example of a baryon multiplet can be seen in Fig. 1.3, and an example of a meson multiplet can be see in Fig. 1.4. The subsequent spectrum and the properties of hadrons eventually led M. Gell-Mann and G. Zweig in 1964 to independently propose that hadrons were not elementary particles, but rather composed of more fundamental objects [10][11]. These constituents were named quarks by Gell-Mann, and much of the hadron spectrum could be understood using this relatively simple model, known as the

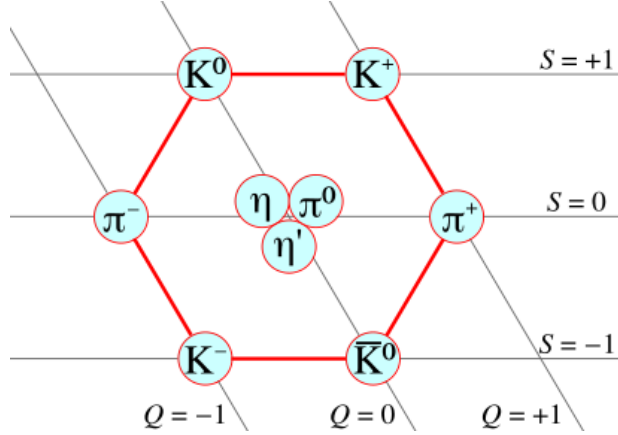


FIG. 1.4: The $SU(3)_{\text{flavor}}$ meson nonet. The vertical axis is the strangeness (S) of the meson, the horizontal axis is organized by the third component of the isospin (I_3), and the diagonal lines are lines of constant electric charge (Q). Public domain image from [12].

constituent quark model. The quark model has been extremely successful at describing and/or predicting a large amount of the hadrons observed in experiments. In the quark model, hadron now refers to any strongly interacting particle composed of quarks, baryons are particles with three quarks (or anti-quarks), and mesons are particles with two quarks (one quark and one anti-quark). Deep inelastic scattering experiments with energy much larger than the mass of the proton have confirmed the composite nature of hadrons [1]. Quarks were confirmed to be spin-1/2 particles through measurements of the angular distribution of hadronic jets [1]. The existence of states described as being composed of three identical quarks (in the quark model) gave rise to the idea of color charge, which then influenced the structure of QCD, see Sec. 1.1.

1.2.1 Hadron Spectroscopy

As mentioned in the previous section, hadron spectroscopy is the study of particles composed of quarks and gluons and their properties. The vast majority of hadrons (all except the proton and atomically bound neutrons) are unstable, short lived states that are

studied in scattering experiments. In scattering theory, unstable states are synonymous with poles in the scattering amplitude. These poles have the form of a Breit-Wigner resonance, with an amplitude

$$\propto \frac{1}{E - E_0 + i\Gamma/2} \quad (1.4)$$

in the non-relativistic case where E_0 is the resonance energy, E is the scattering energy, and Γ is the decay rate. The complex pole can manifest itself as an enhancement in the mass spectra of the decay products of the resonance, and measuring its location and width provides a measure of the state's mass and lifetime.

In addition to a resonance's mass, other properties of the resonance can be inferred based on the properties conserved in strong interactions listed in Table 1.1.

Isospin:

Isospin, I , is the flavour symmetry between up and down quarks which is slightly broken by the mass difference between the two quarks and their electromagnetic charge. Isospin symmetry was first used to describe the symmetrical nature of protons and neutrons under the strong force. Mathematically, the addition of isospin follows the same $SU(2)$ symmetry as spin-1/2 particles, hence the name. Also similar to traditional spin-1/2 addition rules, the third component of isospin is also an (approximately) conserved quantity.

Parity:

Parity is the behavior of a particle's wavefunction under a reversal of the spatial coordinates, i.e.

$$\hat{P}\psi(x, y, z) = P\psi(-x, -y, -z), \quad (1.5)$$

and

$$\hat{\Pi}^2\psi(x, y, z) = P^2\psi(x, y, z) = \psi(x, y, z), \quad (1.6)$$

where $\hat{\Pi}$ is the parity operator and P is the parity eigenvalue (or just parity) of the wavefunction ψ . By inspection $P^2 = 1$, and so $P = \pm 1$.

Charge Conjugation:

Charge Conjugation is the operation that changes a particle into its anti-particle. This is not a good symmetry for charged particles. Similar to parity, for states that are eigenvectors of charge conjugation, the eigenvalues are ± 1 .

G-Parity:

G-parity can be thought of as an extension of charge conjugation for charged particles. G-Parity is a 180° rotation of the particle's isospin and an inversion of its electrical charge.

Baryon Number:

Baryon number, B , comes from the apparent conservation law for the number of baryons in an interaction. Baryons have a B of $+1$, antibaryons have a B of -1 . In the quark model, quarks (antiquarks) have a baryon number of $1/3$ ($-1/3$), and so mesons have a B of 0 .

Flavor:

Quark flavor number is conserved in strong interactions, and it refers to the number of each type of heavy quarks (here meaning not up or down quarks) that make up the meson. N_S , N_C , N_T , N_B are the flavor numbers for strange, charm, top, and bottom quarks, respectively.

Hypercharge:

Hypercharge is a sum of a particle's flavor numbers and baryon number, or

$$Y = N_S + N_C + N_T + N_B + B. \quad (1.7)$$

The hypercharge and the third component of isospin are related to a particle's electric charge by

$$Q = I_3 + \frac{1}{2}Y \quad (1.8)$$

1.2.2 Resonances Beyond The Quark Model

Although the quark model has been successful, it is not the complete picture of the structure of hadrons. For example, deep scattering of leptons off of nucleons has shown that a sea of virtual quarks contributes significantly to the properties of the hadron, compared to the quark model which only needs the valence quarks to explain the hadron's properties [1]. This section will briefly discuss the concept of hybrid hadrons and the observations of resonances known as XYZ states.

Hybrid Hadrons

In QCD, the gluons have color charge, and because of this, color singlets made from both quarks and gluons are possible (e.g. $q\bar{q}g, qq\bar{q}g, \dots$). Searching for states with an excited gluonic field, also known as hybrid hadrons, is one of the main motivations and the namesake of the GlueX experiment. In experimental searches, hybrid mesons are of particular interest due to the possibility of “exotic” quantum number combinations. For a $q\bar{q}$ pair, the parity is $P = (-1)^{L+1}$ and the charge conjugation is (for a neutral state) $C = (-1)^{L+S}$, where L is the orbital angular momentum between the quarks and S is the

spin of the $q\bar{q}$ system. If one computes all of the permutations of these quantum numbers, $J^{PC} = 0^{--}$, odd $^{-+}$, and even $^{+-}$ are not possible in $q\bar{q}$ systems [13]. Therefore, resonances with exotic quantum numbers provide a distinct signature that identifies the meson as being beyond the quark model. The strongest evidence for an exotic meson to date is the $J^{PC} = 1^{-+}$ $\pi_1(1600)$ first observed by the COMPASS experiment in a 3π system [14]. The COMPASS experiment also observed exotic signals in the $\eta\pi$ (the $\pi_1(1400)$) and $\eta'\pi$ (the $\pi_1(1600)$) systems. These two π_1 signals were later analysed and found to be from a single π_1 pole, see Fig. 1.5 [15].

For hybrids without exotic quantum numbers, including hybrid baryons which have no exotic quantum numbers, the identification of states with gluonic degrees of freedom becomes much more challenging. Beyond just counting an excess of states beyond those predicted by the quark model, parsing the intricate spectrum of possible states requires good understanding of models or calculations of scattering resonances from the base theory. There exist many types of models in the literature that attempt to calculate properties of hybrid hadrons, e.g. flux tube models and bag models [13]. Of particular interest, Lattice QCD (LQCD) calculations of the meson spectrum provide predictions of the hadron spectrum based on what is believed to be the fundamental theory for all strong nuclear interactions. One such example of a LQCD spectrum calculation can be seen in Fig 1.6 where hybrid mesons are identified as having large overlap with chromomagnetic gluonic operators [16].

XYZ States

Bottom and charm quark factory experiments, such as BaBar, Belle, BES-II, and LHCb, have observed a larger number of states in the charm and bottom quark spectra than predicted by the quark model. Many of these states, referred to as XYZ states, also do not agree with the expected decay branching ratios for predicted quark model states

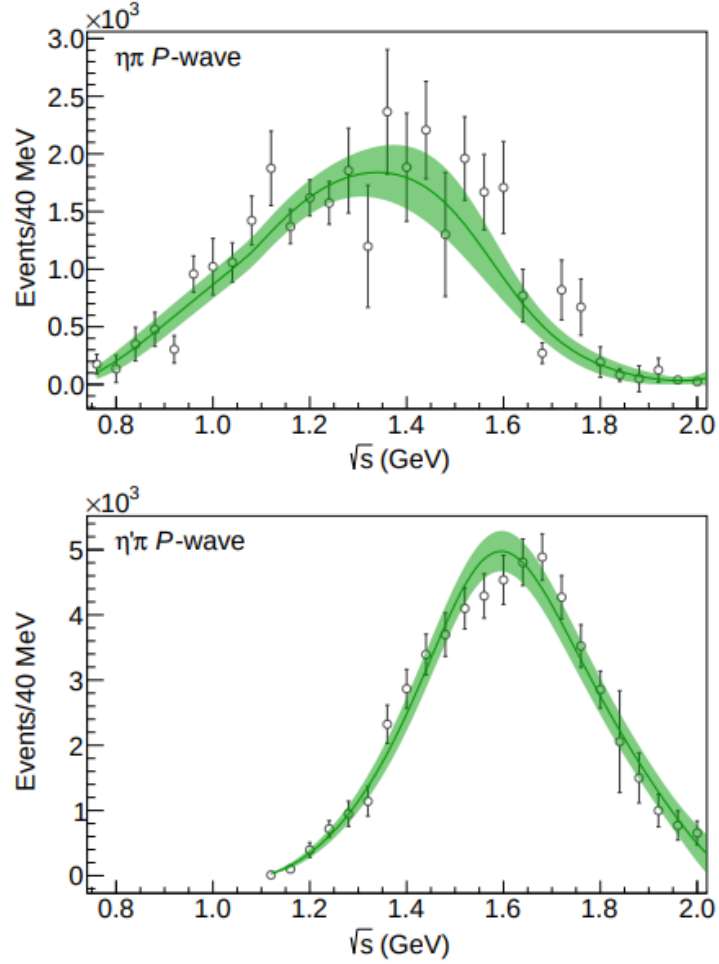


FIG. 1.5: 1^{-+} exotic wave in the $\eta\pi$ and $\eta'\pi$ systems observed by the COMPASS experiment (data are the black points). This data was fit with a coupled channel amplitude model to extract the single exotic pole [15]. This exotic meson is known as the $\pi_1(1600)$.

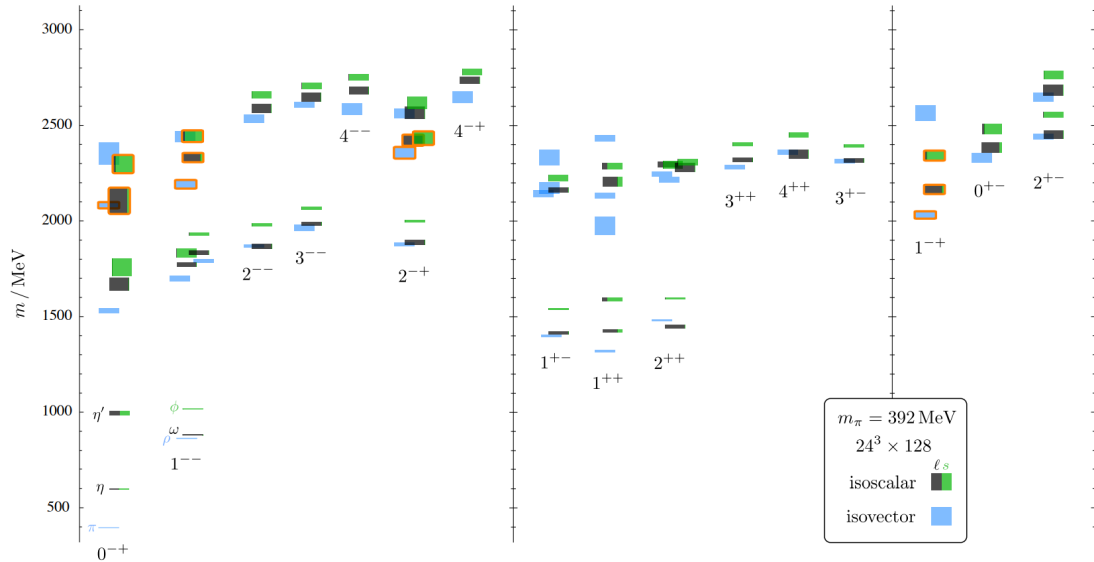


FIG. 1.6: LQCD spectrum plot. Light meson spectrum calculated at a pion mass of $392 \text{ MeV}/c^2$. The members of the lightest hybrid multiplet are outlined in orange. Exotic meson states can be seen in the three columns of the right side of the plot. Image sourced from [16]

[17]. The ‘Z’ states are charged states are observed to decay to $J\psi$ and a charged light meson which implies a minimum of four quarks in their structure [17].

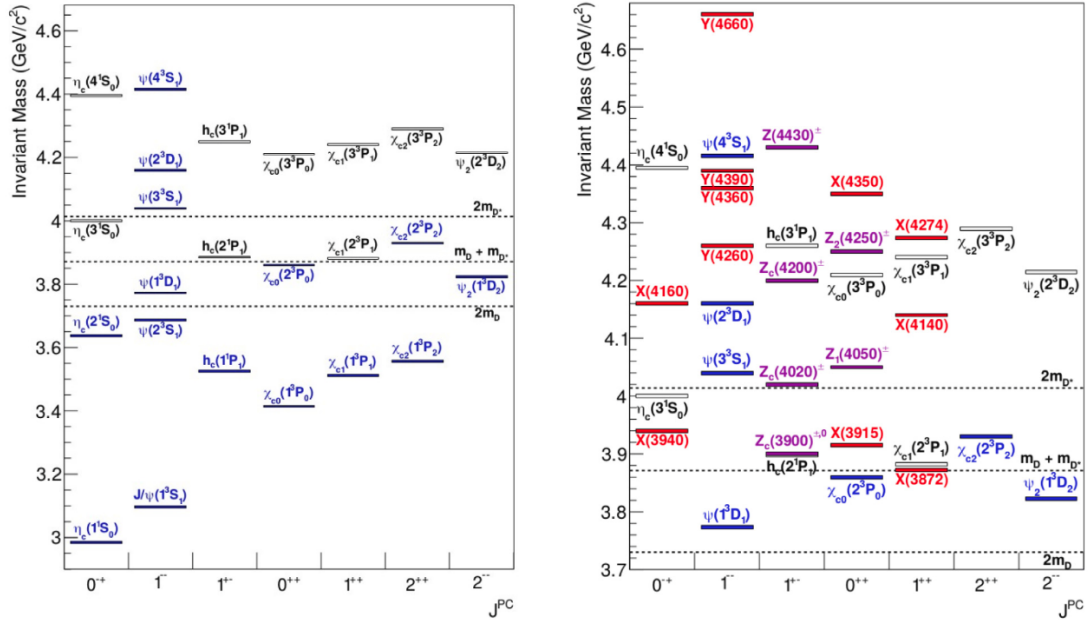
The experimental status of the charmonium ($c\bar{c}$) spectrum before and after the additions of these new XYZ states, and the expected states by the quark model, is shown Fig. 1.7. Of particular interest to the analysis presented in this work is the Y(4260), because it may have a strange quark analogue in the Y(2175), now known as the $\phi(2170)$ (see Sec. 1.3). The Y(4260) is a vector meson ($J^{PC} = 1^{--}$) which was first observed by the BaBar experiment in the reaction $e^+e^- \rightarrow \gamma_{ISR} J/\psi \pi^+ \pi^-$ [18]. The BESIII experiment has observed the Y(4260) in the $\pi^+ \pi^- h_c$, $\omega \chi_{c0}$, and $\pi^+ D^0 D^*$ final states [19]. Potential Models of the vector mesons in the $c\bar{c}$ spectrum predict several states in the mass range measurable by the charm factory experiments. These states are the ground state $c\bar{c}$ vector meson, the J/ψ , and the excited $c\bar{c}$ vector mesons $\psi(2S)$, $\psi(1D)$, $\psi(3S)$, $\psi(2D)$, $\psi(4S)$, $\psi(3D)$, and $\psi(5S)$ [19]. The left plot in Fig. 1.7 show these charmonium states (up to

the $\psi(4S)$) in the 1^{--} column in blue to indicate they were well established before the observation of the XYZ states [17]. The Y(4260) (as well as the other states shown in red or magenta in Fig. 1.7) is inherently a prime candidate to study mesons beyond the simple quark-antiquark model. The interpretation of the Y(4260) remains an active area of investigation in both theory and experiment. More generally, the interpretation of the XYZ states is still largely undetermined; they may be hybrids, meson-meson molecules, tetraquark mesons, or some other type of state or some linear combination of states [17, 20]. The study of the XYZ states and their connection to the light meson spectrum will give insight into what types of resonances beyond conventional quark model interpretations are possible in strong interactions.

Recent results from BESIII have resolved the Y(4260) into two structures in $e^+e^- \rightarrow \gamma_{ISR} J/\psi \pi^+ \pi^-$ [21]. These states have been named Y(4220) and Y(4320) by Ref. [21]. This work will still refer to the Y(4260) as singular state as it remains one of the initial motivations for our interest in the $\phi(2170)$. The existence of two Y states with a small mass splitting (instead of the singular Y(4260)) in a spectrum that was already overpopulated furthers the need to study these and related states.

1.3 Observations and Interpretations of $\phi(2170)$

The strangeonium ($s\bar{s}$) spectrum has only two vector mesons which are well established in experimental observations: the ground state $\phi(1020)$ (often referred to as ϕ) and the $\phi(1680)$. The $\phi(1680)$ likely corresponds to the $\phi(2S)$ seen in both potential quark model calculations [22] and LQCD calculations [23]. The $\phi(2170)$ is a candidate for the $\phi(3S)$ or an analogue to the Y(4260). The mass and width of the $\phi(2170)$ are listed by the PDG as $M = 2162 \pm 7$ MeV and $\Gamma = 100 \pm 31$ MeV [6]. The BaBar experiment first observed an enhancement in the $e^+e^- \rightarrow \gamma_{ISR} \phi \pi^+ \pi^-$ (see Fig. 1.8) and $e^+e^- \rightarrow \gamma_{ISR} \phi f_0(980)$ cross



sections (in which γ_{ISR} is a photon radiated before the e^+e^- interaction). This observation was later confirmed by the Belle experiment [24][25]. The BaBar experiment also saw an enhancement in the $e^+e^- \rightarrow \gamma_{ISR}\phi\pi^0\pi^0$ cross section consistent with the Y(2175). An enhancement consistent with the $\phi(2170)$ was also seen in the $\phi f_0(980)$ system in the decay $J/\psi \rightarrow \eta\phi f_0(980)$ in the BES-III experiment [26]. It is in the $\phi\pi\pi$ and $\phi f_0(980)$ systems that we will first look for the photoproduction of the $\phi(2170)$, see Chapter 4. The $\phi(2170)$ has also been observed to couple to $\phi\eta$, $\omega\eta$, $\phi\eta'$ [6].

The comparison to the Y(4260) was made due to the similarity of the final states in which each state was first observed ($J/\psi\pi^+\pi^-$ vs. $\phi\pi^+\pi^-$). Like many of the XYZ states, the interpretation of $\phi(2170)$ is not quite clear. If the $\phi(2170)$ is an analogue to the Y(4260), then comparison between the two offers an additional means with which to understand both states. Given the recent results that the Y(4260) is really two overlapping Y states [21], a search for similar structure in the $\phi\pi\pi$ system would definitely be of interest. If the $\phi(2170)$ is not a strange analogue to the Y(4260), then it could be one of the excited $s\bar{s}$ vector mesons missing from experimental observation.

The $\phi(2170)$ has been explored theoretically as a radially excited $s\bar{s}$ state [27], an $s\bar{s}s\bar{s}$ tetraquark state [28], a $\Lambda\bar{\Lambda}$ molecule [29], and as a $s\bar{s}g$ hybrid [30]. The calculations in the sources cited all indicate a possible resonance that decays to $\phi\pi^+\pi^-$ within their framework that agrees with the $\phi(2170)$ observation. A more recent LQCD calculation of the $s\bar{s}$ spectrum was unable to separate the $\phi(3S)$ and $s\bar{s}g$ hybrid interpretations [23]. Ideally, as more measurements of what other decay modes the $\phi(2170)$ couples (or does not couple) to, a clearer picture as to the best interpretation of the $\phi(2170)$ will emerge. It has also been proposed to look for an isovector partner with the decay $Y \rightarrow \phi a_0(980)$ [31].

A photoproduction experiment like GlueX is potentially ideal for producing and studying the $\phi(2170)$. Photoproduction is favorable for the production of vector mesons due

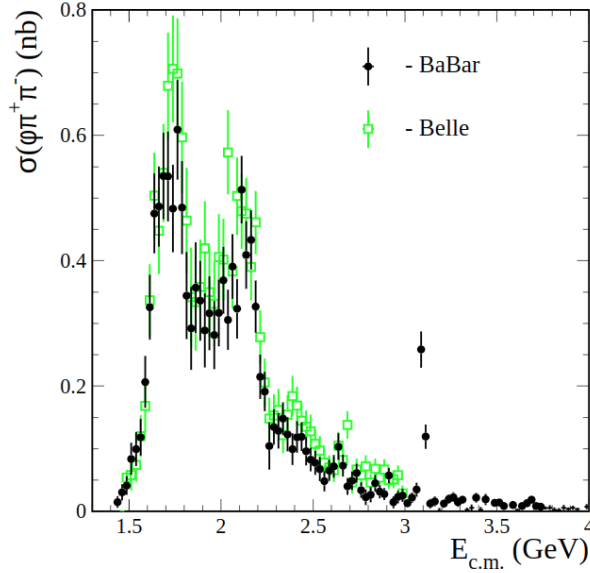
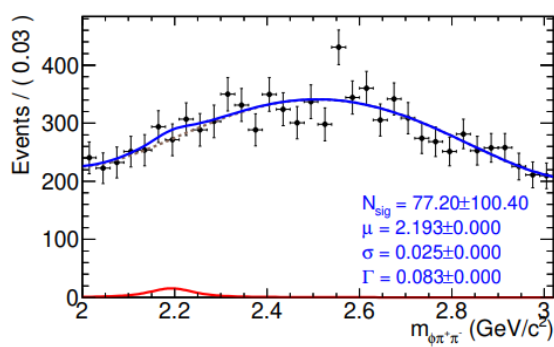


FIG. 1.8: Cross section measurement as a function of e^+e^- center of mass energy showing an enhancement near 2.2 GeV. Image sourced from [24].

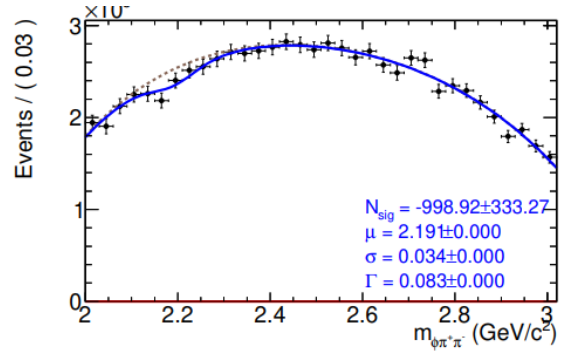
to the photon beam also being a 1^{--} state, modeled as being composed of virtual vector particles, being often referred to as the *vector dominance* model [32]. A. Hamdi also searched for the $\phi(2170)$ using the GlueX apparatus in the reaction $\gamma p \rightarrow K^+ K^- \pi^+ \pi^- p$, but was unable to observe any significant enhancement consistent with the $\phi(2170)$ [33], see Fig. 1.9. The $\phi(2170)$ has not been observed in any photoproduction experiment to date, which is somewhat surprising given the aforementioned *vector dominance* model expected of photoproduction.

1.4 Partial Wave Analysis

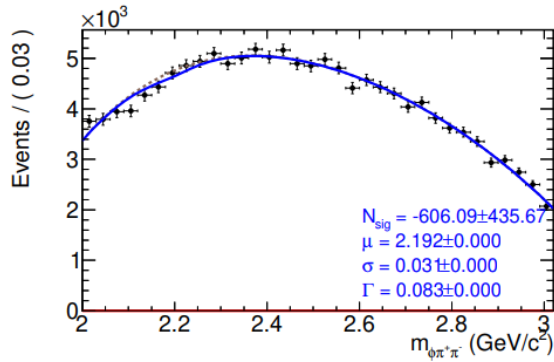
As described in section 1.2, resonances are identified experimentally by measuring their masses, lifetimes, decay modes, and their various quantum numbers. Perhaps the simplest method of identifying a scattering resonance is to look for an enhancement in the cross section as a function of mass or interaction energy. Many quantum numbers can be



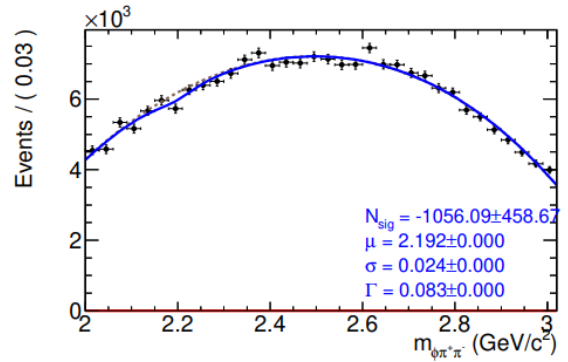
(a)



(b)



(c)



(d)

FIG. 1.9: ϕ yields as a function of the $K^+K^-\pi^+\pi^-$ mass in the 2016 (a), 2017 (b), 2018 Spring (c), and 2018 Fall (d) GlueX data sets, from an analysis independent to the one presented in this work. Note the lack of any clear enhancement near 2.170 GeV. Image sourced from [33].

readily inferred from true conservation laws (*e.g.* electric charge), or approximate conservation laws (*e.g.* quark flavor) based on the possible interactions of the given experiment. Peaks in the mass distribution can be caused by non-resonant effects while resonances may also appear as dips (or not at all) in mass distributions, so some care must be taken in interpreting such features.

For example, in reactions such as $e^+e^- \rightarrow X$, the electron and positron annihilate producing a virtual photon that decays to X. The spin/parity/charge conjugation combination of X must be $J^{PC} = 1^{--}$, the same as the virtual photon. However, in photoproduction reactions, $\gamma p \rightarrow Xp'$, of interest in this work, the J^P (and C where applicable), must be determined in another way since many J^{PC} for X are allowed. The goal of a partial wave analysis (PWA) is to infer the J^P of short lived, intermediate resonances from an analysis of the angular distributions of the resonances' decay products. In addition to identifying the J^P properties of the resonances, an advantage of such an analysis is the ability to separate contributions from resonances with different J^P that may be obfuscated by each other, by non-resonant backgrounds, or interfered with other resonances quantum mechanically. This section introduces the formalism for partial wave analysis used to describe photoproduction off of a proton target with a linearly polarized photon beam.

1.4.1 S-Matrix Scattering

Before describing the partial wave expansion used in PWA, it is useful to discuss how scattering is described using quantum theories. In particle scattering, we often wish to describe the process in which two given incoming, or initial state, particles interact and produce some n selected outgoing, or final state, particles. Summarized here is the approach given in [34]. The probability of this process occurring in the Heisenberg picture

is generally the overlap between the initial state particles constructed at a “far past” time ($t = -T$) and the final state particles constructed at a “far future” time ($t = T$).

$$\mathcal{P} = |_{future}\langle out|in\rangle_{past}|^2. \quad (1.9)$$

In the limit that $T \rightarrow \infty$, the limit of a series of unitary operators relate the $|in\rangle_{past}$ state to the $_{future}\langle out|$ state. The S-matrix is defined in the following relationship [34]:

$$_{future}\langle out|in\rangle_{past} = \lim_{T \rightarrow \infty} \langle out|e^{-iH2T}|in\rangle, \quad (1.10)$$

$$\lim_{T \rightarrow \infty} \langle out|e^{-iH2T}|in\rangle \equiv \langle out|\hat{S}|in\rangle. \quad (1.11)$$

It is useful to rewrite the S-matrix operator as a sum of what happens if there is no interaction between the initial particles and a term that represents any and all interactions, represented by the \hat{T} -operator:

$$\hat{S} = 1 + i\hat{T}. \quad (1.12)$$

The exact form of the wave functions describing the $|in\rangle$ and $\langle out|$ states are not important for this discussion, only that the differential cross section ($d\sigma$) is proportional to the matrix element \mathcal{M} formed by the transition operator \hat{T} with the $|in\rangle$ and $\langle out|$ states, *i.e.*

$$d\sigma \propto |\langle out|\hat{T}|in\rangle|^2 \equiv |\mathcal{M}|^2. \quad (1.13)$$

Often in fixed target experiments, the measurements are made in bins of Mandelstam t (*e.g.* t as defined in Eq. 1.16). and mass M . The quantity of interest is the intensity of produced events as a function of the directions of the final state particles $I(\vec{\Omega})$. In bins of

M and t , this functionally takes the form

$$I(\vec{\Omega}) \equiv \frac{d\sigma}{dtdM d\vec{\Omega}} = \kappa |\mathcal{M}|^2, \quad (1.14)$$

where κ is the phase space factor for the given M and t range.

Omitted here are many details in the derivation that can be explored by more explicitly describing the $|in\rangle$ and $\langle out|$ states as wave packets in momentum space. A fully relativistic relationship between the S-matrix and the cross sections should be easy to find in any relevant textbook, *e.g.* Ref. [34].

1.4.2 PWA with a Polarized Photon Beam in the Reflectivity Basis

The matrix element \mathcal{M} in Eq. 1.13 is a complex amplitude that contains all of the relevant interaction physics between the initial state particles, but it is often useful to decompose \mathcal{M} into more easily interpreted pieces. In this section, Eq. 1.13 is decomposed into a sum of states with definite angular momentum, also known as partial wave amplitudes. The fundamentals of partial wave expansions can be found in many textbooks, *e.g.* Ref. [35].

This section will focus on expanding the intensity in Eq. 1.14 in the context of a specific type of reaction of interest. We will be following [36] to arrive at a partial wave expansion in the reflectivity basis with a linearly polarized photon beam. A diagram of a similar reaction to that studied in [36] is shown in Fig. 1.10. The reaction has the form

$$\vec{\gamma}(\lambda, p_\gamma) p(\lambda_1, p_p) \rightarrow X(p_X) N(\lambda_2, p'_N), \quad (1.15)$$

and we will describe it in the center-of-mass (CoM) frame (described in appendix A). Here,

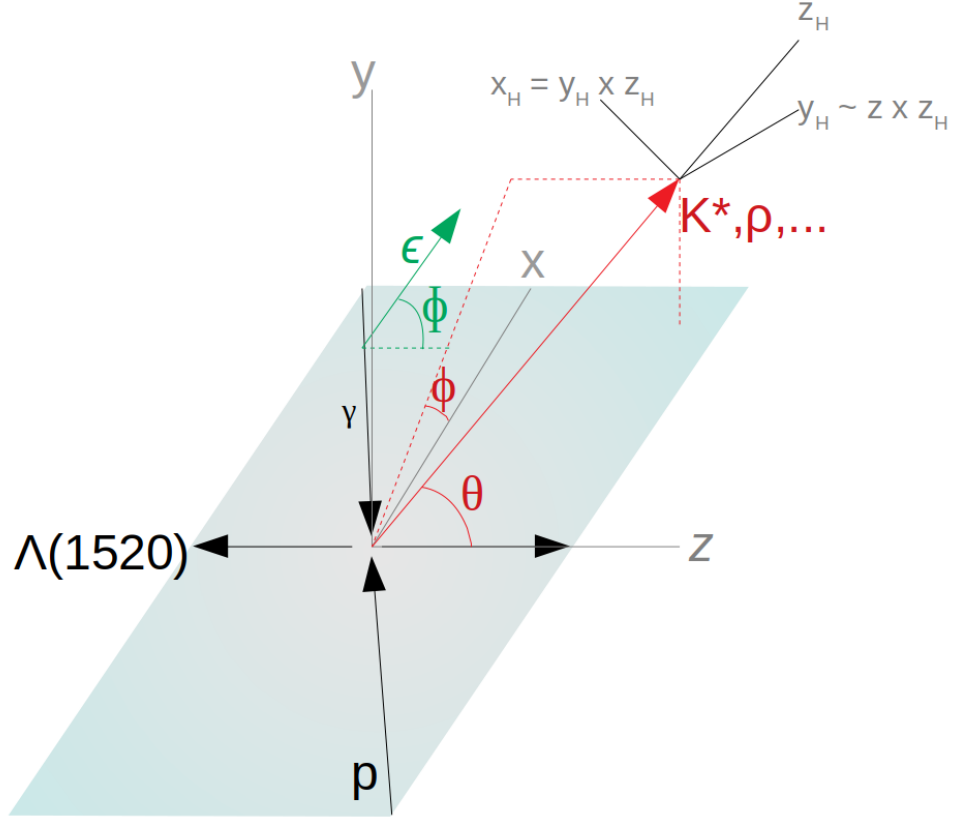


FIG. 1.10: In the Center of Mass frame (CoM), the reaction plane is defined by the proton (p), beam photon (γ), recoil $\Lambda(1520)$, and the $K^+\pi^+\pi^-$ combined system. The green vector and angle Φ represent the direction and angle of the beam's polarization relative to the reaction plane. The red vector illustrates the direction of a vector meson (labeled as the K^*/ρ in this diagram) coming from the decay of some X resonance. Also represented at the tip of the red vector are the axes of the helicity frame of the vector meson (see Appendix A) used to describe its decay.

λ , λ_1 , and λ_2 are the helicities of the incoming photon, incoming proton, and outgoing nucleon ($\Lambda(1520)$ in the case depicted in Fig. 1.10), respectively. For this reaction, we define the Mandelstam t as

$$t = (p'_N - p_p)^2. \quad (1.16)$$

For the reaction in Eq. 1.15, it is actually more convenient to use t' instead of t . t' is

$$t' = t - t_{min}, \quad (1.17)$$

where t_{min} is the minimum t value for the reaction to occur. A description of how t_{min} is calculated is provided in Appendix A.

In the center-of-mass frame, we define the production plane as the plane defined by the incoming coming particles and the recoil $\Lambda(1520)$ which is also depicted in Fig. 1.10. We will consider the case that X is unstable and will decay into two daughter particles. These types of reactions are conveniently described in the reflectivity basis which will be explained below.

The Reflectivity Basis

Ultimately we wish to describe our partial wave analysis in the reflectivity basis, because in this basis there is no longer interference between production mechanisms with different reflectivities [37]. Extracting the reflectivity in high energy processes allows us to determine the “naturalness” of the exchange particle, providing a deeper understanding of the production mechanisms. To demonstrate what is meant by the reflectivity basis we will examine the reflection operator, but first consider the parity operator $\hat{\Pi}$ operating on some state with quantum numbers J and m ($= J_z$), and momentum \vec{p}_z . If $\vec{p}_z = 0$ the parity operator on this state is

$$\hat{\Pi}|0; Jm\rangle = P|0; Jm\rangle, \quad (1.18)$$

where $P = \pm 1$. For $\vec{p}_z \neq 0$, and recasting $|\vec{p}_z; Jm\rangle$ in the helicity frame (see Appendix A) as $|\vec{p}_z; s - \lambda\rangle$, the operation becomes

$$\hat{\Pi}|\vec{p}_z; s\lambda\rangle = \hat{\Pi}\mathcal{L}(\vec{p}_z)|0; s\lambda\rangle = P\mathcal{L}(-\vec{p}_z)|0; s - \lambda\rangle, \quad (1.19)$$

meaning $|\vec{p}_z; s\lambda\rangle$ is not an eigenstate of the parity operator. In order to construct an operator for which this state is an eigenvalue, a rotation by π about the y-axis is introduced to create the reflection operator,

$$\hat{\Pi}_y = \hat{\Pi}e^{-i\pi J_y}, \quad (1.20)$$

and the eigenvalues of the reflection operator can be shown to be

$$K = \epsilon(-1)^{2J}, \quad (1.21)$$

where ϵ is called the reflectivity with $\epsilon = \pm 1$ for bosons and $\epsilon = \pm i$ for fermions [37].

Partial Wave Expansion

To begin formulating the PWA intensity in the reflectivity basis, we rewrite Eq. 1.14 as

$$I(\vec{\Omega}) \equiv \frac{d\sigma}{dtdM d\vec{\Omega} d\vec{\Phi}} = \kappa \sum_{\lambda, \lambda', \lambda_1, \lambda_2} A_{\lambda; \lambda_1 \lambda_2}(\Omega) \rho_{\lambda \lambda'}(\Phi) A_{\lambda'; \lambda_1 \lambda_2}^*(\Omega), \quad (1.22)$$

where $A_{\lambda; \lambda_1 \lambda_2}$ is the amplitude representing the Eq. 1.15 that depends on the angles $\vec{\Omega}$ that describe the direction of the decay products of X in the rest frame of X , and the photon spin density matrix $\rho_{\lambda \lambda'}(\Phi)$ contains the dependence of the reaction on the direction of the

beam polarization. We have introduced the angle Φ which is the angle between the beam polarization direction and the production plane.

Since we do not have a purely polarized beam in our experiment it is useful to define the fraction of polarization in the beam P_γ , with the obvious bounds $0 < P_\gamma < 1$. Including this beam polarization fraction and expanding the spin density matrix explicitly has been done in Ref. [36]. The photon polarization is a linear combination of only 2 possible helicities, $+1$ and -1 . Therefore, the intensity in Eq. 1.22, after expanding the photon spin density matrix and being explicit with the photon beam polarization value, can be written as

$$I(\Omega, \Phi) = \frac{\kappa}{2} [A_-(\Omega)A_-^*(\Omega) + A_+(\Omega)A_+^*(\Omega) - P_\gamma e^{i2\Phi} A_-(\Omega)A_+^*(\Omega) - P_\gamma e^{-i2\Phi} A_+(\Omega)A_-^*(\Omega)], \quad (1.23)$$

where the baryon helicities have been suppressed. This can be simplified by the defining amplitudes, \tilde{A} , rotated by the angle between the photon beam polarization direction and the production plane, Φ ,

$$\tilde{A}_\pm(\Omega, \Phi) \equiv e^{\mp i\Phi} A_\pm(\Omega) \quad (1.24)$$

giving

$$I(\Omega, \Phi) = \frac{\kappa}{4} \left[(1 - P_\gamma) |\tilde{A}_+(\Omega, \Phi) + \tilde{A}_-(\Omega, \Phi)|^2 + (1 + P_\gamma) |\tilde{A}_+(\Omega, \Phi) - \tilde{A}_-(\Omega, \Phi)|^2 \right], \quad (1.25)$$

The amplitudes in Eq. 1.25 are still quite general, and so now we choose to do our partial wave expansion by expanding these amplitudes in an infinite series of amplitudes with definite angular momentum l and spin projection m . We will then transform the helicity amplitudes into the desired reflectivity basis. The helicity expansion is

$$A_{\lambda;\lambda_1\lambda_2}(\Omega) = \sum_{\lambda_1,\lambda_2} \sum_{l,m} T_{\lambda m;\lambda_1\lambda_2}^l X_l^m(\Omega). \quad (1.26)$$

Here the $T_{\lambda m;\lambda_1\lambda_2}^l$ are the helicity amplitudes for producing some resonance X and $X_l^m(\Omega)$ is the decay amplitude of X (described in more detail in Sec. 1.4.3). The relationship between the helicity amplitudes and the reflectivity amplitudes, ${}^{(\epsilon)}T_{-m;\lambda_1\lambda_2}^l$, is given in [36] by

$$T_{-1m;\lambda_1\lambda_2}^l = (-1)^m \left[{}^{(-)}T_{-m;\lambda_1\lambda_2}^l - {}^{(+)}T_{-m;\lambda_1\lambda_2}^l \right] \quad (1.27)$$

$$T_{+1m;\lambda_1\lambda_2}^l = {}^{(-)}T_{m;\lambda_1\lambda_2}^l + {}^{(+)}T_{m;\lambda_1\lambda_2}^l, \quad (1.28)$$

with ϵ taking the values $+$ and $-$. It is also useful to carry the phase rotation in Eq. 1.24 to the decay amplitudes and define phase rotated decay amplitude as

$$Z_l^m(\Omega, \Phi) \equiv X_l^m(\Omega) e^{-i\Phi}. \quad (1.29)$$

Inserting Eqs 1.27 and 1.28 into Eq. 1.26, then substituting that into the intensity in Eq. 1.25, with the Z_l^m s defined in equation 1.29, the intensity in the reflectivity basis is:

$$I(\Omega, \Phi) = \sum_{\lambda_1,\lambda_2} \left(\kappa(1 - P_\gamma) \left| \sum_{l,m} \left({}^{(+)}T_{m;\lambda_1\lambda_2}^l \Re[Z_l^m(\Omega, \Phi)] + i {}^{(-)}T_{m;\lambda_1\lambda_2}^l \Im[Z_l^m(\Omega, \Phi)] \right) \right|^2 \right. \\ \left. + \kappa(1 + P_\gamma) \left| \sum_{l,m} \left({}^{(-)}T_{m;\lambda_1\lambda_2}^l \Re[Z_l^m(\Omega, \Phi)] + i {}^{(+)}T_{m;\lambda_1\lambda_2}^l \Im[Z_l^m(\Omega, \Phi)] \right) \right|^2 \right). \quad (1.30)$$

When this intensity is applied to the PWA in Sec. 6, the $\lambda_2 = \pm \frac{3}{2}$ helicities of the $\Lambda(1520)$ are ignored. This choice was motivated by the current state of the available

amplitudes in the software that was initially developed to model $\gamma p \rightarrow X p'$ reactions where only $\lambda_1, \lambda_2 = \pm \frac{1}{2}$ baryon helicities are necessary. The sum over baryon helicities in Eq. 1.30 is related to the sum over spin “flip” (i.e. if the target proton has the same spin as the recoil baryon or not) through parity invariance by

$$\sum_{\lambda_1, \lambda_2} {}^{(\epsilon)}T_{m; \lambda_1 \lambda_2}^l {}^{(\epsilon')}T_{m'; \lambda_1 \lambda_2}^{*l'} = (1 + \epsilon \epsilon') \sum_k {}^{(\epsilon)}J_{m; k}^l {}^{(\epsilon')}J_{m'; k}^{*l'}, \quad (1.31)$$

where $k = 0$ for spin “flip” and $k = 1$ for “non-flip”. With this simplification the intensity in Eq. 1.30 can be reduced to the form

$$I(\Omega, \Phi) = 2\kappa \sum_{k=0,1} \left((1 - P_\gamma) \left[\left| \sum_{l,m} [J_l]_{m,k}^{(-)} \Im[Z_l^m(\Omega, \Phi)] \right|^2 + \left| \sum_{l,m} [J_l]_{m,k}^{(+)} \Re[Z_l^m(\Omega, \Phi)] \right|^2 \right] + \right. \\ \left. (1 + P_\gamma) \left[\left| \sum_{l,m} [J_l]_{m,k}^{(+)} \Im[Z_l^m(\Omega, \Phi)] \right|^2 + \left| \sum_{l,m} [J_l]_{m,k}^{(-)} \Re[Z_l^m(\Omega, \Phi)] \right|^2 \right] \right), \quad (1.32)$$

where $[J_l]_{m,k}^{(\epsilon)}$ is a complex parameter for the baryon spin flip defined by

$$[J_l]_{m,0}^{(\epsilon)} = {}^{(\epsilon)}T_{m; ++}^l, \\ [J_l]_{m,1}^{(\epsilon)} = {}^{(\epsilon)}T_{m; +-}^l. \quad (1.33)$$

For more on the use of parity conservation and the use of these complex parameters see [36].

1.4.3 Angular Distributions due to Isobar Decays

The intensity in Eq. 1.32 describes the angular distribution of the resonances, X , from Eq. 1.15, but it is often the case that resonances do not directly decay to particles that live long enough to make it to the detector. In nature, we observe that these decays

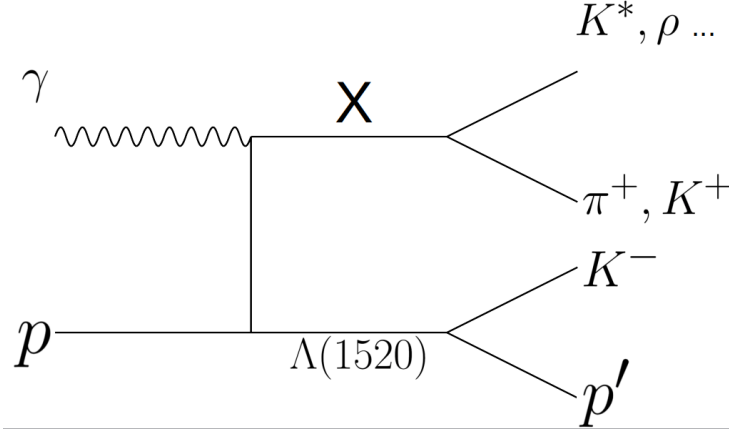


FIG. 1.11: Feynman Sketch of $\gamma p \rightarrow K^+ \pi^+ \pi^- \Lambda(1520)$. The K^* and ρ (at the top of the right side) will also undergo a two body decay before being detected.

can usually be described as a series of two-body decays, each of which introduce an angular dependence on the final detected intensity. The model consisting of subsequent two-body decays is known as the isobar model and is depicted in Fig. 1.11 where the resonance X decays to a detectable meson, π^+ (K^+ , ...) and a K^* (ρ , ...); the K^* or ρ then also has a two body-decay into two detectable particles. In this section, we will discuss the specific case in which X decays in the following way:

$$X \rightarrow V P s_1$$

$$V \rightarrow P s_2 P s_3, \quad (1.34)$$

where V is some short-lived vector resonance (i.e. $J^P = 1^-$), and $P s$ represents pseudo-scalar particles ($J^P = 0^-$) that exist long enough to be detected directly.

The specific type of decay process allows us to be more specific about the form of the decay amplitude in Eq. 1.26, $X_l^m(\Omega)$. First, with the inclusion of an additional decay, $X_l^m(\Omega)$ will also depend on the angular distribution of the decay of the vector particle, by

choice, in its helicity frame (see Appendix A).

$$X_l^m(\Omega) \rightarrow X_l^m(\Omega, \Omega_H), \quad (1.35)$$

where Ω describes the direction of the vector in the rest frame of X and Ω_H describes the direction of the vector's decay products. For a resonance X_i with spin J_i decaying to a pseudoscalar meson and intermediate vector meson with helicity λ_v that decays to two pseudoscalar mesons, the decay amplitude is [37]

$$X_m^l(\Omega, \Omega_H) = \sqrt{\frac{(2l+1)}{4\pi}} \sqrt{\frac{(2(1)+1)}{4\pi}} \sum_{\lambda_v} D_{m\lambda_v}^{J*}(\Omega) D_{\lambda_v 0}^{1*}(\Omega_H) (l0, 1\lambda_v | J\lambda_v), \quad (1.36)$$

where $(l0, 1\lambda_v | J\lambda_v)$ are the Clebsch-Gordan coefficients, and $D_{m\lambda_v}^{J*}(\Omega)$ and $D_{\lambda_v 0}^{1*}(\Omega_H)$ are the complex conjugates of the Wigner-D functions.

Eq. 1.36 only contains the angular dependence of the decays, and so far we have neglected the mass dependence and effects of the *centrifugal-barrier* on vector meson decay. The mass dependence is modelled with a relativistic Breit-Wigner and the *centrifugal-barrier* effects are modelled using the Blatt-Weisskopf centrifugal-barrier factors [37].

CHAPTER 2

GlueX Experiment

In this chapter, a description of the GlueX experimental setup is given in its configuration at the time of data taking for GlueX-I (2016 - 2018); this chapter is a summarized version of [38]. The GlueX experiment was designed to measure exclusive photo-production events with a partially-polarized photon beam and a variety of final state particles in order to map the light quark meson spectrum. The experiment receives a ~ 12 GeV electron beam from Jefferson Lab's Continuous Electron Beam Accelerator Facility (CEBAF). A real photon beam is produced via bremsstrahlung by passing the electron beam through a radiator (either a diamond to produce a polarized photon beam or an aluminum radiator to produce an unpolarized, or amorphous, photon beam). The remaining electrons are swept out of the beamline by a tagging magnet into the Tagger Microscope (TAGM) and Tagger Hodoscope (TAGH) to determine the photon beam energy. After the photon beam has propagated downstream ~ 75 m, it passes through a beam profiler and then a collimator. Once collimated, the photon beam passes through a beryllium foil converter that converts some small fraction of photons into electron-photon pairs that are measured in the pair spectrometer and a triplet polarimeter to measure the beam flux and polarization fraction,

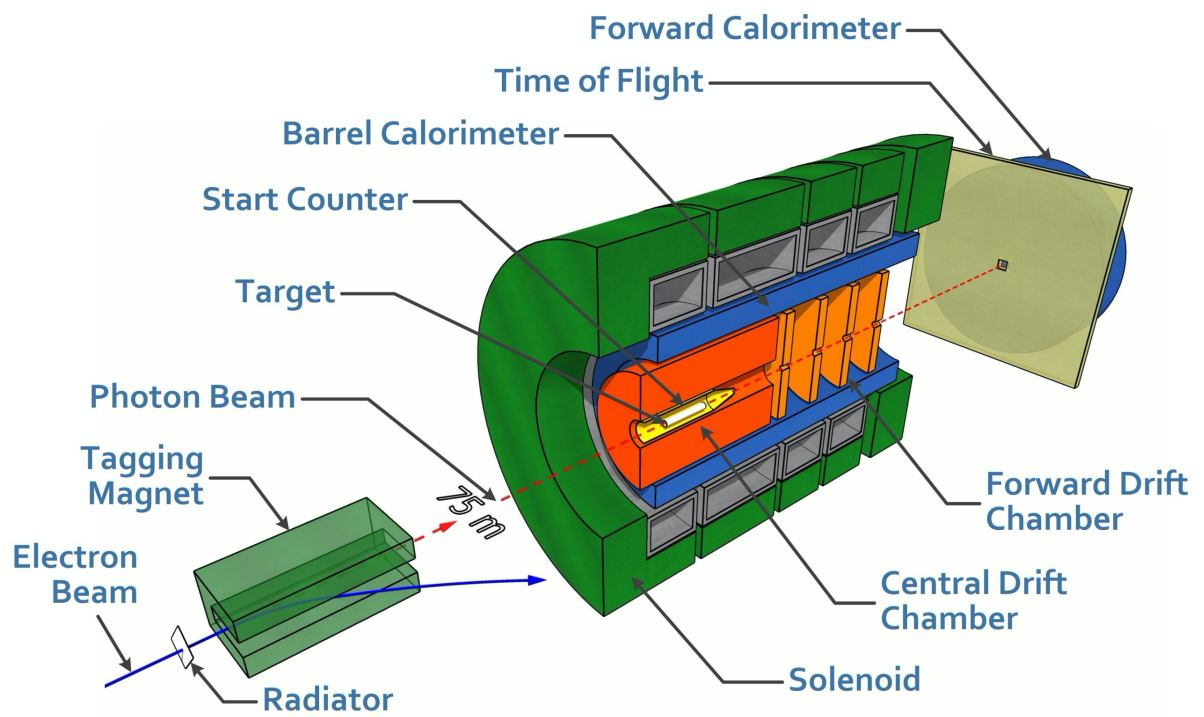


FIG. 2.1: Schematic cartoon of the GlueX detector showing the major sub-detector packages. This cartoon is not to scale.

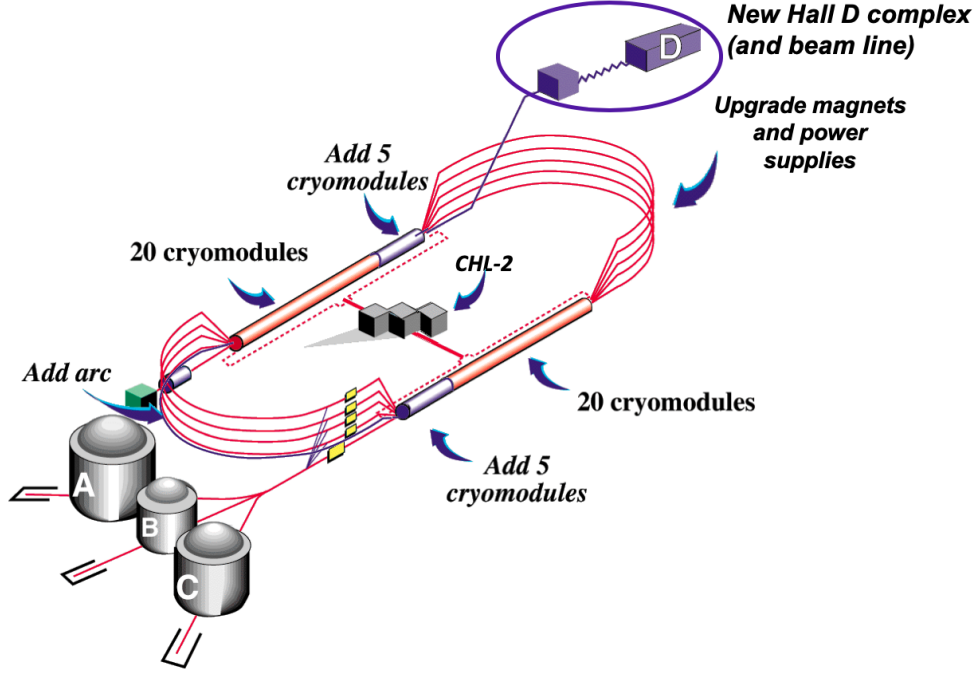


FIG. 2.2: Hall D and other upgrades to the Jefferson Lab accelerator facility. GlueX is located in Hall D shown in the top right of the diagram. Image sourced from [38].

respectively. The photon beam is then incident on a liquid hydrogen target located within the detector. For charged particle tracking, the GlueX detector contains central (CDC) and forward (FDC) drift chambers inside the barrel of a ~ 2 T superconducting solenoid magnet. For energy measurements of final state particles there is a barrel (BCAL) and a forward (FCAL) electromagnetic calorimeter. There is also a start counter (ST) and time of flight detector (TOF) that provide precise timing measurements used in particle identification. All of these detectors are described in greater detail in the following sections, which also provide a description of the experimental triggers, data acquisition system, and detector simulation.

2.1 Jefferson Lab Electron Accelerator

CEBAF is a superconducting radio frequency (SRF) electron beam accelerator located at the Thomas Jefferson National Accelerator Facility in Newport News, Virginia. CEBAF first began delivering a 4 GeV energy electron beam in 1995 to the original three experimental halls, A, B, and C. The energy of the electrons delivered was increased to 6 GeV in 2000, and a significant upgrade to the accelerator provided a 12 GeV electron beam first delivered in 2014 [39]. CEBAF, as seen in Fig. 2.2, consists of two linacs and a series of arcs that steer the beam from one linac to the other. Each linac is comprised of hundreds of superconducting cavities that provide a strong electromagnetic gradient to accelerate the electrons (see Fig. 2.3) [40]. The electron beam makes 5.5 circuits around the accelerator loop, acquiring ~ 1.1 GeV/linac, before entering the Hall D Tagger Hall shown in Fig. 2.4. The nominal repetition rate for Hall D is 249.5 MHz, meaning electrons arrive in bunches separated by ~ 4 ns. GlueX-I ran with an electron beam current of around 150 nA [41].

2.2 Polarized Photon Beam and the GlueX Beamline

This section will describe features of the GlueX beamline and the production of the photon beam. More detail on the GlueX beamline is given in Chapter 2 of [38]. A schematic of the beamline and its relation to the GlueX detector can be seen in Fig. 2.4. The electron beam position and profile can be monitored as it enters the Tagger Hall by a number of harp detectors (e.g. 5C11B is labelled in Fig. 2.4). The nominal energy and beam spot size of the electron beam as it reaches the radiator is given in Table 2.1.

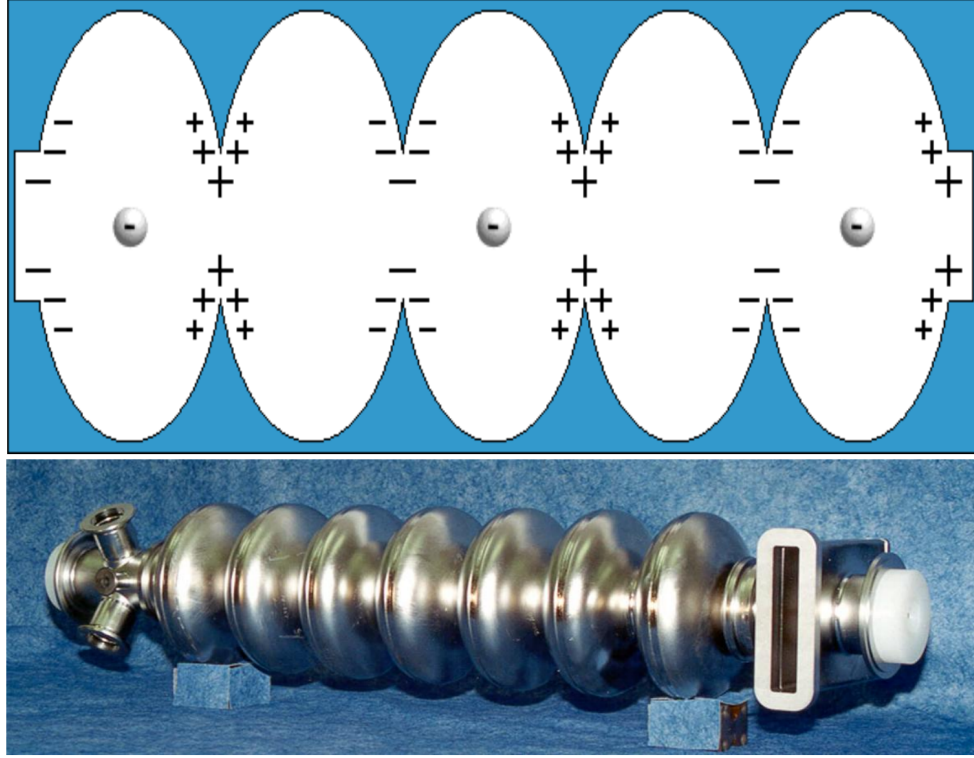


FIG. 2.3: (Top) A illustration of the charge distribution inside a accelerator cavity for accelerating an electron from left to right (in this case). (Bottom) A picture of a superconducting RF cavity used in CEBAF.

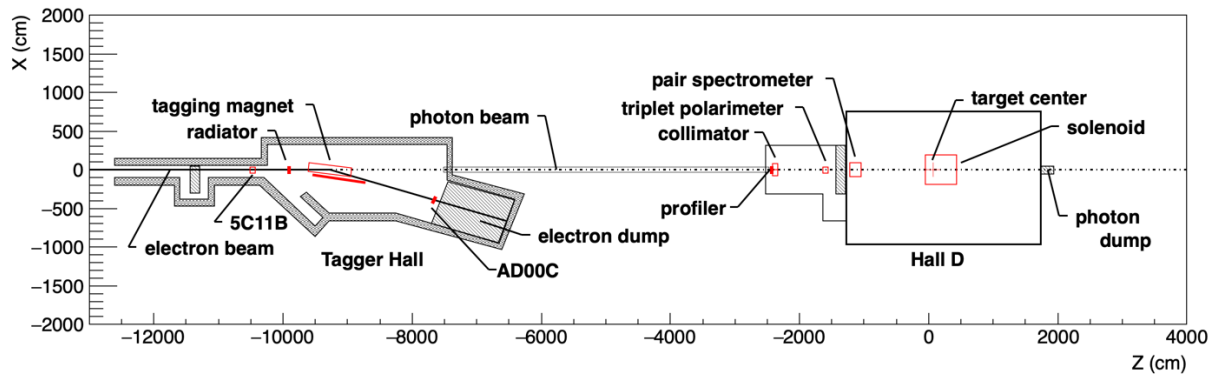


FIG. 2.4: A diagram of the GlueX beamline and detector [38]. Highlighted in this diagram are the devices used to monitor both the electron and photon beams.

Parameter	Design Values
energy	12 GeV
energy spread, RMS	2.2 MeV
transverse x emittance	2.7 mm $\cdot\mu$ rad
transverse y emittance	1.0 mm $\cdot\mu$ rad
x spot size at radiator, RMS	1.1 mm
y spot size at radiator, RMS	0.7mm
x image size at collimator, RMS	0.5 mm
y image size at collimator, RMS	0.5 mm
image offset from collimator axis, RMS	0.2 mm
distance radiator to collimator	75.3 m

TABLE 2.1: Properties of the electron beam as it enters the Hall D Tagger Hall [38].

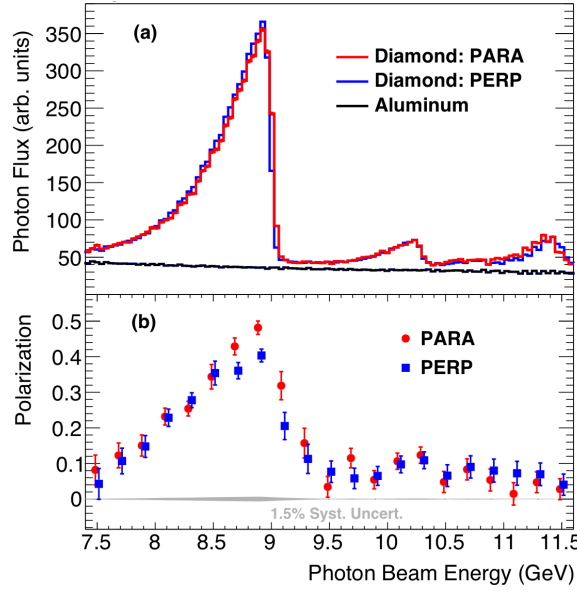


FIG. 2.5: (a) The photon beam flux as a function of beam energy for the diamond radiator (in red and blue) and the aluminum radiator (black). (b) The fraction of polarized photons in the beam as a function of energy. The Labels PARA (parallel) and PERP (perpendicular) refer to the angle of the linear polarization of the beam with respect to the horizontal plane in the lab. Image sourced from [38].

2.2.1 Photon beam production and radiators

As previously mentioned, GlueX uses a real photon beam produced via bremsstrahlung, the effect where photons are radiated from charged particles as they are accelerated (in this case the electrons are slowed as they interact with atomic electrons in the radiator material). The radiators (position shown in Fig. 2.4) are mounted to a goniometer capable of rotating about the x , y , and z axes. Over the course of GlueX-I running, three different diamond radiators were used to produce the polarized photon beam, and an $40\text{ }\mu\text{m}$ aluminum radiator to produce an “amorphous”/unpolarized photon beam.

Diamond Radiators and the Polarized Photon Beam:

Electrons passing through the lattice of a diamond can radiate coherent bremsstrahlung photons. The diamond lattice spacing, coherent radiation fraction, thermal properties, and radiation hardness make them ideal for such applications [42]. During the GlueX-I running, three diamonds were used: one $20\text{ }\mu\text{m}$ thick diamond and two $50\text{ }\mu\text{m}$ thick diamonds. The coherent intensity as a function of beam energy is related to the angle between the incoming electron beam and the normal (2,2,0) lattice vector of the diamond. The orientation of the diamond radiators were chosen to give a coherent peak at 9 GeV, as seen in Fig. 2.5. The fraction of photons that are linearly polarized (*i.e.* for which the components of their electric field component are in phase) as a function of the photon beam energy is also shown in Fig. 2.5. The diamond was set to different orientations throughout the run to give a linearly polarized beam with different polarization plane orientations. These polarization plane orientations were set to be 0° , 90° , -45° , and 45° with respect to the horizontal plane in the lab frame (the experimental hall floor).

Amorphous Radiator:

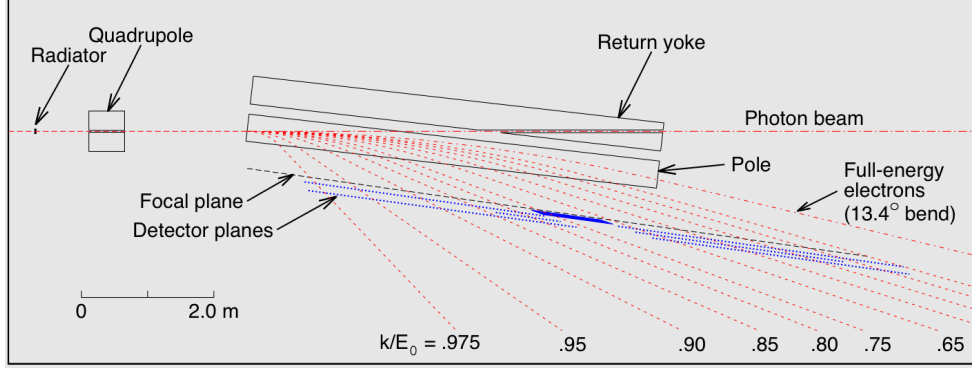


FIG. 2.6: A schematic of the tagging detectors [38]. The Tagger Hodoscope and Microscope are represented by the blue lines; the Tagger Microscope is the denser set of blue points in the center of the detector plane, while the Tagger Hodoscope covers the rest of the area.

In order to normalize the rates measured downstream of the radiators, data was also taken using a number of aluminum radiators, referred to as amorphous radiators. The typical amorphous radiator for GlueX-I was a 40 μm thick aluminum radiator (which has a similar radiation length to a 50 μm diamond), though radiators as thin as 1.5 μm were also used. The flux distribution of the aluminum radiators is also shown in Fig. 2.5, without the coherent enhancement.

2.2.2 Photon Tagging

After the photon beam is produced, the energy of the resulting photons is determined by measuring the energy of the slowed electrons. A 1.5 T dipole magnet referred to as the tagging magnet, shown in Fig. 2.4, sweeps the electrons out of the photon beamline. Electrons that did not radiate any, or very little, energy are swept into an electron beam dump. Electrons that radiated between 25% and 97% of their energy are swept into segmented scintillating detectors. These segmented detectors are the TAGH and TAGM, and are represented by the blue lines in Fig. 2.6. The TAGH spans the full 25 - 97 % energy range, while the more precise TAGM spans just the region for electrons in the

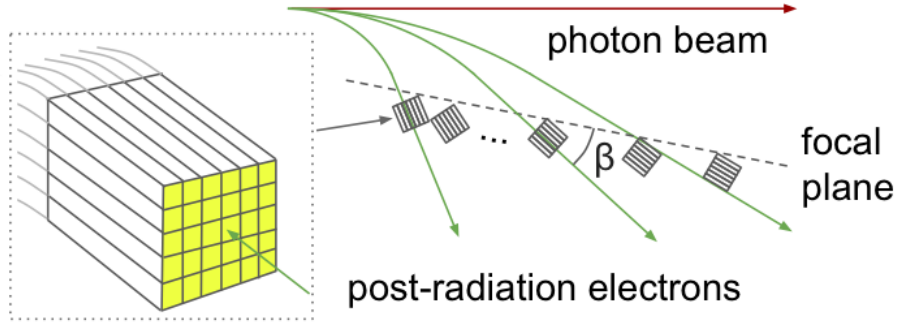


FIG. 2.7: (left) A cross section diagram of the scintillating fibers used in the TAGM [38]. (right) A schematic of the TAGM and its relation to the incoming electrons (β is exaggerated to demonstrate the concept).

coherent peak energy range (*i.e.* for electrons that radiated photons of energy between 8.0 and 9.0 GeV). The TAGH is comprised of 222 scintillating detectors with an electron energy resolution varying between 8.5 and 30 MeV. The TAGM is comprised of a 102x5 array of scintillating fibers as shown in Fig. 2.7, giving an energy resolution on the order of <10 MeV.

2.2.3 Absorber, Profiler, and Collimator

After the electrons are swept out of the beamline, the photon beam passes through the collimator cave. At the entrance of the collimator cave is a $100\ \mu\text{m}$ tungsten foil that filters low energy (10 - 100 keV) photons. These low energy photons cause random hits in the inner layer of the central drift chamber lowering its detection efficiency for real tracks. Downstream of the tungsten filter is a beam profiler consisting of two planes of scintillating fibers that measures the X and Y beam profile, respectively. The photon beam profiler is used during photon beam tuning (not during physics data taking) to ensure the photon beam is centered on the active collimator. The active collimator is a device made up of an array of tungsten pins which detect off-axis photons. The information collected by

the active collimator is used to make minor adjustments to the steering of the electron beam to ensure that the resulting photon beam does not drift far from the center of the collimator. The primary collimator used in GlueX-I data taking is a tungsten block with a 5 mm aperture. In the same block, there is also a 3.4 mm aperture that can be used. The collimator block and the lead shielding around it are followed downstream by additional shielding, a secondary collimator and sweeping magnets to remove any charged particles produced by the primary collimator.

2.2.4 Beam Flux and Polarimetry

Once the photon beam is collimated, it is passed through a thin beryllium foil which produces e^+e^- pairs when the photons interact with the atomic electrons in the foil. A pair spectrometer (PS) and triplet polarimeter (TPOL) use this production to measure the collimated beam flux as a function of beam energy and the polarization fraction of the photon beam. This stage of the beamline is near the GlueX detector and can be seen in Fig. 2.4.

Pair Spectrometer:

A dipole magnet steers the e^+e^- pairs into the two arms of the PS hodoscope and the PS coarse counter (PSC), which are layered on top of each other. The PS hodoscope contains 145 scintillating tiles, and the PSC contains 16 scintillating counters used to trigger on e^+e^- pairs. The pair spectrometer has an e^\pm momentum acceptance between 3 and 6.2 GeV/ c . The PS hodoscope provides 25 MeV energy resolution for each e^+e^- pair, while the PSC gives a timing measurement with a 120 ps resolution. The time and energy can be measured in coincidence with the tagging detectors.

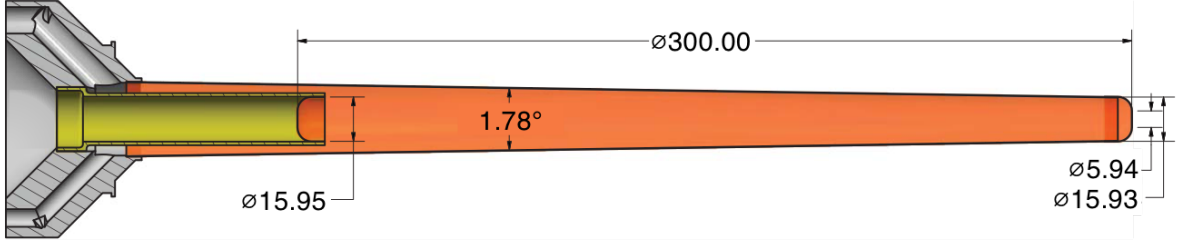


FIG. 2.8: GlueX experiment's target cell [38]. The cavity is filled with liquid hydrogen. Measurements given are in mm.

Triplet Polarimeter:

The triplet polarimeter measures the azimuthal distribution of the recoil electron knocked out of the beryllium converter when the e^+e^- pair is produced. The polarized triplet production cross section depends on the polarization fraction P , beam asymmetry Σ (determined in calibrations), the unpolarized cross section σ_0 and the azimuthal angle ϕ , and is given by [43]:

$$\sigma_{TPOL} = \sigma_0 [1 - P\Sigma \cos(2\phi)]. \quad (2.1)$$

The recoiling electron is detected by a silicon strip detector that records both the azimuthal angle and the energy of the electron. Results of this polarization measurement are shown in Fig. 2.5(b).

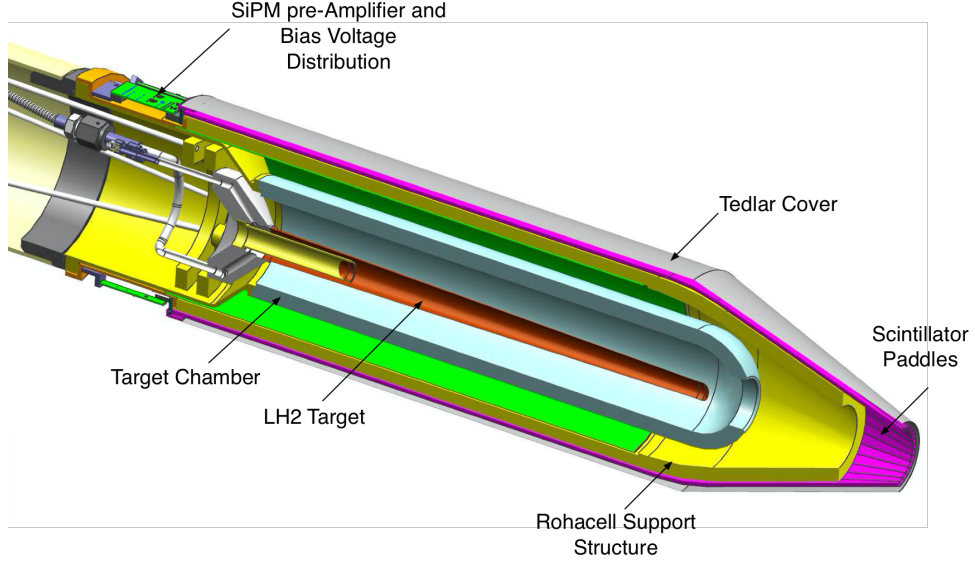


FIG. 2.9: Diagram of the GlueX Start Counter [38]. The ST is located around the target cell, which is used to tag which electron beam bunch produces the photon responsible for an event.

2.3 GlueX Detector

2.3.1 Target

The target system used in GlueX-I is shown schematically in Fig. 2.8, and this section summarizes the information given in Chapter 4 of [38]. The target is a 30 cm long, liquid hydrogen filled, conically shaped cell. The walls of the cell are 100 μm thick and made from polyimide. The LH_2 in the target region is kept at a temperature of ~ 20 K and a pressure of 19 psi. The target is supported by its own cryo-system that chills, circulates, and stores the hydrogen.

2.3.2 Timing Detectors

The Start Counter (ST) and the Time of Flight (TOF) detectors are both scintillating detectors used in the identification of charged particles. The ST, shown schematically in Fig. 2.9, is located around the target. The TOF is a planar hodoscope located downstream of the barrel of the detector, upstream of the Forward Calorimeter. The TOF's relative location can be seen in Fig. 2.1, and a picture of it in Fig. 2.10. More detail on the timing detectors can be found in Sections 8.1 and 8.2 of [38].

Start Counter:

The Start Counter is a system of 30 azimuthally segmented, scintillator paddles supported by a ROHACELL foam support structure around the target. The paddles are arranged in a cylindrical shape and bent in to a nose upstream on the downstream end of the target. The start counter has a $\sigma = 234$ ps time resolution and is used to tag which electron beam bunch produces the photon in a given event. Energy deposited in the start counter provides a dE/dx measurement used in particle identification. When combined with the track momentum information from the tracking detectors (Sec. 2.3.4), the dE/dx value from the ST is sensitive enough to separate protons from charged mesons up to a track momentum of $p = 0.9$ GeV/ c .

Time of Flight Detector:

The TOF is comprised of two orthogonal planes of scintillating bars that provide fast timing measurements for charged particles that pass through it. The TOF, seen in Fig. 2.10, has a polar angle acceptance from 0.6° to 13° in the lab frame. The TOF is designed to have a 12×12 cm² gap around the beamline. The scintillating bars are 6 cm wide (3 cm near the beam hole), which gives a spatial resolution of the two planes together of 6×6 cm² (up to

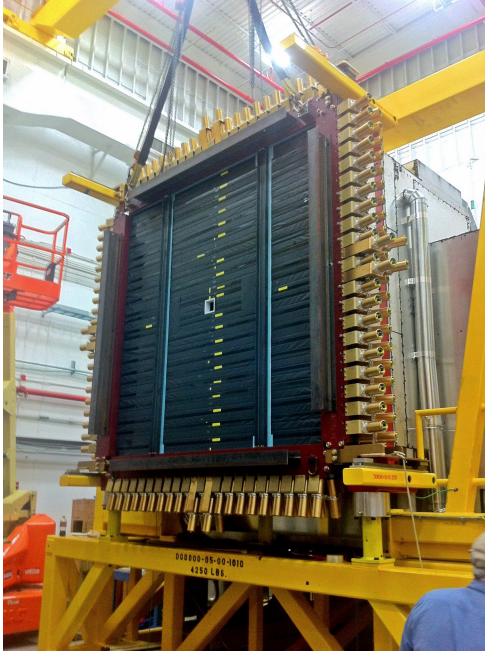


FIG. 2.10: Image of the GlueX Time of Flight Detector. The scintillating paddles are wrapped in black Tedlar, and can be seen spanning the face of the detector. PMTs are housed in the gold colored brackets surrounding the TOF.

$3 \times 3 \text{ cm}^2$ near the beam hole). The average timing resolution for the TOF is 105 ps. From the precise timing of the TOF, and using the track momentum from the tracking detectors, GlueX-I could separate pions from kaons with a 4σ confidence for a track momentum up to $2 \text{ GeV}/c$. Particle identification is discussed in more detail in Sec. 3.

2.3.3 Solenoid Magnet

The GlueX spectrometer is built in and around a large, superconducting solenoid that provides a 2 T magnetic field along the beam axis during typical GlueX-I data taking. The solenoid is made up of four separate superconducting coils connected in series which are cooled by liquid helium which is maintained by a dedicated refrigeration system. The bore of the solenoid is 2 m wide and 4.8 m long. The target, ST, tracking detectors, and barrel calorimeter all reside inside the bore of the solenoid. The high magnetic field produced

by the solenoid gives charged particles a curved trajectory, allowing the momentum of the particles to be determined. Accurate determination of the field is crucial for extracting momenta from the reconstructed particle tracks, and the calculated map is used for this purpose. More detail on the solenoid Magnet is given in Chapter 3 of [38].

2.3.4 Tracking Detectors

GlueX has two tracking detectors that determine the trajectory of charged particles as they pass through the spectrometer. Additionally, they measure timing and energy loss of the charged particles. The central drift chamber (CDC) is cylindrical and surrounds the target, and the forward drift chamber (FDC) is contained within the solenoid barrel downstream of the target (see Fig. 2.1). More information on the tracking detectors can be found in chapter 5 of [38].

Central Drift Chamber:

The polar angle acceptance of the CDC is from 6° to 168° , though its performance is optimal from 29° to 132° . The CDC has 28 layers of straw tubes, 12 of which are axial to the beam line and 16 layers are set at a $\pm 6^\circ$ angle from the axial. The orientation of the off-angle straws can be seen in Fig. 2.11. Each of the 3522 straws are composed of a Mylar tube with a gold plated tungsten wire running through the center. A 50/50 mix of argon and carbon dioxide fills the straws at 1 atm. The wires inside the straws are kept at ~ 2150 V. When charged particles pass through a given straw, the gas mixture becomes ionized and a signal pulse is generated between the signal wire and the ground. The CDC has a spatial resolution of $130 \mu\text{m}$, and if a charged particle passes within 4 mm of one of the straws, each straw has an efficiency over 98%.



FIG. 2.11: Image of the straws of the Central Drift Chamber during construction [38].
The off-angle orientation of the straws is demonstrated here.

Forward Drift Chamber:

The FDC has complete polar angle acceptance from 1° to 10° , and partial coverage up to 20° . The FDC is a series of 4 packages with 6 wire chambers in each package. Each chamber has a plane of sense and signal wires sandwiched between two cathodes as depicted in Fig. 2.12. The sense and field wires are separated by 5 mm each and kept at +2200 V and -500 V respectively. The chambers are filled with a 40/60 argon to carbon dioxide gas mixture. Each chamber in the package is rotated by 60° from its neighboring chambers. The position resolution of the FDC is as low as $60 \mu\text{m}$.

2.3.5 Calorimetry Detectors

The GlueX detector contains two electromagnetic calorimeters that measure the energy deposits and timing information of charged and neutral (that have decayed to $\gamma\gamma$) particles. The Barrel Calorimeter (BCAL) and Forward Calorimeter (FCAL) are depicted in Fig. 2.1 in blue. More detail on the calorimetry detectors is given in Chapter 7 of [38].

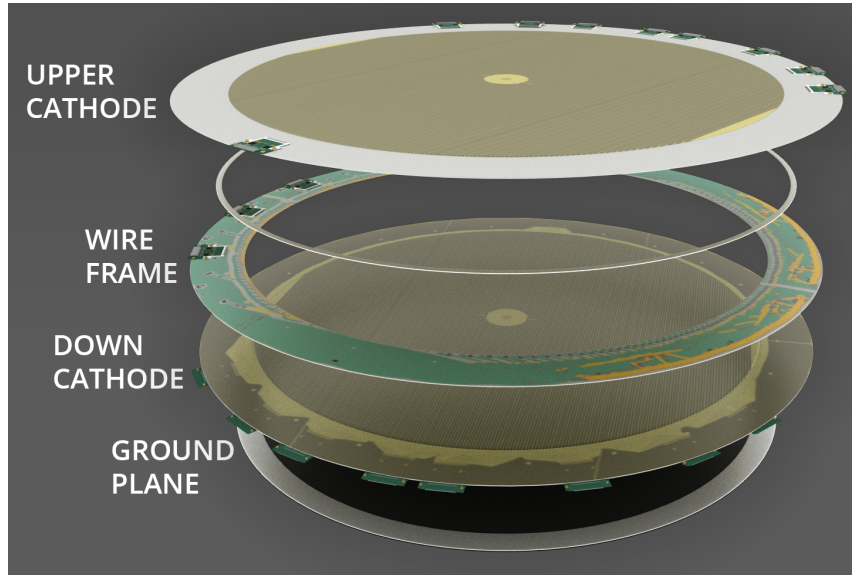


FIG. 2.12: A render of a chamber in the Forward Drift Chamber [38]. The upper cathode faces the upstream direction.

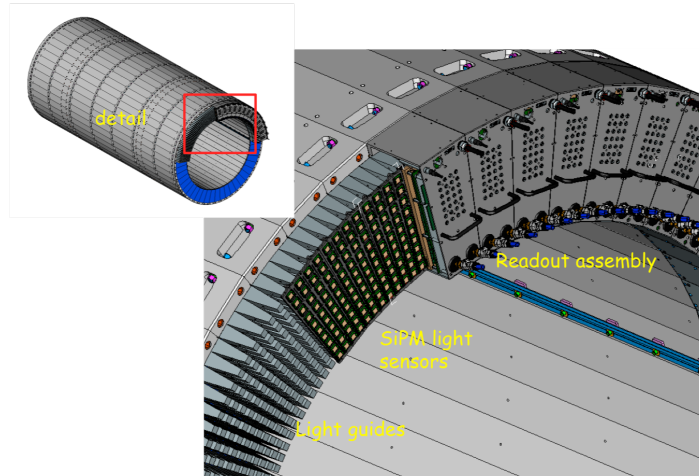


FIG. 2.13: A rendering of the Barrel Calorimeter, and a zoomed-in view of the readout assembly, SiPM orientation, and light guides [38].

Barrel Calorimeter:

As the name implies, the BCAL is located in the barrel of the solenoid magnet, around the CDC and FDC. The BCAL has a polar angle acceptance from 11° to 126° , and a full 2π azimuthal acceptance. The BCAL is comprised of 48 isolated modules arranged in a cylindrical configuration. Each of these modules contains 185 layers of corrugated lead sheets and scintillating fibers. Silicon photomultipliers detect the light generated by the scintillating fibers. The assembly of the BCAL can be seen in Fig. 2.13. The BCAL has a spatial resolution of ~ 2.5 cm along the beam axis, a timing resolution of ~ 150 ps, and photon energy deposit resolution $\sigma_\gamma/E_\gamma < 10\%$.

Forward Calorimeter:

The FCAL, located in the forward region of the detector, covers the 1° to 11° polar angle range and has a full 2π azimuthal acceptance. The FCAL consists of a circular array of 2800 4×4 cm² by 45 cm long lead glass blocks (see Fig. 2.14). Light emitted by particles entering the FCAL block is detected by μ -metal shielded PMTs attached to each block via a light guide. The FCAL has a positional resolution less than 1.1 cm and a photon energy deposit resolution $\sigma_\gamma/E_\gamma < 7\%$ for a broad range of E_γ .

2.4 Trigger and Data Acquisition

This section will describe the trigger system and the triggers used in the typical GlueX data taking mode, as well as the data acquisition system and performance. More detail on the trigger and the data acquisition system can be found in Chapters 9 and 10 of [38].



FIG. 2.14: An image of the interior of the Forward Calorimeter where the grid of lead glass blocks can be seen.

2.4.1 GlueX Trigger

During normal data taking there are a number of triggers that operate simultaneously. These are the nominal physics trigger, a PS trigger for photon beam flux calculations, a random trigger used for modelling and subtracting background events, and an LED trigger synced to LED light pulses in the calorimeters (used for calorimeter calibrations and monitoring). The random trigger is chosen to have a rate of 100 Hz, while the LED trigger is chosen to have a 10 Hz rate. During GlueX-I running, the PS trigger has a rate around 3 kHz. The total trigger rate during GlueX-I data taking was around 40 kHz. A brief description of the trigger system, the physics trigger, and the PS trigger follows.

The trigger system for GlueX consists of a dedicated pipeline of electronics hosted on 55 VXS crates along with the readout electronics. For the main physics trigger, information from the calorimeters is used. The energy data from both the FCAL and BCAL are digitized by FADC modules. The digitized information is summed and passed on to a *crate trigger processor* (CTP). The CTPs pass their information to the *global trigger crate* where

it is combined by the *sub-system processors*. A *global trigger processor* (GTP) then applies a conditional formula to decide whether to trigger or not. The *trigger supervisor* module receives the information from the GTP, and disseminates the trigger to the appropriate data readout crates via a *trigger distribution* module. This system also syncs the clock for the triggers.

The GTP typically followed two formulas/conditions for the nominal physics trigger, and they are

$$2 * E_{FCAL} + E_{BCAL} > 1 \text{ GeV} \ \&\& \ E_{FCAL} > 0 \text{ GeV} \quad (2.2)$$

$$E_{BCAL} > 1.2 \text{ GeV}. \quad (2.3)$$

Eq. 2.2 is useful for events with a significant amount of energy going in the forward direction, while Eq. 2.3 is useful for event with large transverse energy.

The PS trigger is based on coincidence measurements in each arm of the pair spectrometer coarse counter, corresponding to e^+e^- pair production. The 3 kHz PS trigger rate mentioned above corresponded to a typical photon flux of $1.5 \cdot 10^7 \text{ } \gamma/s$ in the coherent peak region.

CHAPTER 3

GlueX DIRC Upgrade

In 2019, the GlueX experiment was upgraded with a new particle identification detector. This type of detector is known as a DIRC, which is an acronym for *Detection of Internally Reflected Cherenkov radiation*. The GlueX DIRC is designed to improve the separation of pions and kaons at charged particle momenta up to ~ 4 GeV. This chapter describes the concept, design, installation, commissioning, and early performance of the GlueX DIRC. Special attention is paid to the characterization and calibration of the photodetectors performed by the author.

3.1 Cherenkov Radiation

Charged particles that travel through dielectric material lose energy as the particles interact with the medium along their path in the form of photon radiation [44]. If the travelling charged particles are relativistic, the radiation is observed with distinct properties that were first observed *and* identified by Pavel Cherenkov in 1934 [45]. Tamm and Frank formulated the theory behind this phenomenon, deriving the energy radiated per unit distance along the charged particle's path in the case where the velocity of the

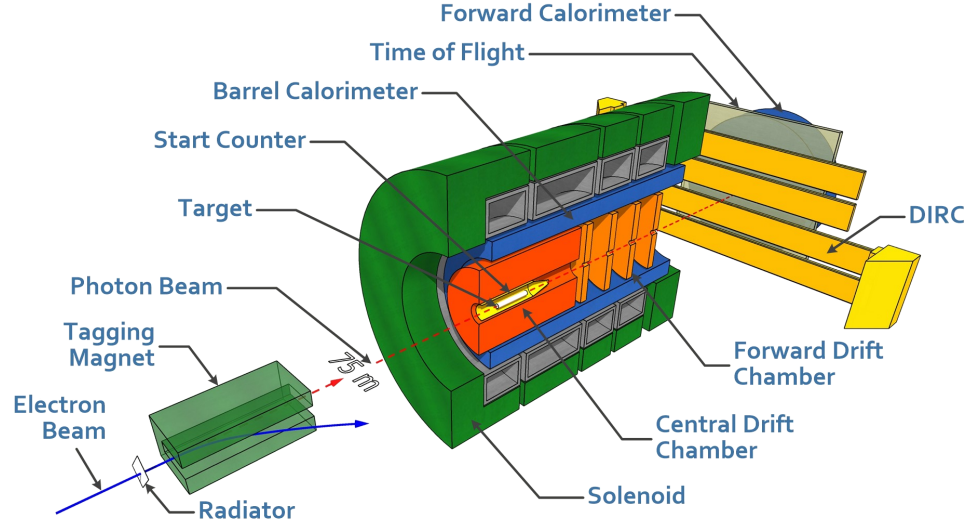


FIG. 3.1: Diagram of the GlueX detector (not to scale) showing the relative position of the DIRC upgrade.

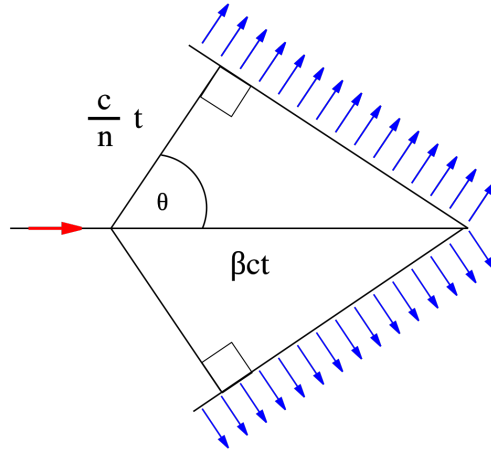


FIG. 3.2: Diagram relating the Cherenkov angle to the relativistic velocity (βc) and the index of refraction (n).

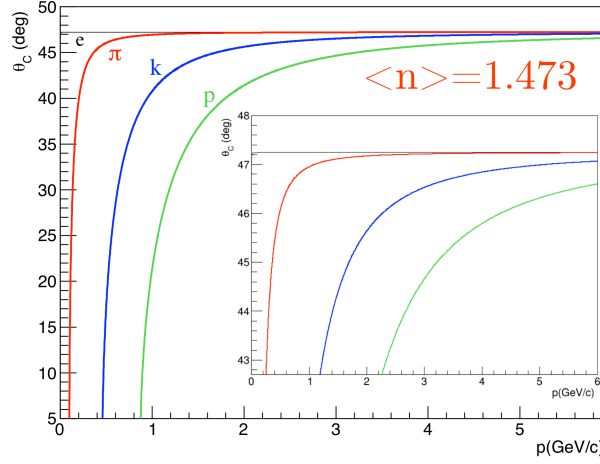


FIG. 3.3: Calculated relationships between the Cherenkov angle θ_c and particle momentum p for pions, kaons, and protons for a fixed index of refraction n .

particle is greater than the phase velocity of light in the same medium [44][46]. Due to the fact that the radiating particle is travelling faster than the speed of light in this case, the radiated light can be described as a ‘shock’ wavefront in the far field limit. The wavefront is emitted in a cone around the path of the charged particle with an opening angle (θ_c) related to the velocity ($v = \beta c$) and index of refraction ($n(\lambda)$) given by

$$\cos \theta_c = \frac{1}{\beta n(\lambda)}. \quad (3.1)$$

A diagram of this wavefront relationship can be seen in Fig. 3.2.

In Cherenkov detectors, including the GlueX DIRC, charged particles travel through a medium with well known properties, and the resulting Cherenkov angle can be measured in order to determine the particle’s velocity. The GlueX DIRC uses the velocity measurement in combination with momenta measurements from the tracking detectors to identify charged particles by determining the mass (see Fig. 3.3, where the calculated relationship Cherenkov angle vs. track momentum is plotted). The next section will describe the specific design of the GlueX DIRC, and how the Cherenkov angle is determined.

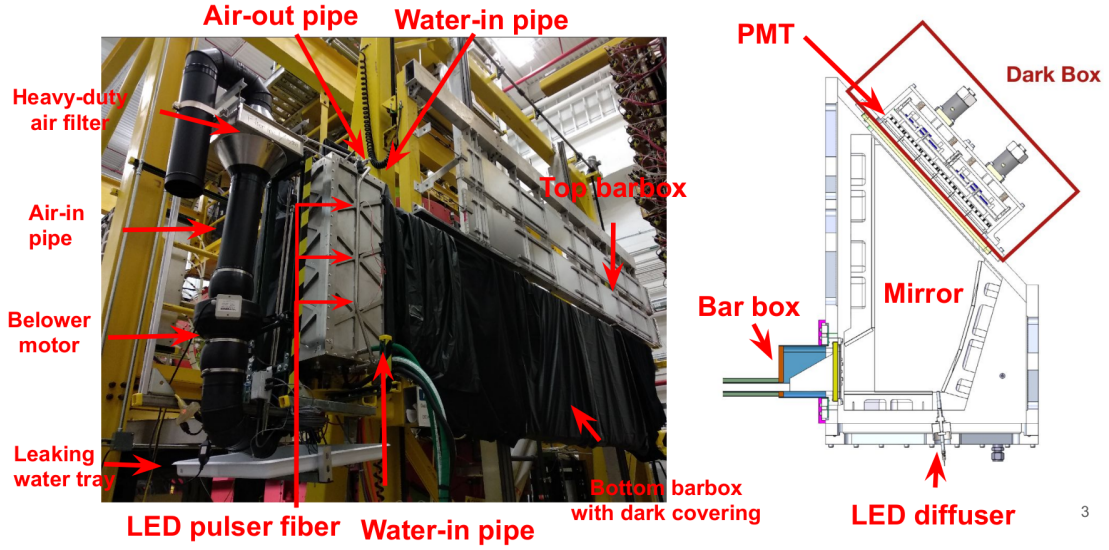


FIG. 3.4: (Left) Picture of the DIRC installed in the GlueX detector with labels. (Right) Diagram of the optical box and PMT housing.

3.2 GlueX DIRC Design

In this section, an overview of the GlueX DIRC design is presented. A schematic of where the DIRC resides within the GlueX experiment can be seen in Fig. 3.1. The GlueX DIRC is a compact (in the z-dimension) detector with an angular acceptance $\theta < 11^\circ$ from the beamline in the lab frame, that uses total internal reflection to direct Cherenkov photons to photodetectors installed in an expansion volume on the ends of the radiators. The GlueX DIRC consists of a set of radiator bars in which the Cherenkov radiation is generated, an optical box that allows photon tracks to diverge in space, and a plane of photo-multiplier tubes (PMTs) used to detect the photons. Each of these main components and their functions are described in the following subsections, and they can be seen in detail in Fig. 3.4.

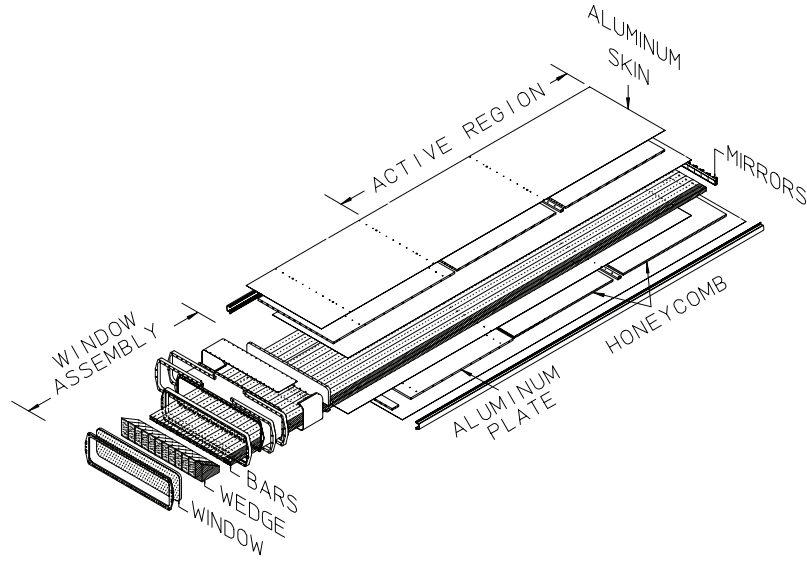


FIG. 3.5: A schematic diagram of the radiator bar assembly for the DIRC [47].

3.2.1 Radiator Bars

The GlueX DIRC inherited four of the twelve DIRC “bar boxes” used in the BaBar experiment at SLAC [47]. These bar boxes each contain twelve fused silica radiator bars (see Fig. 3.5). The fused silica (a synthetic form of quartz) serves as the radiation inducing material for producing the Cherenkov photons, as well as acting as light guides for the photons. The bars have a high average index of refraction of $\langle n \rangle = 1.473$, and are surrounded by nitrogen gas ($n \sim 1$). Each bar is 17.25 mm thick, 35 mm wide, and 4.9 m long. When charged particles enter the radiator bars, Cherenkov photons are produced and are internally reflected down the length of the bar (see Fig. 3.6). The bar boxes are connected on one end to one of two optical boxes (see Fig. 3.7), and the other end of the bars have mirrors to reflect the photons back toward the optical boxes.

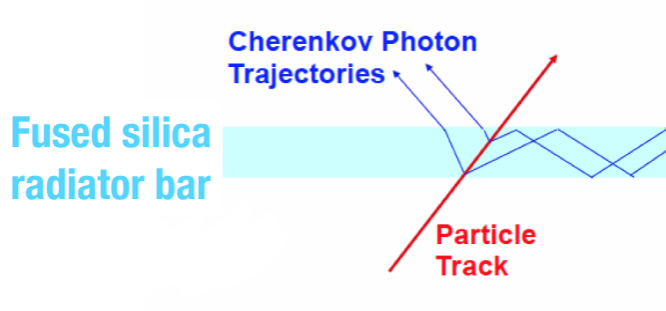


FIG. 3.6: Cartoon depicting the release of Cherenkov photons as a charged particle passes through a radiator bar.

3.2.2 Optical Box

The Cherenkov photons that are produced in the radiator bars make their way down the bars, totally internally reflected, and enter an optical box through a quartz window. The optical box acts as an expansion volume that allows the paths the photons take to the photo-detectors to diverge and reduce the required resolution at the PMT plane. A top down cross section of the optical box can be seen in Fig. 3.4 and Fig. 3.7. The optical box is filled with distilled water ($n \sim 1.3$), which is circulated by a dedicated water pump system. Inside the optical box is a series of mirrors mounted on aluminum strong-backs that are used to focus the photons onto the PMT plane. The mirrors have UV enhanced aluminum reflective surfaces, and have an additional piece of borosilicate glass epoxied in front of their surface to prevent corrosion from reducing the reflectivity of the mirrors. Each optical box also has three ports along the opposite side from the PMT plane to allow LED pulser fibers to enter the box. The LED fibers shine LED light on the PMT plane to monitor and calibrate the PMTs (see Sec. 3.5.9).

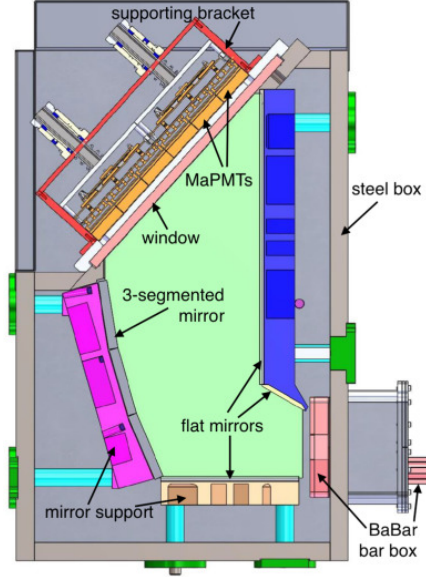


FIG. 3.7: Engineering diagram of the optical box. This diagram shows all of the components of the expansion volume in detail.

3.2.3 PMT Plane and Enclosure

PMT and Dark Box:

The PMTs used to detect the Cherenkov photons are mounted to a fused silica window on one face of the optical box (see Figs. 3.4 and 3.7). The PMTs are coupled to the window with an RTV silicone “cookie” and optical greasing oil that matches the index of refraction of the fused silica window. Each optical box has 90 Multi-Anode Photo-Multiplier Tubes (MAPMTs) arranged in 36 modules (some modules with 2 MAPMTs and some with 3; see Sec. 3.3 for more detail) are held in place with modular brackets that can be seen in Fig. 3.7. More detail on the MAPMTs used in the GlueX DIRC is given in the following sections.

Dark Box and Bar box dark covering:

The MAPMT modules are enclosed in a dark box that is attached to the exterior of the optical box. The dark box is constructed of stainless steel and is designed to protect the MAPMTs from ambient light that could damage them. In addition to the dark box, a

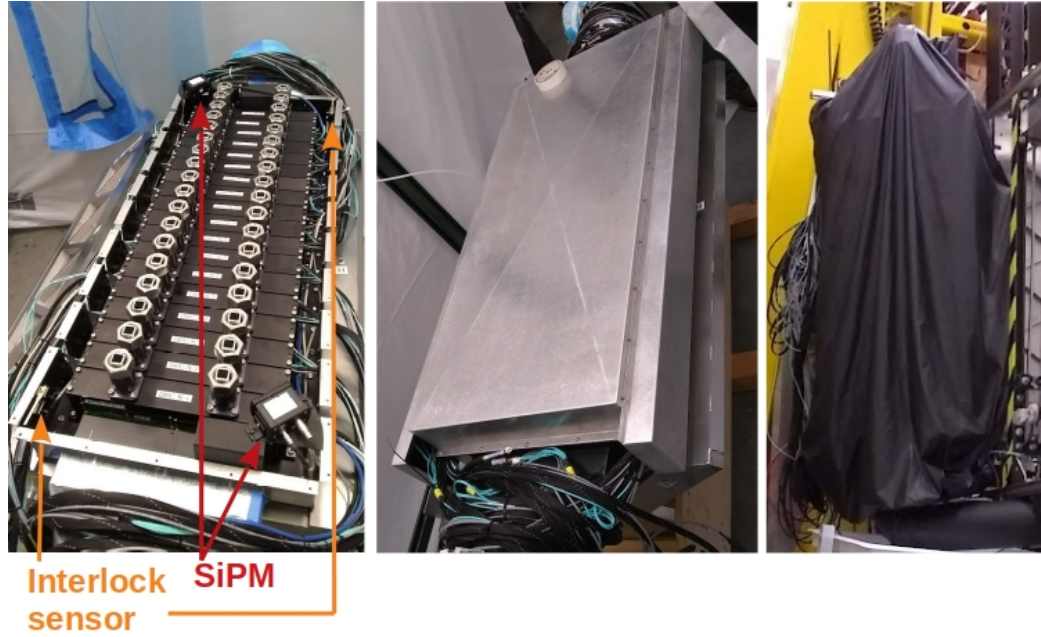


FIG. 3.8: (Left) The dark box (lid off) with all of the MAPMTs installed. The SiPMs monitor for light leaks in the box before high voltage is applied to the MAPMTs, and the interlock sensors prevent the voltage from being applied if the lid is off. (Center) The dark box with the lid covering the MAPMTs. (Left) the dark box covered with an additional optical shroud.

combination of black tape and optics shrouds are used to ensure no ambient light leaks into the MAPMT enclosure, see Fig. 3.8. Interlocking sensors mounted inside the dark box prevent the MAPMTs from receiving high voltage if the stainless steel cover is opened, or not installed properly. The interlocking sensors and SiPMs can be seen in Fig. 3.8. The FPGAs in the dark box are capable of generating a fair amount of heat during their operation, and so a light tight air flow system was designed to keep the environment from overheating. The air flow system consists of a heavy-duty air filter and bellow motor connected by blackened ductwork to the bottom of the dark box. The air exits the top dark box through a darkroom louver connected by more blackened ductwork. The ductwork takes as many 90° turns as space allowed, and the air flow system can be seen labelled in Fig. 3.4.

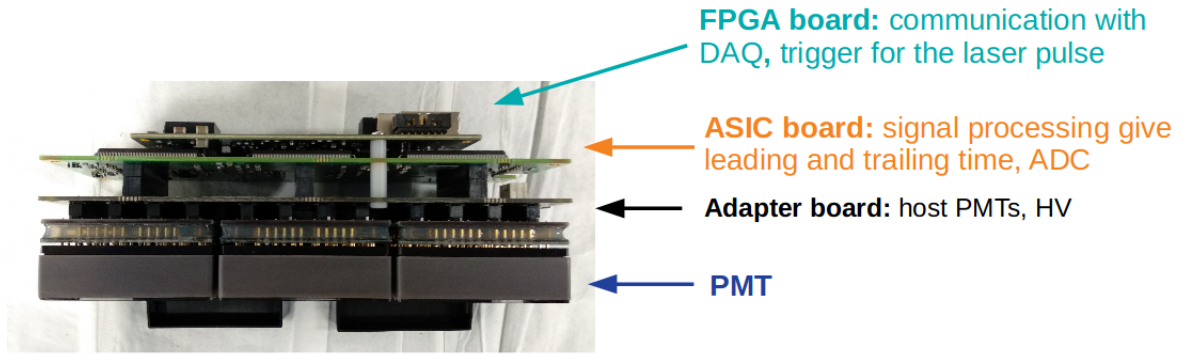


FIG. 3.9: A single MAPMT module with 3 MAPMTs, adapter board, ASIC board with 3 MAROC chips, and an FPGA board

3.3 MAPMT Electronics Stack

The MAPMTs used by GlueX DIRC are mounted to a compact readout board stack developed for the CLAS12 RICH detector. A more detailed summary of the development and description of the electronics can be found in the thesis by Matteo Turisini [48]. The stack, shown in Fig. 3.9, consists of three boards: an adapter board, an ASIC board, and an FPGA board. In the GlueX DIRC, the modules have either three Hamamatsu model H12700 MAPMTs (which are 64 pixel MAPMTs, see Sec 3.4), or two H12700 MAPMTs and a 3-D printed “dummy” PMT in the third slot. The adapter board provides a physical translation from the MAPMTs to the ASIC board and distributes the high voltage to the MAPMTs. The ASIC board contains three multi-anode read-out chips (MAROCs), one for each MAPMT, that convert the analog MAPMT signal into a digital signal. The FPGA board provides the communication between the MAROC chips and the DAQ and contains the operational firmware. The variation in response of the individual components in the electronic board stack was previously studied by the CLAS12 RICH group. Instead of repeating these studies, our modules were tested and installed as an assembled unit in order to study the response of the entire module, rather than individual components. In this way, variations can be studied at the MAPMT+MAROC level, with the caveat that

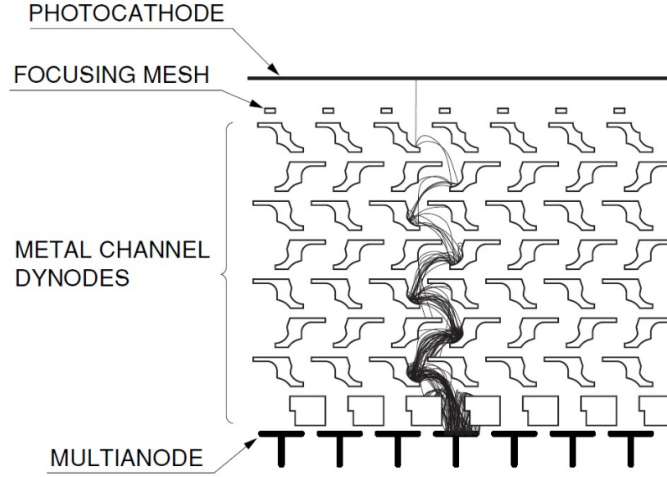


FIG. 3.10: Dynode structure inside the Hamamatsu H12700 MAPMT. Illustrated in this diagram is the cascade of electrons generated and measured in one channel.

if any tubes or ASIC boards are changed, than the module should be retested/calibrated.

3.4 Hamamatsu H12700 Multi-Anode Photo Multiplier Tubes

As previously stated, the GlueX DIRC used the Hamamatsu H12700 MAPMTs [49]. These MAPMTs each have a $48.5 \times 48.5 \text{ mm}^2$ active surface. The surface is divided into an 8×8 grid of $6 \times 6 \text{ mm}^2$ pixels. The pixels are sensitive to a photon wavelength range of 300 to 650 nm, with a peak sensitivity around 380 nm. The photo-cathode material is made from borosilicate glass. Each pixel has 10 metal channel dynodes, see Fig. 3.10.

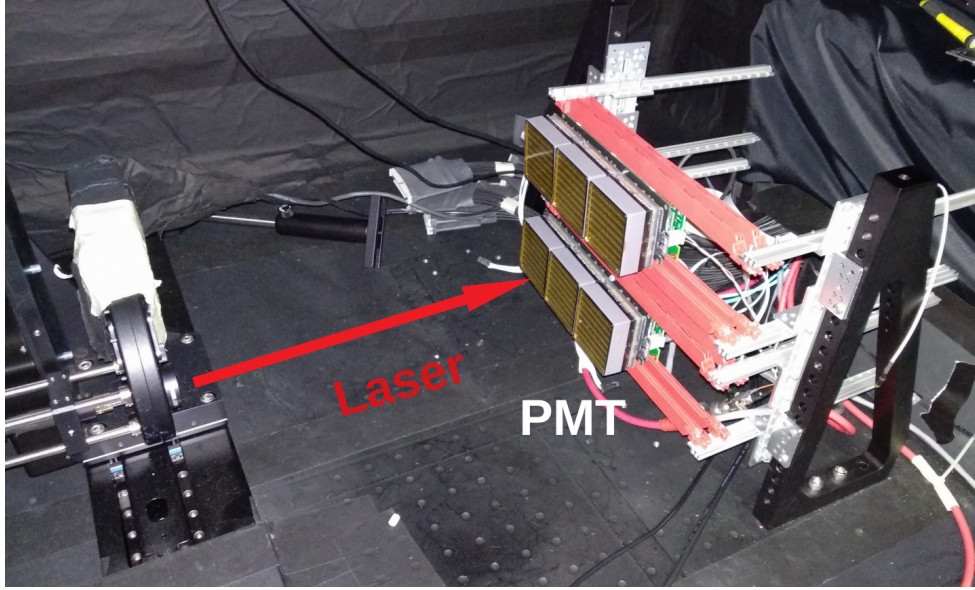


FIG. 3.11: The interior of the laser test setup is shown here. On the left, the laser aperture and diffuser are mounted to a 2-axis mobile platform. On the right is a small custom rack that holds two MAPMT modules. The entire setup shown is inside a dark box, with interlocks to the voltage supply and laser source.

3.5 Laser Bench Test

This section will describe the bench tests used to characterize and calibrate the MAPMTs.

3.5.1 Setup

The MAPMT modules were all tested in a dark-box laser (shown in Fig. 3.11) set-up in order to characterize the response of individual channels, as well as to identify any dead channels, tubes, or boards. Additionally, a study was done on a single module with a magnetic field present in order to characterize the change in response under such conditions. Here we give a brief description of the bench test set-up, though more detailed information can be found in [48]. The laser had a 405 nm wavelength and was fitted with a wheel of multiple diffusers, and was mounted to a movable arm. The laser-diffuser

component could be controlled by the data acquisition computer via motors that allowed the active diffuser to be changed and the laser to move in a plane parallel to the PMT surface. The MAPMT modules were mounted two at a time, on a custom rail system inside the dark box. The modules were supplied high voltage which was applied to the MAPMTs, low voltage which was applied to the FPGA, and a trigger signal that was synced to the pulse of the laser. The data from each module was read out via fiber optic cable. The laser+diffuser was used at a low enough intensity to ensure a pure test of the response to single photo electrons (SPE). The firmware used in the laser bench test allowed the readout of ADC and TDC signals via a “slow” signal shaper and a “fast” signal shaper, respectively, as well as information about the signal time of the analog signal pulse above some threshold (time over threshold or ToT), and pixel occupancy.

3.5.2 Magnetic Field Test

The GlueX DIRC is installed close enough to the superconducting solenoid that the optical box, and subsequently the MAPMTs, is within the fringe magnetic field. This field is predicted to have a magnitude of 20-30 Gauss in the region of the MAPMTs which can have an effect on the performance of the tubes that required study. To study the effect of the field on the tubes, a small Helmholtz coil was placed within the dark box around a single MAPMT module, as seen in Fig. 3.12. This Helmholtz coil was capable of reaching > 30 G as measured by a Hall probe at the face of the MAPMTs. The Helmholtz coil was oriented in two orientations (referred to as “field facing PMT” and “field facing down”) in order to cover multiple possible field conditions. Also tested in the magnetic field were several local, thin metal shielding concepts. The magnetic field tests were conducted at three various Helmholtz coil currents (1 A, 2 A, and 3 A), as well as two controls without any magnetic field. The Helmholtz coil was not large enough to ensure a uniform field, but

in the center, the peak strength corresponded to a peak of ~ 35 G for the 3 A setting (~ 23 G and ~ 12 G for the 2 A and 1 A settings).

In Fig. 3.13, the relative efficiency of the pixels in the magnetic field test are plotted for a single module. The pixels with the largest reduction in relative efficiency compared to the control run correspond to the pixels on the outer edge of the MAPMTs. In order to attempt to mitigate the efficiency loss, the MAPMTs were tested while wrapped with μ -metal shielding. One test was run with μ -metal surrounding each individual MAPMT, one with μ -metal wrapped around the entire module, and one with mu metal around the module that extended past the face of the MAPMTs. The effect of the shielding on the relative efficiency (number of SPE events per trigger normalized to a test run with no magnetic field) is shown in 3.14. The various shielding orientations had a positive effect on the relative efficiency of the channels effected by the magnetic field. The shielding that extended past the end of the MAPMT face reflected more photons onto some of pixels causing spikes in relative efficiency for those channels. The lack of available space in the detector and the few number of channels adversely effected by the magnetic field, it was decided to not install the μ -metal shielding around the MAPMTs. After the MAPMTs were installed and could be tested using LED light in the presence of the actual GlueX solenoid's magnetic field, there was not a noticeable loss of relative efficiency due to the field, and it was determined no shielding was needed after all.

3.5.3 MAPMT ADC Spectrum

The raw signal pulse generated by the cascade of electrons in the MAPMT is shaped and digitized by the MAROCs on the ASIC board. The MAROC 3A designed by the Omega Group was chosen as an ideal readout chip for the MAPMTs used by the GlueX DIRC. This model of chip was originally developed to readout Hamamatsu H7546 MAPMTs

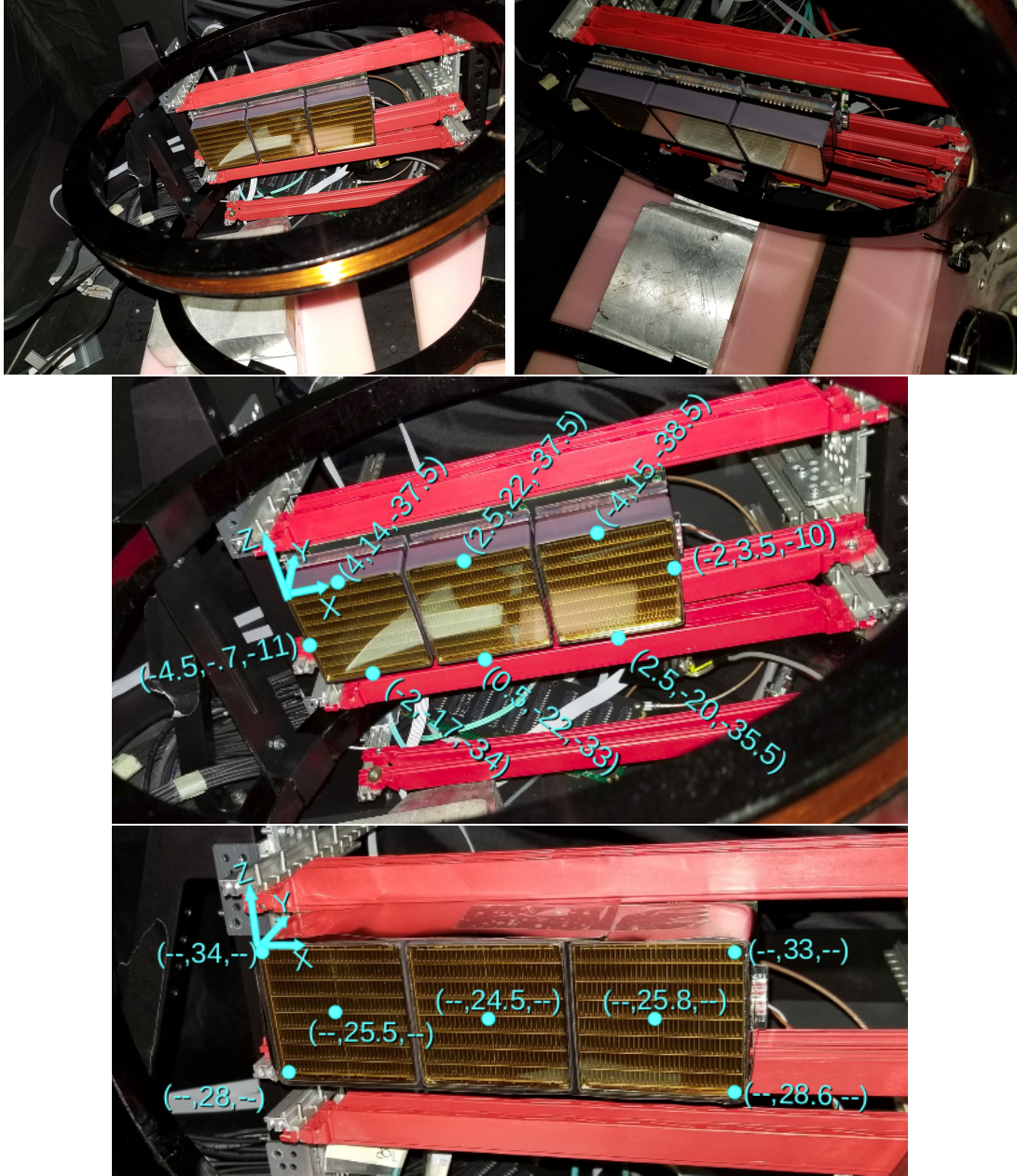


FIG. 3.12: The helmholtz coil used in the magnetic field tests is show in two orientations in the top two figures. The top left shows the ‘field facing down’ configuration, while the right shows the ‘field facing PMT’ configuration. The middle and bottom figures show the magnetic field strength (in Gauss) as measured via Hall probe at each point for the ‘field facing down’ and the ‘field facing PMT’ configurations in the middle and bottom images, respectively.

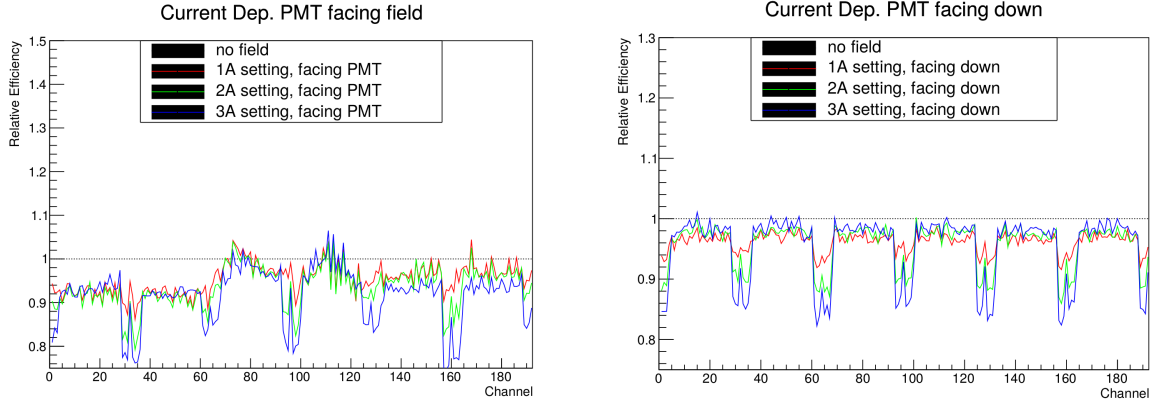


FIG. 3.13: Results from the magnetic field test plotted as a relative efficiency, that is normalized to a run with no field, as a function of channel number. The different color lines correspond to the current supplied to the Helmholtz coil. The left are the results from the ‘field facing PMT’ configuration, and on the right are the results from the ‘field facing down’ configuration. The dips in relative efficiency correspond to pixels on the edge of the module.

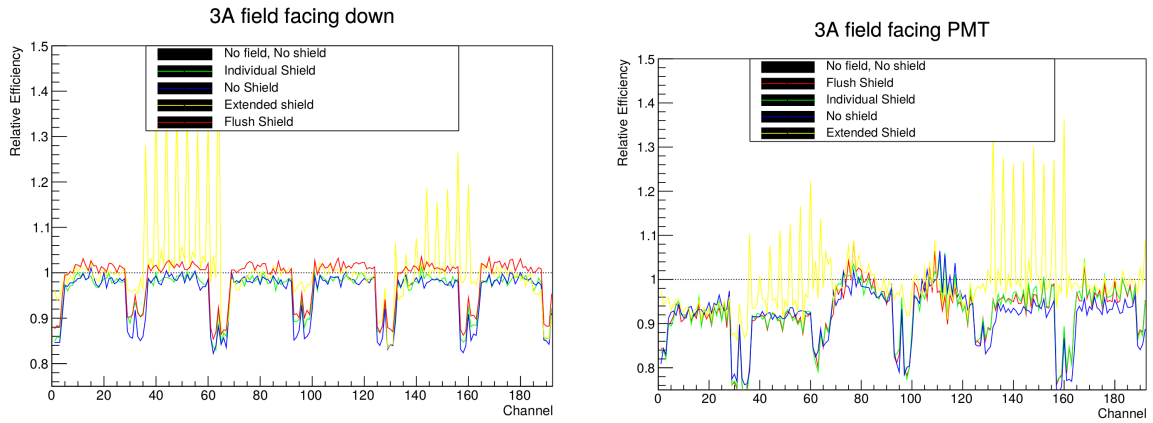


FIG. 3.14: The relative efficiency (normalized to the response with no magnetic field) results from the various local magnetic shielding options in each configuration. The ‘individual’ shield (green) was a layer of μ metal wrapped around each MAPMT, the ‘Flush’ shield (red) was a layer of μ metal wrapped around each module, and the ‘extended’ shield (yellow) was similar to the flush but extended past the face of the MAPMTs. Note that the spikes much higher than 1 correspond to pixels on the module that photons could be reflected into by the extended shielding.

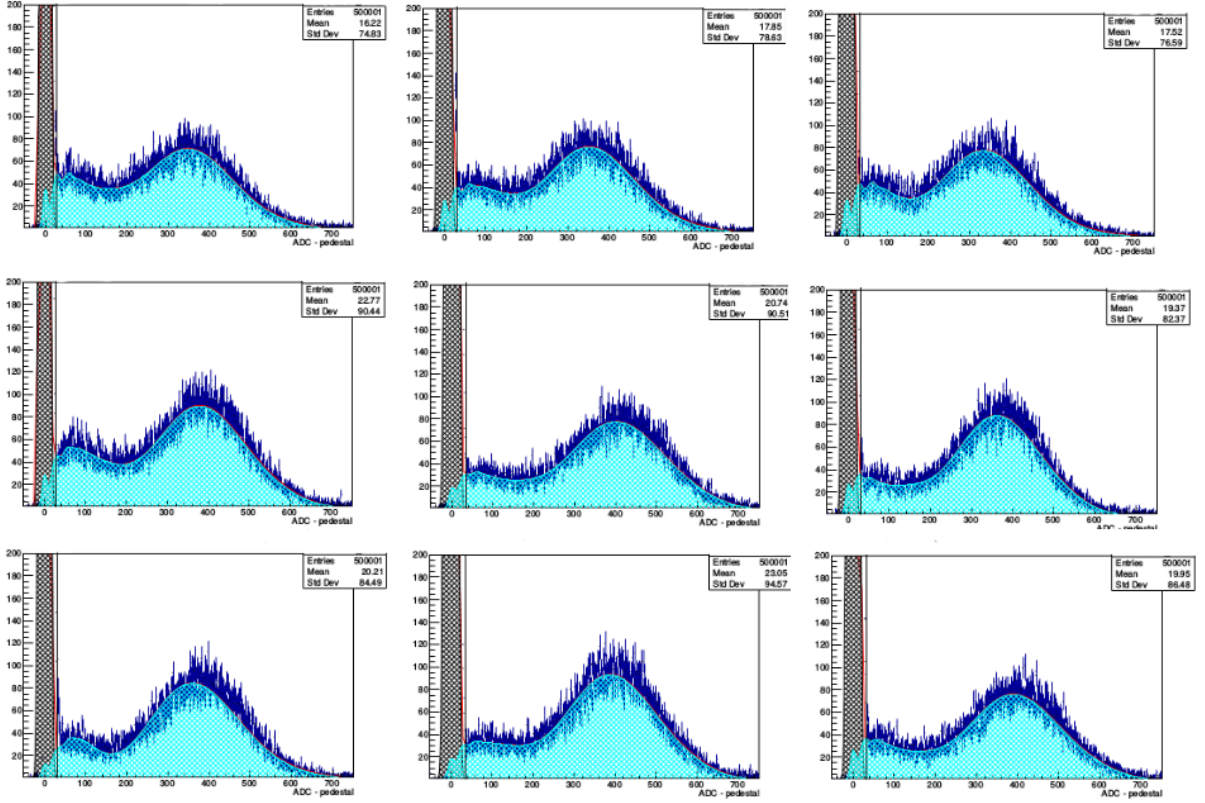


FIG. 3.15: A sample of ADC spectra from the laser bench test for 9 different pixels from the same MAPMT module. The black shaded region corresponds to the pedestal as extracted from the model fit (red line), and the cyan shaded region is the single photo-electron (SPE) region. In the interpretation of the model fit, we see that the ADC spectrum is dominated by pedestal and SPE with minimal contribution from events with a larger number of photo-electrons.

for the ATLAS experiment. The implementation of this model of readout chip with the H12700 MAPMT was developed by the CLAS12 group for their RICH detector. The MAROC 3A contains an embedded ADC to read out the charge of the signal by integrating the pulse formed by a slow shaper, as well as a TDC with a fast shaper that reads out the time a given signal current is above a chosen threshold. In standard operation the ADC cannot be read out at the rate the experiment takes data, and therefore only the fast shaper and the TDC information is used in the GlueX DAQ. The ADC response to single photon events is recorded during the laser bench test in order to compare and correlate to the TDC response that is used in standard operation. The ADC spectrum provides the most information about how the MAPMT+MAROC system responds to single photon events, and its characterization provides valuable insight into the TDC data recorded in standard operation.

3.5.4 General Characteristics of the ADC Spectrum

During the laser bench test outlined above, the MAPMTs were exposed to pulsed monochromatic light and manually triggered in time with the laser pulse. The intensity of the diffused laser light was such that the MAPMT modules would most often read out a “dark” ADC value where no photo-electron was produced, less often the ADC value of a single photo-electron event, and rarely any signal from events with more than one photon per pixel. The histogram of the ADC value for a given run then provides a look at the separation between the single photon response and the pedestal that is read out when no signal is detected. Knowing the separation between the dark pedestal and the single photon response allows thresholds to be set such that erroneous triggers can be avoided in operation, as well as gain matching to generate a uniform response across all of the pixels in the detector. An example of the ADC histogram can be seen in Fig. 3.15. The spectra

in Fig. 3.15 are also fitted with a model that is detailed in section 3.5.6. As expected, the ADC spectrum is dominated by the pedestal and the single photo-electron (SPE) response.

3.5.5 Effect of DAC Threshold Cuts

By also looking at the effect of digital-to-analogue (DAC) threshold cuts on the ADC spectrum, we can be confident that we have a method of removing pedestal events from the DAQ triggers during standard operation. Fig. 3.16 shows the reliability of making a cut on DAC units to remove the pedestal. Shown in the example of Fig. 3.16 is the resulting spectrum after making threshold cuts of 0, 25, 50, 100, and 200 in DAC units (a 1 mV signal corresponds to 1 DAC unit). A threshold cut of 25 DAC units clearly allows events from the pedestal through, while the others do not. To optimize the detector for maximum photon yield with minimal pedestal background, a safe DAC cut of 100 has been chosen for all pixels despite the loss of SPE events in pixels such as the one in Fig. 3.16. A threshold cut of 100 DAC units is sufficiently high to remove pedestal background for all modules, though future tuning could be done to optimize the photon yield in a more granular fashion if it is needed. Such an optimization would likely have a negligible effect on the Cherenkov ring angle determination compared to uncertainties caused by other factors (i.e. tracking, internal and external alignment, timing resolution, etc.)

3.5.6 Model for Fitting the ADC Spectrum

Since the ADC value is proportional to the number of electrons found at the final stage of the PMT, the ADC spectrum is best described with a statistical model for the number of photo-electrons generated at each stage. If we consider the simplest detector that only measures the electrons produced by the photoelectric effect, the ADC value can

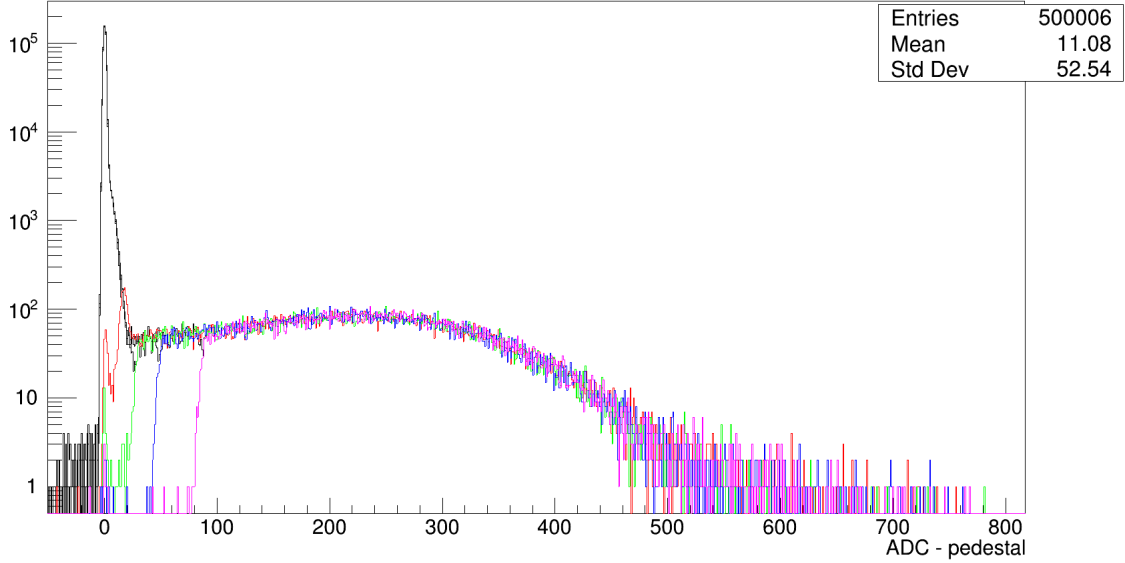


FIG. 3.16: Shown here is an example of the effect of making a DAC cut on the ADC spectrum. The spectrum with no DAC cut is in black, while those with DAC cuts of 25, 50, 100, and 200 are in red, green, blue, and magenta respectively.

be described by the well known Poisson distribution:

$$P(m; \mu) = \frac{\mu^m e^{-\mu}}{m!}, \quad (3.2)$$

where m is the number of photo-electrons produced by the single photon event, and μ is the average number of photo-electrons produced by single photon events. In PMTs, the photo-electrons are subsequently accelerated by a high voltage potential into a dynode to generate even more electrons. The H12700 of interest here has 10 such dynode stages to amplify the initial signal. The number of electrons generated after each stage can ideally be described by a convolution of Poisson distributions that depend on the number of electrons produced at the previous stage of amplification and the response of the given stage. This all depends on some base assumptions, *i.e.* that the response of each stage is well behaved and uniform, which was found to not be the case for these MAPMTs (*i.e.* a simple convolution

of Poisson distributions failed to adequately describe the ADC spectrum). Therefore, the model we chose to describe the ADC response of the H12700 MAPMTs follows from [50], where the author modifies the Poisson convolution with factors aimed at accounting for non-uniform aspects of the PMT dynodes.

Using the terminology in [50], s_{meas} is the signal value read out by the ADC. s_{ped} are signal values that come from zero photo-electron events ($m = 0$), and constitute the so called 'pedestal' distribution that is assumed to be Gaussian with average $\langle s_{ped} \rangle$. It is also useful to define the quantities $s = s_{meas} - \langle s_{ped} \rangle$, $scale \equiv \langle s \rangle_{m=1} = \langle s \rangle / \mu$ (assuming Poisson), and $a = s / scale$. These quantities will be used in the definition and interpretation of the detector response functions $\rho_m(a)$.

For $m \geq 1$, each $\rho_m(a)$ can be expressed as a convolution of $\rho_1^{*m}(a)$. With this we can write down the intrinsic amplitude distribution of the detector as a sum of products of the probability to generate m photo-electrons and the response to m photo-electrons:

$$\phi(a) = \sum_{m=0}^{\infty} P(m; \mu) \rho_m(a) = e^{-\mu} + \sum_{m=1}^{\infty} P(m; \mu) \rho_1^{*m}. \quad (3.3)$$

One additional factor for the system resolution, $R(a)$ (which we assume to be Gaussian with width $\sigma_a = \sigma / scale$) gives the this normalized probability density function (p.d.f.) to model the distribution of a :

$$f(a) = e^{-\mu} R(a) + \sum_{m=1}^{\infty} P(m; \mu) \rho_1^{*m} * R. \quad (3.4)$$

Now that we have the general form for the p.d.f. to model the distribution of a , all we need now is a usable description of the detector response function $\rho_1(a)$. As described previously, the ultimate value of the ADC signal is determined by the number of photo-electrons produced at the window of the PMT, and then the number of electrons produced

at each dynode for each electron produced at the previous stage. Beginning with the first dynode (second stage), n electrons are produced with an average number of electrons ν being produced by a single ($m = 1$) photo-electron. In an analogous method to Eq. (3.3), an amplitude distribution function for the number of electrons after two stages takes the form

$$\phi_2(a) = e^{-\mu} q_0(n) + \sum_{m=1}^{\infty} P(m; \mu) q_1^{*m}(n), \quad (3.5)$$

where $q_m(n)$ is the p.d.f. describing the response function to m photo-electrons. $q_0(n) = 0$ when $n \neq 0$, and $= 1$ when $n = 0$. $q_m(n)$ is a discrete function that plays a similar role as $\rho_m(a)$ in Eq. 3.3.

Given that $f(a)$ in Eq. 3.4 is a continuous function and $\phi_2(a)$ is a discrete amplitude, incorporating Eq. 3.5 into Eq. 3.4 an additional step is required to perform the necessary convolution. This requires weighting Eq. 3.5 with a series of delta functions summed over n , assuming that the measured signal at this stage is directly dependent on the number of electrons generated. The argument of these delta functions is chosen such that $\langle a \rangle = 1$ for $m = 1$ (i.e. one photo-electron). This new discrete function takes the form

$$D(a) = \sum_{n=0}^{\infty} \delta(a - \frac{n}{\nu}) \sum_{m=0}^{\infty} P(m; \mu) q_m(n). \quad (3.6)$$

Taking the convolution of $D(a)$ with the intrinsic system resolution function $R(a)$, recalling that $R(a)$ is assumed to be Gaussian, gives $f(a)$:

$$f(a) = \sum_{m=0}^{\infty} \sum_{n=0}^{\infty} G(a, n; \sigma_a), P(m; \mu) q_m(n) \quad (3.7)$$

$$G(a, n; \sigma_a) = \frac{1}{\sqrt{2\pi\sigma_a^2}} \exp \left[\frac{-(a - n/\nu)^2}{2\sigma_a^2} \right]. \quad (3.8)$$

In principle, this step would need to be repeated for each successive dynode. However, Ref. [50] argues that additional dynode stages can be modelled by an effective smearing of the width of the Gaussian distribution Eq. 3.8. This assumes that the number of electrons knocked out per second stage electron is large enough to consider the spread is purely statistically. We represent the number of electrons produced per second stage electron as ξ and define the new effective Gaussian width as

$$\sigma_{eff}(n) = \sqrt{\sigma_a^2 + \sigma_\xi^2} = \sqrt{\frac{\sigma^2}{scale^2} + \frac{n}{\nu^2\xi}}. \quad (3.9)$$

The σ can be determined experimentally by measuring the width of the pedestal, for which $m = n = 0$.

If the number of electrons generated at the first dynode by a single photo-electron is well behaved, *i.e.* follows a Poisson distribution with $\langle n \rangle = \nu$, then we have an explicit function for $q_m(n)$ in Eq. 3.7 for any $m \geq 1$;

$$q_m(n; \nu) = P(n; m\nu). \quad (3.10)$$

Plugging this into (3.7) and including the new effective Gaussian width gives the p.d.f. for the signal amplitude of

$$f(a) = \sum_{n=0}^{\infty} \left\{ G(a, n; \sigma_{eff}) \left[e^{-\mu} q_0(n) + \sum_{m=1}^{\infty} P(m; \mu) P(n; m\nu) \right] \right\}. \quad (3.11)$$

There are several explicit assumptions about the behavior of any PMT this model is suitable for. Unfortunately this base model is insufficient to describe the ADC spectrum of the Hamamatsu H12700 MAPMTs. Following the laser bench test described in Sec. 3.5.1, a fit to the ADC spectrum using this model failed to adequately describe the spectrum for

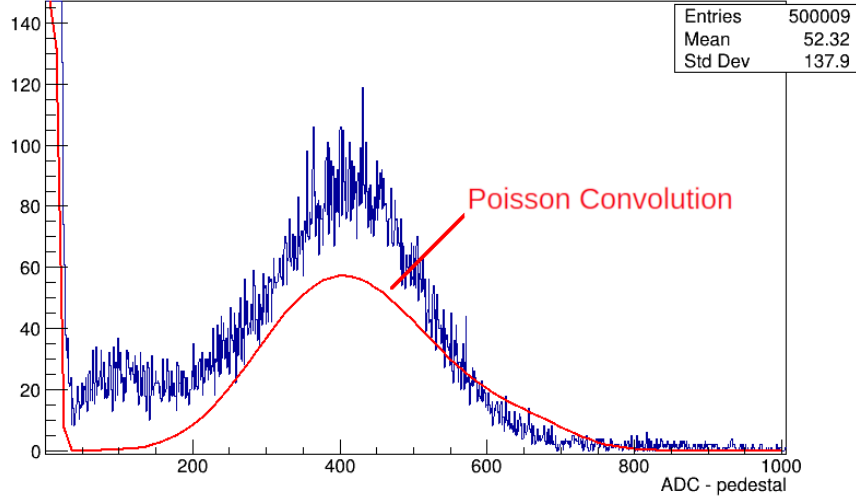


FIG. 3.17: The fit in red uses the Poisson convolution model (3.11). This example shows the failure of the model, in this form, to adequately describe the ADC distribution, and it supports the need for the more complicated model (3.15).

nearly all channels it was tried on, as can be seen in the example shown in Fig. 3.17. This implies that some of the assumptions made about the PMT in arriving at Eq. 3.11 were not realistic. In [50], the author prescribes a method for parameterizing the response of the dynode, i.e. $q_m(n; \nu)$, in a way to account for non-uniformity that we will now describe here. One can think of this as decomposing the first dynode into a number of regions with their own gain value. This is accomplished by changing ν into a vector of average particle gain, and so rather than having one singular Poisson distribution $q_1(m)$ enter the model, we instead have a sum

$$q_1(n; \mathbf{V}_L) = \sum_{u=1}^L \alpha_u P(n; \nu_u), \quad (3.12)$$

where L is the number of different average electron gains. The relative size of the different gain regions of the dynode are described by the α_u values, and these components sum to

1. The average number of electrons produced from this dynode can be represented by

$$\nu_{cL} = \sum_{u=1}^L \nu_u i_u. \quad (3.13)$$

The i_u values can be thought of as the number of photo-electrons that hit each gain region that produces an average number of electrons ν_u (and so must be ≥ 0). The sum of all i_u 's must be equal m , the number of photo-electrons generated at the first stage. This means that the sum in formula (3.13) is combinatorial, and this will introduce multinomial coefficients into the model.

In fits of the H12700 MAPMTs, it was found that $L = 3$ was the minimum value to achieve fits that described the majority of the ADC spectra, and so we will limit our description here to that value. The convolution of $q_1(n; \mathbf{V}_3)$ to determine $q_m(n; \mathbf{V}_3)$ is,

$$q_m(n; \mathbf{V}_3) = q_1^{*m}(n; \mathbf{V}_3) \equiv \left[\sum_{u=1}^3 \alpha_u P(n; \nu_u) \right]^{*m} = \sum_{i_1+i_2+i_3=m} \frac{m!}{i_1!i_2!i_3!} \alpha_1^{i_1} \alpha_2^{i_2} \alpha_3^{i_3} P(n; \nu_c). \quad (3.14)$$

Plugging this more complex response p.d.f. into (3.11), we arrive at the final form of our model for the ADC spectrum of the H12700 MAPMTs:

$$f(a) = \sum_{n=0}^{\infty} \left\{ G(a, n; \sigma_{eff}) \left[e^{-\mu} q_0(n) + \sum_{m=1}^{\infty} P(m; \mu) \sum_{i_1+i_2+i_3=m} \frac{m!}{i_1!i_2!i_3!} \alpha_1^{i_1} \alpha_2^{i_2} \alpha_3^{i_3} P(n; \nu_c) \right] \right\}. \quad (3.15)$$

The fit using this model now has 9 unique free parameters. To keep track of these parameters and their interpretation, they are summarized in Table 3.1.

3.5.7 Fitting the ADC spectra and results

This section will give a brief description of the process for fitting the ADC data from the laser bench tests with the model derived in Sec. 3.5.6. The fitting was done with a

Label	Limits	Interpretation
scale	> 0	Average ADC value generated from single photo-electrons
σ	> 0	Width of the m=0 pedestal
μ	> 0	Average # photo-electrons at stage 1
ν_1	> 0	Average #electrons from stage 2, gain region 1
ν_2/ν_1	$[0, 1]$	Average #electrons from stage 2, gain region 2 relative to region 1
ν_3/ν_1	$[0, 1]$	Average #electrons from stage 2, gain region 2 relative to region 1
α_2	$[0, 1]$	Relative size of gain region 2
$\alpha_3/(1 - \alpha_2)$	$[0, 1]$	Relative size of gain region 3
ξ	> 1	Average # electrons produced in stage 3 by a given stage 2 electron

TABLE 3.1: Free Parameters of the MAPMT pdf model in (3.15).

C++ macro using the CERN ROOT fit function. To ensure stable results across fitting the ADC distributions from 79 MAPMT stacks (2 or 3 64-pixel MAPMTs each) over 72 runs with different settings, it was important to design a simple algorithm to initialize, limit, and/or fix the 9 parameters of Eq. 3.15. The first step was to shift the ADC spectrum so that $\langle s_{ped} \rangle = 0$. Next, the σ of the pedestal is determined by doing fit with a Gaussian function centered at zero. To be as general as possible, the range of this fit was over the bin range $[i, j]$. In this range, i is the ADC bin number ten bins below the bin that contains $s = ADC - pedestal = 0$, and j is the first bin with $s > 0$ and $s(j) < s(j + 1)$ ($s(j)$ being the bin content of bin j). Another complication is that the error bars of the bins in the pedestal region are so small, any deviation from a Gaussian shape is not well accounted for as the fit prioritizes matching the bins at the very peak of the pedestal. Since we want a ‘good enough’ estimation of the width of the pedestal, we temporarily increase the error bars on all of the bins in the pedestal fit region until a Gaussian fit describes the pedestal with a $\chi^2/NDF \sim 1$. After the width of the pedestal is determined, its value is fixed for the rest of the fit procedure. Next we put a limit on the scale value. If we assume that due to the low light environment, the majority of the non-pedestal distribution is from single photo electron (SPE) events and the scale value is just the average value of the ADC spectrum above the pedestal region defined above. To not be too restrictive

in the final fit, the *scale* parameter is limited to be within 25% of the estimated scale value. After studying the fits of a few runs for a few MAPMT stacks, it appeared that some of the parameters were relatively independent of the run conditions and individual MAPMTs. The relative gain values ν_2/ν_1 and ν_3/ν_1 , as well as the later stage electron multiplicity ξ , were stable enough in a random selection of channels to fix these for all subsequent fits. Example plots from one MAPMT stack can be seen in Fig. 3.18 and 3.19. Fixing these three parameters allowed the fits to generally be more stable, and also gave the bonus feature of speeding up the fit process. With this method of setting limits and fixing parameters applied to the fit process, the ADC spectra from all 79 MAPMT stacks for each of the 72 combinations of settings were fit. Examples can be seen in Fig. 3.15. The χ^2/NDF distribution of all the fits can be seen in Fig. 3.20. The χ^2/NDF distribution peaks around 1.3 with a small tail going above 2, which was determined to be an acceptable description of the group of MAPMT ADC spectra. Any channels with poor model descriptions for the purpose of gain matching will be handled using LED-pulser data in the next section.

3.5.8 MAPMT gain matching with ADC

In order to create a more uniform response from the PMT plane it was decided to adjust the internal gain of the MAROCs based on the separation of the SPE distribution from the pedestal. Using the fit information from the laser bench tests was relatively straight forward, assuming a linear relationship between the MAROC gain and the *scale* parameter in Eq. 3.15. The average MAROC gain $\langle g \rangle$ for all the tubes was chosen to be unity (or 64 in the MAROC units). Given this choice, the translation from the ADC fit parameter *scale* to MAROC gain is given by

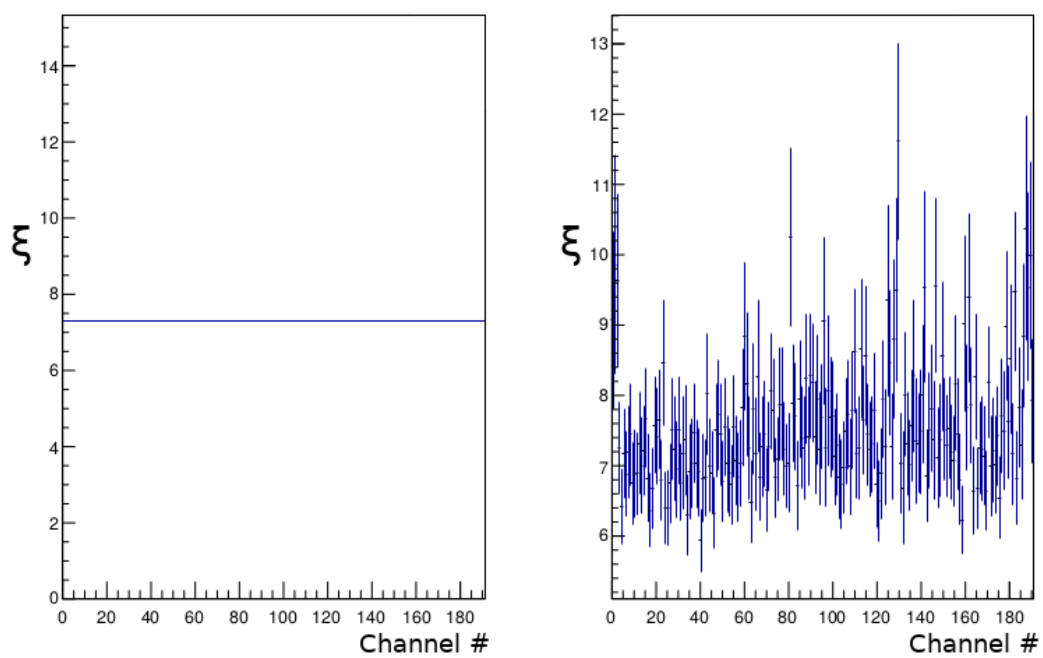


FIG. 3.18: The right plot shows an example of the stability of the ξ value over a single three tube MAPMT stack. The left plot shows the value ξ has been fixed to for later fits

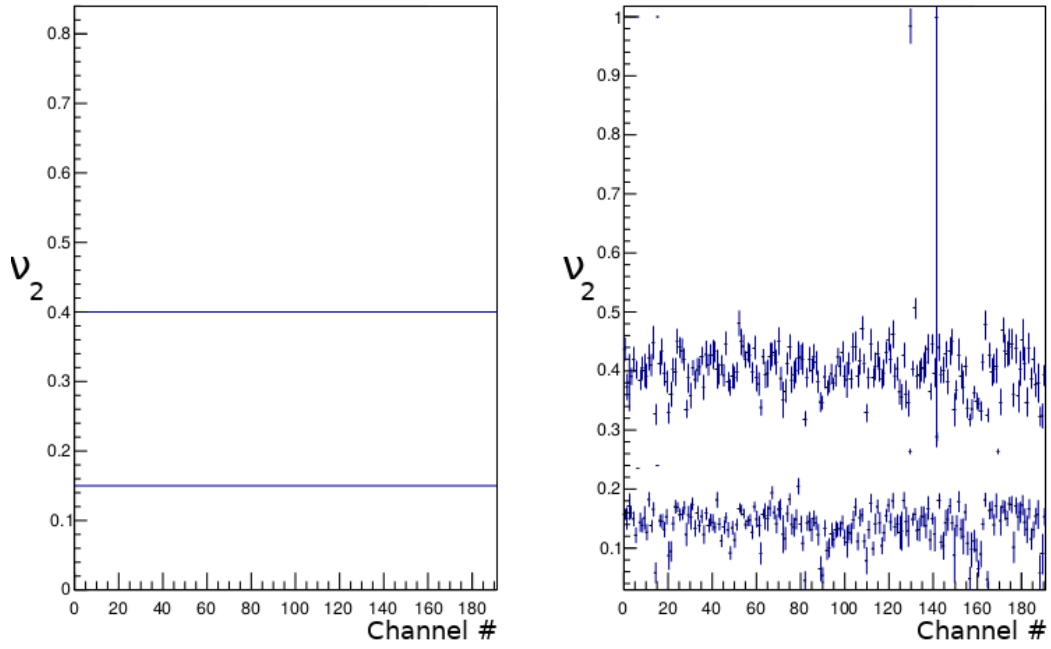


FIG. 3.19: Left shows the values for both ν_2/ν_1 and ν_3/ν_1 (which can be swapped with the corresponding α value). The right shows the fixed values for each of the relative gains ν_2 and ν_3 .

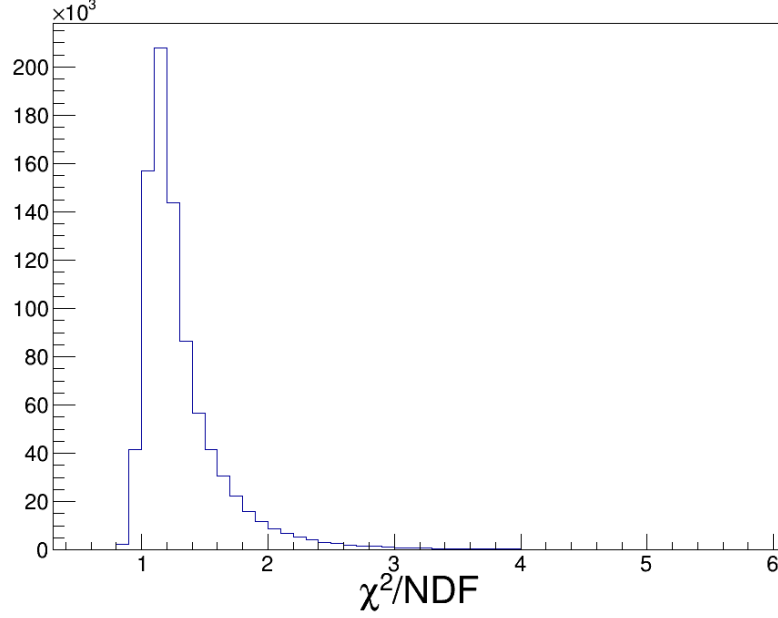


FIG. 3.20: χ^2/NDF for all the MAPMT ADC fits using the model in (3.15) applied as described in section 3.5.7

$$g = \langle g \rangle \frac{\langle scale \rangle - scale}{\langle scale \rangle} + \langle g \rangle, \quad (3.16)$$

where g is the new equalized gain, $\langle scale \rangle$ is the average scale factor from all of the ADC fits, and $\langle g \rangle$ is chosen to be 64.

3.5.9 MAPMT gain matching with TDC

As mentioned previously, the MAMPT stacks do no readout the ADC value when the operational firmware is installed. Therefore, being able to determine gain values through another method using the information available during operation is desirable. Being able to do gain matching using the LED pulser inside the DIRC will allow gain matching to be done with MAPMT stacks that have been hot swapped (and therefore not tested as a unit with the laser on the bench), as well as allowing us to adjust channels in which the fit did

not successfully describe their ADC spectrum (i.e. have a bad *scale* input to (3.16)). From the available information from the TDC, the time-over-threshold distribution was found to have a strong enough correlation with the *scale* parameter in the ADC fit. In particular, the average of the TDC time-over-threshold spectrum (ToT or ΔT) was found to be the most useful, assuming the pedestal was removed from the TDC with a sufficient threshold cut. Using the data from the laser bench test, we can plot the correlation between the equalized gain, as determined from the ADC *scale* parameter, and the TDC ΔT in Fig. 3.21. The scatter plot was then fit with a function of the form: $p_1 + p_0 * \ln(x)$. The logarithmic fit was found to have a better χ^2/NDF than linear or quadratic polynomials, and more complicated functions did not improve the fit quality beyond the given form. In an analogous way to (3.16), we arrive at the following formula to determine a pixel's "gain-matched" gain value:

$$g_{\Delta T} = \langle g \rangle e^{p_0^{-1}(\langle \Delta T \rangle - \Delta T)}, \quad (3.17)$$

where $g_{\Delta T}$ is the new MAROC gain, $\langle g \rangle$ is the chosen average gain (64), $\langle \Delta T \rangle$ is the average ΔT for all the pixels in a given DIRC box, p_0 is input from the correlation fit, and ΔT is that of the pixel of interest. Its important to note that repeating the process for 1075 V and 1100 V had a negligible effect on the parameters of the fit to the correlation of ΔT and *scale* determined equalized gain.

In the installed configuration, the process to do gain matching now is to take LED pulser data with all of the internal MAROC gains set to 64, then determine the average ΔT for each box, and finally use (3.17) to arrive at the new equalized gain for each pixel. Fig. 3.22 shows what the time-over-threshold distributions look like for each pixel under unity gain, ADC fit's *scale* determined gain, and the gain determined by the ΔT method. By inspection of Fig. 3.22, one can see that the effect of the ADC fit-determined gains

brought the peaks of the time-over-threshold distributions better in line with each other, and that the method of using the ΔT value to find gains that do the same thing works as intended. Further comparing the two methods, one can ask if there is a significant effect on the relative efficiency of the pixel using one set of gains compared to the other. Defining the relative efficiency as

$$\varepsilon = \left(\frac{LED_{hits}}{LED_{Triggers}} \right)_{V1} / \left(\frac{LED_{hits}}{LED_{Triggers}} \right)_{V2}, \quad (3.18)$$

plots of these relative efficiencies in the x-y space of the MAPMT planes can be seen in Fig. 3.23. In Fig. 3.23, one would expect the relative efficiency to be uniformly distributed around one if both methods were working perfectly and the correlation between ΔT and *scale* gains in Fig. 3.21 was reasonable. This seems true for most pixels, however some outlying pixels do exist in Fig. 3.23. The blue pixels with relative efficiency much lower than 1 come from channels in which the ADC fits were not accurately describing their ADC spectrum, and therefore had gains determined from their *scale* parameter that were much too high. The block of pixels in the North DIRC box towards the left side with relative efficiencies ~ 1.3 come from a MAPMT stack that had the electronics boards swapped while leaving the MAPMTs installed. We do not expect the laser test data, and therefore the ADC fit-determined gains, to apply when different MAROCs are used for the same MAPMTs, and so the difference in that block is understandable. Overall, the method of using the LED pulser to determine gain matching works well, and allows hardware to be easily changed out without the need to go back to the laser tests for every new stack configuration.

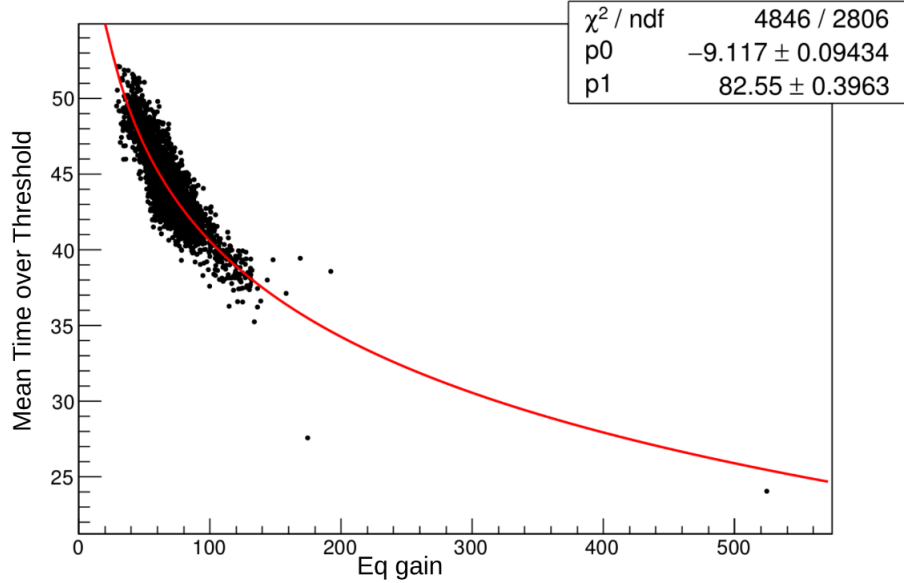


FIG. 3.21: TDC ΔT vs Equalized gain. The average TDC time over threshold for all MAPMT pixels taken with gain 64, voltage 1000 V, and a TDC threshold value of 100. The equalized gain determined from fits to the ADC spectrum taken with the same settings using (3.16). The red line is a simple log function, $p_1 + p_0 * \ln(x)$, used to fit the data.

3.6 DIRC Simulation

The GlueX DIRC is simulated in the GEANT4 based GlueX simulation package. Understanding the effects of the geometry and the materials on the photon distribution resulting from a charged particle producing Cherenkov radiation is vital for accurately reconstructing the correct Cherenkov angle, as described in section 3.7. In this section, a brief description of the GlueX DIRC simulation is given. A more detailed description of the simulation can be found in [51].

The internal structure of the radiator bar boxes, including geometry and material properties, was originally modelled and simulated by the BaBar collaboration (also see Fig. 3.5), and this information was migrated into the GlueX simulation. The support structure for the DIRC bars was also simulated, as the added material affects the modelling and performance of the detectors downstream of the DIRC, such as via electromagnetic

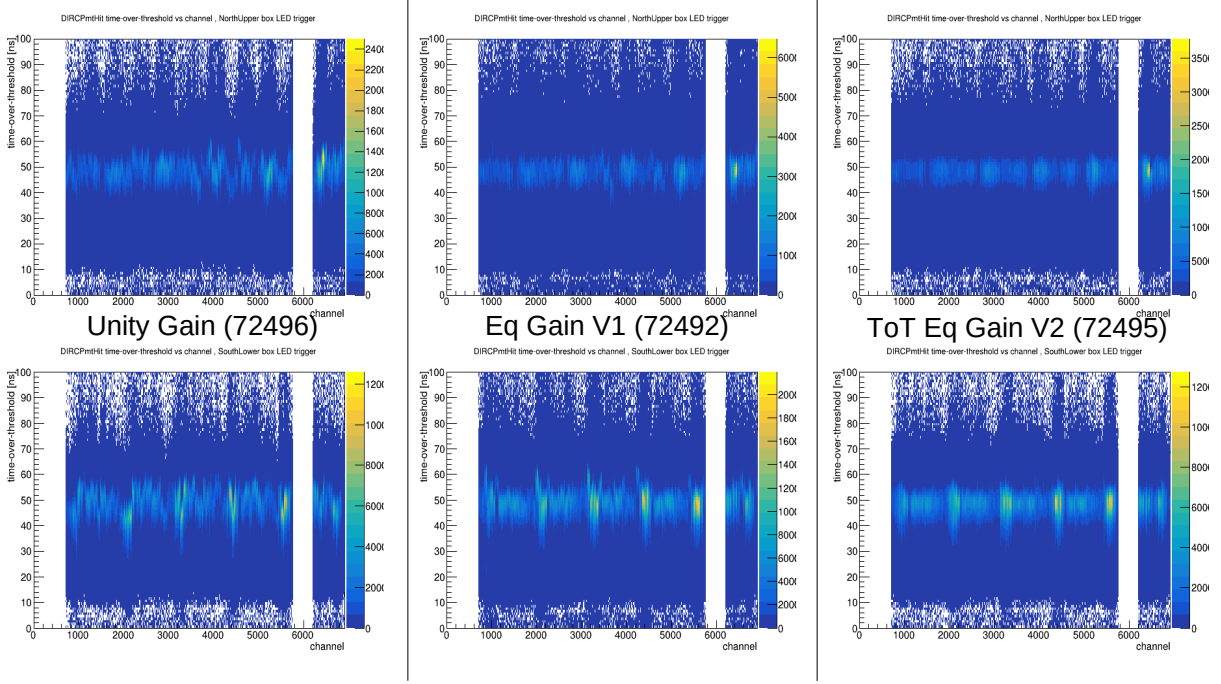


FIG. 3.22: These 2D plots have the TDC time-over-threshold on the Y axis and an arbitrary pixel number on the X axis. The top row are all from the north DIRC box, and the bottom row are from the south DIRC box. The average time-over-threshold value for each X bin is the ΔT of that pixel. The leftmost column contains LED pulser data taken with all of the MAROC gains set to unity ($= 64$). The center column contains LED pulser data taken with equalized gains determined from ADC fit information. The rightmost column contains LED pulser data taken with gains adjusted using the ΔT information from the leftmost column.

$$\text{Relative efficiency} = (\text{LED hits} / \text{LED trigger})_{\text{EQ V2}} / (\text{LED hits} / \text{LED trigger})_{\text{EQ V1}}$$

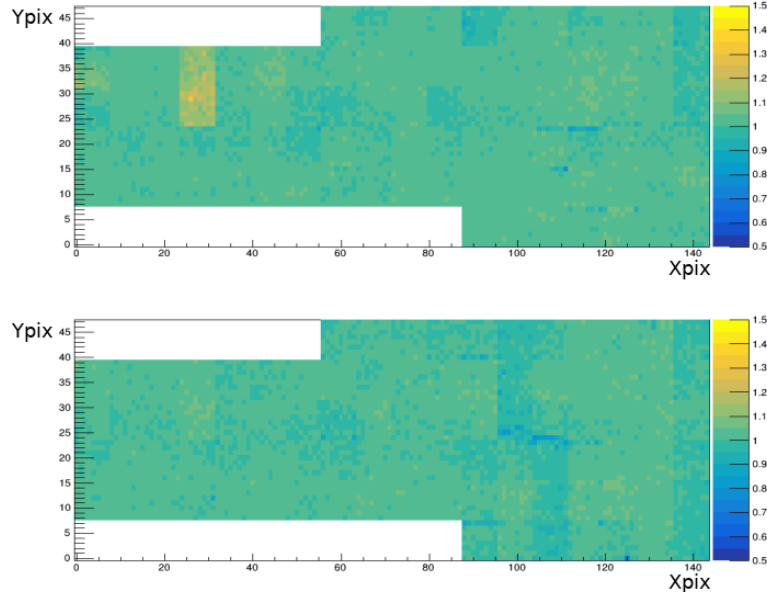


FIG. 3.23: Relative efficiency comparing the ADC fit determined gains (V1) and TDC ΔT determined gains (V2) plotted on the z-axis in the physical x-y map of the North (top) and South (bottom) DIRC MAPMT planes.

showers in the FCAL. The optical box and its internal components (see Fig. 3.7) also needed accurate geometrical simulation, especially that of the internal mirrors and the orientation of the PMT plane. The relative position and orientation of all the optical components needs to be known to a greater degree of accuracy than survey measurements can provide. Therefore, data was used to calibrate the GEANT4 simulation of the DIRC.

3.7 Cherenkov Angle Reconstruction

As described above, when a relativistic charged particle enters the fused silica bars in the GlueX DIRC, it radiates Cherenkov photons. The Cherenkov photons are emitted in a cone around the charged particle's direction of motion with an angle related to its relativistic velocity as given in Eq. 3.1. In the GlueX DIRC, the Cherenkov photons are

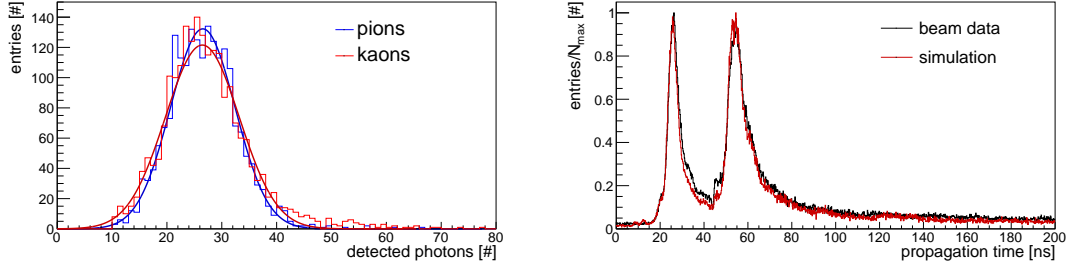


FIG. 3.24: (Left) The detected photon yield for 2000 pions and kaons in GlueX data (identified from ρ and ϕ decays, respectively). (right) Timing of both the data and the simulated photons. Image source from [52].

then internally reflected down the length of the quartz bar, and into the optical box. Some of the photons travel relatively directly to the optical box, referred to as direct photons, and others travel to the opposite end of the bar from the optical box before travelling the length of the bar to reach the optical box and the MAPMTs, referred to as reflected photons. An example of the timing of the direct and reflected photons can be seen in Fig. 3.24(b).

The Cherenkov angle is heavily distorted in this process (see the pattern for 1000 pions with $|\vec{p}| \sim 3$ GeV from data in Fig. 3.25) but is preserved through the series of reflections. Using the end position on the PMT plane, the time of arrival of every Cherenkov photon, and the position along the bar of the charge particle hit, that is detected, allows the Cherenkov angle to be reconstructed. There exist several complementary methods for reconstructing the Cherenkov angle using this information which will be discussed in this section. The main focus will be on the default method currently used by GlueX, the geometrical reconstruction, while the other methods will just be mentioned briefly.

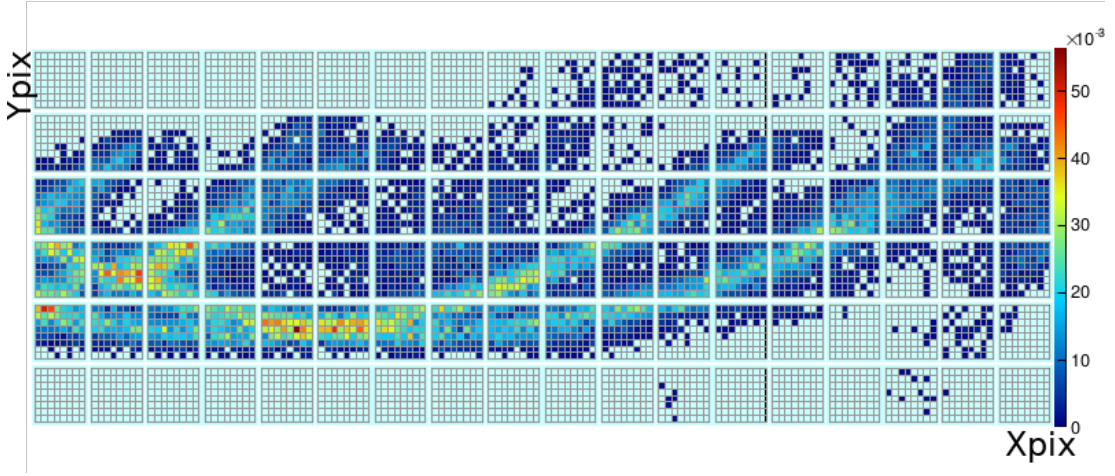


FIG. 3.25: Pattern of photons detected by the MAPMTs for 1000 pions with $|\vec{p}| \sim 3$ GeV that all passed through the DIRC radiator bars in the same position bin from GlueX data. The Cherenkov cone pattern is distorted by the internal reflections of the photons as the travel to the MAPMTs. The axes are the position of each pixel on the MAPMT plane.

3.7.1 Geometrical Reconstruction

The geometrical reconstruction method is currently considered the nominal method for determining the Cherenkov angle of a given event in the GlueX DIRC. In this method, a look-up table (LUT) is constructed in advance by simulating a large number of photons, in GEANT4, beginning at the end surface of each radiator bar where the bar meets the optical box (see Fig. 3.26(a)). The photons are generated over the whole surface of the end of the radiator bar and propagated through the geometry and simulated material of the optical box to the PMT pixels. The LUT then returns the possible photon directions calculated in the simulation, given the bar the photon originated from and the pixel that detects it. The computation cost for generating the LUT is large, but is done and stored before data are processed. For the Cherenkov angle of real photons in data, the radiator bar that is hit is known from the information provided by the tracking detectors, and the pixel and bar information can then be used to determine the Cherenkov angle on a photon-by-photon basis (see Fig. 3.26(b)). The one additional complication in this method

is that the number of internal reflections is not known, and so there are ambiguities in the determination of the Cherenkov angle from each individual photon. Depending on the number of (unknown) reflections, the inverse of each of the components of the photon's vector is as valid as the original hypothesis given in the LUT. This leads to a maximum of 8 ambiguous Cherenkov angles for each photon detected by the MAPMTs. Some of the ambiguous Cherenkov angles can be immediately eliminated if they are greater than the critical angle for internal reflection (i.e. would not physically arrive in the optical box due to internal reflection). Ambiguities that arise from the possibility of the photon being a direct photon or one reflected from the far end of the bar can be separated using the expected-measured time difference. The DIRC will typically detect between 20 and 40 photons for each charged particle that passes through the radiator bars, see Fig. 3.24. Determining the Cherenkov angle despite the remaining ambiguities is done by creating a histogram using all of the remaining possible Cherenkov angles for all of the photons in the event. This histogram peaks at the true Cherenkov angle for the event with a width that is taken to be the uncertainty and referred to as the *single photon resolution* (SPR). Fig. 3.27 shows an example of this peak for samples of 2000 pions and 2000 kaons with momentum near 3.5 GeV/c (selected from ρ and ϕ decays respectively), where the smooth background comes from the ambiguous Cherenkov angles.

3.7.2 Other Methods

FastDIRC

Although the FastDIRC method of reconstructing Cherenkov angle is not currently used for analyzing data, it was used in several studies during R&D of the GlueX DIRC. In the FastDIRC method, the pattern of Cherenkov photons is simulated assuming different PID hypotheses. The results of the fast simulation is then used to calculate a probability

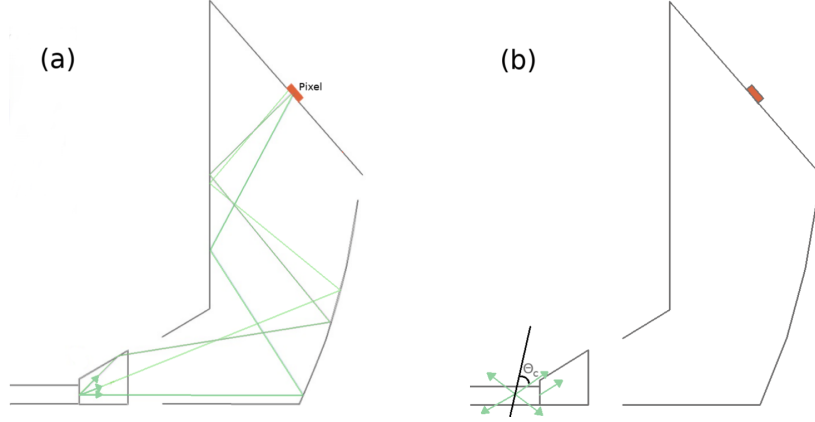


FIG. 3.26: Cartoon depicting the issue of the paths photons may take to the MAPMTs. (a) A demonstration of the paths simulated from the end of the bars used in the creation of the geometrical look up table. (b) a depiction of the different angles that can reproduce the same angle the photon has at the end of the bar. There are up to 8 ambiguous angles for every pixel hit.

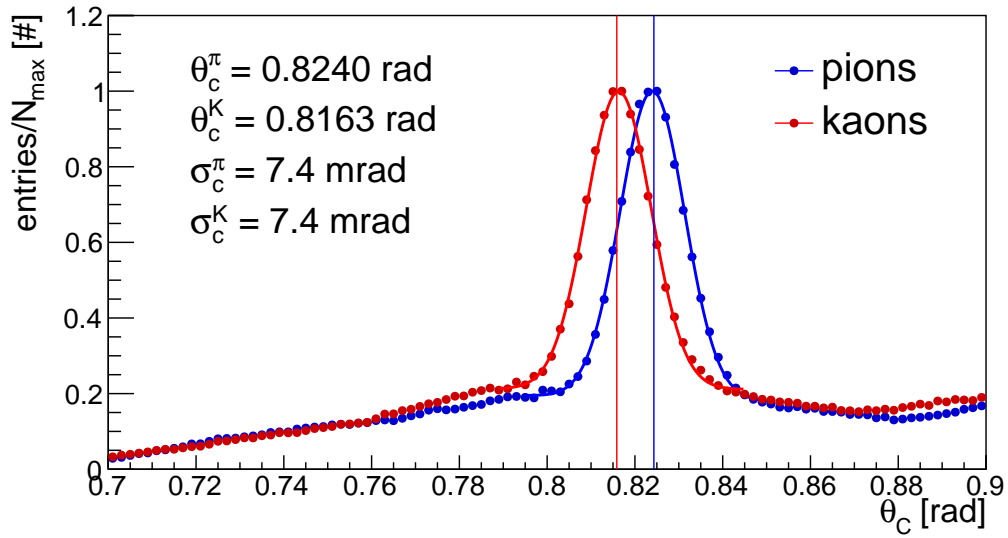


FIG. 3.27: A sample of 2000 pions and kaons were selected with $|p| = 3.5$ GeV from ρ and ϕ decays respectively to demonstrate the single photon Cherenkov resolution. The vertical lines mark the expected Cherenkov angles from the two particle types, given as θ_c^π and θ_c^K with standard deviations σ_c^π and σ_c^K , respectively. [53]

density function that is used to test the hypotheses on the data [54].

Time Imaging Reconstruction

The Belle-II collaboration developed a method that uses a comparison of the expected photon arrival times and the measured ones [55]. Hypotheses for the expected times can be calculated or determined using Monte Carlo simulations assuming the mass of the particle. An extended log likelihood for the different PID hypotheses is calculated and the identity of the charged particle is determined by taking the difference between log likelihood of the hypotheses.

Machine Learning Methods

Machine learning methods for interpreting the photon hit patterns have been investigated for use in the GlueX DIRC [56][57]. These studies used convolutional neural networks to identify pions and kaons. Training samples can be selected using well identified particles, kaons from ϕ decays and pions from ρ decays as well as simulated data.

3.8 Early DIRC Performance

The target π/K separation power for the GlueX DIRC is $\sim 3.0 \sigma$ separation for charged particles with momentum around 3 GeV/ c . The separation power depends on how certain the Cherenkov angle can be determined. The uncertainty using the geometric reconstruction method is given by

$$\sigma_{\theta_c}^{track} = \sqrt{\left(\frac{\sigma_{\theta_c}^{photon}}{\sqrt{N_{photons}}}\right)^2 + (\sigma^{correlated})^2}, \quad (3.19)$$

where $N_{photons}$ is the number of photons and $\sigma_{\theta_c}^{photon}$ is the SPR defined in section 3.7.1. Contributions to $\sigma^{correlated}$ include: the track resolution, multiple scattering effects, mismatches between the DIRC geometry and simulation, chromatic smearing, and other

smaller effects. Geometry mismatches and degradation of the optical components leading to loss of photons are two sources of error under an ongoing investigation to improve the performance of the GlueX DIRC. The estimated uncertainty and the Cherenkov angle distribution can be combined with information from the tracking detectors to form PID extended log-likelihood of the form [58],

$$\log \mathcal{L}_k = \sum_{i=1}^N \sum_{j=1}^{N_i^{amb}} \ln(S_k^{ij} + B_k^{ij}) + \ln P_N(N_e). \quad (3.20)$$

S_k^{ij} and B_k^{ij} is the signal and background PDFs for mass hypothesis k respectively. N_e is the expected number of photons detected including backgrounds, N is the actual number of pixel hits, and P_N is a Poisson probability to measure N photons if N_e are expected. N_{amb} is the number of reconstructed photons including the ambiguous ones. The maximum extended log-likelihood for a given PID hypothesis for a charged particle, compared to the log-likelihood of other hypotheses, is then used to infer the identity of the particle. An example of the separation power can be seen in Fig. 3.28, where samples of kaons and pions were also identified through being produced in well known decays. In Fig. 3.28, the charged particles were selected to have come from high-occupancy regions of the DIRC radiators, in individual bars, and they are chosen to have momenta around 3.5 GeV to demonstrate the separation ability. As seen in Fig. 3.28, the target of 3.0σ separation for this track momenta has been achieved.

Further calibrations and improvements to the performance of the GlueX DIRC are ongoing as well as studies of its application to a variety of analyses.

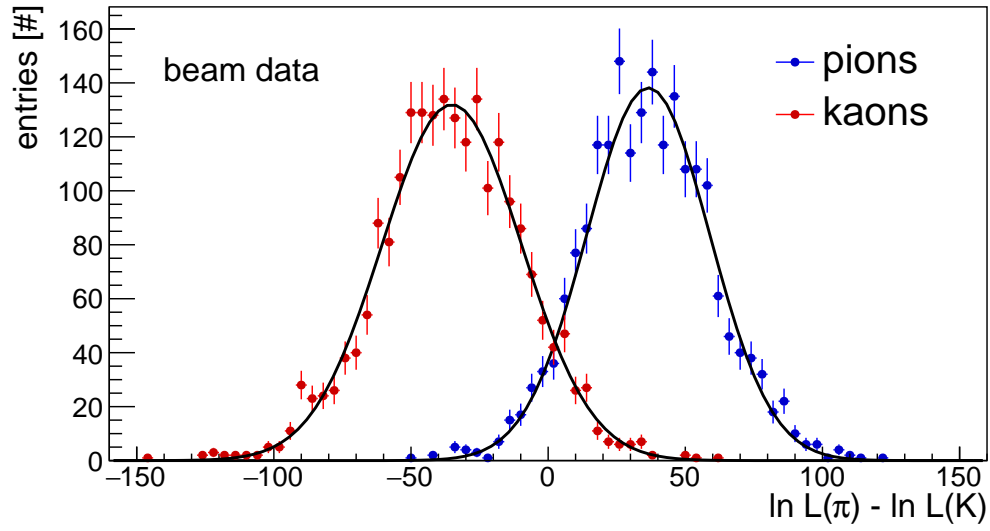


FIG. 3.28: Log likelihood difference for 4000 \sim 3.5 GeV/ c momenta pions (blue) and kaons (red). The separation power for these \sim 3.5 GeV/ c momenta tracks is $3.0 \pm 0.1 \sigma$ [52].

CHAPTER 4

Reconstruction and Selection of the

$K^+K^-\pi^+\pi^-p$, $K^+K^-\pi^0\pi^0p$, and

$K^+K^-\pi^0\eta p$ **Final States**

In Section 1.3, observations and interpretations of $\phi(2170)$ were discussed which includes decays in various final states. This chapter concerns the study using GlueX-I of three reactions,

- $\gamma p \rightarrow K^+K^-\pi^+\pi^-p'$,
- $\gamma p \rightarrow K^+K^-\pi^0\pi^0p'$,
- $\gamma p \rightarrow K^+K^-\pi^0\eta p'$,

related to the $\phi(2170)$ using GlueX-I data. Recall the $\phi(2170)$ was first observed to decay to $\phi\pi^+\pi^-$, and other possible decay modes for the $\phi(2170)$ that result in some of these final states are: $\phi(2170) \rightarrow K^*(892)^0\bar{K}^{*0}(892)^0$, $\phi(2170) \rightarrow K_1(1460)^+K^- + \text{c.c.}$, $\phi(2170) \rightarrow K_1(1270)^+K^- + \text{c.c.}$, and $\phi(2170) \rightarrow K_1(1400)^+K^- + \text{c.c.}$ [6]. The $K^*(892)^0\bar{K}^{*0}(892)^0$

decay was briefly investigated some using this data, but are not presented here as the focus will be on the $\phi\pi^+\pi^-$ decay mode.

4.1 Data Set

The GlueX-I data set used in this analysis was taken in three run periods over two years using the GlueX detector setup described in Chapter 2, except the $K^+K^-\pi^0\pi^0p$ final state which only used the data set recorded in 2017. The three run periods used are named 2017_01, 2018_01, 2018_08 and had integrated luminosity in the coherent peak region ($8.2 < E_\gamma < 8.8$ GeV) of 21.8 pb^{-1} , 63.0 pb^{-1} , and 40.1 pb^{-1} respectively. Each run period has data taken with the diamond radiator in each of the four different orientations, as well as a fraction of events with the amorphous radiator where the beam is unpolarized (see Sec. 2.2.1). The results in this chapter utilize all of the beam polarization conditions summed together. The 2017_01 data set was taken with electron beam currents of 100 nA and 150 nA, and the 2018_01 and 2018_08 run periods used electron beam currents between 250 nA and 350 nA.

4.2 Event Selection

This section will detail the event selection process and the analysis cuts applied to the data sets to arrive at the appropriate subsets for each reaction of interest.

The first step is to skim the reconstructed data set and select candidate events that match with the desired final state. For every charged particle in the selected final state, there must be a charged track in the drift chambers with timing information provided by the following detectors: TOF, ST, BCAL, or FCAL. Photons in the final state are identified as showers in the FCAL or BCAL with no associated charged track. For all of

the final states discussed here, each event requires a tagged beam photon, see Sec. 2.2.2. The tagged beam photons for events of interest must correspond to the expected electron beam bunch, but events with out-of-time beam photons are also kept and used to subtract the “accidental” background under the prompt radio-frequency peak, see Fig. 4.1.

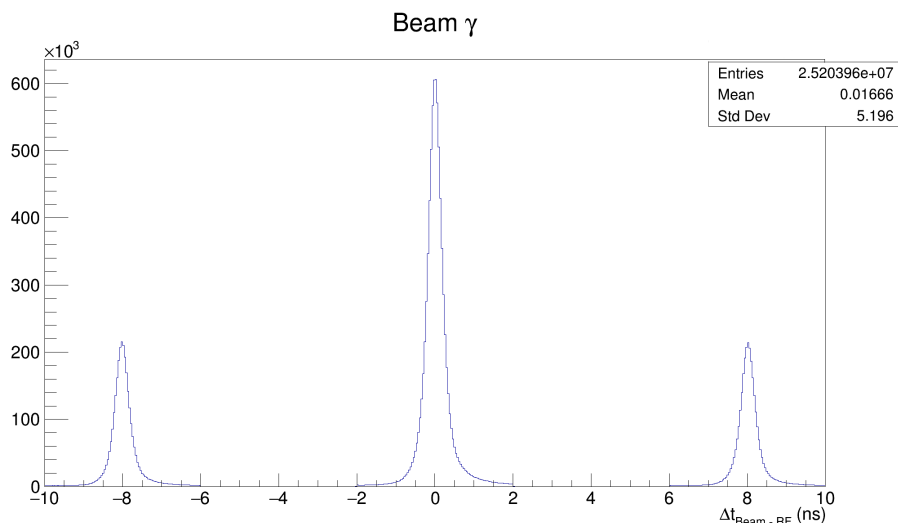


FIG. 4.1: Beam timing bunches. The X axis is the difference between the photon used in the event and the expected time based on the electron beam RF timing. The prompt peak (at $\Delta t = 0$ ns) are the photons in time with the tagged electron beam bunch. Events from the side peaks are kept to subtract events under the prompt peak that come from other bunches. The prompt peak has tails that extend under the $|\Delta t| = 4$ ns peaks, and so events from that bunch are not kept for background subtraction. Plot taken from the $K^+K^-\pi^0\eta p$ final state.

For each candidate event that contains the specified number and type of particles (i.e. number of photons and charged tracks), a kinematic fit is applied to every combination of tracks available. The kinematic fit varies the kinematic variables of the particles involved within the uncertainties in the momentum and position measurements and enforces energy and momentum conservation. If the kinematic fit converges, the event (and all of the combinations therein) are written out to the skimmed ROOT file for further analysis; how well the kinematic fit works is evaluated later in the analysis process. More detail on the

kinematic fit and this process is given in Section 15.3 of [38]. Further analysis cuts are applied to the skimmed data and are described below.

Particle Track Timing Cuts:

Once the kinematic fit has been applied and the particle energies and momenta have been adjusted accordingly, timing cuts are applied to both the neutral and charged tracks. These timing cuts have two purposes: 1) ensuring the tracks correspond to the same RF bunch as the beam photon used for that event, and 2) a simple PID selection. The timing cuts are applied to the Δt from the expected time of hit in BCAL, TOF, FCAL, or ST based on the tracking and PID hypothesis. Which detector the timing cut is applied to is prioritized based on timing resolution (cuts are only made for the highest priority detector that the particular track has information for). For charged tracks the priority list is: TOF, BCAL, then ST. For neutral hits, the priority list is: BCAL then FCAL.

Missing Mass Squared Cuts:

The *missing mass squared* cut is used to ensure that any given event is an exclusive event that matches the chosen final state (*i.e.* if the event has an extra (missing) particle the MM^2 will be negative (positive) or ~ 0 if the event has the right number of particles). The missing mass squared is, as its name implies,

$$MM^2 = \left| p_\gamma^{beam} + p_p^{target} - (p_p^{recoil} + \sum_i p_i) \right|^2, \quad (4.1)$$

where p_p^{recoil} is the detected proton and the sum over p_i is the sum over the rest of the reconstructed final state particles' 4-vectors.

Kinematic Fit Confidence Level:

Earlier in the event selection, the convergence of the kinematic fit was used to determine whether an event was written to the skimmed ROOT file or not, however how well the kinematic fit performed for a combination of initial and final state kinematics and hypothesis is used to make a more stringent selection. The kinematic fit itself is determined through a χ^2 minimization, and a cut can be made on the χ^2/NDF (NDF = Number of Degrees of Freedom) for a combination, or equivalently a confidence level (CL) which is the probability of obtaining the χ^2 for a given NDF .

Beam Energy Cut:

The photon beam flux information and polarization fraction (see Fig. 2.5) peaks at 8.8 GeV. If polarization information is not being taken into account (*e.g.* an unpolarized cross section measurement), a minimum photon beam energy cut is often applied to remove the so-called baryon *resonance* region. In the baryon resonance region, events in which the target proton absorbs the incoming photon and forms an excited baryon which subsequently decays is the dominant process. In the analyses presented here, we are more interested in diffractive production that occurs at higher beam energies. For partial wave analyses and other analyses that include a dependence on the beam polarization, a cut is placed on the photon beam energy to be in the vicinity of the polarized peak and thereby ensure a maximal percentage of events due to polarized photons.

Photon Shower Quality Cut:

The *photon shower quality* (Q_γ) variable is determined by a machine learning algorithm that separates hadronic, electromagnetic, and accidental showers in the calorimeters [59]. The algorithm was trained using real data from ω meson decays which contain both photons and charged hadrons. The photon shower quality value can be thought of as a probability, between 0 and 1, of whether or not the shower in the calorimeter was produced by a photon. A shower with a photon shower quality of 1 is considered very photon-like and 0 is not photon-like at all.

4.3 $K^+K^-\pi^0\eta p$ Event Selection

For the reaction $\gamma p \rightarrow K^+K^-\pi^0\eta p$, the proton, K^+ and K^- are directly detected in the drift chamber, while the π^0 and η decay almost instantly ($\sim 10^{-17}s$ for the π^0 and $\sim 10^{-19}s$ for the η) before reaching the detector. For this reaction, the reconstructed data is skimmed for events with two positively charged tracks, a negatively charged track, and four neutral showers. One of the positively charged particle tracks must have a proton mass hypothesis, the other must have a kaon mass hypothesis, and the negatively charged track must have a kaon mass hypothesis (although other hypotheses may be present for the same track). The four neutral showers in this reaction correspond to the π^0 and η each decaying to two photons. The kinematic fit is applied over these particles for all of the different hypotheses, or possible combinations, allowed. For example, if the neutral showers are identified as photons and labelled a-d, the kinematic fit will be performed with the hypothesis that the π^0 (η) decays to $\gamma_a\gamma_b$ ($\gamma_c\gamma_d$), and again for the hypotheses $\gamma_a\gamma_c$ ($\gamma_b\gamma_d$), $\gamma_a\gamma_d$ ($\gamma_b\gamma_c$), $\gamma_b\gamma_c$ ($\gamma_a\gamma_d$), and $\gamma_b\gamma_d$ ($\gamma_a\gamma_c$). As previously stated, for each combination for which the kinematic fit converges, the combination will be saved. The analysis cuts on the skimmed $\gamma p \rightarrow K^+K^-\pi^0\eta p$ events are described in the remainder of this section.

The charged track timing cuts are given in Table 4.1.

PID	Δt (ns) TOF	Δt (ns) BCAL	Δt (ns) FCAL	Δt (ns) ST
p	± 0.5	± 1.0	None	None
K^+	± 0.3	± 1.0	None	None
K^-	± 0.3	± 1.0	None	None
γ	N/A	± 1.5	± 2.5	N/A

TABLE 4.1: $\gamma p \rightarrow K^+ K^- \pi^0 \eta p$ particle timing cuts.

The rest of the analysis cuts for $\gamma p \rightarrow K^+ K^- \pi^0 \eta p$ are listed in Table 4.2.

Cut Variable	Condition
$M_{\pi^0 \rightarrow \gamma\gamma}$	$[0.08, 0.15] \text{ GeV}/c^2$
$M_{\eta \rightarrow \gamma\gamma}$	$[0.35, 0.75] \text{ GeV}/c^2$
$ MM^2 $	$< 0.02 (\text{GeV}/c^2)^2$
CL	> 0.001
E_γ	$> 7.0 \text{ GeV}$
Q_γ	> 0.5

TABLE 4.2: $\gamma p \rightarrow K^+ K^- \pi^0 \eta p$ analysis cuts. The $M_{\gamma\gamma}$ cuts are loose mass cuts on the two photon masses. $|MM|^2$ is the missing mass squared, CL is the confidence level, E_γ is the beam energy, and Q_γ is the photon shower quality.

The MM^2 for $\gamma p \rightarrow K^+ K^- \pi^0 \eta p$ is plotted in Fig. 4.2 after applying a $|MM^2| < 0.02 (\text{GeV}/c^2)^2$ cut.

Plots of the kinematic fit χ^2/NDF and confidence level are shown in Fig. 4.3. Plots of the beam energy before and after the beam energy cuts are shown in Fig. 4.4.

4.4 Features of the $K^+ K^- \pi^0 \eta p$ Final State

In Sec. 1.3, it was proposed to look for an isovector companion to the $\phi(2170)$. Because the $\phi(2170)$ was first observed decaying to $\phi f_0(980)$, the motivation for exploring the $K^+ K^- \pi^0 \eta p$ state is to search for this isovector companion in the analogous decay

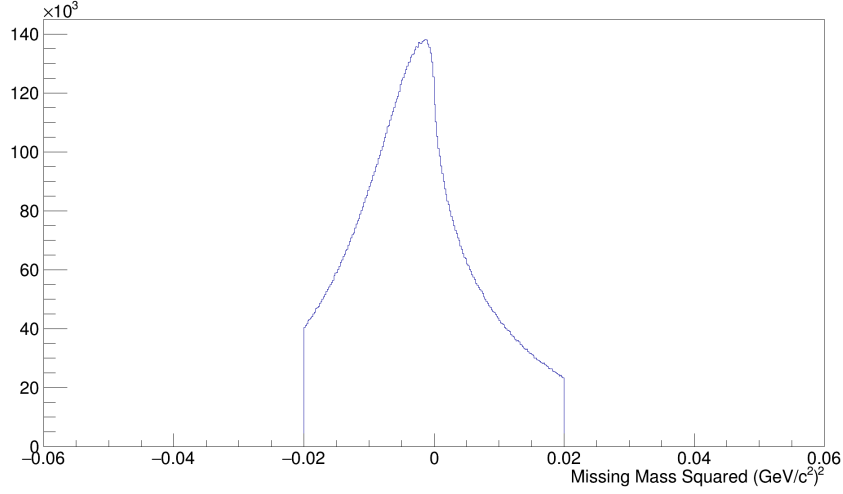


FIG. 4.2: $\gamma p \rightarrow K^+ K^- \pi^0 \eta p$ MM^2 after a $|MM^2| < 0.02 \text{ (GeV}/c^2)^2$ cut is applied.

$X \rightarrow \phi a_0(980)$ with $\phi \rightarrow K^+ K^-$ and $a_0(980) \rightarrow \pi^0 \eta$. This section describes the 2-D side band subtraction to statistically remove the non- $K^+ K^- \pi^0 \eta p$ events from the $K^+ K^- \gamma \gamma \gamma p$ events whose selection is detailed in Sec. 4.3. Then the invariant mass distributions of various final state particle combinations are explored for interesting features. And finally, an attempt to observe novel signals through $\phi \pi^0 \eta$ yields is presented.

In the selection process, events with combos in the $K^+ K^- \gamma \gamma \gamma p$ final state that were selected with the hypothesis that the photons were consistent with a π^0 ($M_{\gamma\gamma} = [0.08, 0.15] \text{ GeV}/c^2$) and an η ($M_{\gamma\gamma} = [0.35, 0.75] \text{ GeV}/c^2$). Even with requiring the kinematic fit to converge and the cuts made in Table 4.2, a significant background of non- $K^+ K^- \pi^0 \eta p$ combos exist. These backgrounds are subtracted using the 2-D background subtraction method used in [60]. The signal region is defined such that the 2- γ mass corresponding to the π^0 is between 0.115 and 0.155 GeV or the 2- γ mass corresponding to the η is between 0.505 and 0.585 GeV. Sidebands with half the width of the signal regions were defined on either side of signal regions in the 2- γ masses. In the 2-dimensional space, the sideband regions overlap in four regions, and the signal region overlap in the region corresponding

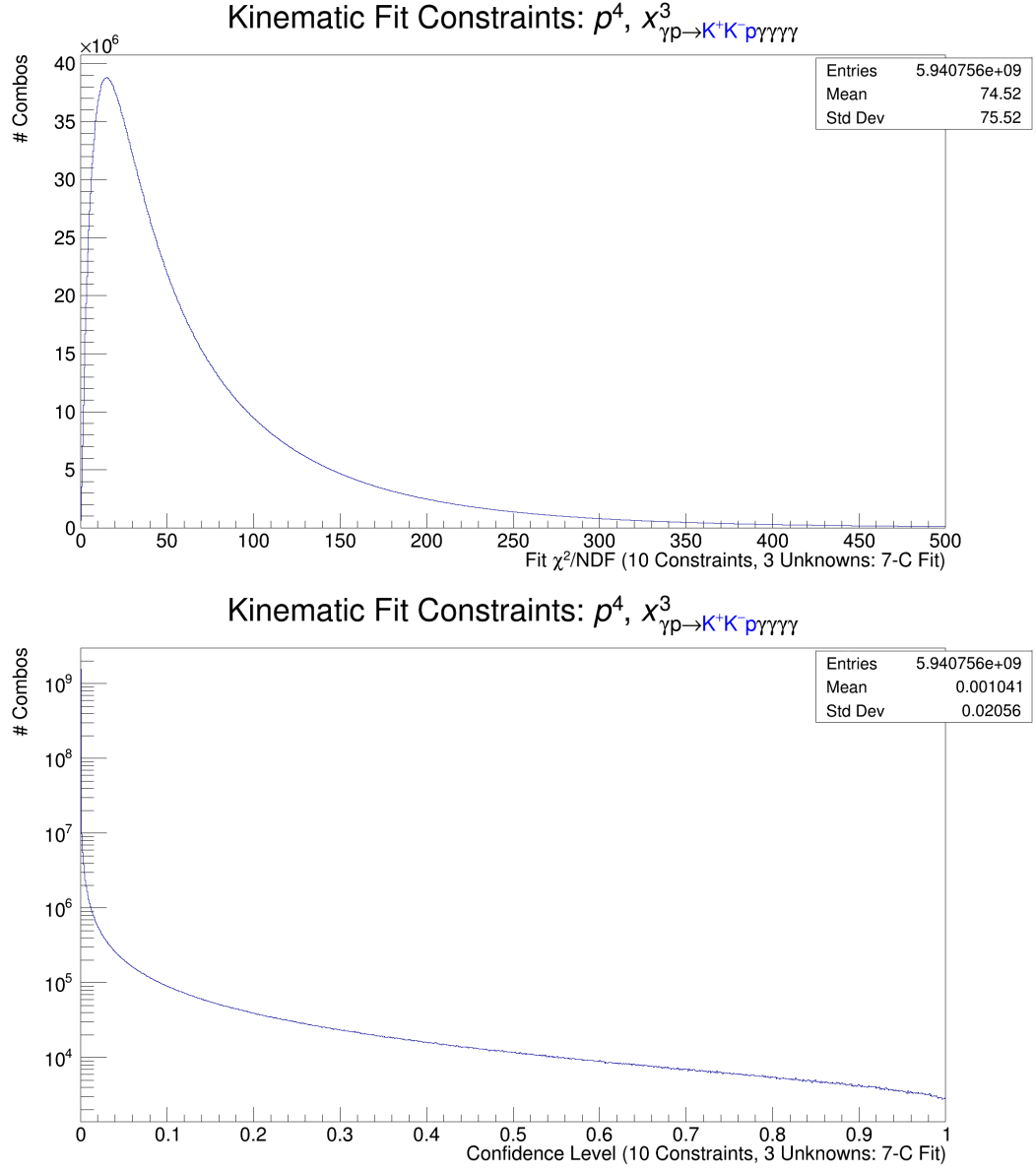


FIG. 4.3: $\gamma p \rightarrow K^+ K^- \pi^0 \eta p$ MM^2 Kinematic fit χ^2/NDF (top) and confidence level (bottom).

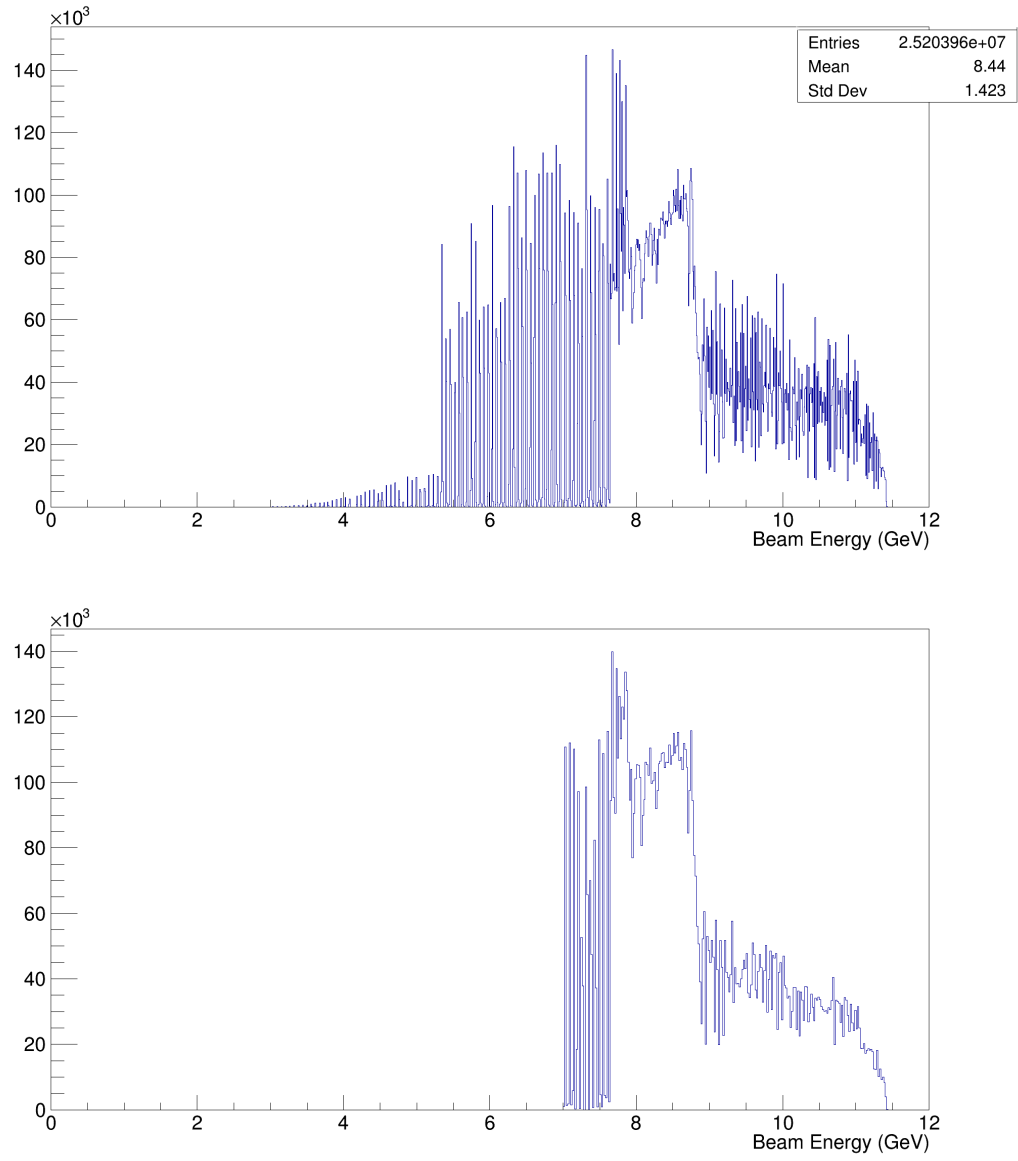


FIG. 4.4: $\gamma p \rightarrow K^+ K^- \pi^0 \eta p$ photon beam energy before (top) and after (bottom) 7.0 GeV cut.

to events with a π^0 and an η . The π^0 and η signal regions are weighted with weight 1, non-overlapping sideband regions carry weight -1, and the overlapping sideband regions carry a weight of -5/2, and every other combo not in these regions is removed from the analysis. The weights are applied to all of the subsequent plots presented in this reaction. Note, this implementation of this 2D sideband sideband subtraction method may not be optimal or suitable for this reaction and should be revisited in any future works.

4.4.1 Mass Distributions

The motivation to study the $\gamma p \rightarrow K^+ K^- \pi^0 \eta p$ was to search for a proposed intermediate meson [61] that decays to $\phi a_0(980)$ and/or $\phi \pi^0 \eta$. We will look for enhancements in the mass spectra of the $K^+ K^-$ and the $\pi^0 \eta$, and the $K^+ K^- \gamma \gamma \gamma$ systems. The mass spectra of interest are shown in Fig. 4.5. In the two meson mass spectra, the $\pi^0 \eta$ mass spectrum shows an enhancement near $0.98 \text{ GeV}/c^2$, and the $K^+ K^-$ spectrum shows a narrow enhancement near $1.02 \text{ GeV}/c^2$ and broad enhancement near $1.3 \text{ GeV}/c^2$. The $\pi^0 \eta$ $0.98 \text{ GeV}/c^2$ peak may be due to the $a_0(980)$. The $1.02 \text{ GeV}/c^2$ peak in $K^+ K^-$ is treated as the ϕ , while the $1.3 \text{ GeV}/c^2$ peak may be caused by events with $\rho \rightarrow \pi^+ \pi^-$ where the two pions are both reconstructed as kaons (i.e. when the pions are misidentified as kaons, the kinematic fit adjusts their 4-momentum which can shift the mass of the resonance in the KK mass spectrum). The $K^+ K^- \gamma \gamma \gamma$ mass spectrum shows no enhancements at all.

4.4.2 Yields

From the mass spectrum plots in Fig. 4.5, there exist events with ϕ mesons decaying to $K^+ K^-$ and events with $a_0(980)$ mesons decaying to $\pi^0 \eta$. The next step in the survey is to see if there is an enhancement in the number of events with ϕ mesons and events with $\phi a_0(980)$ together as a function of the $K^+ K^- \pi^0 \eta$ mass.

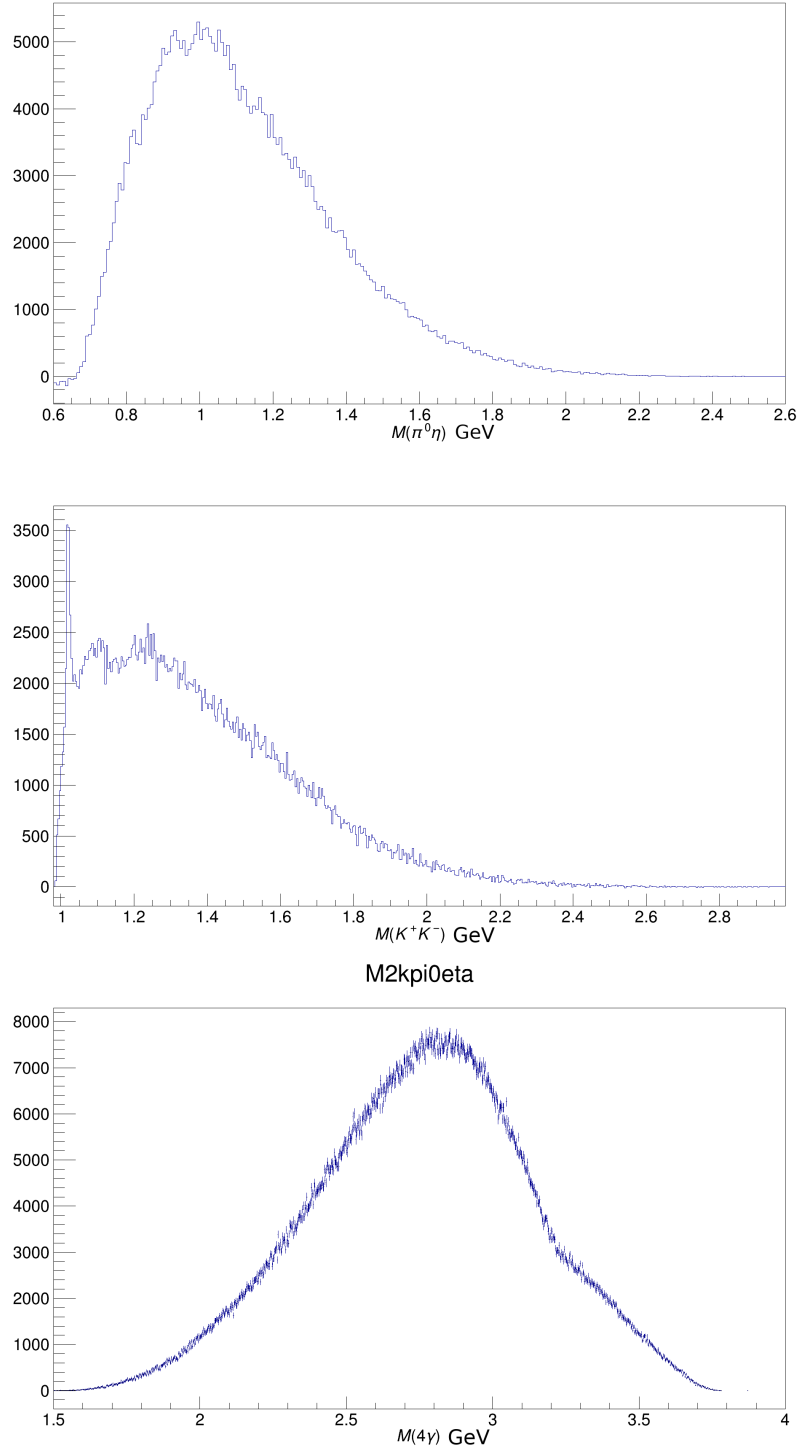


FIG. 4.5: Meson Mass Spectra in $\gamma p \rightarrow K^+K^-\pi^0\eta p$. From top to bottom: the $\pi^0\eta$ mass spectrum, the K^+K^- mass spectrum, and the $K^+K^-\gamma\gamma\gamma$ mass spectrum.

As far as $\gamma p \rightarrow \phi a_0(980)p$ events are concerned, we first look at the ϕ yield as a function of $\pi^0\eta$ mass to estimate the total number of events. The ϕ yield is evaluated by fitting the K^+K^- with a Gaussian signal function + polynomial background in the corresponding mass bins, see example in Fig. 4.6, and integrating the Gaussian portion. The ϕ yield as a function of the $\pi^0\eta$ mass is shown in Fig. 4.7(a), and the rest of the individual fits are shown in Appendix B. From the plot in Fig. 4.7(a), there is an enhancement consistent with the $a_0(980)$, but there are much fewer than 1000 events in that peak. The small number of potential $\gamma p \rightarrow \phi a_0(980)p$ events precludes any attempt to resolve $\phi a_0(980)$ as a function of $K^+K^-\pi^0\eta$ mass.

In order to search for enhancements in the $\phi\pi^0\eta$ production as a function of $K^+K^-\pi^0\eta$ mass, the same procedure of fitting the $\phi \rightarrow K^+K^-$ yield in each of the relevant $K^+K^-\pi^0\eta$ mass bins. The $\phi\pi^0\eta$ yields are plotted in Fig. 4.7(b), and the fits are shown in Appendix B. The ϕ yield in Fig. 4.7(b) does not show any significant enhancement with which to claim an observation of an intermediate state decaying to $\phi\pi^0\eta$.

The error on the extracted $\phi \rightarrow K^+K^-$ yield is estimated from the error of the integral of the fit function around the ϕ peak. Based on the bin-to-bin variations seen in Fig. 4.7(a), especially in the lower yield bins, the errors are likely under-estimated. This is likely due to the fact that relatively small changes to the width of the Gaussian, which was a free parameter in the fits, do not greatly effect the fit quality, but can vary the integral of the function significantly. This error was not quantified for the purposes of this survey, but would be essential if one wanted to report a cross section measurement.

4.5 $K^+K^-\pi^0\pi^0p$ Event Selection

For the reaction $\gamma p \rightarrow K^+K^-\pi^0\pi^0p$, the proton, K^+ and K^- are directly detected in the drift chambers, while the two π^0 s each decay to two photons which are detected in

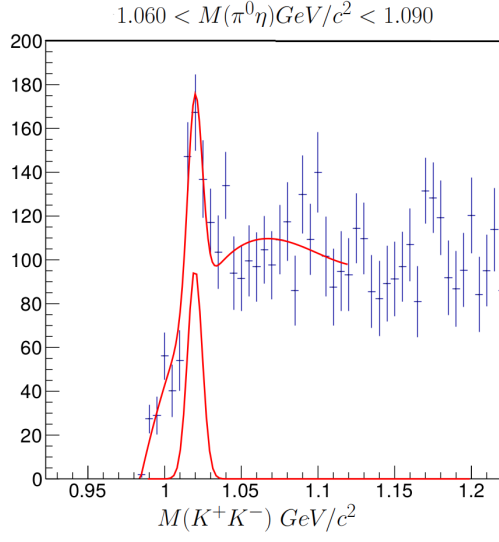


FIG. 4.6: An example of the ϕ Yield Fit in the mass bin $1.06 < M(\pi^0\eta) < 1.09$ GeV/c^2 .

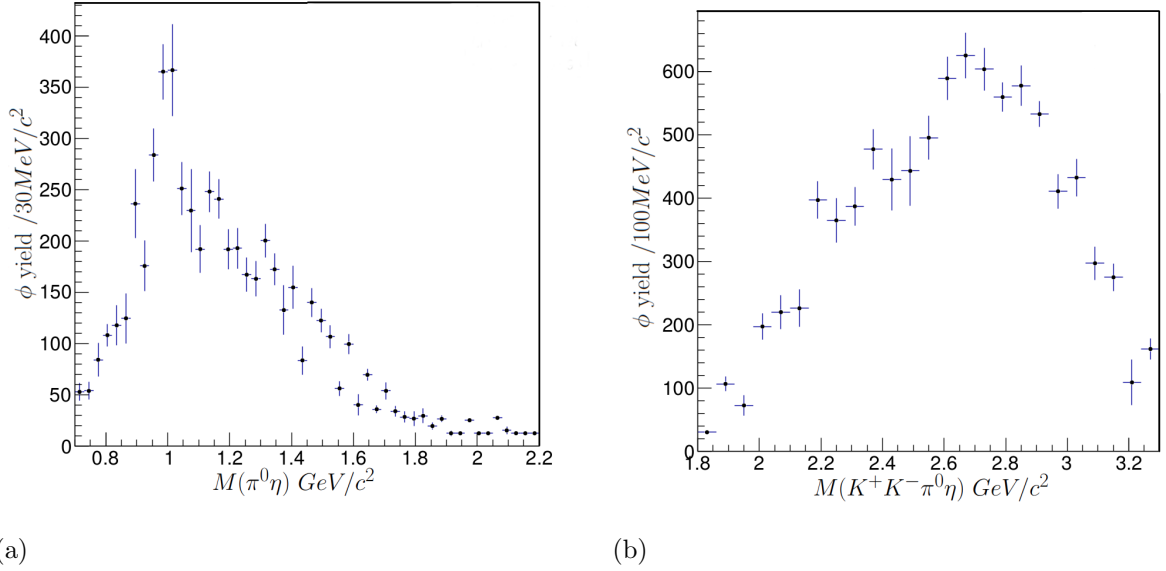


FIG. 4.7: (a) ϕ Yield vs. $\pi^0\eta$ mass, and (b) the ϕ Yield vs $K^+K^-\pi^0\eta$. See Fig. 4.6 fit for an example of how each bin is determined in these yield plots.

the calorimeters. The mass hypotheses and neutral combinatorics are similar to that of Sec. 4.3. The analysis cuts on the skimmed $\gamma p \rightarrow K^+ K^- \pi^0 \pi^0 p$ events are described in the remainder of this section.

The charged track timing cuts are given in Table 4.3.

PID	Δt (ns) TOF	Δt (ns) BCAL	Δt (ns) FCAL	Δt (ns) ST
p	± 0.5	± 1.0	None	None
K^+	± 0.3	± 1.0	None	None
K^-	± 0.3	± 1.0	None	None
γ	N/A	± 1.5	± 2.5	N/A

TABLE 4.3: $\gamma p \rightarrow K^+ K^- \pi^0 \pi^0 p$ charged particle timing cuts

The rest of the analysis cuts for $\gamma p \rightarrow K^+ K^- \pi^0 \pi^0 p$ are listed in Table 4.4.

Cut Variable	Condition
$M_{\gamma\gamma \rightarrow \pi^0}$	$[0.08, 0.15] \text{ GeV}/c^2$
$ MM^2 $	$< 0.05 (\text{GeV}/c^2)^2$
CL	> 0.00001
E_γ	None

TABLE 4.4: $\gamma p \rightarrow K^+ K^- \pi^0 \pi^0 p$ analysis cuts. The $M_{\gamma\gamma}$ cuts are loose mass cuts on the two photon masses. $|MM|^2$ is the missing mass squared, CL is the confidence level, and E_γ is the beam energy.

The MM^2 for $\gamma p \rightarrow K^+ K^- \pi^0 \pi^0 p$ is plotted in Fig. 4.8 before applying any other cuts. Plots of the kinematic fit χ^2/NDF and confidence level are shown in Fig. 4.9. The cut on the kinematic fit confidence level was looser than that chosen in the $K^+ K^- \pi^0 \eta p'$ final state selection in order to increase statistics despite allowing for more background events. The plot of the beam energy is shown in Fig. 4.10. The plots presented here do not contain a cut on the beam energy, but a cut should be applied in future works.

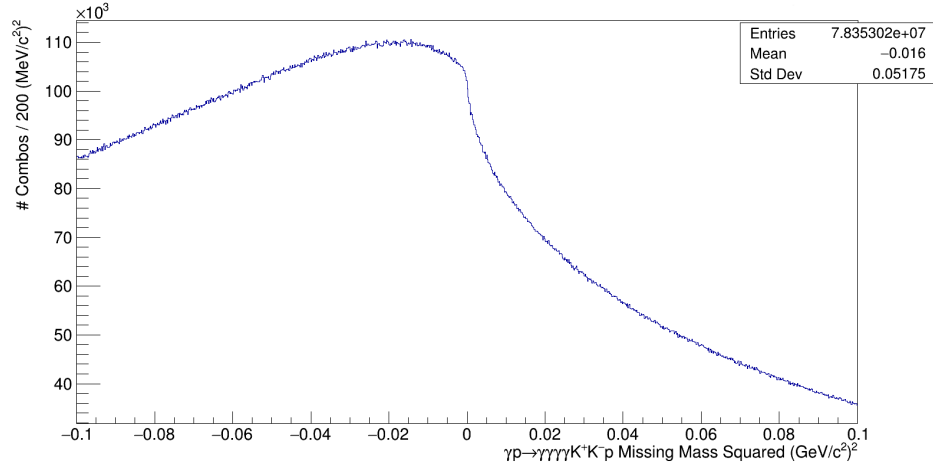


FIG. 4.8: $\gamma p \rightarrow K^+ K^- \pi^0 \pi^0 p$ MM^2 before Kinematic fit cut applied.

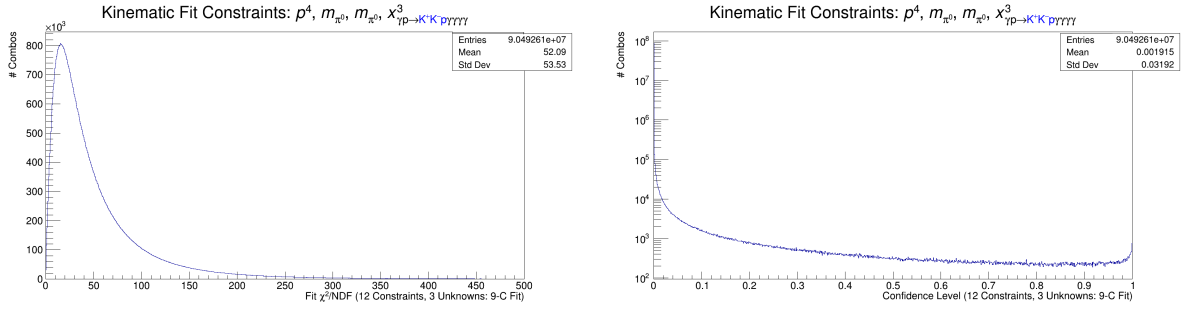


FIG. 4.9: $\gamma p \rightarrow K^+ K^- \pi^0 \pi^0 p$ MM^2 Kinematic fit χ^2/NDF (left) and confidence level (right).

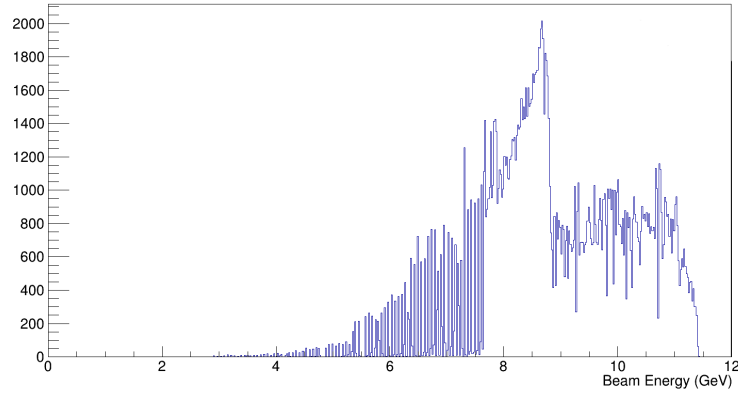


FIG. 4.10: $\gamma p \rightarrow K^+ K^- \pi^0 \pi^0 p$ photon beam energy

4.6 Features of the $K^+K^-\pi^0\pi^0p$ Final State

This section details the search for the $\phi(2170)$ in the $K^+K^-\pi^0\pi^0p$ final state using the data from the GlueX-I 2017_01 run period. As seen in Sec. 1.3, the $\phi(2170)$ was seen to decay to $\phi f_0(980)$. In this final state we consider the decays $\phi \rightarrow K^+K^-$ and $f_0(980) \rightarrow \pi^0\pi^0$, with each π^0 decaying to $\gamma\gamma$. This final state was explored as a complementary study to the $K^+K^-\pi^+\pi^-p$ final state. This final state has the advantage of not containing contributions from ρ in the $\pi^0\pi^0$ mass spectrum (as opposed to the $\pi^+\pi^-$ mass spectrum in Sec. 4.8 which is dominated by the ρ , see Fig. 4.17(b)).

This section will begin by examining the relevant invariant mass spectra, and then signs of the $\phi(2170)$ will be searched for as an enhancement of $\phi\pi^0\pi^0$ and $\phi f_0(980)$ yields in a similar manner to the previous section.

4.6.1 Mass Distributions

The aforementioned mass distributions of interest are shown in Fig 4.11. The $\pi^0\pi^0$ invariant mass spectrum in Fig. 4.5(a) does not show any enhancement in the $f_0(980)$ mass region. The K^+K^- mass spectrum in Fig. 4.5(b) shows a strong enhancement consistent with the ϕ meson, as well as the same misidentified pion peak above $1.2 \text{ GeV}/c^2$ described in Sec. 4.4.1. Fig. 4.11(c) shows the $K^+K^-\pi^0\pi^0$ mass spectrum which has no identifiable resonant-like features.

4.6.2 Yields

Following the same methods outline in Sec. 4.4.2, the ϕ yield is determined as a function of the $\pi^0\pi^0$ mass and the $K^+K^-\pi^0\pi^0$ mass.

The ϕ yield as a function of $\pi^0\pi^0$ mass is shown in Fig. 4.12(a), and the distribution has a small enhancement just below $1 \text{ GeV}/c^2$. This enhancement may be consistent with

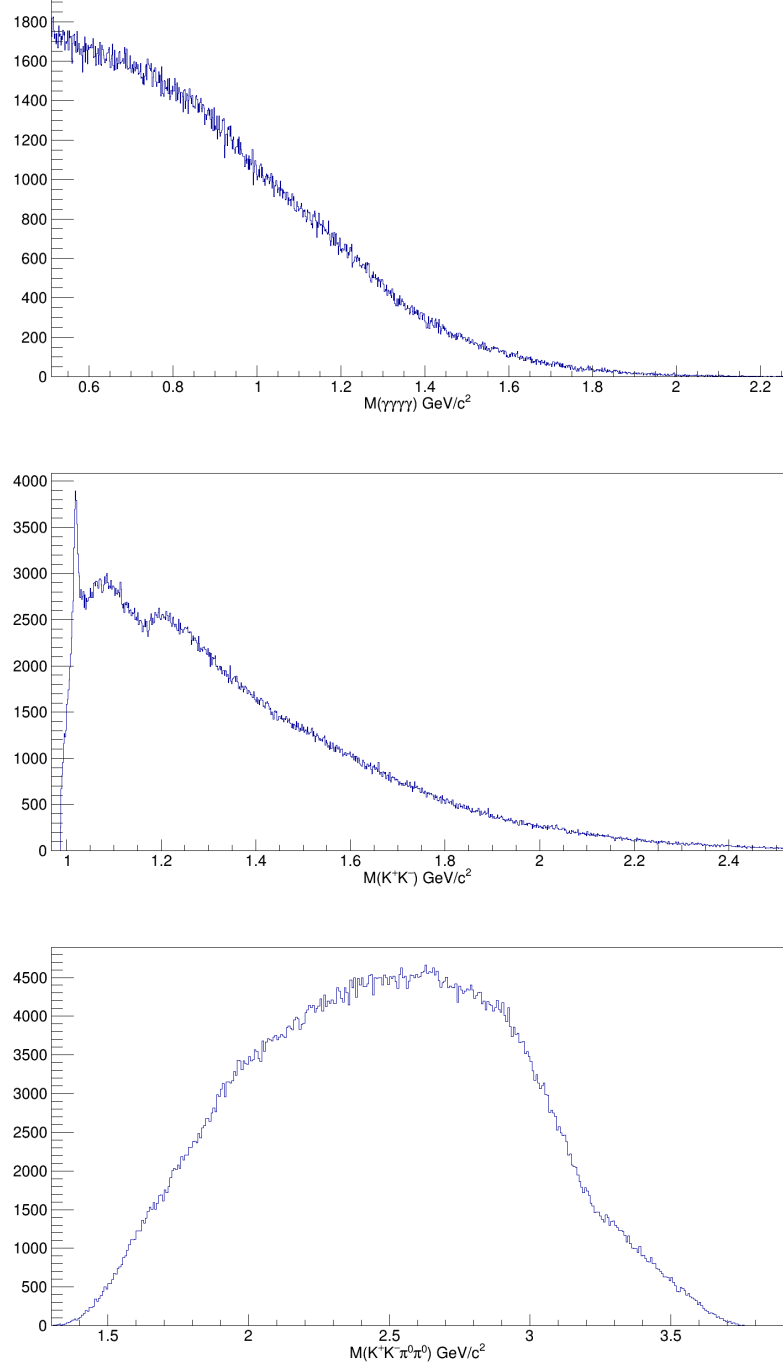


FIG. 4.11: Invariant mass spectra in $\gamma p \rightarrow K^+ K^- \pi^0 \pi^0 p$. Top is the $\pi^0 \pi^0$ mass, middle is the $K^+ K^-$ mass, and bottom is the $K^+ K^- \pi^+ \pi^-$ mass.

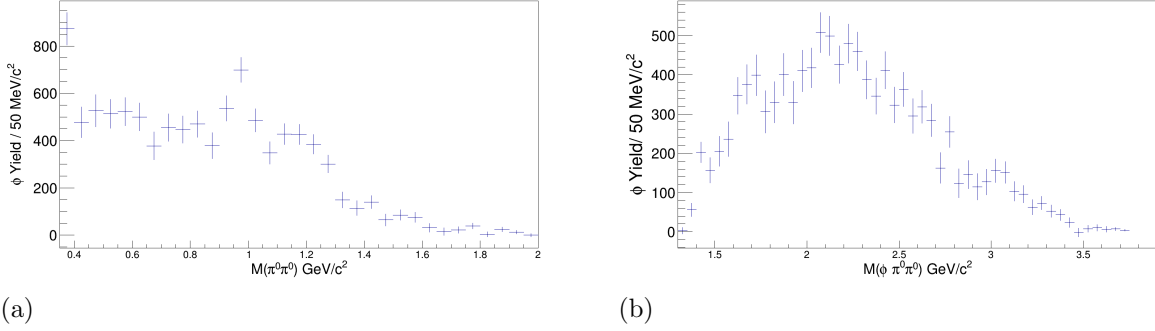


FIG. 4.12: (a) ϕ yield vs. $\pi^0\pi^0$ mass, and (b) ϕ Yield vs $K^+K^-\pi^0\pi^0$ mass. ϕ yields determined from fits to the K^+K^- mass.

the $f_0(980)$, but the same caveats on the bin-to-bin fluctuations with the yield discussed in Sec. 4.4.2 also apply here.

The ϕ yield as a function of the $K^+K^-\pi^0\pi^0$ mass is shown in Fig. 4.12(b). This yield distribution has some fluctuations, but none that could be considered a significant enhancement given the concern with uncertainties in the yield determination.

4.7 $K^+K^-\pi^+\pi^-p$ Selection

For the reaction $\gamma p \rightarrow K^+K^-\pi^+\pi^-p$, the proton, K^+ , K^- , π^+ , and π^- are all directly detected in the drift chambers. For this reaction, the reconstructed data is skimmed for events with three positively charged tracks, and two negatively charged tracks. The charged particles can be rearranged into combos if multiple mass hypotheses exist for like-charged tracks, meaning there is still often more than one combo per event for which the kinematic fit converges. For example, if both negatively charged tracks have a mass hypotheses consistent with a pion and a kaon, there will be a combo with one treated like a kaon (the other as a pion) and another combo with the reverse. The analysis cuts on the skimmed $\gamma p \rightarrow K^+K^-\pi^+\pi^-p$ events are described in the remainder of this section.

The charged track timing cuts are given in Table 4.5.

PID	Δt (ns) TOF	Δt (ns) BCAL	Δt (ns) FCAL	Δt (ns) ST
p	± 0.5	± 1.0	None	None
K^+	± 0.3	± 1.0	None	None
K^-	± 0.3	± 1.0	None	None
π^+	± 0.3	± 1.0	None	None
π^-	± 0.3	± 1.0	None	None

TABLE 4.5: $\gamma p \rightarrow K^+ K^- \pi^+ \pi^- p$ charged particle timing cuts

The rest of the analysis cuts for $\gamma p \rightarrow K^+ K^- \pi^+ \pi^- p$ are listed in Table 4.6.

Cut Variable	Condition
$ MM^2 $	$< 0.02 \text{ (GeV}/c^2)^2$
CL	> 0.001
E_γ	$> 8.0 \text{ GeV}$

TABLE 4.6: $\gamma p \rightarrow K^+ K^- \pi^+ \pi^- p$ Analysis cuts. $|MM|^2$ is the missing mass squared, CL is the confidence level, and E_γ is the beam energy.

The MM^2 for $\gamma p \rightarrow K^+ K^- \pi^+ \pi^- p$ is plotted in Fig. 4.13 after applying a $|MM^2| < 0.02 \text{ (GeV}/c^2)^2$ cut.

Plots of the kinematic fit χ^2/NDF and confidence level are shown in Fig. 4.14. For comparison, plots of the χ^2/NDF and confidence level for a signal Monte Carlo sample is shown in Fig. 4.15. The signal Monte Carlo sample used for these plots does not have any non- $K^+ K^- \pi^+ \pi^- p$ backgrounds, and the sample was passed through the GlueX detector acceptance simulation. The χ^2/NDF distribution for the data in Fig. 4.14 has a large amount of background that has not been cut yet which is why distribution peaks much higher than 1. The χ^2/NDF distribution for the Monte Carlo sample peaks much closer to 1 as expected since it does not contain any background. A plot of the beam energy after the beam energy cut is shown in Fig. 4.16.

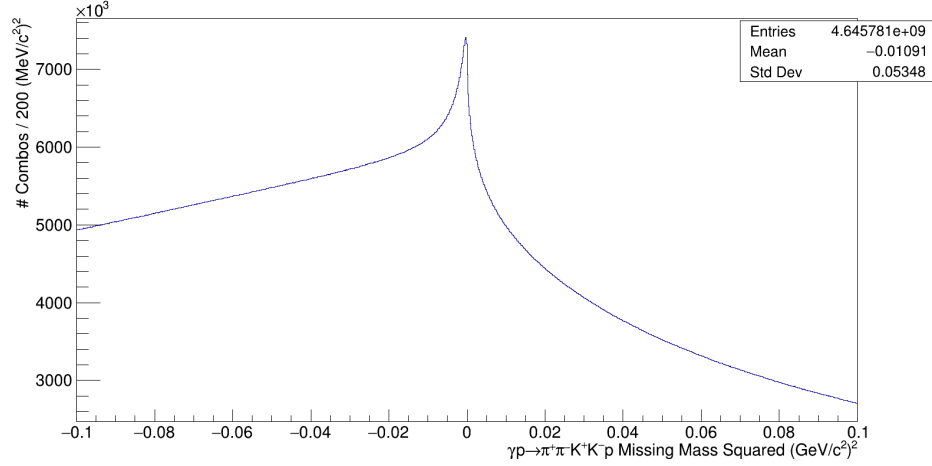


FIG. 4.13: $\gamma p \rightarrow K^+ K^- \pi^+ \pi^- p$ MM^2 before any analysis cuts are applied.

4.8 Features of the $K^+ K^- \pi^+ \pi^- p$ Final State

As with the previous two sections, this section will explore some mass spectra relevant to the $\phi(2170)$ search. This section will begin by looking at some intermediate mass spectra, then background processes (to the possible production of $\phi(2170)$) will be examined and cut using a *van Hove* analysis, and finally we will look at ϕ yields as a function of $K^+ K^- \pi^+ \pi^-$ and $\pi^+ \pi^-$ mass.

4.8.1 Mass Distributions

The invariant mass distributions presented in this section are those relevant to the search for the $\phi(2170)$, as well as those that will be useful in the following sections and the amplitude analysis in Sec. 6.

The mass spectra in Fig. 4.17 are formed from the two meson invariant masses: $K^+ K^-$, $\pi^+ \pi^-$, $K^+ \pi^-$, and $K^- \pi^+$. The $K^+ K^-$ mass spectrum shows a strong enhancement centered near $1.02 \text{ GeV}/c^2$ consistent with the ϕ meson, as well as higher mass enhancements (potentially from bad PID as discussed in Sec. 4.4.1). The $\pi^+ \pi^-$ mass

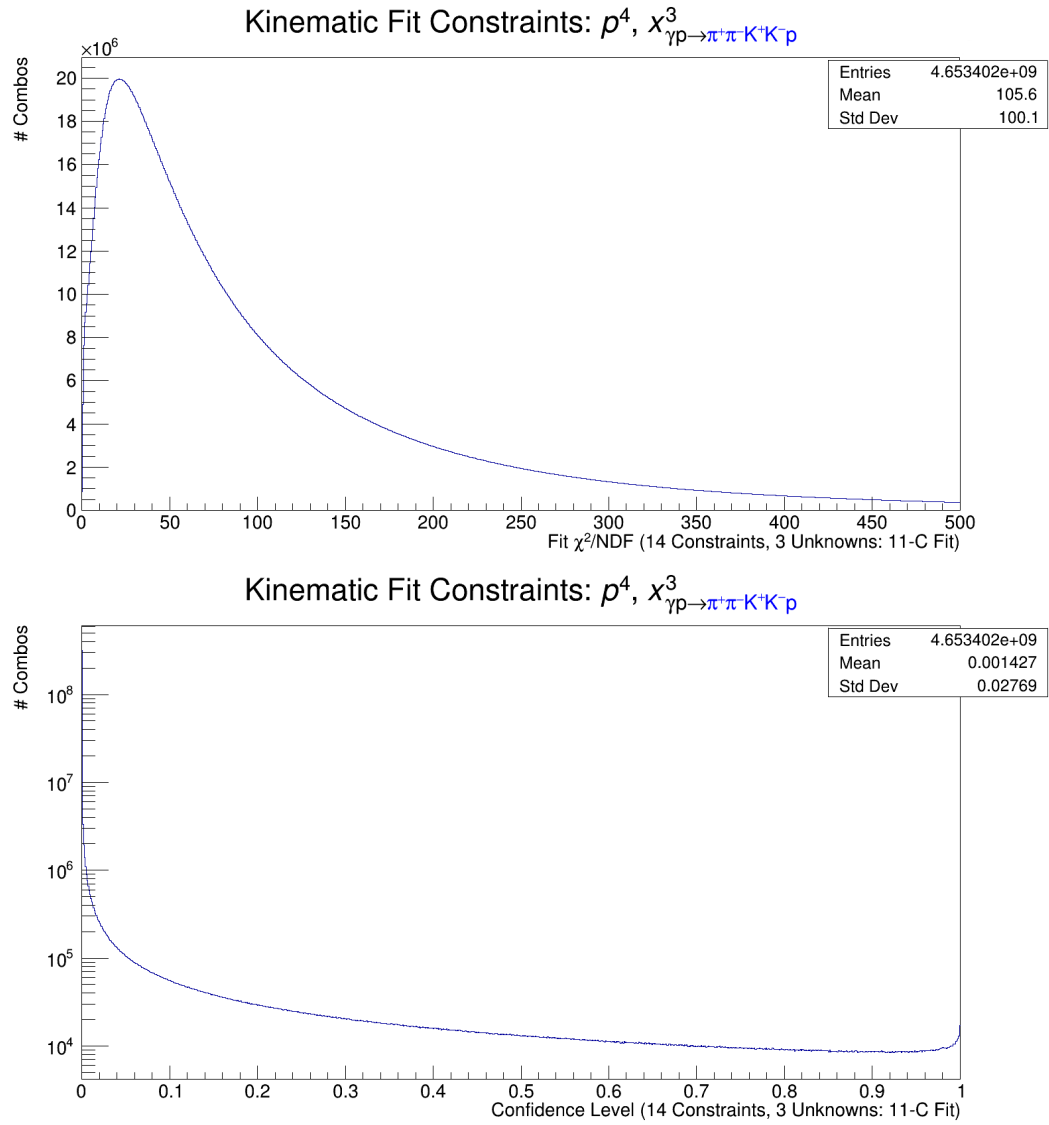


FIG. 4.14: $\gamma p \rightarrow K^+ K^- \pi^+ \pi^- p$ GlueX data Kinematic fit χ^2/NDF (top) and confidence level (bottom).

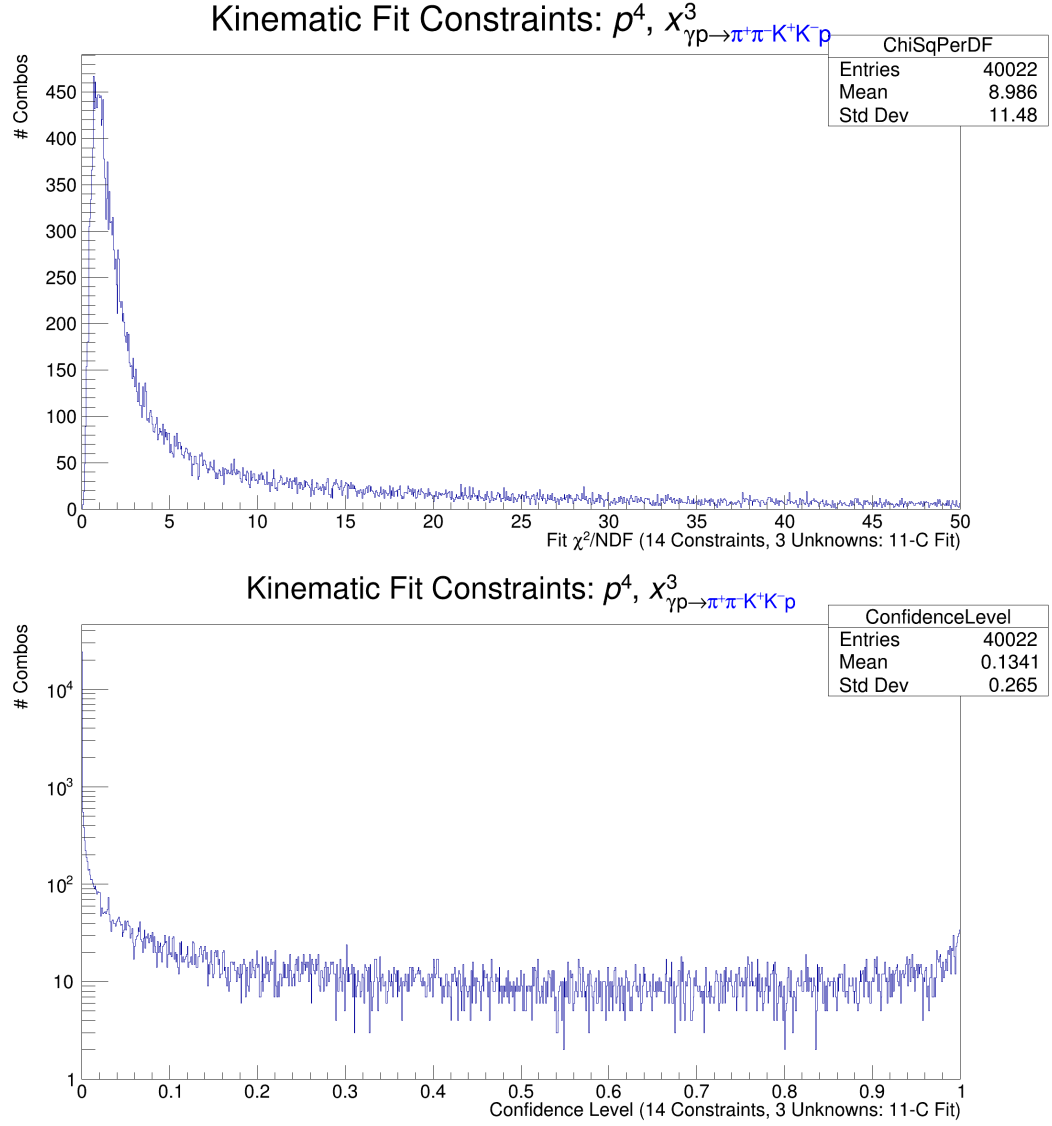


FIG. 4.15: Monte Carlo $\gamma p \rightarrow K^+ K^- \pi^+ \pi^- p$ Kinematic fit χ^2/NDF (top) and confidence level (bottom). The Monte Carlo sample was generated with $K^+ K^- \pi^+ \pi^- p$ and passed through the simulation of the GlueX detector acceptance simulation.

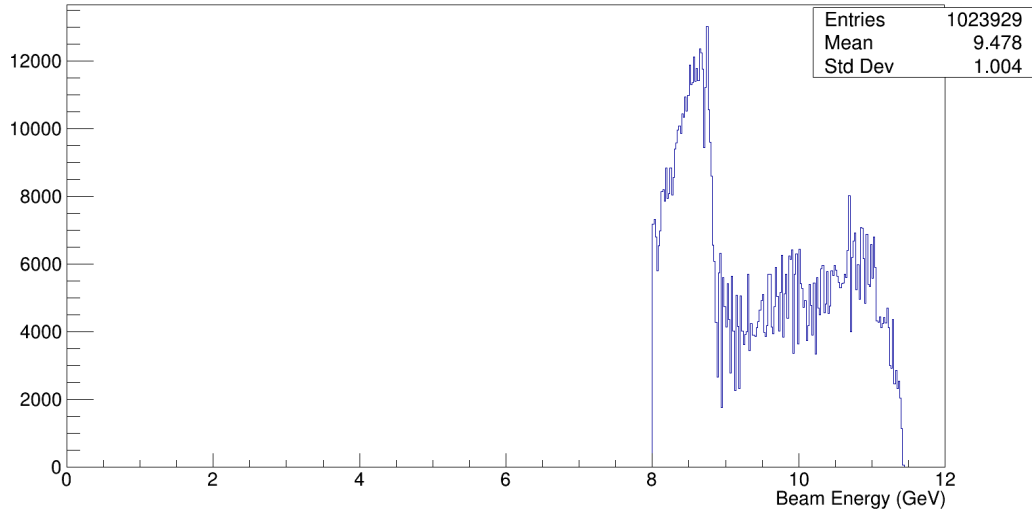


FIG. 4.16: $\gamma p \rightarrow K^+ K^- \pi^+ \pi^- p$ photon beam energy after 8.0 GeV cut.

spectrum shows enhancements centered near 0.5, 0.77, 0.98, and 1.25 GeV/c^2 that are possibly caused by the production of the K_s^0 , ρ , $f_0(980)$, and the $f_2(1270)$, respectively. The $K^+ \pi^-$ and $K^- \pi^+$ mass spectra both show strong enhancements centered near 0.89 GeV/c^2 and a smaller enhancement centered near 1.4 GeV/c^2 , which are consistent with the $K^{*0}(892)$ and the $K^{*0}(1430)$. The ϕ and $f_0(980)$ will be used in the search for the $\phi(2170)$, while the ρ and $K^{*0}(892)$ will be relevant for the amplitude analysis in Chapter 6.

The masses in the spectra in Fig. 4.18 are calculated from the combination of $K^- \pi^+ \pi^-$ and $K^- \pi^+ \pi^-$ which one would expect to see signs of known excited kaons. Enhancements between 1.3 and 1.5 GeV that are readily seen in these spectra can be any number of these known excited kaons that will be explored further in Chapter 6.

The four-meson mass spectrum in Fig 4.19 shows the invariant mass of the $K^+ K^- \pi^+ \pi^-$ mass spectrum. Without any cuts applied, there is not any clear structure associated with any known resonances, and so this mass spectrum will be revisited in Sec. 4.8.4 once some of the backgrounds have been subtracted.

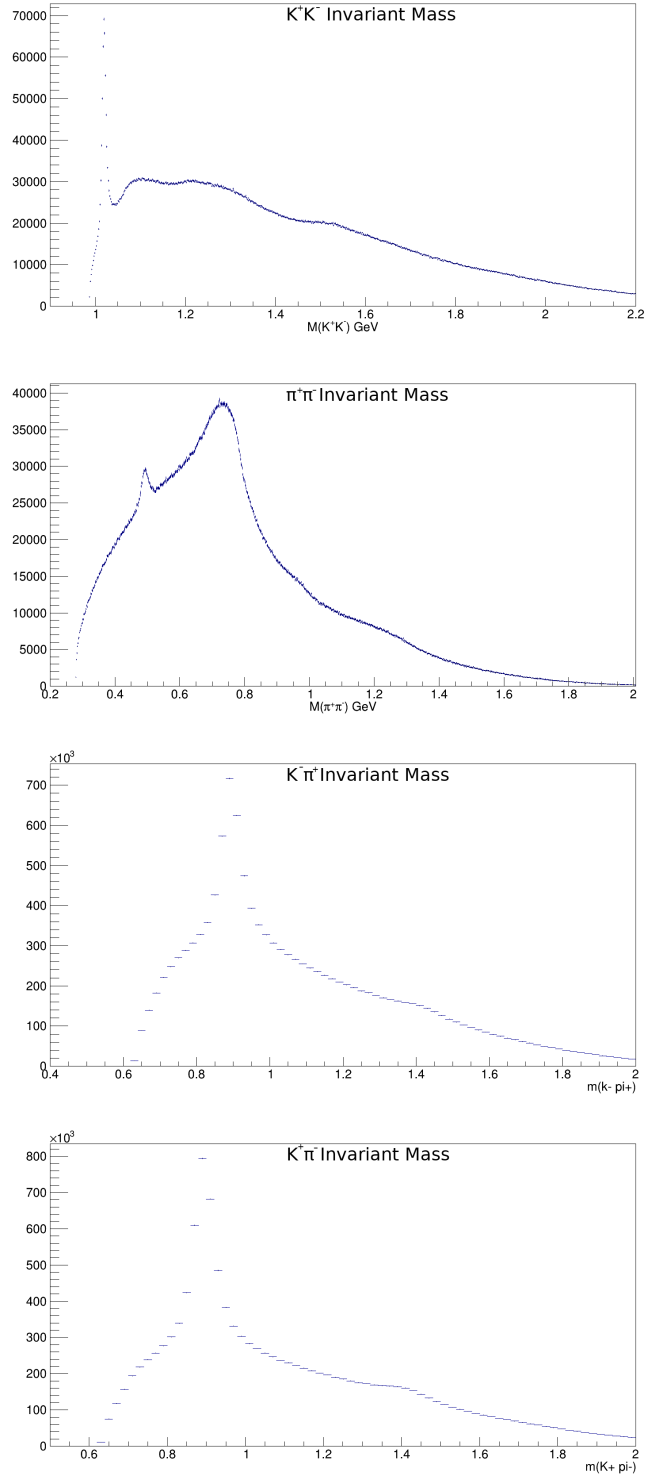
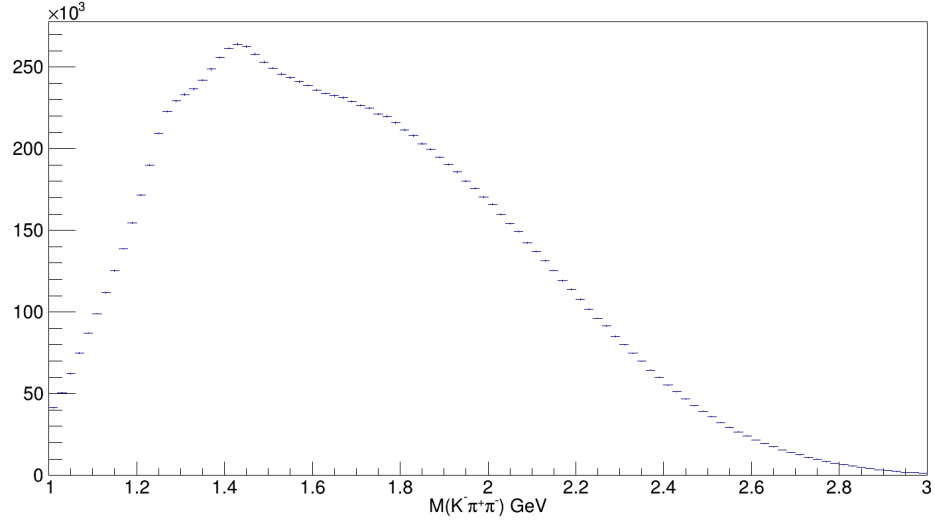
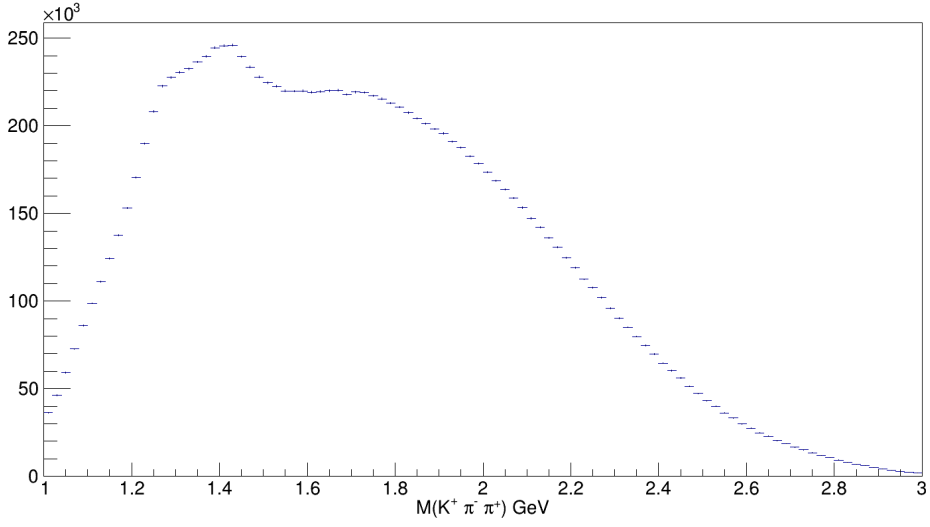


FIG. 4.17: Mass spectra in $\gamma p \rightarrow K^+ K^- \pi^+ \pi^- p$. From top to bottom: the $K^+ K^-$ mass spectrum, the $\pi^+ \pi^-$ mass spectrum, the $K^- \pi^+$ mass spectrum, and the $K^+ \pi^-$ mass spectrum.



(a)



(b)

FIG. 4.18: Mass spectra in $\gamma p \rightarrow K^+ K^- \pi^+ \pi^- p$. The top plot is the $K^- \pi^+ \pi^-$ mass spectrum. The bottom plot is the $K^+ \pi^+ \pi^-$ mass spectrum

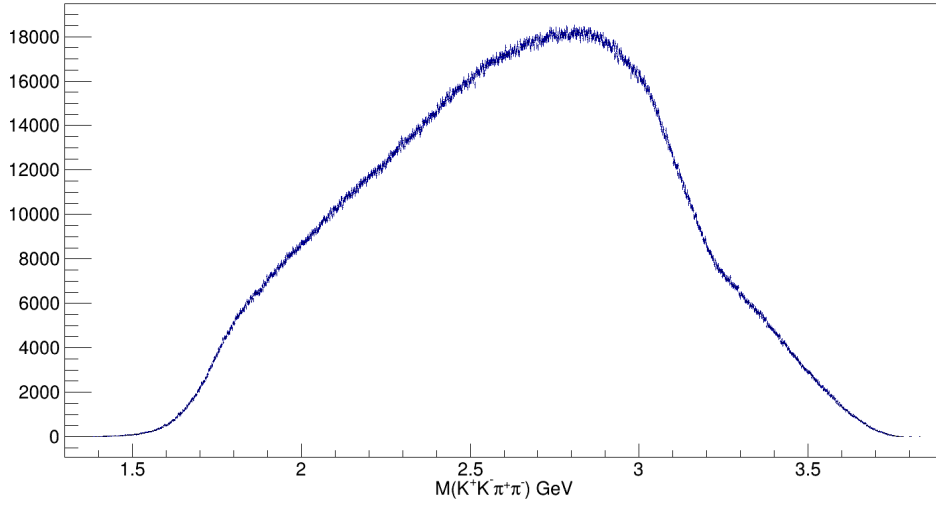


FIG. 4.19: Mass spectrum of $K^+K^-\pi^+\pi^-$ in $\gamma p \rightarrow K^+K^-\pi^+\pi^-p$

4.8.2 Baryon Excitations in $\gamma p \rightarrow K^+K^-\pi^+\pi^-p$.

In the context of diffractive, t -channel production, such as the sought after $\gamma p \rightarrow \phi(2170)p$ reaction, processes with an excitation of the proton (and subsequent decay) are a background that can obfuscate the processes of interest. Fig. 4.20 shows the mass spectra of systems involving the proton and one or more mesons. The $p\pi^+$ mass spectrum shows a very large and wide enhancement consistent with the Δ^{++} baryon. The $p\pi^-$ spectrum shows a narrow peak just above $1.1 \text{ GeV}/c^2$ consistent with the Λ baryon, as well as several higher-mass excited baryon peaks. The peak centered around $1.5 \text{ GeV}/c^2$ in the pK^- mass spectrum is consistent with the $\Lambda(1520)$, and there also exists an enhancement that may be due to a higher mass Λ baryons or a baryon decaying to $p\pi^-$ where the π^- is reconstructed as a K^- . And finally, the $p\pi^+\pi^-$ mass spectrum shows a couple of enhancements that may be due to baryons with masses near 1.5 and $1.65 \text{ GeV}/c^2$. In the cases where the events involving excited baryons are significant backgrounds, it would be useful to be able to remove those background events without cutting away too many events of interest. Based on the location and some of the widths of some of these baryons, simple mass vetos may

not be ideal when searching for indications of processes which are limited by statistics, and so the next section will explore a *van Hove* analysis for separating baryon excitations from t -channel processes.

4.8.3 van Hove Analysis

In 1969, Léon van Hove published a method for visualizing and distinguishing various categories of processes that lead to the same final state [62]. This method leverages the empirical behavior of hadron collisions that the transverse momenta of the final state particles in the center-of-mass frame (CoM) are small, the longitudinal momenta are large (especially compared to the particle masses), and that different types of processes will have different distributions of longitudinal momenta. For reactions with multiple final state particles, the longitudinal momentum phase space is much more manageable in terms of dimensionality while using more kinematic information than searched-for peaks in mass spectra. This section will describe the four final state particle van Hove phase space plots and their application in removing excited baryon processes in $\gamma p \rightarrow K^+ K^- \pi^+ \pi^- p$.

First consider a $2 \rightarrow n$ reaction in the CoM frame, where n is the number of final state particles. The i th final state particle has energy E_i , mass m_i , longitudinal momentum p_{Li} (chosen to be the component of momentum parallel with the incoming momenta of one of the initial state particles), and transverse momentum p_{Ti} . In the CoM frame the conservation of energy and momentum equations are given by

$$\sum_{i=1}^n E_i = W, \quad (4.2)$$

$$\sum_{i=1}^n p_i^L = 0, \quad (4.3)$$

$$\sum_{i=1}^n p_i^T = 0, \quad (4.4)$$

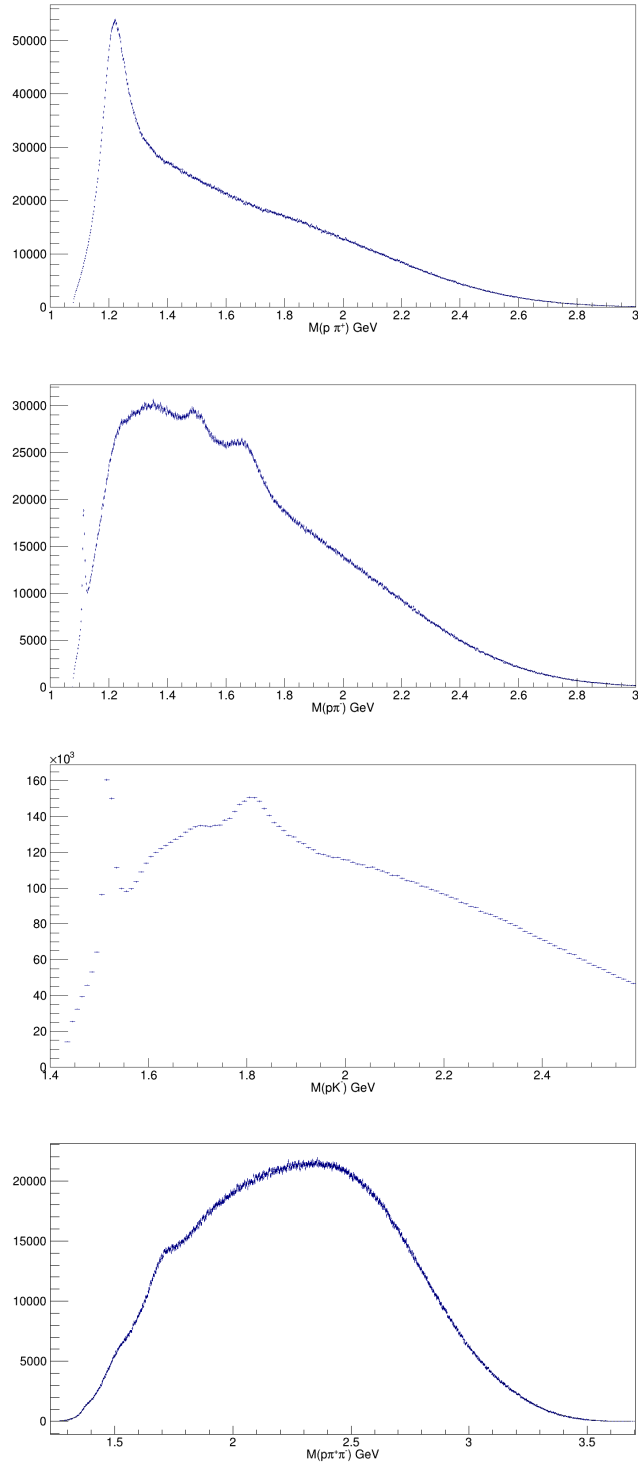


FIG. 4.20: Baryon Mass Spectra in $\gamma p \rightarrow K^+ K^- \pi^+ \pi^- p$. From top to bottom, the $p\pi^+$ mass spectrum, $p\pi^-$ mass spectrum, the pK^+ mass spectrum, and the $p\pi^+\pi^-$ mass spectrum.

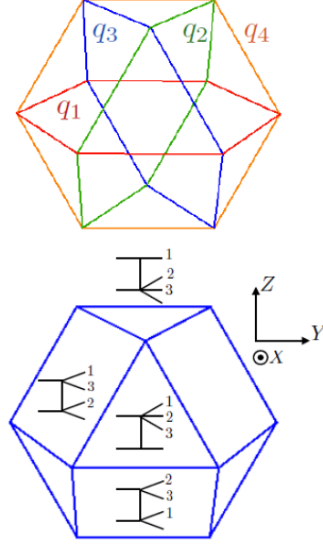


FIG. 4.21: The van Hove Cubeoctahedron. The planes indicated in the top image are the planes of $p_{Li} = 0$. The bottom image depicts what processes correspond to which region of the surface.

where W is the total energy. If $p_{Li} \gg p_{Ti}$ and $p_{Li} \gg m_i$, then the set of coordinates $\{p_{Li} \dots p_{Ln}\}$ lie on an $n - 2$ hypersurface in longitudinal momentum phase space. This hypersurface is the surface of a polyhedron defined by

$$\sum^n |p_i^L| \cong W \quad (4.5)$$

The sides and vertices of this polyhedron define the regions on the surface that have $p_{Li}, \dots = 0$. The hypersurface for an $n = 3$ final state is a hexagon, the hypersurface for a $n = 4$ final state is the surface of a cubeoctahedron (see Fig 4.21), and final states with $n > 4$ have surfaces with higher dimension than is useful for this visualization.

The reaction $\gamma p \rightarrow K^+ K^- \pi^+ \pi^- p$ of interest is $n = 5$ on the surface, but the van Hove analysis can still be applied if two of the particles treated as one isobar (e.g. by treating $K^+ + K^-$ as ϕ). The longitudinal phase space needs to be parameterized so that events can be plotted, and the parameters are chosen such that the $z = 0$ plane corresponds to

$p_{L1} = 0$ and the $p_{Li \neq 1} = 0$ planes equally span the phase space. The choice of coordinates is

$$z = p_{L1}, \quad (4.6)$$

$$x = \sqrt{\frac{3}{8}} \left(p_{L3} - p_{L2} \right), \quad (4.7)$$

$$y = \sqrt{\frac{1}{8}} \left(2p_{L1} + 3p_{L2} + 3p_{L3} \right). \quad (4.8)$$

The square faces of the cuboctahedron shown in Fig. 4.21 correspond to regions of the phase space where two particles are going forward (i.e. $p^L > 0$) and two particles are going backwards (i.e. $p^L < 0$). The triangular faces correspond to regions where three particles are going in one direction and one is going in the opposite direction. The cuboctahedron can be projected onto a 2-D plane using the typical spherical angles, see Fig. 4.22. Also shown in Fig. 4.22 are the projections of the great circles that define the four p_i^L planes, and each region is labelled by which of the p_i^L are positive or negative in that region. The great circle projections are given by

$$G_1(\phi) = \tan^{-1} \left(2\sqrt{2} \sin(\phi - \pi/3) \right), \quad (4.9)$$

$$G_2(\phi) = \tan^{-1} \left(2\sqrt{2} \sin(\phi - \pi) \right), \quad (4.10)$$

$$G_3(\phi) = \tan^{-1} \left(2\sqrt{2} \sin(\phi - 5\pi/3) \right), \quad (4.11)$$

$$G_4(\phi) = \pi/2. \quad (4.12)$$

As stated previously, to use the $n = 4$ van Hove plots, two particles must be combined in the choice of the set of momenta $\{ p_1^L \dots p_n^L \}$ in the final state of interest. Different

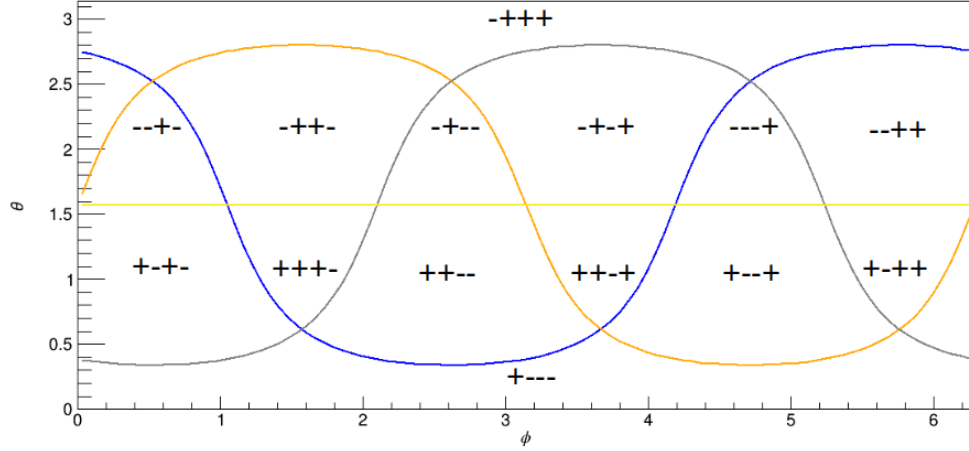


FIG. 4.22: The projected van Hove cubeoctahedron. The top image in Fig. 4.21 shows the $p_{Li} = 0$ planes of the van Hove cubeoctahedron, which are now projected onto this 2D diagram. the $\pm\pm\pm\pm$ labels in each of the regions indicated the sign of the $p_{L1} p_{L2} p_{L3} p_{L4}$ in the center of momentum frame.

choices of which particles to combine were chosen and used simultaneously to find a set of cuts to remove the baryon backgrounds. To study these cuts, five toy Monte Carlo samples were generated; one with a $\phi(2170)$ produced with no baryon excitation and the decay $\phi(2170) \rightarrow \phi f_0(980)$, and three samples generated with different excited baryons seen in Fig. 4.20 (a Δ^{++} , $\Lambda(1520)$, and $N^* \rightarrow p\pi^-$) with the appropriate decays and kinematics for GlueX. To give an example of how the cuts were selected, we reference Fig. 4.23, where the van Hove phase space plots (for the choice of $p + K^-$, $p + \pi^+$, and $p + \pi^-$ as particle $i = 4$) are shown for the Monte Carlo sample generated with a recoil $\Lambda(1520)$, the Monte Carlo with the $\phi(2170)$, and the data. In this example, if we want to remove the majority of events with a $\Lambda(1520)$ but keep events with the $\phi(2170)$, then we choose to throw out events in the $p + \pi^+$, and $p + \pi^-$ choice of particle $i = 4$ with $\theta < G_1$. Cuts are then chosen to remove the other excited baryons using similar cuts; the effect of these cuts on the Monte Carlo samples are given in Table 4.7. The cuts are effective in cutting events with excited baryons (see $p + \pi^+$ mass plots before and after the van Hove cuts in Fig. 4.24) with the price of cutting up to $\sim 15\%$ of the desired signal events. The van

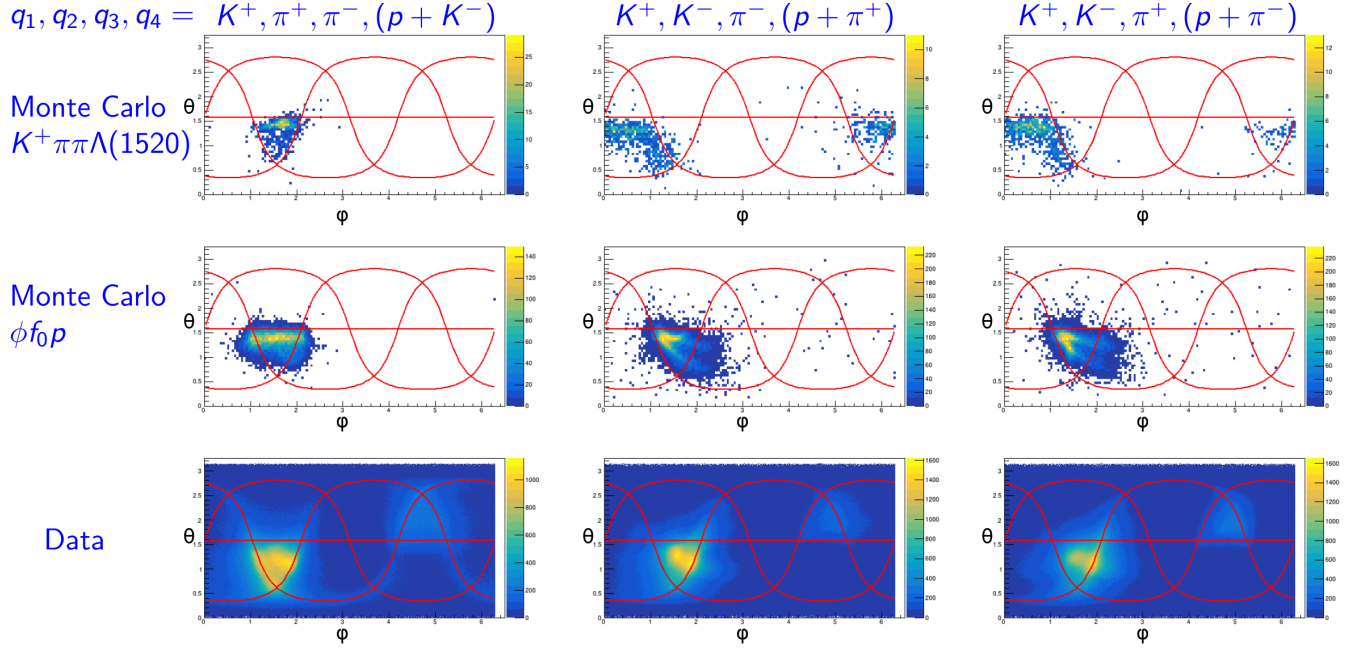


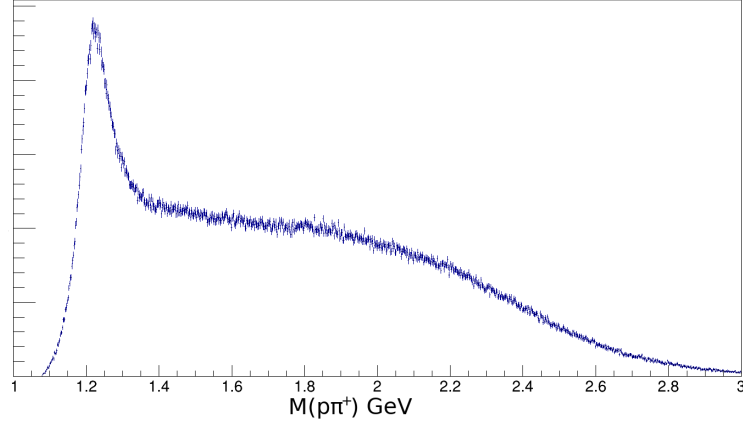
FIG. 4.23: Example of how the van Hove plot is used to differentiate different processes. The columns are for different pairs of particles being treated as the isobar. The columns (from top to bottom) histogram the events from a $\gamma p \rightarrow K^+ \pi^+ \pi^- \Lambda(1520)$ Monte Carlo sample, a $\gamma p \rightarrow \phi f_0 p$ Monte Carlo sample, and the data. If one wants to separate events with baryon excitation from ones without, one need only choose a region of this phase space only occupied by the desired events.

Hove cuts are applied going into the following section where the ϕ yields are shown and discussed.

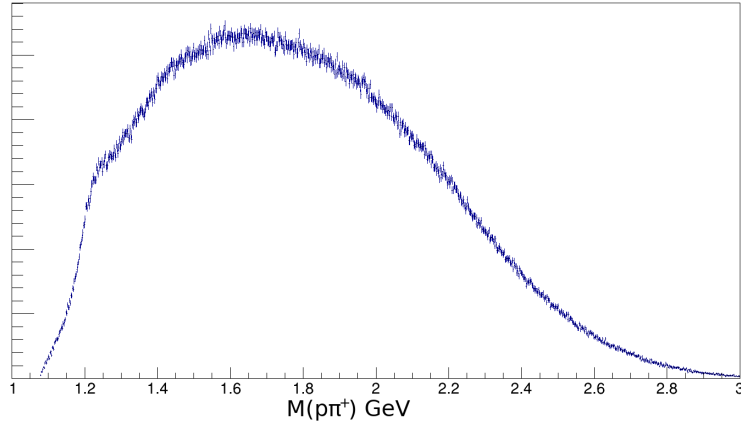
4.8.4 Yields

Following the methods used in Sections 4.4.2 and 4.6.2, ϕ yields as a function of $K^+ K^- \pi^+ \pi^-$ mass and $\pi^+ \pi^-$ are extracted to search for the $\phi(2170)$.

Fig. 4.25(a) shows the ϕ yield as a function of the $\pi^+ \pi^-$, where there is a enhancement near 0.8 and 1.0 GeV/c^2 . Comparing to Sec. 4.6.2, there do seem to be events consistent with $\gamma p \rightarrow \phi f_0(980)$, but there are too few to attempt to determine their distribution as a function of $K^+ K^- \pi^+ \pi^-$ invariant mass.



(a)



(b)

FIG. 4.24: An example of the efficacy of the van Hove cut. Top is the plot of the $p\pi^+$ mass before the Δ^{++} van Hove cut is applied, and (b) is a plot of the $p\pi^+$ mass after the cut. The line shape in the bottom shows that a large amount of the Δ^{++} peak is removed. The top plot is from a subset of the GlueX-I data and the bottom is from the whole GlueX-I data set, and so the Y-axis event counts are hidden to encourage the comparison of the line shape of each plot despite the sample size difference.

MC Sample	N^* vH Cut	$\Lambda(1520)$ vH Cut	Δ^{++} vH Cut
$K^+K^-\pi^-\Delta^{++}$	0.55 %	1.64 %	93.7 %
$K^+\pi^+\pi^-\Lambda(1520)$	5.00 %	93.6 %	3.12 %
$K^+K^-\pi^+N^*$	95.30 %	4.6%	5.91 %
$\phi(2170)p$	14.5 %	3.8 %	15.31 %

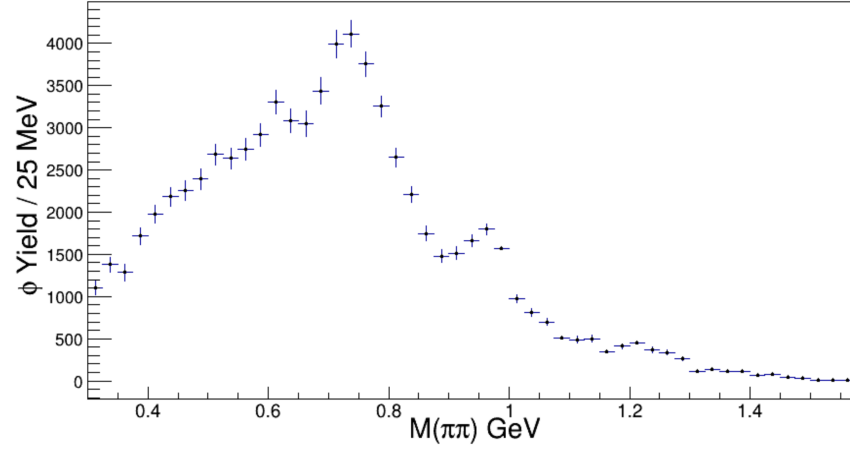
TABLE 4.7: Percent of event cut in van Hove Cut Study on Monte Carlo data. Cuts were defined similar to the example in Fig 4.23. The % value refers to the percentage of events cut from the specified sample.

The ϕ yield as a function of $K^+K^-\pi^+\pi^-$ in 4.25(b) does not show any clear resonant-like structure, although there seems to be some effect between 2.0 and 2.2 GeV/ c^2 that appears to look more like noise than structure. This noise could be caused by events with excited baryons that the van Hove cuts did not remove. It was learned from studying the Monte Carlo data that excited baryon events that survived the van Hove cuts also happened to lie in the region of $K^+K^-\pi^+\pi^-$ mass that we see noise in the ϕ yields. Whether the noise in the ϕ yield can be attributed to the inefficiencies of the van Hove cuts or not requires more study. Regardless of the source of the noise, the $\phi(2170)$ signal remains elusive in the GlueX-I data set.

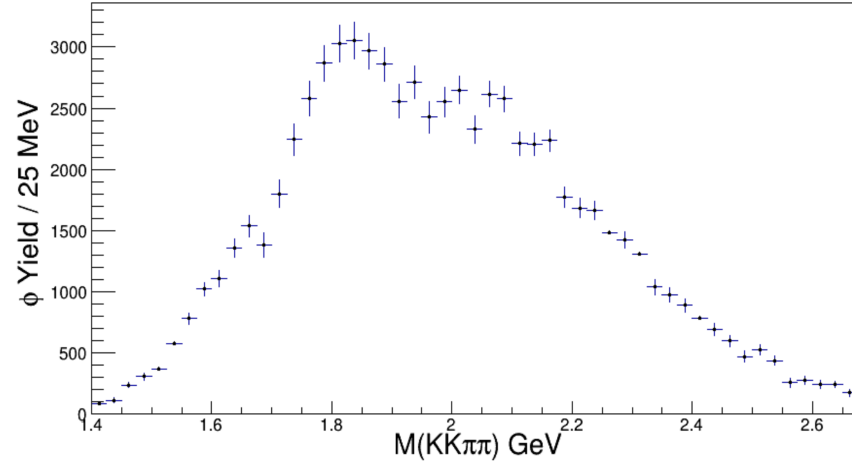
4.9 Discussion of Final State Surveys

From surveying the mass spectra of all three of the reactions, it is clear there is a rich variety of processes that produce these final states. Ultimately, none of the channels proved to yield a significant enhancement consistent with the $\phi(2170)$ in this search. All three of the reactions were too statistically limited to resolve any potential signal through calculating yields. The van Hove analysis in Sec. 4.8.3 showed the large amount of non t-channel backgrounds that dilute the search for the $\phi(2170)$ in the $K^+K^-\pi^+\pi^-p$ final state.

As discussed in Sec. 1.3, the thesis work of A. Hamdi [33] independently sought



(a)



(b)

FIG. 4.25: ϕ yields in $\gamma p \rightarrow K^+K^-\pi^+\pi^-p$. (a) is the ϕ yield as a function of $\pi^+\pi^-$ mass, and (b) is the yield as a function of $K^+K^-\pi^+\pi^-$ mass.

to measure the $\gamma p \rightarrow \phi(2170)p$ cross section in the $K^+K^-\pi^+\pi^-p$ final state in greater detail than the surveys presented here. The result in Ref. [33] was an upper limit on the photoproduction cross section. Therefore, the search for the $\phi(2170)$ in photoproduction awaits a larger data set in order to resolve the statistical and systematic uncertainties. The GlueX-II data set, with the DIRC upgrade, projects to increase the data set size by a factor 5 while also improving the π/K separation. The improved π/K separation will ideally decrease the systematic uncertainties in selecting the $K^+K^-\pi^+\pi^-p$ final state, and the improved statistics would answer whether the hints of the $\phi(2170)$ are real or not.

This analysis will now shift focus away from searching for peaks in mass distributions for the $\phi(2170)$ towards a deeper look at the excited kaons in the $K^+K^-\pi^+\pi^-p$ final state. To do this, events with a recoil $\Lambda(1520)$ (see 4.20) will be selected and a partial wave analysis of the $K^+\pi^+\pi^-$ system will be performed.

CHAPTER 5

Partial Wave Analysis Tools

The partial wave analysis of the reaction $\gamma p \rightarrow K^+ \pi^+ \pi^- \Lambda(1520)$ serves two purposes in the context of this work:

1. The $K^+ \pi^+ \pi^-$ system is the final state for numerous excited kaons which can be studied in the reaction.
2. Excited baryons are a large background when studying the 4-mesons system, $K^+ K^- \pi^+ \pi^-$, as discussed in Sec. 4.8 and need to be well understood to search for states like the $\phi(2170)$.

The known excited kaons that eventually decay to $K\pi\pi$ with mass below $1.6 \text{ GeV}/c^2$ are listed in Table 5.1 along with their widths, relevant decays, and relevant branching fractions. Its easily seen in Table 5.1 that in the mass range from $K\pi\pi$ threshold to $1.6 \text{ GeV}/c^2$ has several overlapping resonances with a variety of J^P quantum numbers that require a PWA to untangle. The $1.6 \text{ GeV}/c^2$ cut-off for the partial wave analysis was chosen for this analysis due to limited statistics, and also to avoid the need to include intermediate isobar decays involving higher-mass excited kaons that do not necessarily

Resonance	J^P	Mass (MeV)	Width (MeV)	Decay	Γ_i/Γ
$K(1460)$	0^-	1400 - 1482	250 - 335	$K\rho$	seen
				$K^*(892)\pi$	seen
$K_1(1270)$	1^+	1253	~ 100	$K\rho$	42%
				$K^*(892)\pi$	16%
$K_1(1400)$	1^+	1403	~ 175	$K^*(892)\pi$	94%
				$K\rho$	3%
$K^*(1410)$	1^-	1414	~ 230	$K^*(892)\pi$	>40%
				$K\rho$	< 7%
$K_2^*(1430)$	2^+	1427	~ 100	$K^*(892)\pi$	24%
				$K\rho$	8.7%
$K_2(1580)$	2^-	~ 1580	~ 110	$K^*(892)\pi$	seen

TABLE 5.1: Excited kaons with mass between 1.1 and 1.6 GeV/ c^2 with decays to $K^+\pi^+\pi^-$. Mass and width values come from the PDG averages [6]. All of the relevant decays are to a vector pseudoscalar pair.

follow the vector pseudoscalar decay model we wish to use from Sec. 1.4. The formalism for partial wave analysis was described in Sec. 1.4, and in this chapter will describe the tools used in the partial wave analysis of the reaction $\gamma p \rightarrow K^+\pi^+\pi^-\Lambda(1520)$.

5.1 Fitting with IU AmpTools

AmpTools is package of libraries developed by the experimental elementary particle physics group at Indiana University Bloomington for performing unbinned maximum likelihood fits using amplitude based models [63]. The GlueX collaboration maintains additional libraries used with AmpTools that contain amplitudes and other relevant factors developed for use in GlueX analyses that can be found in the HALLD_SIM repository on GitHub¹. The amplitudes in HALLD_SIM are used to construct the intensity function described in Sec. 1.4.3 and utilized in this analysis.

¹https://github.com/JeffersonLab/halld_sim

5.1.1 Extended Unbinned Maximum Likelihood

This section describes the unbinned maximum likelihood method used in AmpTools. For a given amplitude model, the real and imaginary components of the amplitudes are free parameters that are adjusted to find the best fit to the input data as possible using an intensity model. The intensity used in this analysis was first described back in Sec. 1.4.2, but it will be repeated here for convenience. The intensity function is

$$I(\Omega, \Phi) = 2\kappa \sum_{k=0,1} \left((1 - P_\gamma) \left[\left| \sum_{l,m} [J_l]_{m,k}^{(-)} \Im[Z_l^m(\Omega, \Phi)] \right|^2 + \left| \sum_{l,m} [J_l]_{m,k}^{(+)} \Re[Z_l^m(\Omega, \Phi)] \right|^2 \right] + (1 + P_\gamma) \left[\left| \sum_{l,m} [J_l]_{m,k}^{(+)} \Im[Z_l^m(\Omega, \Phi)] \right|^2 + \left| \sum_{l,m} [J_l]_{m,k}^{(-)} \Re[Z_l^m(\Omega, \Phi)] \right|^2 \right] \right), \quad (5.1)$$

where P_γ is the polarization fraction, the $[J_l]_{m,k}^{(-)}$ are the spin flip production amplitudes, and Z_l^m are the phase-rotated decay amplitudes. The Z_l^m amplitudes carry the angular dependencies that are fit, and in the case of a vector-pseudoscalar decay, they have the form

$$Z_l^m(\Omega, \Phi) \equiv X_l^m(\Omega) e^{-i\Phi},$$

$$X_m^l(\Omega, \Omega_H) = \sqrt{\frac{(2l+1)}{4\pi}} \sqrt{\frac{(2(1)+1)}{4\pi}} \sum_{\lambda_v} D_{m\lambda_v}^{J*}(\Omega) D_{\lambda_v 0}^{1*}(\Omega_H) (l 0 s \lambda_v | J \lambda_v). \quad (5.2)$$

Here, Φ is the angle between the beam polarization and the production plane, θ and ϕ are the angles of the decay products of the resonance, and θ_H and ϕ_H are the angles of the decay of the vector isobar.

The fit procedure using the AmpTools package relies on the unbinned maximum likelihood method to estimate the best parameters to describe the data with a given model. The likelihood function can also be used in model selection, see Sec. 5.2. The likelihood

function is a joint probability density function of making a set of observations given a model with a given set of parameters. In a simple form, the likelihood has the form [64]

$$\mathcal{L}(\mathbf{X}|\boldsymbol{\theta}) = \prod_{i=1}^N \mathcal{P}(X_i|\boldsymbol{\theta}), \quad (5.3)$$

where \mathbf{X} is the set of N observations/data points, $\boldsymbol{\theta}$ is a set of k model parameters, and $\mathcal{P}(X_i|\boldsymbol{\theta})$ is the probability density function (p.d.f.) of X_i given the model with parameters $\boldsymbol{\theta}$. The AmpTools package uses a form with a different normalization, or

$$\mathcal{L}(\mathbf{x}|\boldsymbol{\theta}) = \frac{e^{-\mu}\mu^N}{N!} \prod_{i=1}^N \mathcal{P}(x_i|\boldsymbol{\theta}). \quad (5.4)$$

where \mathbf{x} is a vector that describes the phase space of the reaction. In the case of this analysis, the vector \mathbf{x} is a 5-dimensional vector in the angular phase space $\{\Phi, \theta, \phi, \theta_H, \phi_H\}$ described in Sec 1.4.3. μ is the number of observed events predicted by the model and its parameters $\boldsymbol{\theta}$, [65]

$$\mu = \int \mathcal{I}(\mathbf{x};\boldsymbol{\theta})\eta(\mathbf{x}). \quad (5.5)$$

Here, $\mathcal{I}(\mathbf{x};\boldsymbol{\theta})$ is the intensity function in Eq. 5.1. $\eta(\mathbf{x})$ is the *efficiency* function that describes the fraction of events that will be detected and survive any event selection cuts at any point of kinematic phase space for the reaction. In AmpTools, μ is calculated using large Monte-Carlo samples that are passed through the GlueX detector simulation. If a Monte-Carlo sample of size M_g is generated, and M_a events survive the simulation and analysis cuts, the μ can be estimated by the average value:

$$\langle \mathcal{I}(\mathbf{x};\boldsymbol{\theta})\eta(\mathbf{x}) \rangle = \frac{1}{M_g} \sum_{i=1}^{M_a} \mathcal{I}(\mathbf{x};\boldsymbol{\theta}). \quad (5.6)$$

The p.d.f. \mathcal{P} can also be rewritten in terms of the intensity,

$$\mathcal{P} = \frac{1}{\mu} \mathcal{I}(\mathbf{x}; \boldsymbol{\theta}) \eta(\mathbf{x}). \quad (5.7)$$

Rather than compute and maximize the potentially large product in Eq. 5.4, it is advantageous to compute and minimize the value of $-2\ln\mathcal{L}(\boldsymbol{\theta})$ instead. $-2\ln\mathcal{L}(\boldsymbol{\theta})$ also happens to be a useful quantity in information theory which will be used in Sec. 5.2 [66]. Collecting all of the factors that do not depend on the parameters $\boldsymbol{\theta}$ into a constant (c) and using Eq 5.4, $-2\ln\mathcal{L}(\boldsymbol{\theta})$ becomes

$$-2\ln\mathcal{L}(\boldsymbol{\theta}) = -2 \left(\sum_{i=1}^N \ln \mathcal{I}(\mathbf{x}; \boldsymbol{\theta}) \eta(\mathbf{x}) - \int \mathcal{I}(\mathbf{x}; \boldsymbol{\theta}) \eta(\mathbf{x}) \right) + c. \quad (5.8)$$

5.1.2 Error Estimation

AmpTools uses the MINUIT package to minimize $-2\ln\mathcal{L}(\boldsymbol{\theta})$. In MINUIT, the errors on each parameter is the amount of variation of that parameter that increases $-2\ln\mathcal{L}(\boldsymbol{\theta})$ by 1, this corresponds to a $1; \sigma$ Gaussian uncertainty interval [6]. Investigations of the error in other analyses using AmpTools with high a dimensionality of the parameter space have suggested that these errors are greatly underestimated. The fit results presented in Chapter 6 are reported with these underestimated errors. Bootstrapping, a method in which parameter uncertainties are estimated by fitting numerous sets of resampled data, is suggested as the preferred method of determining parameter errors for future works [66].

5.2 Model Selection Techniques

In this section, a few different statistical methods for comparing the fit results of different models are discussed. These tests are:

1. Likelihood Ratio Test (LRT)
2. Akaike’s Information Criterion (AIC)
3. Bayesian Information Criterion (BIC)

One of the most difficult tasks in performing a partial wave amplitude analysis is model selection. In principle, the sum over partial wave amplitudes is an infinite sum, and all partial waves that are physically allowed should be included. In practice, the sum over partial waves must be truncated and so the question becomes what is the best truncated model to fit the data. The challenge that arises, is that different combinations of partial waves can both be good fits to the data but with very different inferences. To that end, the three tests chosen for this analysis all follow parsimonious principles, or stated another way, they prefer simple models over more complicated ones to avoid “over fitting” the data. With that being stated, it is still important that any model used is still well motivated by the underlying physics. The specific models these tests will be applied to are described in Sec. 6.3.

5.2.1 Likelihood Ratio Tests

The maximum likelihood method was described in Sec. 5.1.1 for parameter estimation, but the value of the maximum likelihood is not limited to that use. In information theory, the Kullback-Leibler (K-L) distance is a measure of the “distance” between two models [67]. The ratio of likelihoods of two models is fundamentally related to the K-L distance [66], and allows one to asses the relative quality of fit between the two models.

Wilks’ theorem provides a useful test statistic in evaluating the likelihood ratio of two models, assuming one model is nested in the other, ‘parent’ model. The relevant value is,

$$R = -2\ln(\mathcal{L}_0/\mathcal{L}), \tag{5.9}$$

where \mathcal{L}_0 is the maximum likelihood of the parent model, and \mathcal{L} is the maximum likelihood of the nested model. Wilks' theorem states that the value R is distributed by a χ^2 distribution in the limit that the data set goes to infinity. The χ^2 distribution has a mean equal to the difference in degrees of freedom between the two models of question. This allows a confidence level to be defined in the usual way with any χ^2 distribution to evaluate the significance of adding features to a model.

If the data set is sufficiently large, the χ^2 behavior of R will approximately hold, but if the data is overdispersed in the phase space, R will not be χ^2 distributed. This is potentially a concern with the analysis in this work. A comparison of models that are not nested is also needed. Given these concerns, R will be considered in model selection when applicable, but having other test statistics is necessary.

5.2.2 Akaike's Information Criterion

The K-L distance mentioned in the previous section requires full knowledge of the two models being compared. In 1973 Hirotugu Akaike proposed a criterion, known as Akaike's Information Criterion (AIC), to estimate the distance between a known model and the "full-reality" using the maximum value of the log likelihood [66]. The criterion statistic is given by

$$AIC = -2\ln(\mathcal{L}(\hat{\boldsymbol{\theta}})) + 2K, \quad (5.10)$$

where K is the number of free parameters, and $\hat{\boldsymbol{\theta}}$ is the set of parameters that maximize the likelihood of the model in question. AIC was derived from studying the relationship between the K-L distance and estimators of the K-L distance, but the full derivation is beyond the scope of this work.

The value of AIC is not a useful value in and of itself, but rather differences in AIC between two models fit to the same data set gives some indication of which model is better.

In effect, the model with the smallest AIC should have the smallest estimated distance to reality, and so one could select the model with the smallest AIC. By inspection, it can be seen that Eq. 5.10 has a penalty for increasing the number of parameters, keeping with the parsimonious principle of seeking the simplest possible model that describes the data.

5.2.3 Bayesian Information Criterion

In 1978, Gideon Schwarz introduced an information criteria using Bayesian arguments, now known as Bayesian Information Criterion (BIC) [68]. A subtle difference in the conceptual path of BIC from AIC is that there is an assumption that there exists a true model. The derivation will not be presented here, but the end result is a criterion that is similar in form to AIC. BIC is defined by the formula

$$BIC = -2\ln(\mathcal{L}(\hat{\boldsymbol{\theta}})) + K\ln(N), \quad (5.11)$$

where K is the number of free parameters, N is the number of observed events, and $\hat{\boldsymbol{\theta}}$ is the set of parameters that maximize the likelihood of the model in question [66].

Similar to AIC, the absolute value of the BIC for a model isn't relevant, but the lowest BIC value is preferred (assuming the same data set is fit with all models being considered). The penalty for adding parameters to a model is higher than in AIC, so of our criteria, BIC will prefer the simplest model with the fewest free parameters.

CHAPTER 6

PWA Fit Results

This chapter will discuss our partial wave analysis of the process $\gamma p \rightarrow K^+ \pi^+ \pi^- \Lambda(1520)$. The models used in this chapter are angular distributions of the form discussed in Sec. 1.4, but with a finite number of terms in the sum. The model is fit to the GlueX I data using the log likelihood method described in Chapter 5.

6.1 Event Selection

The data selection for this partial wave analysis begins with the same event selection and analysis cuts used in Sec. 4.7. The amplitudes described in Sec. 1.4.2 depend on the beam polarization, and we wish to enhance the dependence of the production mechanism on the polarization. Therefore, data taken with the amorphous radiator is not used and the beam energy is restricted to the coherent peak region (*i.e.* we require $8.2 \leq E_\gamma < 8.8$ GeV). Analyzing angular distributions for the process $\gamma p \rightarrow K^+ \pi^+ \pi^- \Lambda(1520)$ requires modelling, selecting on, or statistically subtracting background processes. For the analysis presented here, a side band subtraction was used in the pK^- mass distribution around the $\Lambda(1520)$. Future work on this analysis may be advised to model the background to include

Region	Lower $M(K^-p)$ Limit (GeV/c^2)	Upper $M(K^-p)$ Limit (GeV/c^2)	Value
Lower Side Band	1.4375	1.4705	-1
Signal Band	1.487	1.553	1
Upper Side Band	1.5695	1.6025	-1

TABLE 6.1: $\Lambda(1520)$ Side Band Subtraction Regions.

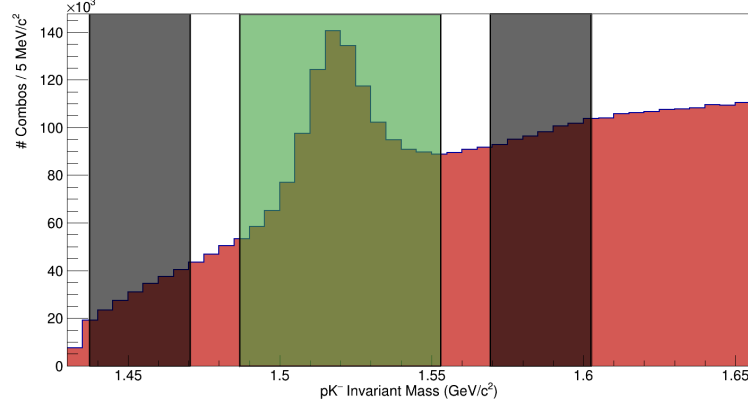


FIG. 6.1: pK^- invariant mass plot (red) with the signal region shaded in green and the side band regions shaded in black. For side band subtraction, the events in the signal region will be weighted with a value of 1, while events in the side band will be weighted with a value of -1.

in the partial wave model fits. The signal region is between 1.487 and 1.553 GeV/c^2 in pK^- mass, and there is a side band region on either side of the signal region with ranges (1.4375,1.4705) and (1.5695,1.6025) GeV/c^2 respectively, see Fig. 6.1. The side band and signal region ranges and weights are listed in Table 6.1. The mass distributions of the $K^+\pi^+\pi^-$, $K^+\pi^-$, and $\pi^+\pi^-$ after the side band subtraction are shown in Fig. 6.2, as well as the t' distribution.

6.2 Input/output tests with Monte-Carlo

Input/output tests are essential for determining the reliability of the PWA procedure. These studies rely on generating *signal* Monte Carlo, in which the amplitudes contributing

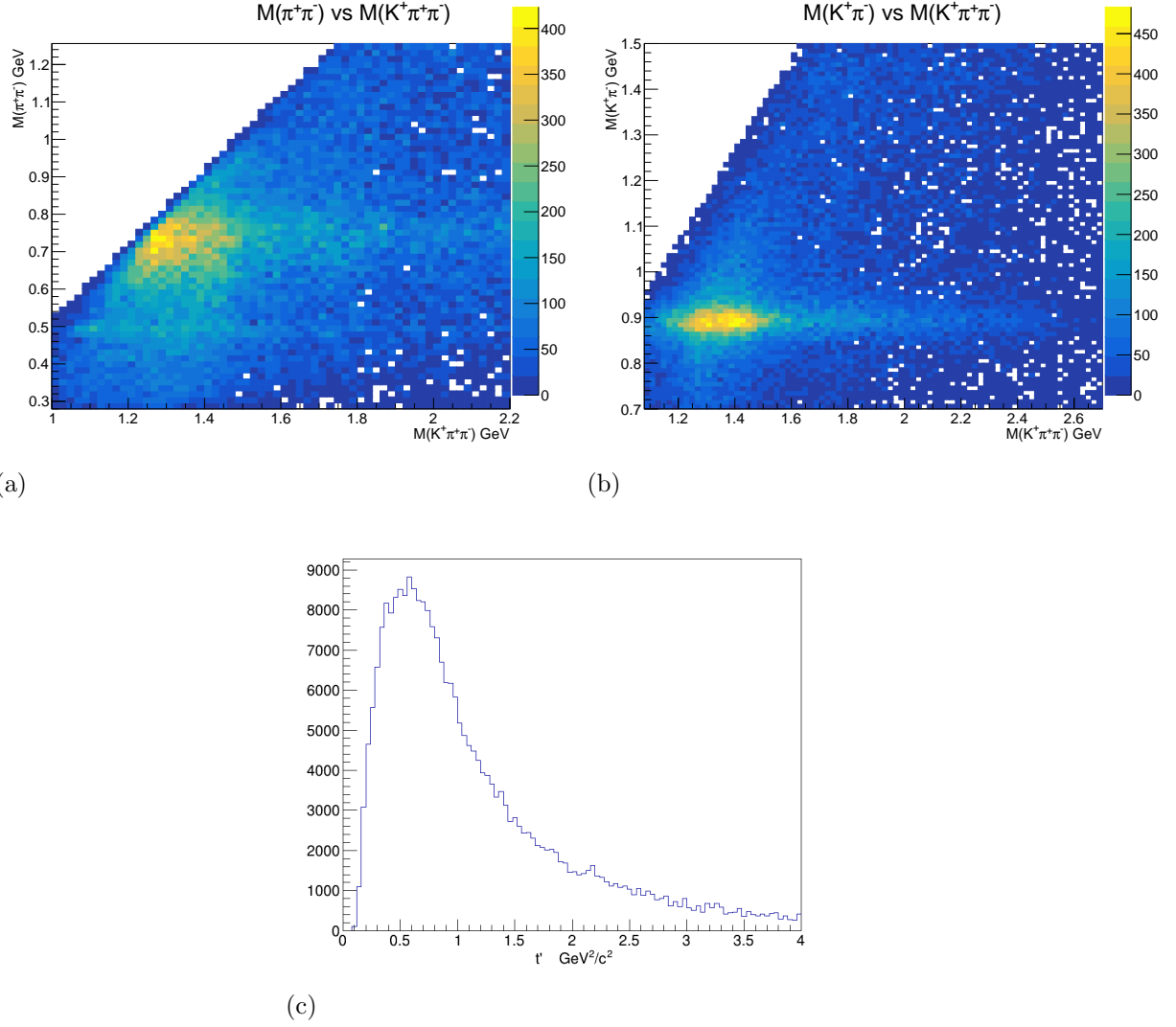
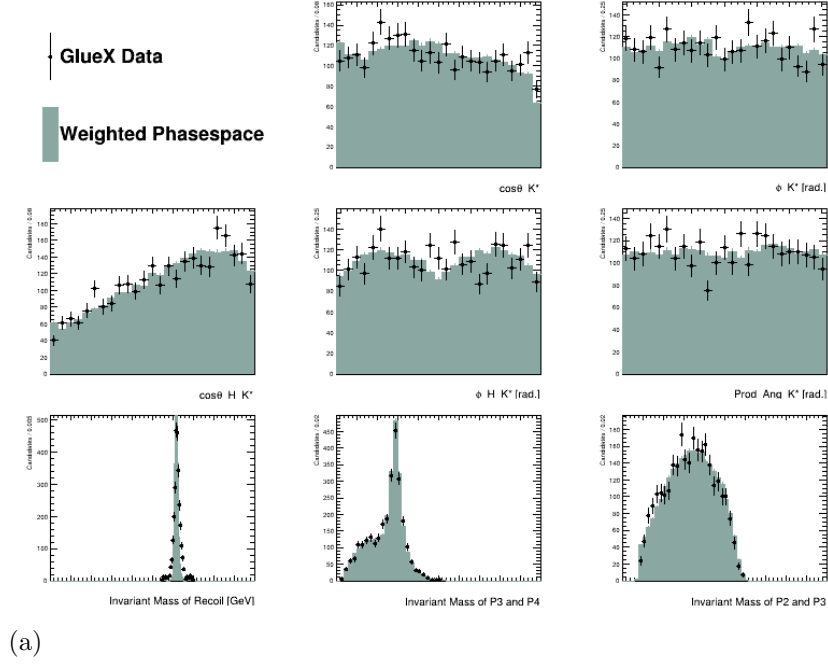


FIG. 6.2: After the $\Lambda(1520)$ side band subtraction, (a) $\pi^+\pi^-$ vs $K^+\pi^+\pi^-$ invariant mass, (b) $K^+\pi^-$ vs $K^+\pi^+\pi^-$ invariant mass, and (c) the t' distribution. The large peak in (a) corresponds to the ρ in the $\pi^+\pi^-$ mass. The large peak in (b) corresponds to the K^* in the $K^+\pi^-$ mass.

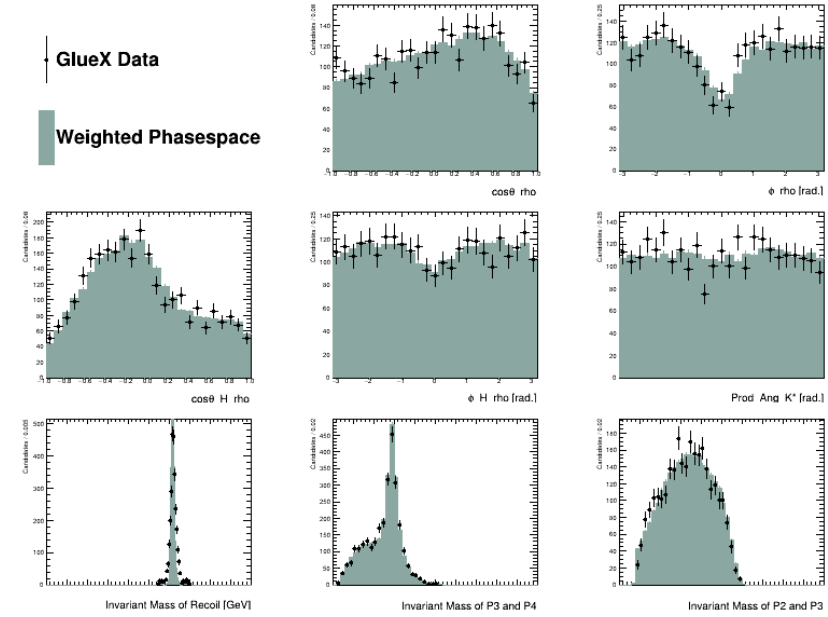
to the angular distributions are known. Then fits are performed with models using various combinations of amplitudes that may or may not be included in model used to generate the *signal* Monte Carlo. Some simple input/output tests are presented here as an example of this type of study in order to demonstrate the methods, as well as show what difficulties may be present in fitting the data.

6.2.1 Signal Monte Carlo Example

The signal Monte Carlo model sample presented in this section contains the amplitudes found in Table 6.2, and the relative strength among the amplitudes was based on a preliminary fit to the GlueX data with the same model. The 1^+ and 1^- amplitudes do not have any mass dependence built into the model, while the $\Lambda(1520)$, K^* and ρ are modelled using relativistic Breit-Wigner mass distributions with the PDG [6] masses and widths. The S and D wave decays in the 1^+ amplitudes are constrained to be the same ratio across all spin projections m for the two decays. 200 K events with $K^+\pi^+\pi^-$ invariant mass between 1.0 and 1.3 GeV/ c^2 were generated using an event generator that includes the appropriate beam properties, final state kinematics, and angular distributions (from the input model). The 200 K events were evenly distributed across the four possible beam polarization orientations, see Sec. 2.2. The generated events were then passed through the GlueX reconstruction software where the acceptance is simulated. Additionally, a 10 M event phase space sample was generated with a uniform mass and angular distribution model and passed through the same reconstruction simulation in order to correct for detector inefficiency as defined in Eq. 5.5.



(a)



(b)

FIG. 6.3: Plots of the angular distributions that are fit in the PWA I/O test. The black points here are signal Monte Carlo that is treated like the GlueX data, and the green histograms are phase space weighted by the model used to fit the data. In both (a) and (b), the top row is the $\cos\theta$ and ϕ of the vector isobar in the $K^+\pi^+\pi^-$ rest frame, the left two plots in the middle row are the $\cos\theta_H$ and ϕ_H of the decay of the isobar in the isobar rest frame, the right plot of the middle row is the production angle Φ , and the bottom row plots are the pK^- , $K^+\pi^-$, and $\pi^+\pi^-$ invariant masses. The angular distribution plots in (a) are shown as if the isobar decays to $K^+\pi^-$, and the plots in (b) are treated as if the isobar decays to ρK^+ .

(J^P)	L	Spin Projection (m)	Reflectivity	Decay	D/S constrained
1^+	0, 2	-1, 0, 1	$+, -$	$K^*\pi^+, \rho K^+$	✓
1^-	1	-1, 0, 1	$+, -$	$K^*\pi^+, \rho K^+$	N/A

TABLE 6.2: I/O Test signal Monte Carlo amplitudes.

Fitting With the Correct Model

As a reminder, the angular distributions in Sec. 1.4 of interest are Φ and $\Omega = (\theta, \phi, \theta_H, \phi_H)$, where Φ is the angle between the beam polarization and the production plane, θ and ϕ are the decay angles of the $K^+\pi^+\pi^-$ resonance, and θ_H and ϕ_H are the decay angles of the intermediate isobar, see Fig. 1.10. The angular distributions and results of fitting the signal Monte Carlo with the same model used to generate the Monte Carlo can be seen in fit diagnostic plots in Fig. 6.3. The black points in the plots of these angular distributions and invariant masses are from the signal Monte Carlo sample, and the green filled histograms are the phase space Monte Carlo weighted with the results of the model fit. For a fit that describes the data well, the weighted phase space histograms will match the data points. The diagnostic plots are split into two set of eight plots; one with the resonance decay angles calculated as if the first step of the decay chain is $X \rightarrow K^*\pi^+$, and one as if the decay chain is $X \rightarrow \rho K^+$. The two plots on the top row of each set of plots are the $\cos\theta$ and ϕ angular distributions of the direction of the K^* (ρ) in the $K^+\pi^+\pi^-$ rest frame. The middle row of the plots show the $\cos\theta_H$ and ϕ_H angular distributions of the direction of the π^- in the K^* (ρ) rest frame, as well as the production angle Φ (which is the same in both set of plots). The bottom row of plots in each set are the invariant mass spectra of the pK^- , $K^+\pi^-$, and $\pi^+\pi^-$ systems.

While the diagnostic plots in Fig. 6.3 show good agreement between the signal Monte Carlo angular and mass distributions and the fit results, its more important that the fit extracts the same relative strength of individual partial waves. The fraction of the total

$[J_m^P]^\epsilon$ L (VPs)	Model Frac.	Fit Frac.	$[J_m^P]^\epsilon$ L (VPs)	Model Frac.	Fit Frac.
$[1_1^+]^+ S (K^*\pi)$	0.00099	0.00095 ± 0.00103	$[1_1^+]^+ D (\rho K)$	0.02100	0.01944 ± 0.00497
$[1_1^+]^- S (K^*\pi)$	0.01462	0.01437 ± 0.00318	$[1_1^+]^- D (\rho K)$	0.04077	0.04346 ± 0.00508
$[1_0^+]^+ S (K^*\pi)$	0.01675	0.01844 ± 0.00630	$[1_0^+]^+ D (\rho K)$	0.03292	0.03106 ± 0.00541
$[1_0^+]^- S (K^*\pi)$	0.07053	0.06525 ± 0.00843	$[1_0^+]^- D (\rho K)$	0.02151	0.02248 ± 0.00441
$[1_{-1}^+]^+ S (K^*\pi)$	0.01469	0.01343 ± 0.00318	$[1_{-1}^+]^+ D (\rho K)$	0.04158	0.04029 ± 0.00728
$[1_{-1}^+]^- S (K^*\pi)$	0.00270	0.00265 ± 0.00148	$[1_{-1}^+]^- D (\rho K)$	0.00952	0.00884 ± 0.00237
$[1_1^+]^+ D (K^*\pi)$	0.00036	0.00033 ± 0.00036	$[1_1^+]^- P (\rho K)$	0.04590	0.05033 ± 0.01112
$[1_1^+]^- D (K^*\pi)$	0.00516	0.00500 ± 0.00110	$[1_1^+]^- P (\rho K)$	0.05527	0.05703 ± 0.00926
$[1_0^+]^+ D (K^*\pi)$	0.00652	0.00642 ± 0.00219	$[1_0^+]^+ P (\rho K)$	0.06247	0.05752 ± 0.00703
$[1_0^+]^- D (K^*\pi)$	0.02496	0.02271 ± 0.00293	$[1_0^+]^- P (\rho K)$	0.02271	0.02490 ± 0.00655
$[1_{-1}^+]^+ D (K^*\pi)$	0.00477	0.00467 ± 0.00110	$[1_{-1}^+]^+ P (\rho K)$	0.01896	0.01971 ± 0.00671
$[1_{-1}^+]^- D (K^*\pi)$	0.00100	0.00092 ± 0.00051	$[1_{-1}^+]^- P (\rho K)$	0.01528	0.0162 ± 0.00415
$[1_1^+]^+ S (\rho K)$	0.02258	0.0228 ± 0.00582	$[1_1^+]^+ P (K^*\pi)$	0.02680	0.02600 ± 0.00703
$[1_1^+]^- S (\rho K)$	0.04614	0.05098 ± 0.00596	$[1_1^+]^- P (K^*\pi)$	0.08844	0.09784 ± 0.01647
$[1_0^+]^+ S (\rho K)$	0.03519	0.03639 ± 0.00633	$[1_0^+]^+ P (K^*\pi)$	0.04151	0.03913 ± 0.00584
$[1_0^+]^- S (\rho K)$	0.02626	0.0263 ± 0.00517	$[1_0^+]^- P (K^*\pi)$	0.02828	0.02857 ± 0.00564
$[1_{-1}^+]^+ S (\rho K)$	0.04759	0.04725 ± 0.00853	$[1_{-1}^+]^+ P (K^*\pi)$	0.04500	0.04148 ± 0.00989
$[1_{-1}^+]^- S (\rho K)$	0.00952	0.01037 ± 0.00278	$[1_{-1}^+]^- P (K^*\pi)$	0.03131	0.03118 ± 0.01054

TABLE 6.3: Fractions of the intensity for the generating Model and the results of the fit to the Monte Carlo. The waves are named by their spin J, parity P, spin projection m, reflectivity ϵ , the relative angular momentum of its decay L, and the decay products V Ps.

intensity of each partial wave for the signal Monte Carlo is plotted in Fig. 6.4(a). The fraction of the PWA fit intensity using the same model as the signal Monte Carlo is plotted in Fig. 6.4(b), and the difference, or residual, of the model's intensity fractions and the fit intensity fraction is plotted in Fig. 6.4(c). The numerical values of model intensity fractions and the fit intensity fractions are given for every partial wave included in Table 6.3. The AmpTools fit, using the same model as the signal Monte Carlo, accurately determines which partial waves contribute to the intensity and which do not. In the next section an example of the performance of the PWA when a model is used that includes additional partial wave amplitudes that are not the signal Monte Carlo.

Fitting with a Model Containing Additional Amplitudes

In this section we give a single example of fitting the signal Monte Carlo sample with a model that contains partial wave amplitudes beyond than those included in the generation

(J^P)	L	Spin Projection (m)	Reflectivity	Decay	D/S constrained
1^+	0, 2	-1, 0, 1	$+, -$	$K^*\pi^+, \rho K^+$	✓
1^-	1	-1, 0, 1	$+, -$	$K^*\pi^+, \rho K^+$	N/A
2^+	2	-2, -1, 0, 1, 2	$+, -$	$K^*\pi^+, \rho K^+$	N/A

TABLE 6.4: I/O Test Fit Model Amplitudes

of the Monte Carlo sample. Many different models with various combinations of partial waves were studied on the same signal Monte Carlo sample in order to gain some intuition on the evaluation of a PWA fit and on the model selection used later in Sec. 6.3. The model used in this example includes the addition of $J^P = 2^+$ partial waves to the original model used to generate the signal Monte Carlo, see Table 6.4. This model was chosen as the example because it had the best model selection criteria (see Sec. 5.2) after the original model used to generate signal Monte Carlo, and the result provides insight into some potential problems in interpreting fits to the real data.

The diagnostic plots in Fig. 6.5 show that the $1^+1^-2^+$ model in Table 6.4 has good agreement with the 1^+1^- signal Monte Carlo sample. Ideally, using a $1^+1^-2^+$ model to fit the 1^+1^- signal Monte Carlo should result in a fit where all of the 2^+ amplitudes have contributions consistent with 0, and rest of the amplitudes having close to the same contribution as the original model. Fig. 6.6(b) and the residuals in Fig. 6.6(c), show that some of the 2^+ amplitudes have a fit fraction greater than zero and there are some significant disagreements in the fit fractions of other amplitudes; the numerical values are given in Table 6.5.

6.2.2 Test of Model Selection Criteria

With both fits to the signal Monte Carlo converging and both agreeing well with the signal Monte Carlo (see Figs. 6.3 and 6.5), but having disagreement among the relative fit fraction of some of the partial wave amplitudes, it is important to have a method of

$[J_m^P]^r$ L (VPs)	Model Frac.	Fit Frac.	$[J_m^P]^r$ L (VPs)	Model Frac.	Fit Frac.
$[1_1^+]^+ S (K^*\pi)$	0.001	0.00152 ± 0.0012	$[1_{-1}^-]^+ P (\rho K)$	0.01896	0.01938 ± 0.00562
$[1_1^+]^- S (K^*\pi)$	0.01462	0.0174 ± 0.00316	$[1_{-1}^-]^- P (\rho K)$	0.01528	0.01178 ± 0.00452
$[1_0^+]^+ S (K^*\pi)$	0.01675	0.02719 ± 0.0068	$[1_1^-]^+ P (K^*\pi)$	0.0268	0.01784 ± 0.00792
$[1_0^+]^- S (K^*\pi)$	0.07053	0.04853 ± 0.00634	$[1_1^-]^- P (K^*\pi)$	0.08844	0.09664 ± 0.0142
$[1_{-1}^+]^+ S (K^*\pi)$	0.01469	0.01044 ± 0.00274	$[1_0^+]^+ P (K^*\pi)$	0.04151	0.03907 ± 0.00536
$[1_{-1}^+]^- S (K^*\pi)$	0.0027	0.00022 ± 0.00037	$[1_0^+]^- P (K^*\pi)$	0.02828	0.02697 ± 0.00497
$[1_1^+]^+ D (K^*\pi)$	0.00036	0.00053 ± 0.00042	$[1_{-1}^-]^+ P (K^*\pi)$	0.045	0.05139 ± 0.01042
$[1_1^+]^- D (K^*\pi)$	0.00516	0.00605 ± 0.0011	$[1_{-1}^-]^- P (K^*\pi)$	0.03131	0.03793 ± 0.01015
$[1_0^+]^+ D (K^*\pi)$	0.00652	0.00946 ± 0.00237	$[2_2^+]^+ D (\rho K)$	0	0.00847 ± 0.00293
$[1_0^+]^- D (K^*\pi)$	0.02496	0.01689 ± 0.00221	$[2_2^+]^- D (\rho K)$	0	0.00134 ± 0.00112
$[1_{-1}^+]^+ D (K^*\pi)$	0.00477	0.00363 ± 0.00095	$[2_1^+]^+ D (\rho K)$	0	0.0092 ± 0.003
$[1_{-1}^+]^- D (K^*\pi)$	0.001	$7.70\text{E-}05 \pm 0.00013$	$[2_1^+]^- D (\rho K)$	0	0.00056 ± 0.00069
$[1_1^+]^+ S (\rho K)$	0.02258	0.0285 ± 0.00528	$[2_0^+]^+ D (\rho K)$	0	0.00328 ± 0.00214
$[1_1^+]^- S (\rho K)$	0.04614	0.05002 ± 0.00664	$[2_0^+]^- D (\rho K)$	0	0.00253 ± 0.00157
$[1_0^+]^+ S (\rho K)$	0.03519	0.03608 ± 0.00502	$[2_{-1}^+]^+ D (\rho K)$	0	0.00149 ± 0.00103
$[1_0^+]^- S (\rho K)$	0.02626	0.03384 ± 0.00557	$[2_{-1}^+]^- D (\rho K)$	0	0.00058 ± 0.00086
$[1_{-1}^+]^+ S (\rho K)$	0.04759	0.02761 ± 0.0063	$[2_{-2}^+]^+ D (\rho K)$	0	0.00094 ± 0.00094
$[1_{-1}^+]^- S (\rho K)$	0.00952	0.00912 ± 0.0037	$[2_{-2}^+]^- D (\rho K)$	0	0.00202 ± 0.00149
$[1_1^+]^+ D (\rho K)$	0.02101	0.0243 ± 0.0045	$[2_2^+]^+ D (K^*\pi)$	0	0.00139 ± 0.00149
$[1_1^+]^- D (\rho K)$	0.04077	0.04265 ± 0.00566	$[2_2^+]^- D (K^*\pi)$	0	0.00576 ± 0.00235
$[1_0^+]^+ D (\rho K)$	0.03292	0.0308 ± 0.00429	$[2_1^+]^+ D (K^*\pi)$	0	0.00056 ± 0.00079
$[1_0^+]^- D (\rho K)$	0.02152	0.02888 ± 0.00475	$[2_1^+]^- D (K^*\pi)$	0	0.00592 ± 0.00198
$[1_{-1}^+]^+ D (\rho K)$	0.04158	0.02354 ± 0.00537	$[2_0^+]^+ D (K^*\pi)$	0	$7.10\text{E-}05 \pm 0.00026$
$[1_{-1}^+]^- D (\rho K)$	0.00952	0.00777 ± 0.00315	$[2_0^+]^- D (K^*\pi)$	0	0.00115 ± 0.00101
$[1_1^-]^+ P (\rho K)$	0.0459	0.02772 ± 0.00497	$[2_{-1}^+]^+ D (K^*\pi)$	0	0.00011 ± 0.00029
$[1_1^-]^- P (\rho K)$	0.05527	0.04278 ± 0.00787	$[2_{-1}^+]^- D (K^*\pi)$	0	0.00038 ± 0.00069
$[1_0^-]^+ P (\rho K)$	0.06247	0.0698 ± 0.00711	$[2_{-2}^+]^+ D (K^*\pi)$	0	0.00102 ± 0.00115
$[1_0^-]^- P (\rho K)$	0.02271	0.03102 ± 0.00594	$[2_{-2}^+]^- D (K^*\pi)$	0	0.0012 ± 0.00113

TABLE 6.5: Fractions of the intensity for the generating Model and the results of the fit to the Monte Carlo using additional amplitudes. The waves are named by their spin J, parity P, spin projection m, reflectivity r, the relative angular momentum of its decay L, and the decay products vector V and pseudoscalar Ps.

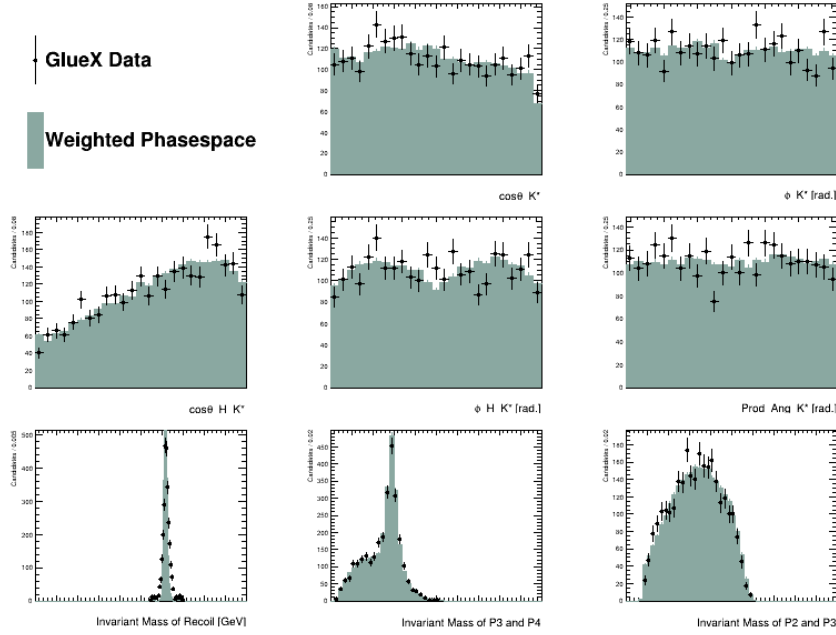


FIG. 6.5: Diagnostic plots showing the signal Monte Carlo sample as GlueX data in black, phase space Monte Carlo weighted by the model fit in green. From left to right, top to bottom, the plots are the $\cos\theta$, ϕ , $\cos\theta_H$, ϕ_H , Φ , pK^- mass, $K^+\pi^-$ mass, and $\pi^+\pi^-$ mass.

model selection that can select the best model among successful fits. The model selection criteria for the correct model, 1^+1^- , and the incorrect model, $1^+1^-2^+$, are listed in Table 6.6. The log likelihood ratio test (see Sec. 5.2.1) value, if both models are just as good at describing the data, should be $\overline{\chi^2} = 93 - 53 = 40$, up to a standard deviation of $\sqrt{2(93 - 53)} = 8.94$. The log likelihood ratio of 109.851 would imply that the 2^+ partial waves have a $\sim 12\sigma$ significance, and should be included. The AIC value should be the lowest for the best model, see Sec. 5.2.2, and so AIC in this case prefers the incorrect, $1^+1^-2^+$ model. Similarly, the BIC value should be the lowest for the best model, see Sec. 5.2.3, and the BIC value, in this case, correctly prefers the 1^+1^- model.

From studying fits to this signal Monte Carlo with the models presented here (as well as other models not presented here, including those missing amplitudes used to generate the signal Monte Carlo), the PWA of the $\gamma p \rightarrow K^+\pi^+\pi^-\Lambda(1520)$ reaction is best evaluated

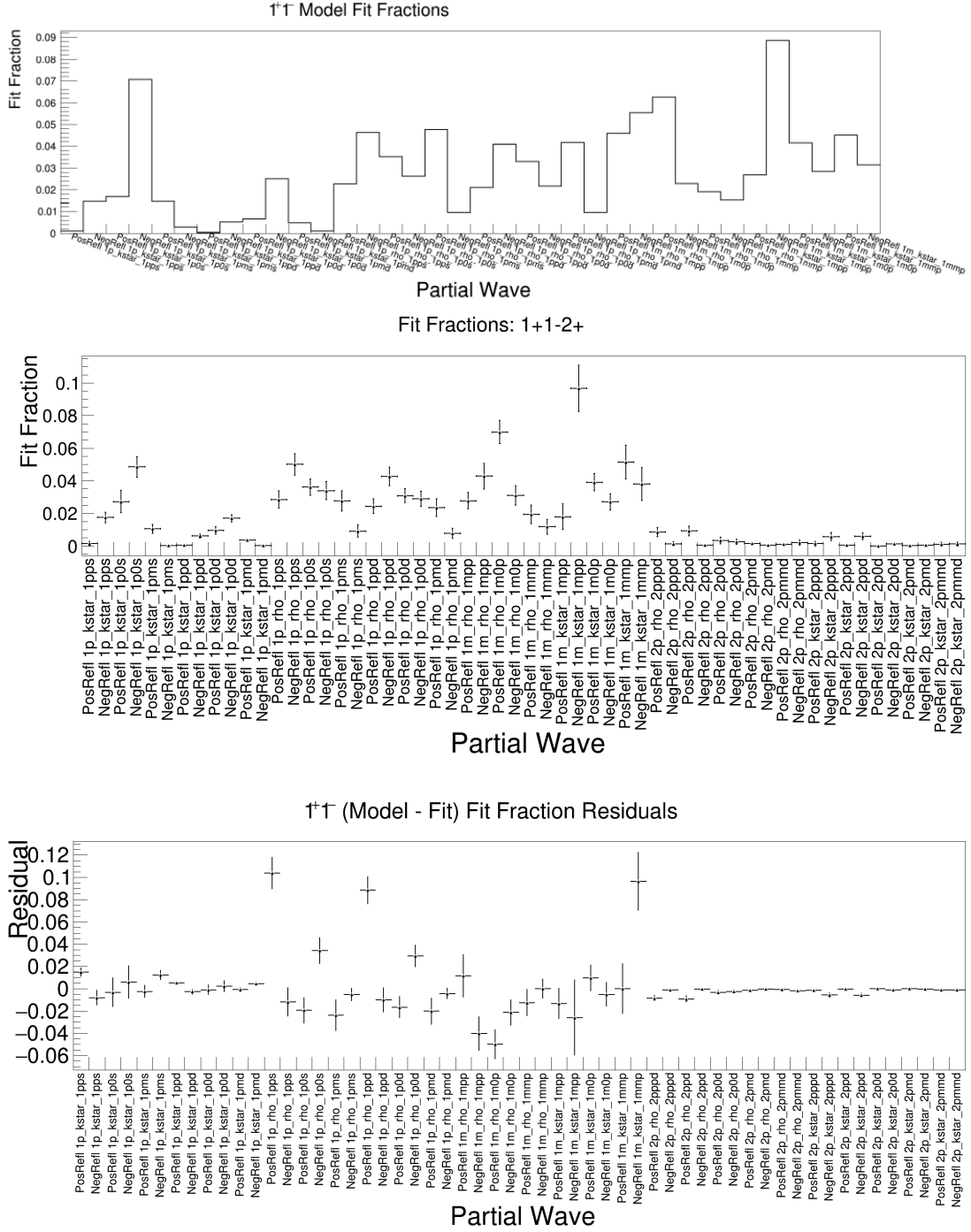


FIG. 6.6: Fractions of the total intensity for each individual amplitude in the (top) model used to generate the signal Monte Carlo and (middle) the results of the fit to the signal Monte Carlo with the same model. Plot (bottom) is the difference between plots on the top and in the middle.

Model	N.D.F.	$-2\ln(\mathcal{L})$	AIC	BIC
1^+1^-	53	-215865.287	-215759.287	-215372.82
$1^+1^-2^+$	93	-215974.581	-215788.894	-215110.754
Criteria				
$-2\ln(\mathcal{L}_{1^+1^-}/\mathcal{L}_{1^+1^-2^+})$	-	109.607	-	-
ΔAIC	-	-	29.607	-
ΔBIC	-	-	-	-262.066

TABLE 6.6: I/O Model Selection Criteria

using the BIC criterion. The BIC criterion has a stronger penalty for including degrees of freedom in the model, and so it is more capable of correctly identifying cases when unnecessary amplitudes have been added to the model (at least in these studies). When fits are done to the data, ideally all three criteria will agree as to which models are better than others, but in any case where they do not agree, the BIC value will be considered more heavily over the other criteria, based on these studies.

6.3 Model Selection in Fits to Data

This section will describe the process of selecting the best model to fit the GlueX-I data. As discussed in Sec. 5.2, its important to choose a set of possible models that are motivated by the underlying physics, and a balance between model simplicity and fit quality is to be optimized. With that in mind, the models that were selected fall within the well known J^P kaon amplitudes listed in Table 5.1. The models for which the fit converged (at least once in 20 attempts with random starting parameters) are listed in Table 6.7. All of the models are some combination of the amplitude included in *Model 12*, which has all of the known kaon $J^P + L$ with all combinations of decay, reflectivities, spin projections.

For model selection, all of the models were fit to the data in the mass and t range $1.0 < M(K^+\pi^+\pi^-) \leq 1.3 \text{ GeV}/c^2$ and $0.0 < t' \leq 2.0 \text{ GeV}^2/c^2$. The AIC and BIC are

Model	(J^P)	L	Spin Projection (m)	Reflectivity	Decay	D/S constrained
Model 1	1^+	0, 2	-1, 0, 1	$+, -$	$K^* \pi^+, \rho K^+$	\checkmark
	1^-	1	-1, 0, 1	$+, -$	$K^* \pi^+, \rho K^+$	N/A
Model 2	1^-	1	-1, 0, 1	$+, -$	$K^* \pi^+, \rho K^+$	N/A
	2^+	2	-2, -1, 0, 1, 2	$+, -$	$K^* \pi^+, \rho K^+$	N/A
Model 3	1^+	0, 2	-1, 0, 1	$+, -$	$K^* \pi^+, \rho K^+$	\checkmark
	2^+	2	-2, -1, 0, 1, 2	$+, -$	$K^* \pi^+, \rho K^+$	N/A
Model 4	1^+	0, 2	-1, 0, 1	$+, -$	$K^* \pi^+, \rho K^+$	\checkmark
	1^-	1	-1, 0, 1	$+, -$	$K^* \pi^+, \rho K^+$	N/A
	2^+	2	-2, -1, 0, 1, 2	$+, -$	$K^* \pi^+, \rho K^+$	N/A
Model 5	1^+	0, 2	-1, 1	$+, -$	$K^* \pi^+, \rho K^+$	\checkmark
	1^-	1	-1, 1	$+, -$	$K^* \pi^+, \rho K^+$	N/A
	2^+	2	-1, 1	$+, -$	$K^* \pi^+, \rho K^+$	N/A
Model 6	1^+	0, 2	-1, 0, 1	$+$	$K^* \pi^+, \rho K^+$	\checkmark
	1^-	1	-1, 0, 1	$+$	$K^* \pi^+, \rho K^+$	N/A
	2^+	2	-2, -1, 0, 1, 2	$+$	$K^* \pi^+, \rho K^+$	N/A
Model 7	1^+	0, 2	-1, 0, 1	$-$	$K^* \pi^+, \rho K^+$	\checkmark
	1^-	1	-1, 0, 1	$-$	$K^* \pi^+, \rho K^+$	N/A
	2^+	2	-2, -1, 0, 1, 2	$-$	$K^* \pi^+, \rho K^+$	N/A
Model 8	1^+	0, 2	0	$+, -$	$K^* \pi^+, \rho K^+$	\checkmark
	1^-	1	-1, 0, 1	$+, -$	$K^* \pi^+, \rho K^+$	N/A
	2^+	2	-2, -1, 0, 1, 2	$+, -$	$K^* \pi^+$	N/A
Model 9	1^+	0, 2	0, 1	$+$	$K^* \pi^+, \rho K^+$	\checkmark
	1^+	0, 2	1	$-$	$K^* \pi^+, \rho K^+$	\checkmark
	1^-	1	-1, 1	$+, -$	$K^* \pi^+$	N/A
	1^-	1	0, 1	$+$	ρK^+	N/A
	1^-	1	-1, 0	$-$	ρK^+	N/A
	2^+	2	1, 2	$+$	$K^* \pi^+$	N/A
	2^+	2	-1	$-$	$K^* \pi^+$	N/A
Model 10	1^+	0, 2	0, 1	$+$	$K^* \pi^+, \rho K^+$	\checkmark
	1^+	0, 2	1	$-$	$K^* \pi^+, \rho K^+$	\checkmark
	1^-	1	-1, 0	$+$	$K^* \pi^+$	N/A
	1^-	1	-1, 0, 1	$-$	$K^* \pi^+$	N/A
	1^-	1	0, 1	$+$	ρK^+	N/A
Model 11	1^+	0, 2	-1, 0, 1	$+, -$	ρK^+	\checkmark
	1^+	0, 2	-1, 0, 1	$+$	$K^* \pi^+, \rho K^+$	\checkmark
	1^+	0, 2	0, 1	$-$	$K^* \pi^+, \rho K^+$	\checkmark
	1^-	1	-1, 0, 1	$+, -$	$K^* \pi^+$	N/A
	1^-	1	0, 1	$+$	ρK^+	N/A
	1^-	1	-1, 0	$-$	ρK^+	N/A
	2^+	2	-2, -1, 0	$+$	$K^* \pi^+$	N/A
	2^+	2	1, 2	$-$	$K^* \pi^+$	N/A
	2^+	2	-1	$+, -$	ρK^+	N/A
Model 12	0^-	1	0	$+, -$	$K^* \pi^+, \rho K^+$	N/A
	1^+	0, 2	-1, 0, 1	$+, -$	$K^* \pi^+, \rho K^+$	\checkmark
	1^-	1	-1, 0, 1	$+, -$	$K^* \pi^+, \rho K^+$	N/A
	2^+	2	-2, -1, 0, 1, 2	$+, -$	$K^* \pi^+, \rho K^+$	N/A

TABLE 6.7: Fit Models for Data.

tabulated in Table 6.8. Based on the AIC and BIC values in Table 6.8, Model 11 is chosen as the best model (by BIC and nearly by AIC). Results of fits to the data using this model will be discussed in the following section.

Model	AIC	AIC Minimum	BIC	BIC Minimum
1	-261114	-	-260623	-
2	-257605	-	-257003	-
3	-261106	-	-260458	-
4	-261549	✓	-260688	-
5	-260229	-	-259757	-
6	-260334	-	-259872	-
7	-260588	-	-260125	-
8	-260650	-	-260122	-
9	-260920	-	-260550	-
10	-260829	-	-260542	-
11	-261420	-	-260846	✓
12	-260450	-	-259964	-

TABLE 6.8: AIC and BIC values for fits to data in the range $1.0 < M(K^+\pi^+\pi^-) \leq 1.3 \text{ GeV}/c^2$ and $0.0 < t' \leq 2.0 \text{ GeV}^2/c^2$.

6.4 Fit Results

Results of using Model 11 on Table 6.8 to fit the GlueX I data set are evaluated in this section. The fit was performed in 100 MeV-wide $K^+\pi^+\pi^-$ mass bins ranging from 1.1 to 1.6 GeV/c^2 in a single bin in t' from 0.0 to 2.0 GeV^2/c^2 . The binning was chosen to ensure that enough events were available in each mass bin, while also attempting to be narrow enough to see any mass-dependent structure. Diagnostic plots like the ones described in Sec. 6.2.1 for each fit in each of the mass bins are shown in Fig. 6.7. The diagnostic plots show reasonable agreement between the data and the fit results in all of the mass bins.

The acceptance corrected intensity extracted by the fit is shown in Fig. 6.8. Based on the properties of the known kaons listed in Table 5.1, the 1^- and the 2^+ intensities with

enhancement in the 1.2 - 1.3 GeV/ c^2 bin may be an indication that some of 1^+ amplitude from the $K_1(1270)$ is “leaking” into the other J^P amplitudes in that mass bin. The 1^+ and the 1^- amplitudes peaking in the 1.3 - 1.5 range is expected based on the $K_1(1400)$ and the $K^*(1410)$ masses and broad widths. The 2^+ amplitude is a small contribution to in the intensity; one may expect it to have a possible enhancement around the $K_2^*(1430)$ mass. In the following sections, the amplitudes contributing to the 1^+ and 1^- intensities will be explored (the total 2^+ intensity is too small to justify looking at the contributing amplitudes).

6.4.1 1^+ amplitudes

The 1^+ amplitudes can be decomposed either by their decay mode or by the reflectivity, which is shown in Fig. 6.9. Figs. 6.9(a) and 6.9(b) show the intensities of the $1^+ \rightarrow \rho K^+$ and $1^+ \rightarrow K^* \pi^+$ respectively. Figs. 6.9(c) and 6.9(d) show the positive and negative 1^+ intensities. All of the plots in 6.9(a) peak around 1.4 GeV/ c^2 . There is a lack of any enhancement in these amplitudes from the $K_1(1270)$ which one might expect based on the known kaon spectrum. Furthermore, the branching ratios of the $K_1(1400)$ to ρK (3%) and $K^* \pi$ (94%) would give the expectation that the $K^* \pi$ intensity would be much larger than the ρK , but this is not the case in these results. Comparing the contributions from the two reflectivities, these results imply that the 1^+ amplitude is produced through a relatively equal amount of natural (*e.g.* K^{*-}) and unnatural (*e.g.* K^-) exchange mechanisms. The presence of both natural and unnatural exchange is not unreasonable given the large range of t used in this analysis.

6.4.2 1^- amplitudes

Similarly to the previous section, this section looks at the contributions of the two decay modes and the two reflectivities to the 1^- intensity. Figs. 6.10(a) and 6.10(b) show the intensities of the $1^+ \rightarrow \rho K^+$ and $1^+ \rightarrow K^* \pi^+$, and Figs. 6.9(c) and 6.9(d) show the positive and negative 1^- reflectivity intensities. The ρK intensity is enhanced in both the 1.2-1.3 and the 1.4-1.5 GeV/ c^2 mass bins. Again, the enhancement of the ρK intensity near 1.2 GeV/ c^2 is possibly due to events from a $K_1(1270)$, a 1^+ state, being fit as 1^- events. With the available binning, the $1^- K^* \pi$ intensity does not show any clear enhancement, though the expected 1^- state is expected to have a width of 230 MeV/ c^2 . The relative strength of the 1^- reflectivity intensities imply that, like in the 1^+ amplitude, the 1^- is produced through both unnatural and natural exchange mechanisms. The positive reflectivity intensity has a dip in the same bin that the 1^+ positive reflectivity peaks perhaps also suggesting leakage.

6.4.3 Unaccounted-for Systematic Errors

The errors reported on the results in the previous sections in this chapter are those calculated by AmpTools, see Sec. 5.1.2, and are likely underestimated. In addition to reevaluating the fit errors using bootstrapping, there are many possible sources of systematic errors that have not yet been accounted for in this analysis. Further studies on these systematics need to be performed in order to give a more accurate account of the uncertainty of these results.

The effect of event selection on the performance of the PWA could be studied in more detail and quantified. Any of the event selection could also be systematically varied in order to estimate their effect on the PWA results. Studies were done on the effect of misidentifying the K^+ as the π^+ (and vice versa) on the reliability of the PWA in

I/O tests. It was determined in studies of signal Monte Carlo that around 10-15% of the combos that survive all the cuts have the wrong π^+/K^+ identification, and that this can have a noticeable effect on the PWA results. A systematic study with Monte Carlo where the fraction of combos with misidentified particles can be controlled would indicate quantitatively how these combos effect the results. Additionally, a choice of signal and side band regions for the $\Lambda(1520)$ background subtraction introduce another possible source of systematic error. Varying the signal and side band regions or comparing side band subtraction to other methods of background suppression is another useful systemic study to be considered.

The maximum log likelihood method used in AmpTools relies on accurate Monte Carlo simulation of the GlueX detector in order to correct for the acceptance in Eq 5.8. Systematic studies on how mismatches between data and simulation effect the PWA results, as well as determine how large the mismatches could be, would allow these uncertainties to be quantified.

Quantifying the uncertainties from model selection would be difficult given the number of amplitudes/combinations to choose from. There were also assumptions made about the spin behavior of the $\Lambda(1520)$ in deriving the form of the intensity in Eq. 1.32. Whether or not this assumption is valid or its effect on the results presented in this chapter have not been studied.

6.4.4 PWA conclusions

The largest uncertainty in this partial wave analysis lies in the model selection and/or ambiguities among the amplitudes used to construct the models. Another possible improvement may be to introduce a dependence on the $K^+\pi^+\pi^-$ mass in the amplitudes rather than performing a mass-independent fit. Mass dependent fits have been used in

other reactions being analysed in GlueX. Several other sources of systematic errors that have not been accounted for and possible studies to address them were discussed in the previous section.

Ultimately, the model chosen through the information criteria fits the data distributions well, as seen in Fig 6.7. The $K_1(1270)$, $K_1(1400)$, $K^*(1410)$, and $K_2^*(1430)$ with mass(width) in MeV of 1253(100), 1403(175), 1410(230), and 1427(1000) are broad overlapping resonances. With the wide mass binning, a claim of observation and extraction of the properties of any of these resonances cannot be done. The 1^+ and 1^- amplitudes do show some enhancement in the ~ 1400 MeV/ c^2 region as expected, but no well defined structures can be identified.

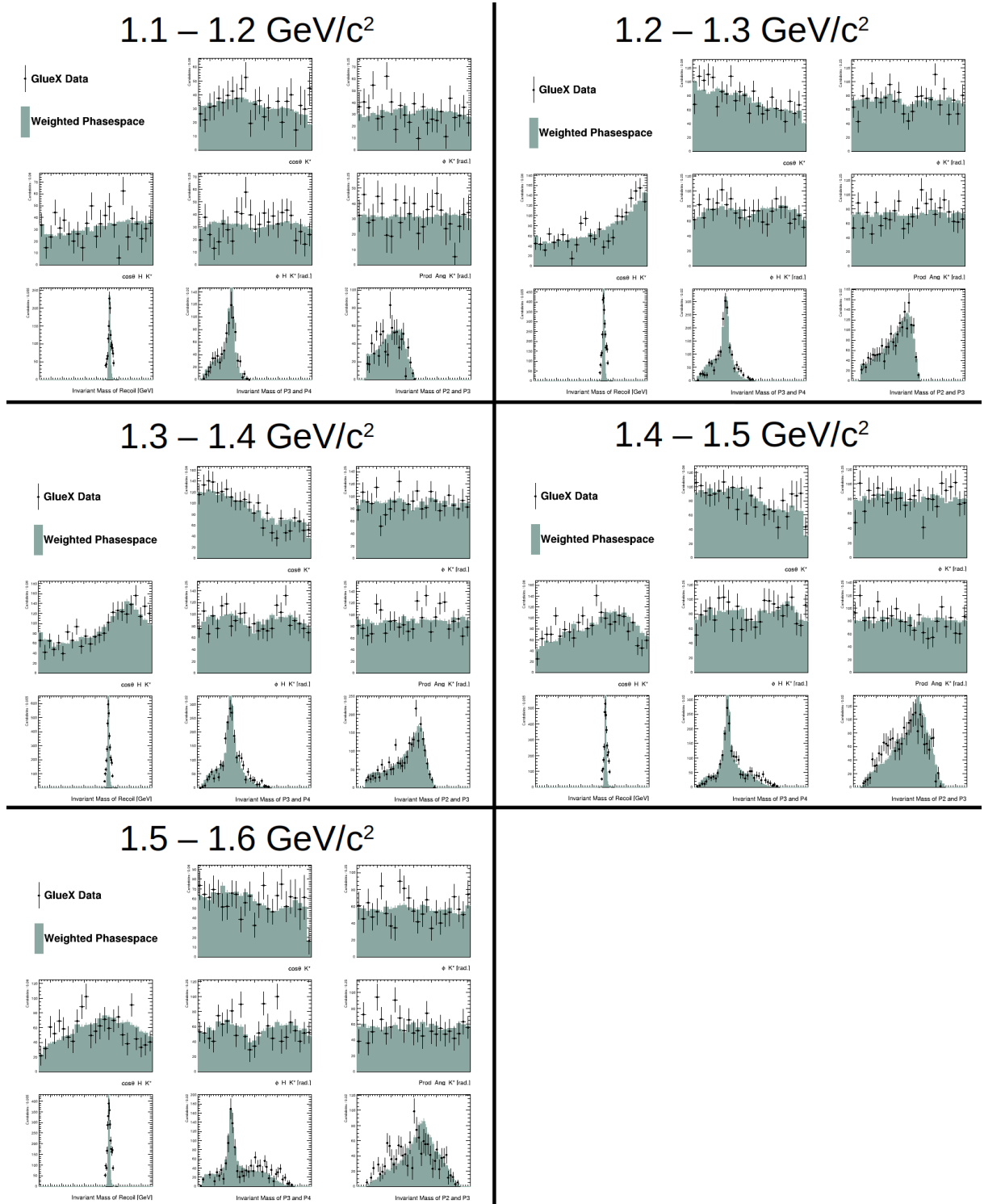


FIG. 6.7: Plots of the GlueX data and phase space Monte Carlo weighted by PWA Model 11 fit to the data in 100 MeV/c^2 -wide $K^+\pi^+\pi^-$ mass bins. The plots are of the angular distributions relevant to the partial wave model and intermediate mass distributions.

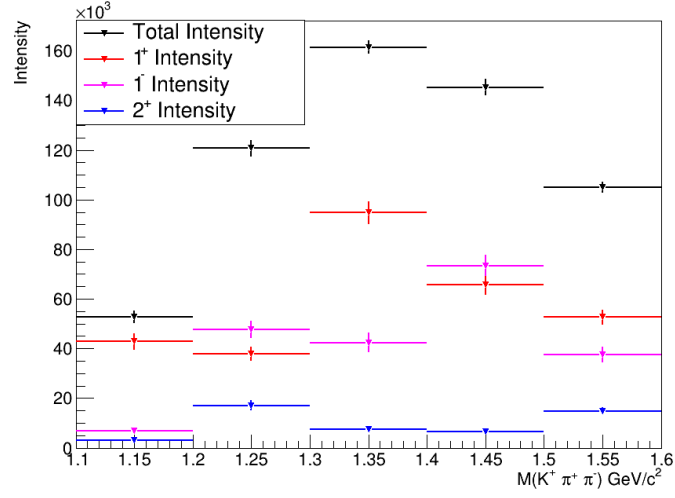


FIG. 6.8: Plot of the total, 1^+ , 1^- , and 2^+ intensities. These intensities are extracted from the results of fitting Model 11 to the GlueX I data.

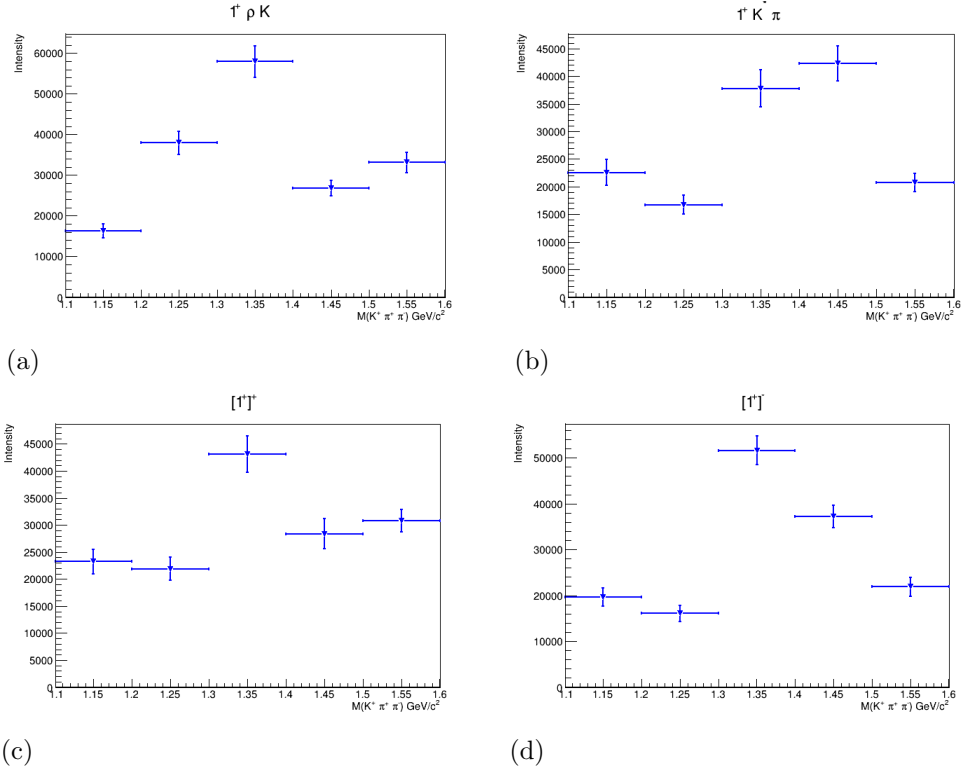


FIG. 6.9: Amplitudes contributing to the 1^+ amplitude: (a) The $1^+ \rho K$ intensity, (b) The $1^+ K^* \pi$ intensity, (c) the 1^+ positive reflectivity intensity, and (d) the 1^+ negative reflectivity intensity.

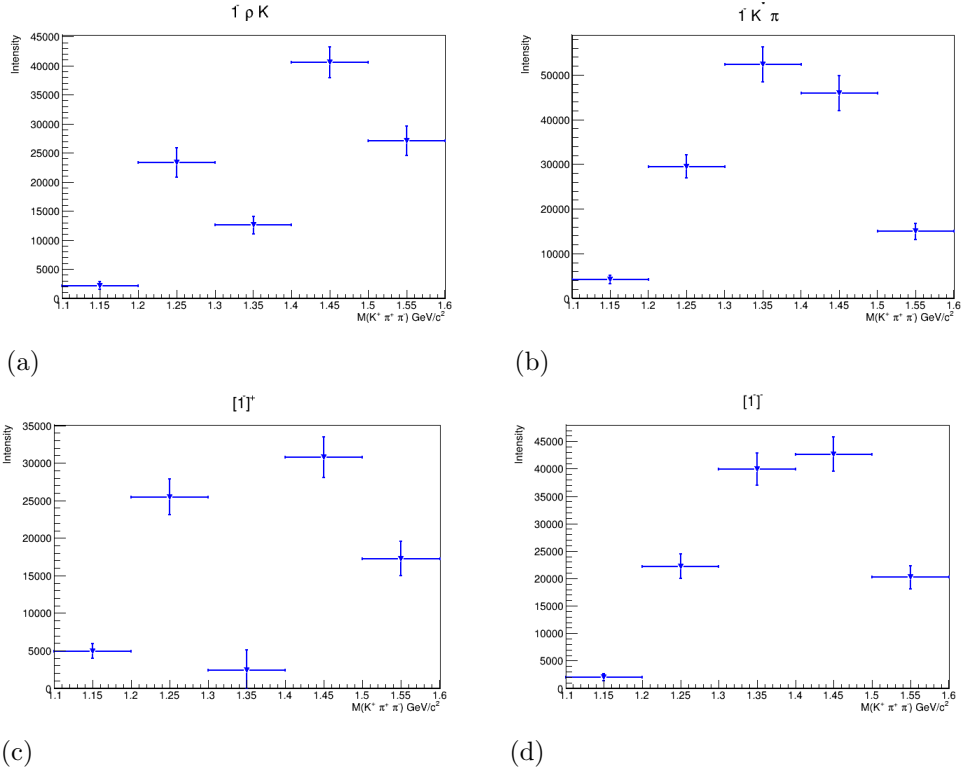


FIG. 6.10: Amplitudes contributing to the 1^- amplitude: (a) The $1^- \rho K$ intensity, (b) The $1^- K^* \pi$ intensity, (c) the 1^- positive reflectivity intensity, and (d) the 1^- negative reflectivity intensity.

CHAPTER 7

Summary and Discussion

7.1 Summary

Hadron spectroscopy stands as an important field of study in the larger endeavor to understand strong nuclear interactions. The GlueX experiment collected a world-leading photoproduction data set with just its first phase of data collection (2016-2018), with an integrated luminosity of $\sim 125 \text{ pb}^{-1}$ in the coherent peak region. The second phase of GlueX has not completed is data taking, but in 2020 alone the second phase more than doubled the integrated luminosity of the entire GlueX I data set. The contribution to the understanding of light hadron spectroscopy in the coming years should be significant. Presented in this dissertation are the contributions to the GlueX DIRC upgrade, exploratory analyses of the $\gamma p \rightarrow K^+ K^- \pi^+ \pi^- p$, $\gamma p \rightarrow K^+ K^- \pi^0 \pi^0 p$, $\gamma p \rightarrow K^+ K^- \pi^0 \eta p$ reactions, and a partial wave analysis of the reaction $\gamma p \rightarrow K^+ \pi^+ \pi^- \Lambda(1520)$.

The GlueX DIRC upgrade was presented in Chapter 3. The GlueX DIRC was commissioned in 2019, ahead of the start of GlueX II. In GlueX I, the π/K separation was provided by the Time-of-Flight system to yield $\sim 3\sigma$ for particle momentum $\sim 2 \text{ GeV}/c^2$,

and pions and kaons were indistinguishable if their momentum was much larger than that. The GlueX DIRC uses Cherenkov radiation to increase the 3σ identification confidence up to $3.7 \text{ GeV}/c^2$. The multi-anode photomultiplier tubes were the main focus of this work. The MAPMT modules were bench-tested using pulsed laser light. The bench tests were used to characterize all of the pixels in every MAPMT. The characterization information was used to gain-match the pixels in order to create a uniform response across the entire MAPMT plane. A method of gain matching was developed to use LED pulser data, so that modules can be switched out and calibrated without returning to bench tests.

In Chapter 4, the exploratory analyses of the $\gamma p \rightarrow K^+ K^- \pi^+ \pi^- p$, $\gamma p \rightarrow K^+ K^- \pi^0 \pi^0 p$, $\gamma p \rightarrow K^+ K^- \pi^0 \eta p$ reactions sought evidence of the $\phi(2170)$ (or an isovector partner to the $\phi(2170)$ in $\gamma p \rightarrow K^+ K^- \pi^0 \eta p$). The search for features in the invariant mass spectra in these reactions showed a rich variety of intermediate states that contributed to these reactions. The $\phi(2170)$ was not observed in any of these analyses. If the $\phi(2170)$ is produced in photoproduction, the cross section must be small or have interference with some other process. The GlueX II data set would either allow the observation of the $\phi(2170)$ (with the advantage of better π/K separation), or provide a stringent upper limit on the photoproduction cross section.

The partial wave analysis in Chapter 6 of $\gamma p \rightarrow K^+ \pi^+ \pi^- \Lambda(1520)$ is the first measurement of this reaction. In the mass range the PWA was performed, there could be contributions from the $K_1(1270)$, $K_1(1400)$, $K^*(1410)$, and $K_2^*(1430)$ resonances. Model selection was done using information criteria and input/output studies with signal Monte Carlo samples. The model that was selected by the information criteria was used to fit the GlueX I data in 100 MeV wide mass bins with a t range of $(0.0, 2.0) \text{ GeV}^2/c^2$. The fits to the data had good agreement in all of the relevant angular distributions. The PWA turned out to be too statistically limited to identify any structure in the results. A number of systematic error studies were proposed for future work. The inclusion of the GlueX II

data may allow the PWA to be done in finer bins of mass and/or t . This work provides an important background model for a $K^+K^-\pi^+\pi^-$ amplitude analysis to more directly search for the $\phi(2170)$ in a PWA of the $\phi\pi^+\pi^-$ system.

7.2 Discussion

7.2.1 On the Search for the $\phi(2170)$

As discussed in Sec. 1.2.2, there are many types of states beyond the traditional $q\bar{q}$ mesons and qqq ($\bar{q}\bar{q}\bar{q}$) baryons (anti-baryons). The XYZ states that have been observed in bottom and charm factory experiments provide strong evidence for states beyond the constituent quark model. As an example, the $Y(4260)$ was discussed, a vector meson in the $c\bar{c}$ spectrum's mass range. The vector mesons predicted by the quark model with similar masses to the $Y(4260)$ in the $c\bar{c}$ spectrum had already been well-established experimentally when the $Y(4260)$ was first observed. This made the $Y(4260)$ a compelling state to study our understanding of hadrons. The recent results that the $Y(4260)$ was a structure with two contributors, the $Y(4220)$ and the $Y(4230)$, only further motivates the study of these states new states.

The GlueX experiment does not have the beam energy to produce states in the excited charmonium spectrum, but instead we focused on another state that had been observed in e^+e^- collider experiments, the $\phi(2170)$. The $\phi(2170)$ was first observed in a similar reaction to the $Y(4260)$ (*i.e.* $e^+e^- \rightarrow \gamma_{ISR}\phi(2170) \rightarrow \gamma_{ISR}\phi\pi^+\pi^-$ vs. $e^+e^- \rightarrow \gamma_{ISR}Y(4260) \rightarrow \gamma_{ISR}J/\psi\pi^+\pi^-$), and so the $\phi(2170)$ has been investigated as a strangeonium analogue to the $Y(4260)$. If there exist strangeonium analogues to the XYZ states in the charmonium spectrum, then the $\phi(2170)$ may also be multiple states contributing to it as in the case of the $Y(4260)$. In turn, studying the strangeonium spectrum may help to better understand

the complicated charmonium spectrum. It could also be that the $\phi(2170)$ is the $\phi(3S)$ predicted by the quark model that had yet to be observed like many of the excited $s\bar{s}$ states also predicted by the quark model.

Due to the *vector dominance* model of photoproduction, it was thought that the GlueX experiment would be an ideal experiment to produce and study the $\phi(2170)$. The non-observation of the $\phi(2170)$ with the available statistics could imply that either the $\phi(2170)$ does not couple to photoproduction with a proton target, or that $\phi(2170)$ photoproduction interferes with some other process. In the first case, the lack of coupling to photoproduction could potentially offer constraints on the interpretation of the $\phi(2170)$ that would require significant theoretical work to fully understand. The case that some other process is interfering with the production of the $\phi(2170)$ further motivates the desire to pursue a partial wave analysis of the $\phi\pi\pi$ in future work.

7.2.2 On the Excited Kaon Spectrum

The partial wave analysis of the $\gamma p \rightarrow K^+\pi^+\pi^-\Lambda(1520)$ reaction had two motivations. The first motivation was to study the excited kaon states that decay to $K^+\pi^+\pi^-$, and the second was to determine a model for one of the excited baryon backgrounds that are needed in order to pursue a partial wave analysis of the $\gamma p \rightarrow K^+K^-\pi^+\pi^-p'$ reaction.

Concerning the second motivation, the partial wave analysis conducted here selected a model that could accurately model the relevant angular and mass distributions. This model is not required to be physically accurate in describing the excited kaon spectrum to be a useful model to describe the $\Lambda(1520)$ background in a future $\gamma p \rightarrow K^+K^-\pi^+\pi^-p'$ partial wave analysis. The tools and methods applied here may also be readily adapted to model the other excited baryon backgrounds in this reaction such as $\gamma p \rightarrow K^+K^-\pi^-\Delta^{++}$.

Concerning the first motivation, we have determined that the GlueX-I data set (taken

between 2017 and 2018) had insufficient statistics to extract information about excited kaon resonances decaying to $K^+\pi^+\pi^-$ from a partial wave analysis. Due to this lack of statistics, we are unable to make any statement on the properties of the excited kaons or the production mechanisms present in the experiment.

7.2.3 Outlook

As mentioned in the summary in Sec. 7.1, GlueX II has already begun taking data with the GlueX DIRC upgrade. The increased statistics and the additional π/K separation will be vital to furthering the analysis of the reactions studied in this work. If the $\phi(2170)$ continues to elude observation in photoproduction, upper limits should be set on the cross section to further constrain models that seek to understand the $\phi(2170)$. It would also be interesting to study the charmonium spectrum in a higher energy photoproduction experiment. It would be interesting to know if the $Y(4260)$ also has a small or non-existent coupling to photoproduction similar to the $\phi(2170)$ in order to test if they are truly analogues of each other. Cross sections of several XYZ states produced in photon-induced processes has been estimated in Ref. [69]. The photoproduction of XYZ states could be done at the planned Electron-Ion Collider (see Ref. [70]) or an upgraded CEBAF with double the current beam energy.

APPENDIX A

Rest Frames

A.1 Center of Mass frame

The Center of Mass (CoM) frame chosen such that $\vec{p}_\gamma + \vec{p}_p = 0$. The boost from the lab frame is done along the z-axis (beam direction).

A.1.1 t' Definition

In reactions such as Eq. 1.15 in the CoM frame, it is useful to define the quantity

$$t' = -t + t_{min}, \quad (\text{A.1})$$

where t is Mandelstam t (Eq. 1.16) and t_{min} is the minimum t for the nucleon to recoil. t_{min} is defined for a reaction such as Eq. 1.15 as

$$|t_{min}| = |m_X^2 - 2E_\gamma^*(E_X^* - p_X^*)|. \quad (\text{A.2})$$

E_γ is calculated from measured quantities using

$$E_\gamma^* = \frac{(s - m_N^2)}{2\sqrt{s}}, \quad (\text{A.3})$$

where $s = (p_X + p_N)^2$ is Mandelstam s , and m_N is the invariant mass of the recoil nucleon.

E_X^* is defined as

$$E_X^* = (s + m_X^2 - m_N^2), \quad (\text{A.4})$$

where m_X is the invariant mass of X . p_X^* is

$$p_X^* = \sqrt{E_X^* - m_X^2}. \quad (\text{A.5})$$

A.2 Gottfried-Jackson frame

The choice of axes in the $K^+\pi^+\pi^-$ rest frame used in Sec. 6 is known as the Gottfried-Jackson frame. The axes are defined by

$$\begin{aligned} \hat{z}_{GJ} &= \frac{\vec{p}_\gamma}{|\vec{p}_\gamma|} \\ \hat{y}_{GJ} &= \frac{\hat{z}_{GJ} \times \vec{p}_{\Lambda(1520)}}{|\hat{z}_{GJ} \times \vec{p}_{\Lambda(1520)}|} \\ \hat{x}_{GJ} &= \hat{y}_{GJ} \times \hat{z}_{GJ}, \end{aligned} \quad (\text{A.6})$$

where \vec{p}_γ and $\vec{p}_{\Lambda(1520)}$ are the momenta of the beam photon and $\Lambda(1520)$ in the $K^+\pi^+\pi^-$ rest frame.

A.3 Helicity frame

The helicity frame is in the rest frame of the vector meson, boosted from the Gottfried-Jackson frame along the direction of the vector meson. The axes are defined by

$$\begin{aligned}\hat{z}_H &= \frac{\vec{p}_V}{|\vec{p}_V|} \\ \hat{y}_H &= \frac{\hat{z}_{GJ} \times \hat{z}_H}{|\hat{z}_{GJ} \times \hat{z}_H|} \\ \hat{x}_H &= \hat{y}_H \times \hat{z}_H,\end{aligned}\tag{A.7}$$

where \vec{p}_V is the momentum of the Vector meson in the Gottfried-Jackson frame.

APPENDIX B

Fits to the K^+K^- Mass for ϕ Yields

Plots of the K^+K^- that were fit with a Gaussian + polynomial background in order to calculate the ϕ yield.

Fig. B.1 and B.2 are the K^+K^- mass in 30 MeV wide bins of $\pi^0\eta$ mass. Fig. B.3 are the K^+K^- mass in 60 MeV wide bins of $K^+K^-\pi^0\eta$ mass.

Fig. B.4 are the K^+K^- mass in 50 MeV wide bins of $\pi^0\eta$ mass. Fig. B.5 are the K^+K^- mass in 50 MeV wide bins of $K^+K^-\pi^0\pi^0$ mass.

Fig. B.6 and B.7 are the K^+K^- mass in 25 MeV wide bins of $\pi^0\eta$ mass. Fig. B.8 and B.9 are the K^+K^- mass in 25 MeV wide bins of $K^+K^-\pi^+\pi^-$ mass.

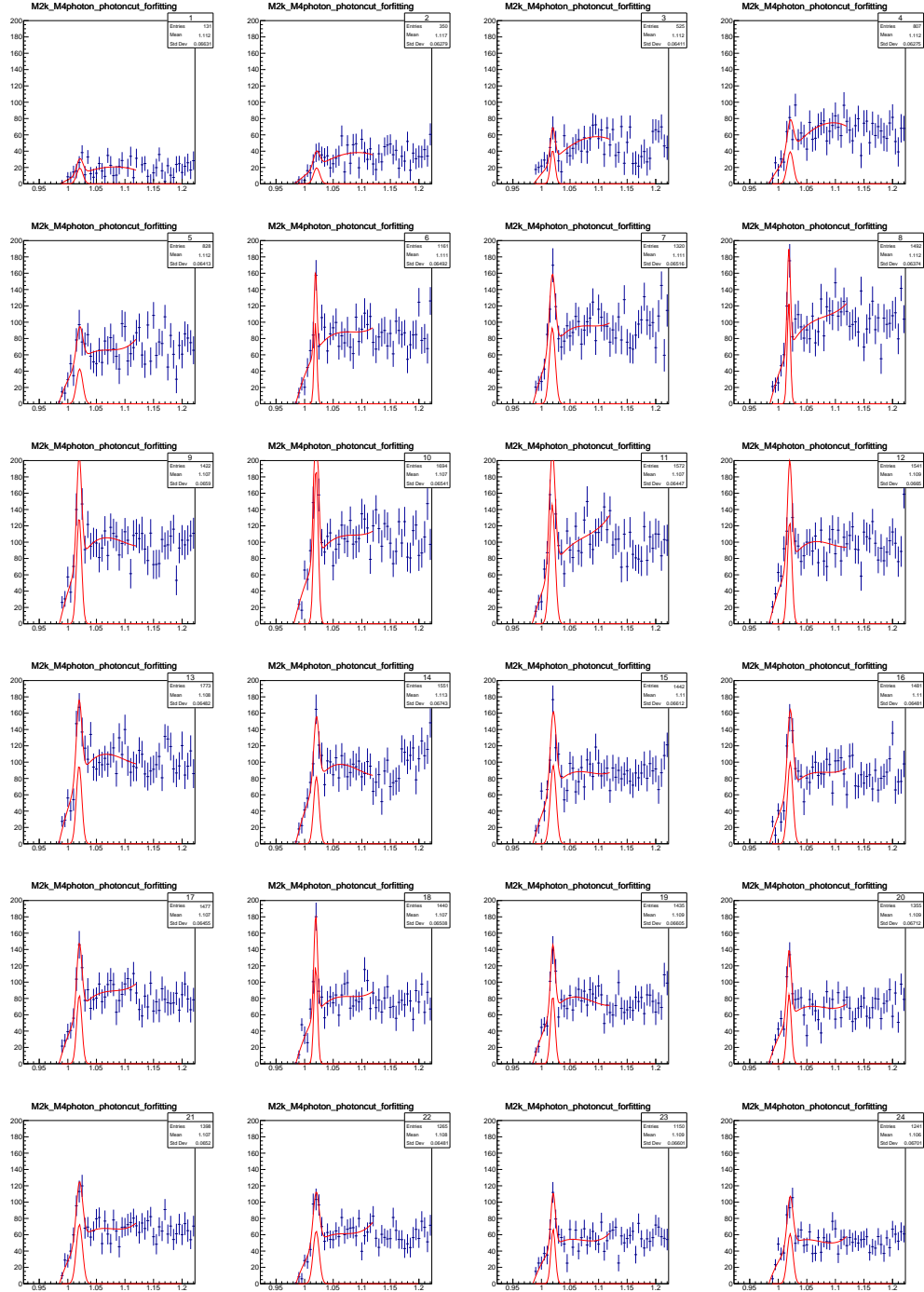


FIG. B.1: Fits to the ϕ peak in the K^+K^- mass in $30 \text{ MeV}/c^2$ bins of the $\pi^0\eta$ mass. The Gaussian + polynomial function that is used to fit the data is shown in red. The Gaussian extracted from the fit is also shown in red. The first mass bin starts at $0.7 \text{ GeV}/c^2$ $\pi^0\eta$ mass and the last bin is $1.42 \text{ GeV}/c^2$. ϕ yields determined from these fits are plotted in Fig. 4.7(a).

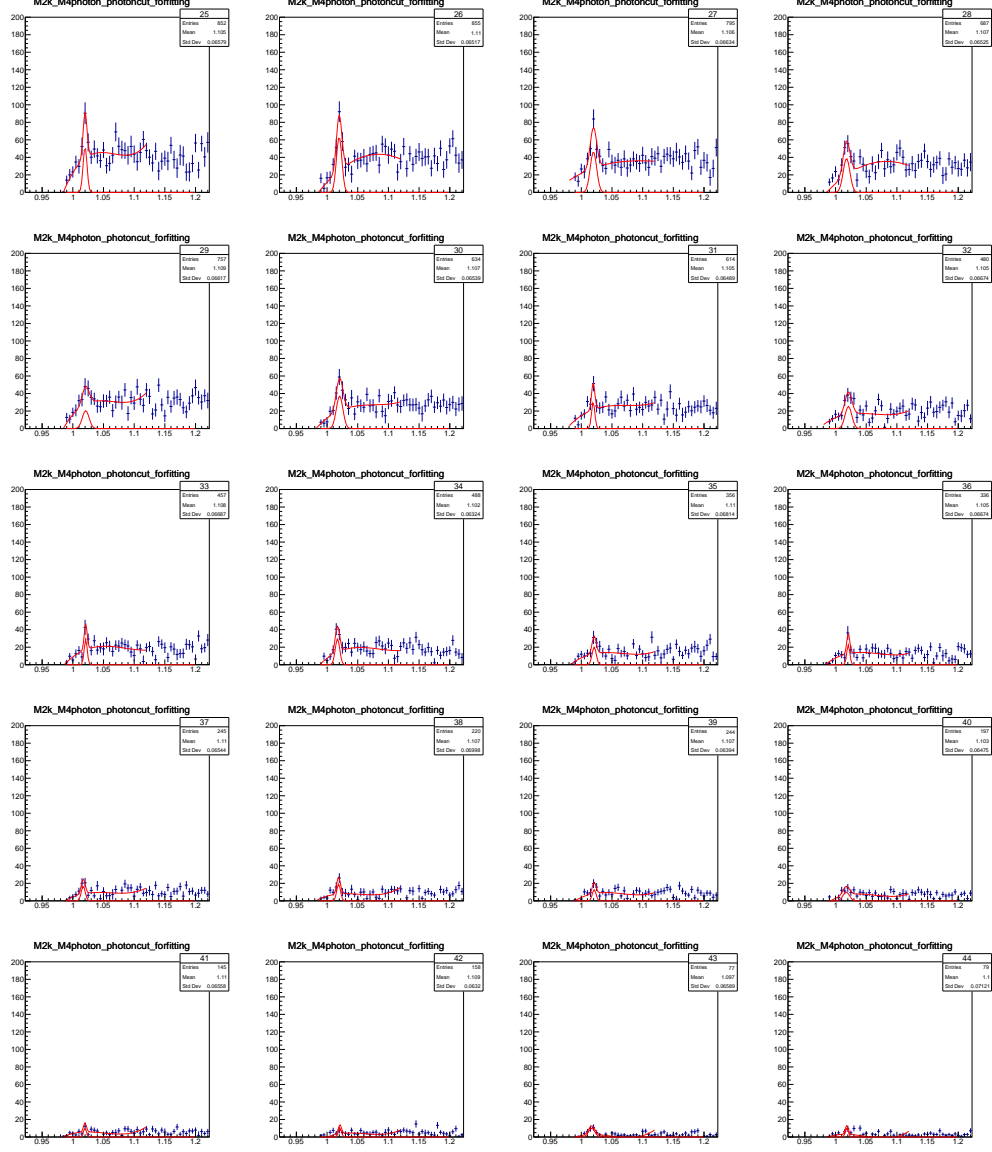


FIG. B.2: Fits to the ϕ peak in the K^+K^- mass in $30 \text{ MeV}/c^2$ bins of the $\pi^0\eta$ mass. The Gaussian + polynomial function that is used to fit the data is shown in red. The Gaussian extracted from the fit is also shown in red. The first mass bin starts at $1.47 \text{ GeV}/c^2$ $\pi^0\eta$ mass and the last bin is $2.04 \text{ GeV}/c^2$. ϕ yields determined from these fits are plotted in Fig. 4.7(a).

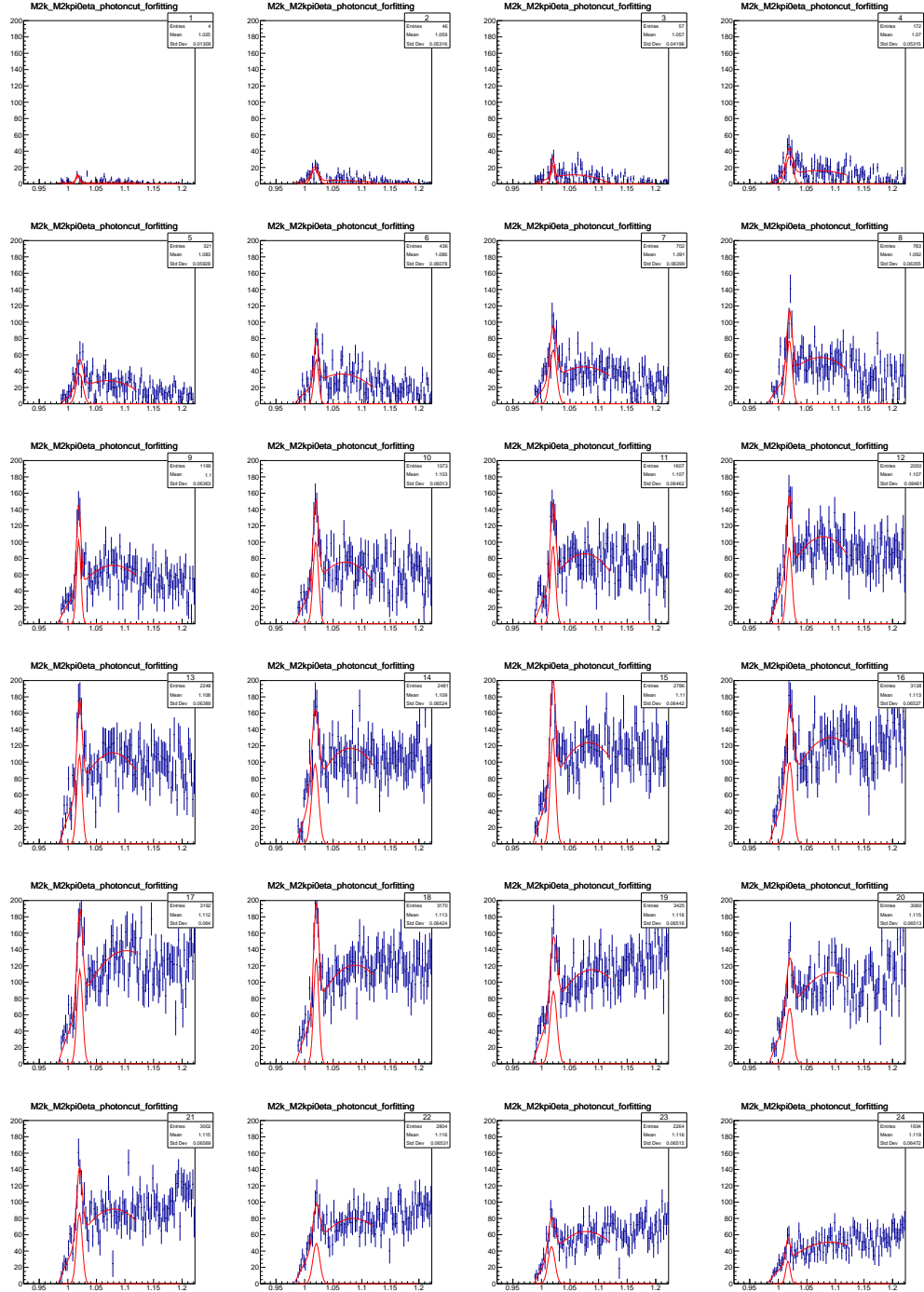


FIG. B.3: Fits to the ϕ peak in the K^+K^- mass in $60 \text{ MeV}/c^2$ bins of the $K^+K^-\pi^0\eta$ mass. The Gaussian + polynomial function that is used to fit the data is shown in red. The Gaussian extracted from the fit is also shown in red. The first mass bin starts at $1.8 \text{ GeV}/c^2$ $K^+K^-\pi^0\eta$ mass and the last bin is $1.42 \text{ GeV}/c^2$. ϕ yields determined from these fits are plotted in Fig. 4.7(b).

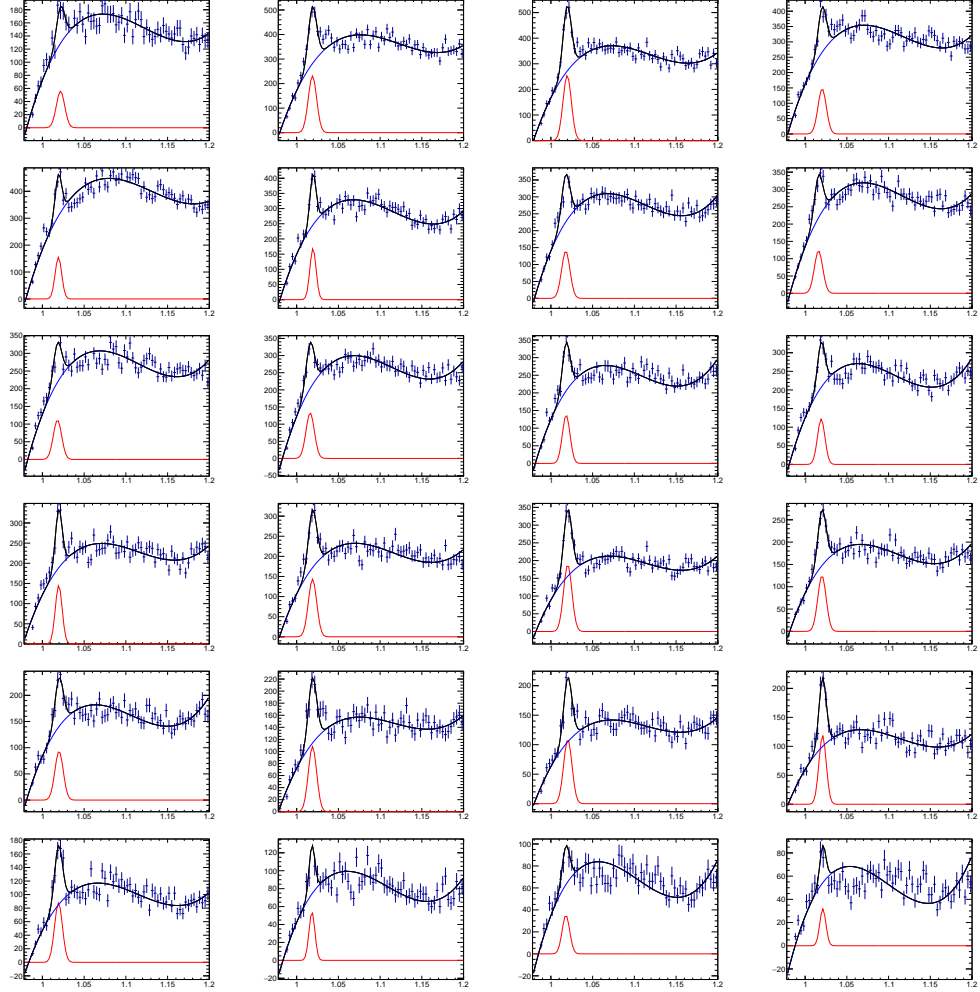


FIG. B.4: Fits to the ϕ peak in the K^+K^- mass in $50 \text{ MeV}/c^2$ bins of the $\pi^0\pi^0$ mass. The black line is the Gaussian + polynomial function fitted to the data. The red line is the Gaussian function and the blue line is the polynomial background extracted from the fit. ϕ yields determined from these fits are plotted in Fig. 4.12(a).

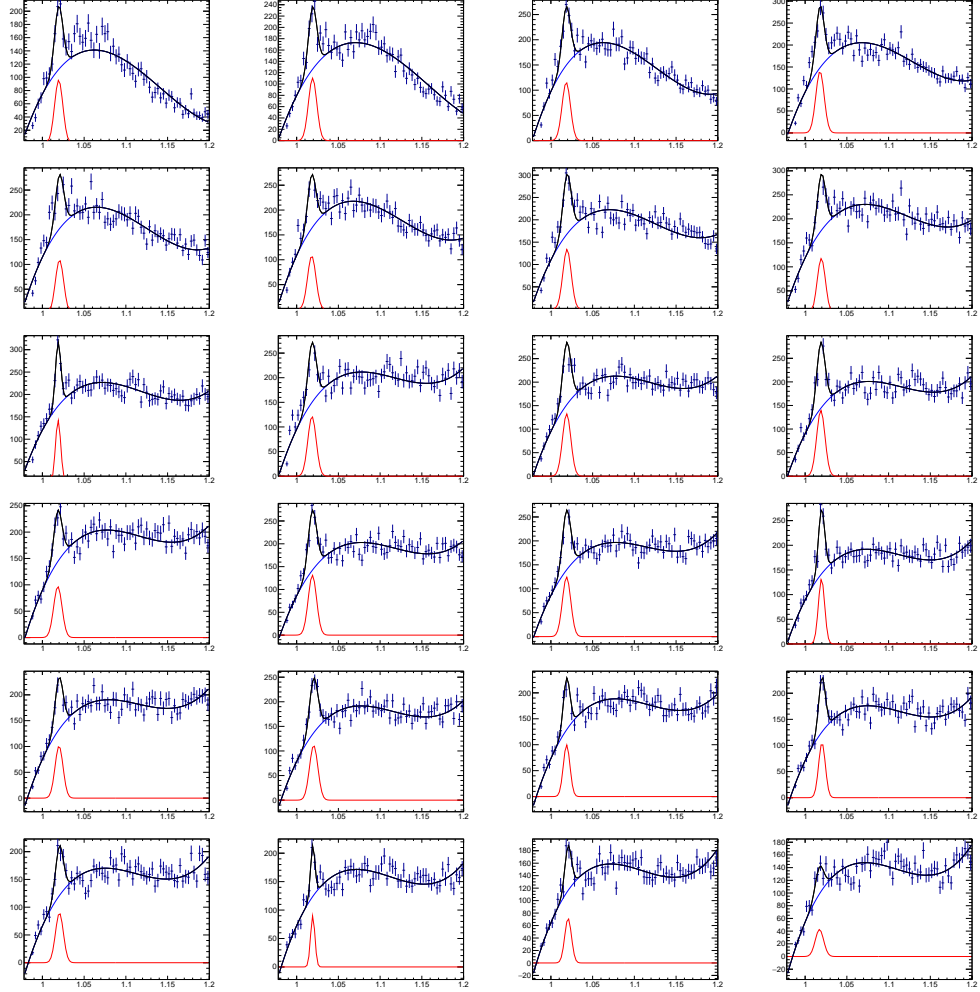


FIG. B.5: Fits to the ϕ peak in the K^+K^- mass in $50 \text{ MeV}/c^2$ bins of the $K^+K^-\pi^0\pi^0$ mass. The black line is the Gaussian + polynomial function fitted to the data. The red line is the Gaussian function and the blue line is the polynomial background extracted from the fit. ϕ yields determined from these fits are plotted in Fig. 4.12(b).

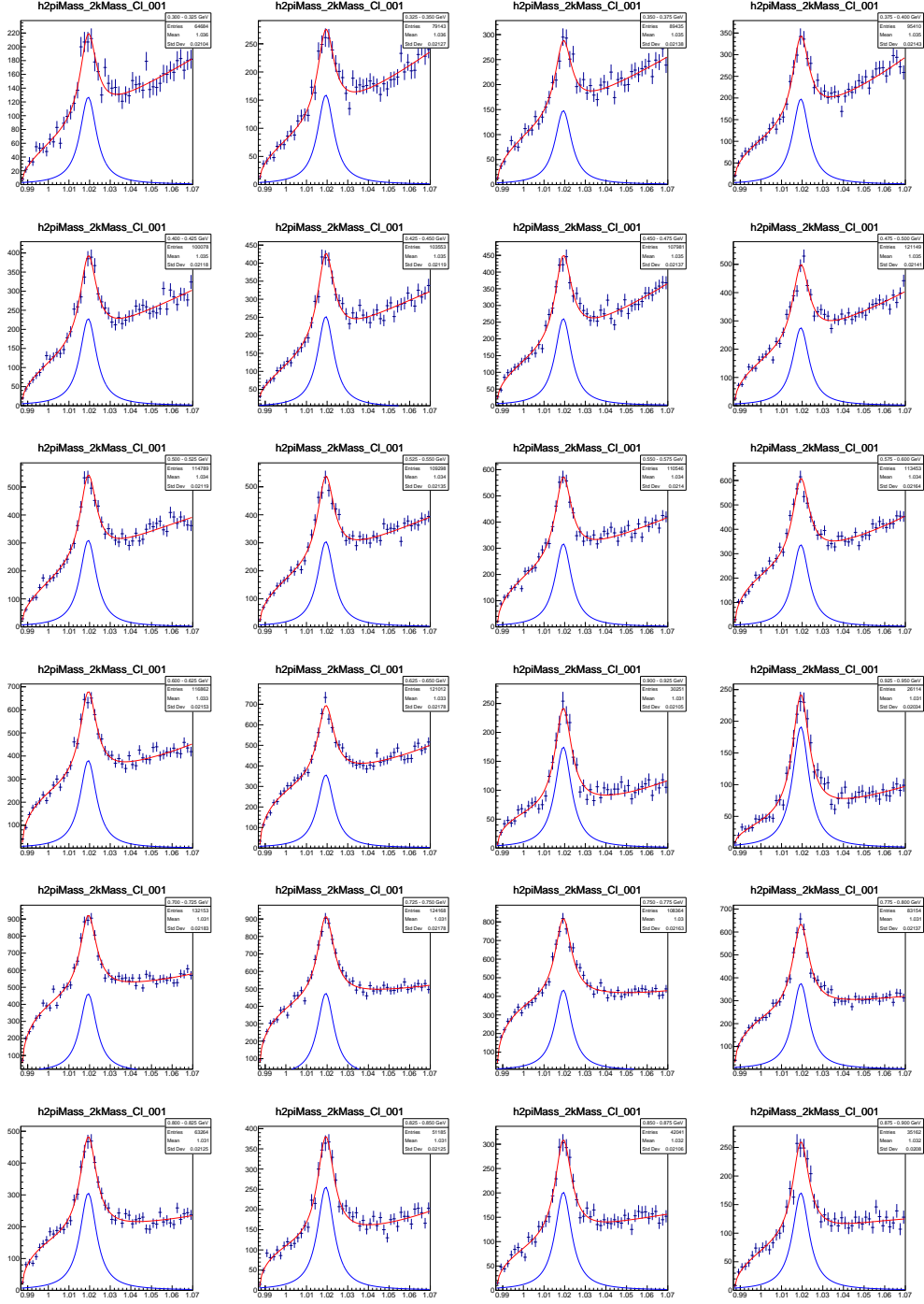


FIG. B.6: Fits to the ϕ peak in the K^+K^- mass in 25 MeV/c^2 bins of the $\pi^+\pi^-$ mass. The red line is the Gaussian + polynomial function fitted to the data. The blue line is the Gaussian function extracted from the fit. ϕ yields determined from these fits are plotted in Fig. 4.25(a).

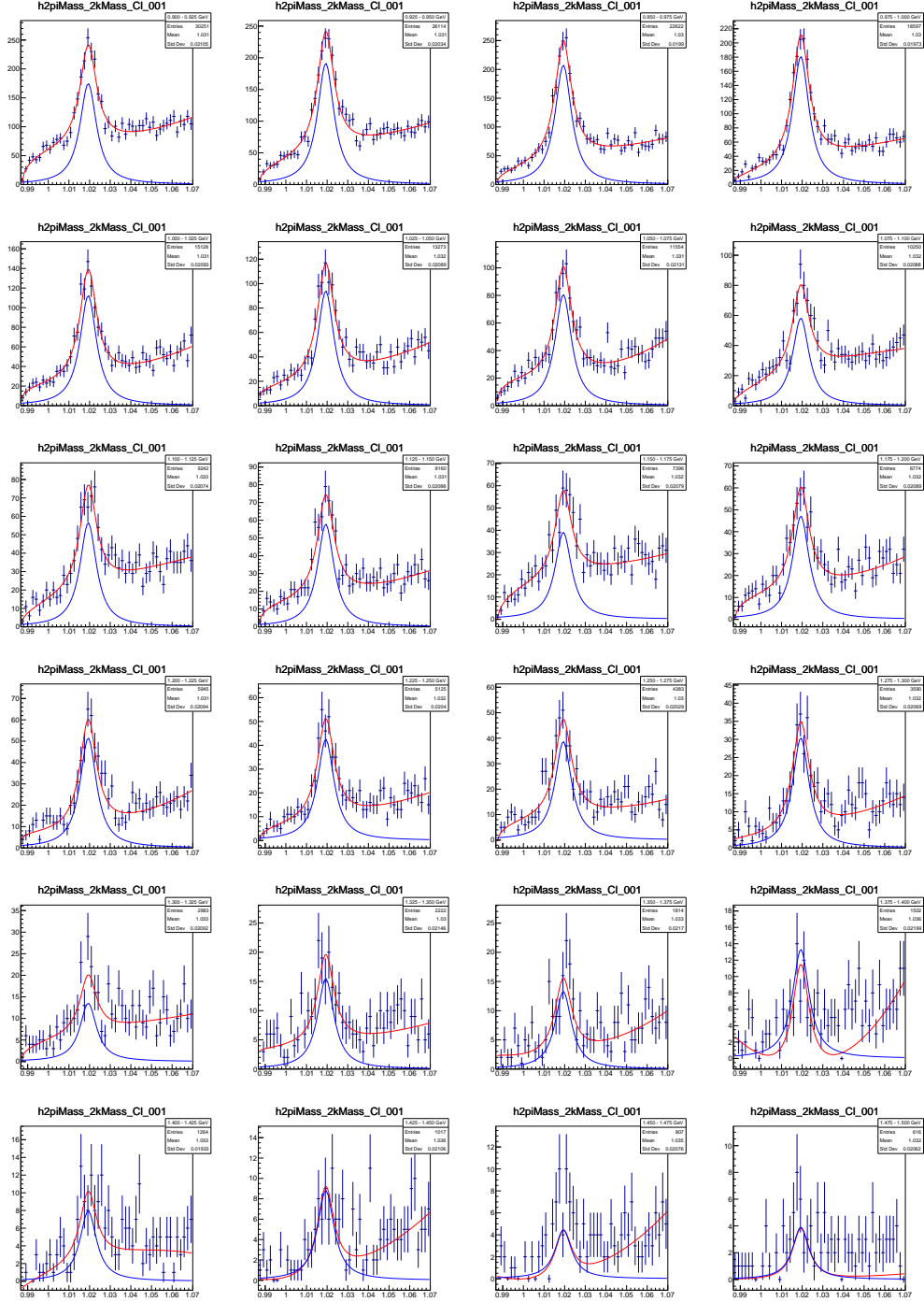


FIG. B.7: Fits to the ϕ peak in the K^+K^- mass in 25 MeV/c^2 bins of the $\pi^+\pi^-$ mass. The red line is the Gaussian + polynomial function fitted to the data. The blue line is the Gaussian function extracted from the fit. ϕ yields determined from these fits are plotted in Fig. 4.25(a).

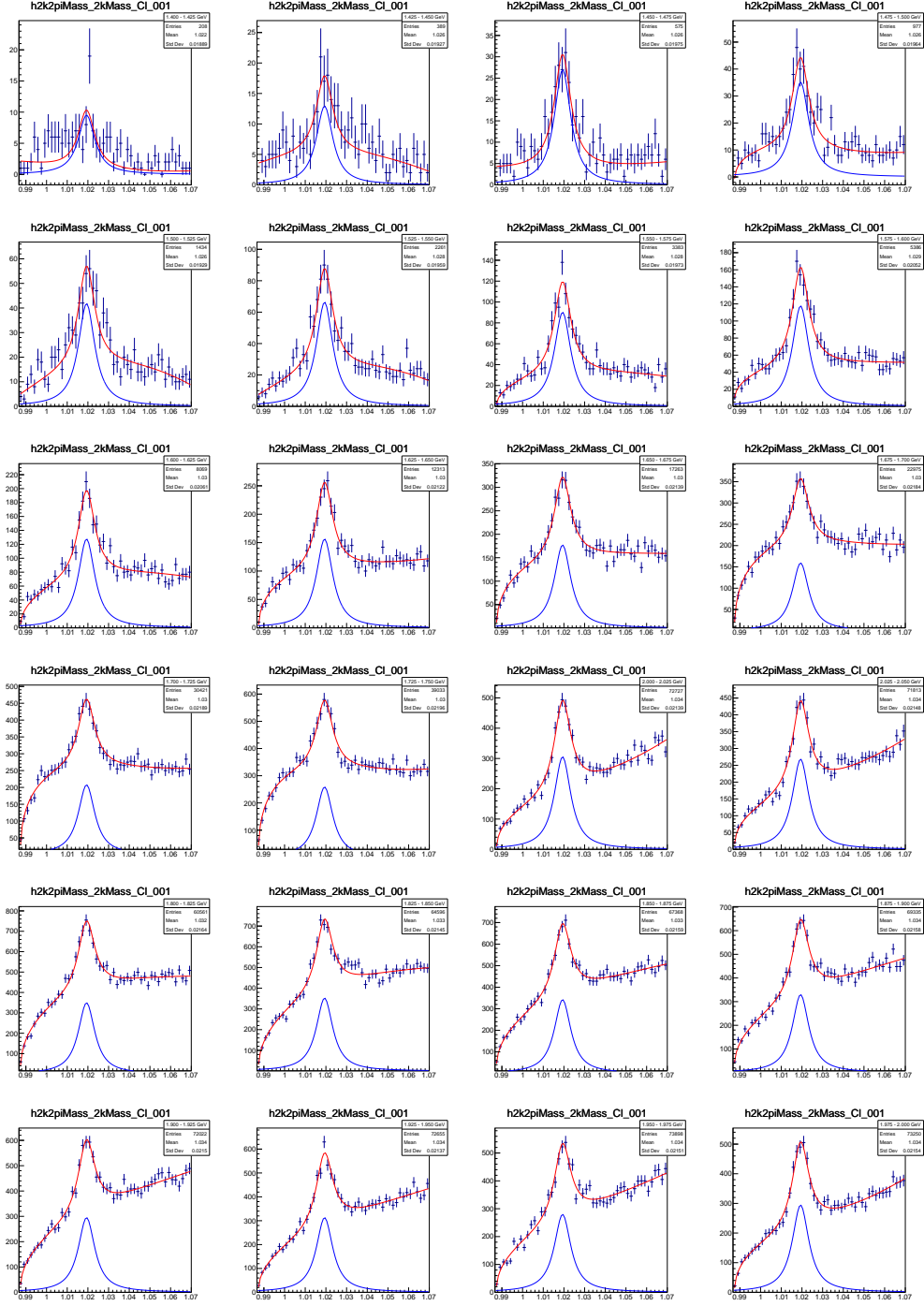


FIG. B.8: Fits to the ϕ peak in the K^+K^- mass in 25 MeV/c^2 bins of the $K^+K^-\pi^+\pi^-$ mass. The red line is the Gaussian + polynomial function fitted to the data. The blue line is the Gaussian function extracted from the fit. ϕ yields determined from these fits are plotted in Fig. 4.25(b).

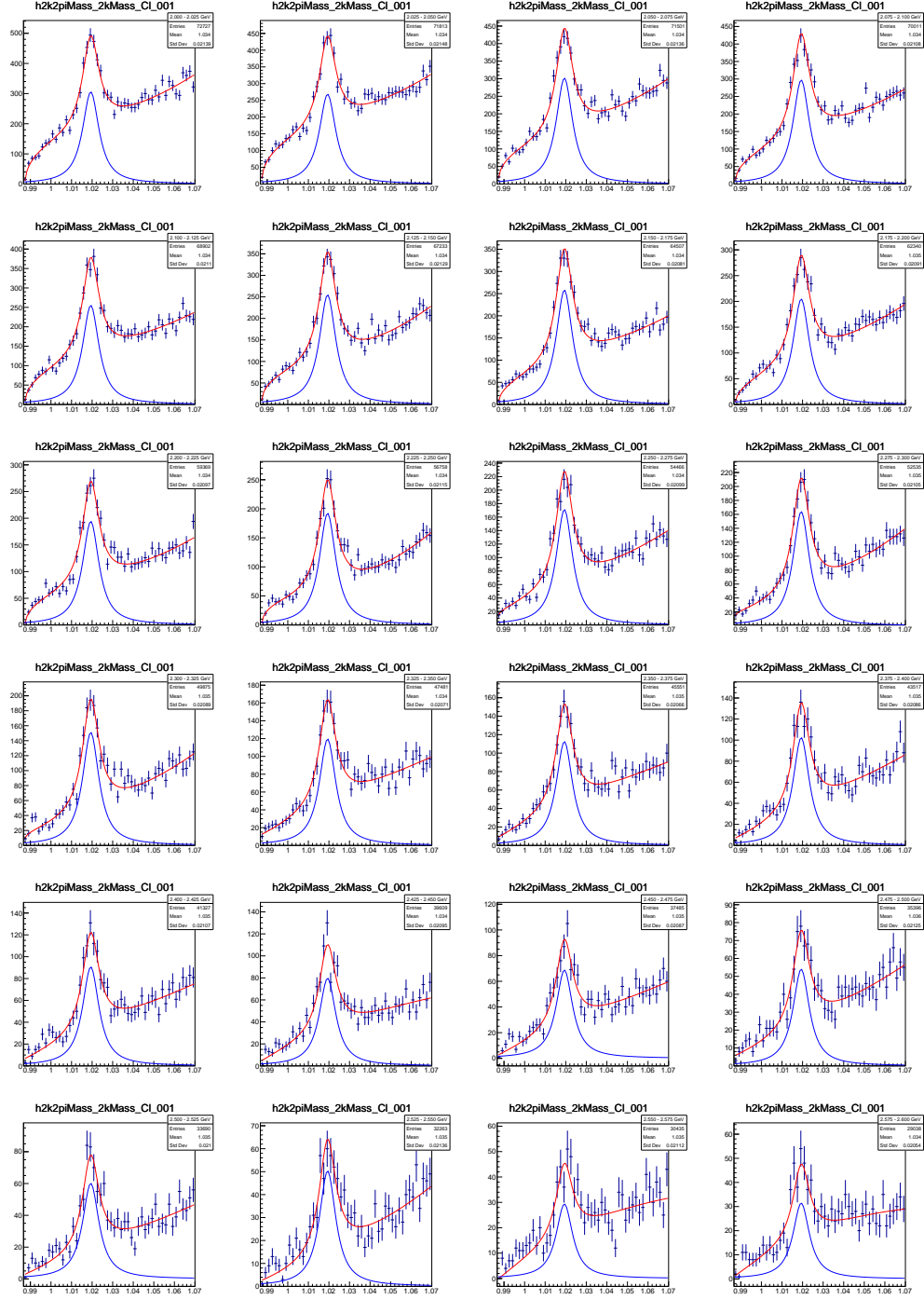


FIG. B.9: Fits to the ϕ peak in the K^+K^- mass in 25 MeV/c^2 bins of the $K^+K^-\pi^+\pi^-$ mass. The red line is the Gaussian + polynomial function fitted to the data. The blue line is the Gaussian function extracted from the fit. ϕ yields determined from these fits are plotted in Fig. 4.25(b).

BIBLIOGRAPHY

- [1] P. Langacker, *The Standard Model and Beyond, 2nd Ed.* (CRC Press, 2017), URL <https://web.sas.upenn.edu/pgl/standard-model-and-beyond-2nd-edition/>.
- [2] CMS, Physics Letters B **716**, 30 (2012), ISSN 0370-2693, URL <https://www.sciencedirect.com/science/article/pii/S0370269312008581>.
- [3] F. Englert and R. Brout, Phys. Rev. Lett. **13**, 321 (1964), URL <https://link.aps.org/doi/10.1103/PhysRevLett.13.321>.
- [4] P. W. Higgs, Phys. Rev. Lett. **13**, 508 (1964), URL <https://link.aps.org/doi/10.1103/PhysRevLett.13.508>.
- [5] G. S. Guralnik, C. R. Hagen, and T. W. B. Kibble, Phys. Rev. Lett. **13**, 585 (1964), URL <https://link.aps.org/doi/10.1103/PhysRevLett.13.585>.
- [6] R. L. Workman and Others (Particle Data Group), PTEP **2022**, 083C01 (2022).
- [7] W. Commons, *The octet of light baryons* (2008), URL https://commons.wikimedia.org/wiki/File:Baryon_octet.svg.
- [8] M. Gell-Mann, Cal Tech **Report CTSL-20** (1961), URL <https://www.osti.gov/biblio/4008239>.
- [9] Y. Ne'eman, Nuclear Physics **26**, 222 (1961), ISSN 0029-5582, URL <https://www.sciencedirect.com/science/article/pii/0029558261901341>.

- [10] M. Gell-Mann, Phys. Lett. **8**, 214 (1964), URL <https://www.sciencedirect.com/science/article/pii/S0031916364920013>.
- [11] G. Zweig, Tech. Rep., CERN, Geneva (1964), URL <http://cds.cern.ch/record/352337>.
- [12] W. Commons, *The spin-0 nonet of mesons* (2008), URL https://en.wikipedia.org/wiki/Meson#/media/File:Meson_nonet_-_spin_0.svg.
- [13] C. Meyer and E. Swanson, Progress in Particle and Nuclear Physics **82**, 21 (2015), ISSN 0146-6410, URL <https://www.sciencedirect.com/science/article/pii/S0146641015000162>.
- [14] M. G. Alekseev, V. Y. Alexakhin, Y. Alexandrov, G. D. Alexeev, A. Amoroso, A. Austregesilo, B. Badelek, F. Balestra, J. Ball, J. Barth, et al. (COMPASS Collaboration), Phys. Rev. Lett. **104**, 241803 (2010), URL <https://link.aps.org/doi/10.1103/PhysRevLett.104.241803>.
- [15] A. Rodas, A. Pilloni, M. Albaladejo, C. Fernández-Ramírez, A. Jackura, V. Mathieu, M. Mikhasenko, J. Nys, V. Pauk, B. Ketzer, et al. (Joint Physics Analysis Center), Phys. Rev. Lett. **122**, 042002 (2019), URL <https://link.aps.org/doi/10.1103/PhysRevLett.122.042002>.
- [16] J. J. Dudek, R. G. Edwards, P. Guo, and C. E. Thomas (for Hadron Spectrum Collaboration), Phys. Rev. D **88**, 094505 (2013), URL <https://link.aps.org/doi/10.1103/PhysRevD.88.094505>.
- [17] S. L. Olsen, 53rd International Winter Meeting on Nuclear Physics (2015), URL <https://arxiv.org/abs/1511.01589>.

- [18] B. Aubert, R. Barate, D. Boutigny, F. Couderc, Y. Karyotakis, J. P. Lees, V. Poireau, V. Tisserand, A. Zghiche, E. Grauges, et al. (BABAR Collaboration), Phys. Rev. Lett. **95**, 142001 (2005), URL <https://link.aps.org/doi/10.1103/PhysRevLett.95.142001>.
- [19] C.-Z. Yuan, National Science Review **8** (2021), ISSN 2095-5138, nwab182, <https://academic.oup.com/nsr/article-pdf/8/11/nwab182/41602771/nwab182.pdf>, URL <https://doi.org/10.1093/nsr/nwab182>.
- [20] G. Mezzadri and S. Spataro, Reviews in Physics **8**, 100070 (2022), ISSN 2405-4283, URL <https://www.sciencedirect.com/science/article/pii/S2405428322000028>.
- [21] M. Ablikim, M. N. Achasov, P. Adlarson, M. Albrecht, R. Aliberti, A. Amoroso, M. R. An, Q. An, X. H. Bai, Y. Bai, et al. (BESIII Collaboration), Phys. Rev. D **106**, 072001 (2022), URL <https://link.aps.org/doi/10.1103/PhysRevD.106.072001>.
- [22] Q. Li, L.-C. Gui, M.-S. Liu, Q.-F. Lü, and X.-H. Zhong, Chinese Physics C **45**, 023116 (2021), URL <https://dx.doi.org/10.1088/1674-1137/abcf22>.
- [23] Y. Ma, Y. Chen, M. Gong, and Z. Liu, Chinese Physics C **45**, 013112 (2021), URL <https://dx.doi.org/10.1088/1674-1137/abc241>.
- [24] J. P. Lees, V. Poireau, E. Prencipe, V. Tisserand, J. Garra Tico, E. Grauges, M. Martinelli, D. A. Milanes, A. Palano, M. Pappagallo, et al. (BABAR Collaboration), Phys. Rev. D **86**, 012008 (2012), URL <https://link.aps.org/doi/10.1103/PhysRevD.86.012008>.
- [25] C. P. Shen, C. Z. Yuan, P. Wang, X. L. Wang, I. Adachi, H. Aihara, K. Arinstein, V. Aulchenko, A. M. Bakich, E. Barberio, et al. (Belle Collaboration), Phys.

- Rev. D **80**, 031101 (2009), URL <https://link.aps.org/doi/10.1103/PhysRevD.80.031101>.
- [26] M. Ablikim, M. N. Achasov, X. C. Ai, O. Albayrak, M. Albrecht, D. J. Ambrose, A. Amoroso, F. F. An, Q. An, J. Z. Bai, et al. (BESIII Collaboration), Phys. Rev. D **91**, 052017 (2015), URL <https://link.aps.org/doi/10.1103/PhysRevD.91.052017>.
- [27] T. Barnes, N. Black, and P. R. Page, Phys. Rev. D **68**, 054014 (2003), URL <https://link.aps.org/doi/10.1103/PhysRevD.68.054014>.
- [28] H.-X. Chen, X. Liu, A. Hosaka, and S.-L. Zhu, Phys. Rev. D **78**, 034012 (2008), URL <https://link.aps.org/doi/10.1103/PhysRevD.78.034012>.
- [29] L. Zhao, N. Li, S.-L. Zhu, and B.-S. Zou, Phys. Rev. D **87**, 054034 (2013), URL <https://link.aps.org/doi/10.1103/PhysRevD.87.054034>.
- [30] G.-J. Ding and M.-L. Yan, Physics Letters B **650**, 390 (2007), ISSN 0370-2693, URL <https://www.sciencedirect.com/science/article/pii/S0370269307006107>.
- [31] C. Vaquera-Araujo and M. Napsuciale, Physics Letters B **681**, 434 (2009), ISSN 0370-2693, URL <https://www.sciencedirect.com/science/article/pii/S0370269309012465>.
- [32] S. Godfrey and J. Napolitano, Rev. Mod. Phys. **71**, 1411 (1999), URL <https://link.aps.org/doi/10.1103/RevModPhys.71.1411>.
- [33] A. Hamdi, PhD Thesis, Goethe University Frankfurt (2020), URL <https://www.osti.gov/biblio/1768393>.
- [34] M. E. Peskin and D. V. Schroeder, *An Introduction to Quantum Field Theory* (Westview Press, 1995).

- [35] J. J. Sakurai and J. Napolitano, *Modern Quantum Mechanics, 2nd Ed.* (Pearson, 2013).
- [36] V. Mathieu, M. Albaladejo, C. Fernández-Ramírez, A. W. Jackura, M. Mikhasenko, A. Pilloni, and A. P. Szczepaniak (Joint Physics Analysis Center Collaboration), *Phys. Rev. D* **100**, 054017 (2019), URL <https://link.aps.org/doi/10.1103/PhysRevD.100.054017>.
- [37] C. W. Salgado and D. P. Weygand, *Physics Reports* **537**, 1 (2014), ISSN 0370-1573, on the Partial-Wave Analysis of Mesonic Resonances Decaying to Multiparticle Final States Produced by Polarized Photons, URL <https://www.sciencedirect.com/science/article/pii/S0370157313004328>.
- [38] S. Adhikari, C. Akondi, H. Al Ghouli, A. Ali, M. Amaryan, E. Anassontzis, A. Austregesilo, F. Barbosa, J. Barlow, A. Barnes, et al., *Nuclear Instruments and Methods in Physics Research Section A: Accelerators, Spectrometers, Detectors and Associated Equipment* **987**, 164807 (2021), ISSN 0168-9002, URL <https://www.sciencedirect.com/science/article/pii/S0168900220312043>.
- [39] A. Freyberger, in *Proc. 6th International Particle Accelerator Conference (IPAC'15), Richmond, VA, USA, May 3-8, 2015* (JACoW, Geneva, Switzerland, 2015), no. 6 in International Particle Accelerator Conference, pp. 1–5, ISBN 978-3-95450-168-7, <https://doi.org/10.18429/JACoW-IPAC2015-MOXGB2>, URL <http://jacow.org/ipac2015/papers/moxgb2.pdf>.
- [40] C. W. Leemann, D. R. Douglas, and G. A. Krafft, *Annual Review of Nuclear and Particle Science* **51**, 413 (2001), <https://doi.org/10.1146/annurev.nucl.51.101701.132327>, URL <https://doi.org/10.1146/annurev.nucl.51.101701.132327>.

- [41] R. Suleiman, P. Adderley, J. Grames, J. Hansknecht, M. Poelker, and M. Stutzman, AIP Conference Proceedings **1970**, 050007 (2018), <https://aip.scitation.org/doi/pdf/10.1063/1.5040226>, URL <https://aip.scitation.org/doi/abs/10.1063/1.5040226>.
- [42] H. Bilokon, G. Bologna, F. Celani, B. Piazzoli, R. Falcioni, G. Mannocchi, and P. Picchi, Nuclear Instruments and Methods in Physics Research **204**, 299 (1983), ISSN 0167-5087, URL <https://www.sciencedirect.com/science/article/pii/0167508783900613>.
- [43] M. Dugger, B. Ritchie, N. Sparks, K. Moriya, R. Tucker, R. Lee, B. Thorpe, T. Hodges, F. Barbosa, N. Sandoval, et al., Nuclear Instruments and Methods in Physics Research Section A: Accelerators, Spectrometers, Detectors and Associated Equipment **867**, 115 (2017), ISSN 0168-9002, URL <https://www.sciencedirect.com/science/article/pii/S0168900217305715>.
- [44] J. Jackson, *Classical Electrodynamics, 2nd Ed.* (Wiley, 1975).
- [45] P. A. Čerenkov, Phys. Rev. **52**, 378 (1937), URL <https://link.aps.org/doi/10.1103/PhysRev.52.378>.
- [46] I. M. Frank and I. E. Tamm, Compt. Rend. Acad. Sci. URSS **14**, 109 (1937), URL https://doi.org/10.1007/978-3-642-74626-0_2.
- [47] I. Adam, R. Aleksan, L. Amerman, E. Antokhin, D. Aston, P. Bailly, C. Beigbeder, M. Benkebil, P. Besson, G. Bonneaud, et al., Nuclear Instruments and Methods in Physics Research Section A: Accelerators, Spectrometers, Detectors and Associated Equipment **538**, 281 (2005), ISSN 0168-9002, URL <https://www.sciencedirect.com/science/article/pii/S0168900204020753>.

- [48] T. Matteo, PhD. Thesis, Istituto Nazionale di Fisica Nucleare, Ferrara (2017), URL https://www.fe.infn.it/u/mcontalb/TALKs/RICH/Tesi_Matteo_to_referee.pdf.
- [49] *H12700 Series / H14220 Series Data Sheet*, Hamamatsu (2019), URL https://www.hamamatsu.com/content/dam/hamamatsu-photonics/sites/documents/99_SALES_LIBRARY/etd/H12700_H14220_TPMH1379E.pdf.
- [50] P. Degtiarenko, Nuclear Instruments and Methods in Physics Research Section A: Accelerators, Spectrometers, Detectors and Associated Equipment **872**, 1 (2017), ISSN 0168-9002, URL <https://www.sciencedirect.com/science/article/pii/S0168900217308252>.
- [51] Y. Yang, PhD. Thesis, Massachusetts Institute of Technology (2021), URL <https://hdl.handle.net/1721.1/142690>.
- [52] A. Ali, F. Barbosa, J. Bessuille, E. Chudakov, R. Dzhygadlo, C. Fanelli, J. Frye, J. Hardin, A. Hurley, E. Ihloff, et al., *Initial performance of the gluex dirc detector* (2022), URL <https://arxiv.org/abs/2205.11382>.
- [53] A. Ali et al., in *International Conference on Technology and Instrumentation in Particle Physics* (2022), 2205.11382, URL <https://arxiv.org/abs/2205.11382>.
- [54] J. Hardin and M. Williams, Journal of Instrumentation **11**, P10007 (2016), URL <https://doi.org/10.1088/1748-0221/11/10/p10007>.
- [55] M. Starič, K. Inami, P. Križan, and T. Iijima, Nuclear Instruments and Methods in Physics Research Section A: Accelerators, Spectrometers, Detectors and Associated Equipment **595**, 252 (2008), ISSN 0168-9002, RICH 2007, URL <https://www.sciencedirect.com/science/article/pii/S0168900208009893>.

- [56] M. McEneaney, Undergraduate Honors Thesis, William & Mary (2020), URL <https://scholarworks.wm.edu/honorstheses/1477>.
- [57] J. O’Cain, Undergraduate Honors Thesis, William & Mary (2022), URL <https://scholarworks.wm.edu/honorstheses/1868>.
- [58] M. Starič, Nuclear Instruments and Methods in Physics Research Section A: Accelerators, Spectrometers, Detectors and Associated Equipment **639**, 252 (2011), ISSN 0168-9002, proceedings of the Seventh International Workshop on Ring Imaging Cherenkov Detectors, URL <https://www.sciencedirect.com/science/article/pii/S0168900210022473>.
- [59] R. Barsotti and M. Shepherd, Journal of Instrumentation **15**, P05021 (2020), URL <https://doi.org/10.1088/1748-0221/15/05/p05021>.
- [60] M. Ablikim, M. Achasov, P. Adlarson, S. Ahmed, M. Albrecht, A. Amoroso, Q. An, Y. Bai, O. Bakina, R. Baldini Ferroli, et al., Physics Letters B **813**, 136059 (2021), ISSN 0370-2693, URL <https://www.sciencedirect.com/science/article/pii/S0370269320308625>.
- [61] C. Vaquera-Araujo and M. Napsuciale, Physics Letters B **681**, 434 (2009), ISSN 0370-2693, URL <https://www.sciencedirect.com/science/article/pii/S0370269309012465>.
- [62] L. Van Hove, Nuclear Physics B **9**, 331 (1969), ISSN 0550-3213, URL <https://www.sciencedirect.com/science/article/pii/0550321369901333>.
- [63] M. Shepherd, R. Mitchell, J. Stevens, and A. Austregesilo, *mashephe/amptools: Version 0.13.0 release (unpublished)* (2022), URL <https://doi.org/10.5281/zenodo.6047744>.

- [64] F. James, *Statistical Methods in Experimental Physics, 2nd Ed.* (World Scientific, 2012).
- [65] M. Shepherd, Tech. Rep., Indiana University (2021), URL https://github.com/mashephe/AmpTools/blob/master/AmpTools_User_Guide.pdf.
- [66] K. P. Burnham and D. R. Anderson, *Model Selection and Multimodel Inference: A practical Information Theoretic Approach, 2nd Ed.* (Springer, 1995).
- [67] S. Kullback and R. A. Leibler, The Annals of Mathematical Statistics **22**, 79 (1951), URL <https://doi.org/10.1214/aoms/1177729694>.
- [68] G. Schwarz, The Annals of Statistics **6**, 461 (1978), ISSN 00905364, URL <http://www.jstor.org/stable/2958889>.
- [69] M. Albaladejo, A. N. H. Blin, A. Pilloni, D. Winney, C. Fernández-Ramírez, V. Mathieu, and A. Szczepaniak (Joint Physics Analysis Center), Phys. Rev. D **102**, 114010 (2020), URL <https://link.aps.org/doi/10.1103/PhysRevD.102.114010>.
- [70] R. Abdul Khalek et al., Nucl. Phys. A **1026**, 122447 (2022), 2103.05419.